Study of Neodymium isotope records from the Arabian Sea and the Amundsen Sea: Spatio-temporal evaluation of water mass circulation during the late Cenozoic

A THESIS SUBMITTED IN PARTIAL FULFILLMENT FOR THE DEGREE OF

DOCTOR OF PHILOSOPHY

IN THE SCHOOL OF EARTH, OCEAN, AND ATMOSPHERIC SCIENCES

GOA UNIVERSITY

By

Priyesh Prabhat

National Centre for Polar and Ocean Research

Headland Sada, Vasco da Gama

Goa

November 2023

DECLARATION

I, Priyesh Prabhat, hereby declare that this thesis represents work that has been carried out by me and that it has not been submitted, either in part or full, to any other University or Institution for the award of any research degree.

Place: Taleigao Plateau

Priyesh Prabhat

Date:

CERTIFICATE

I hereby certify that the above Declaration of the candidate, Priyesh Prabhat, is true, and the work was carried out under my supervision.

Dr Waliur Rahaman

Research Supervisor
Scientist E
National Centre for Polar and Ocean Research
Vasco-da-Gama, Goa 403 804

Acknowledgements

Dreams and dedication form a potent alliance for success, but they are of little value without the wishes of the people near and dear to us. I am profoundly grateful to all the people who have been a source of inspiration and strength through their blessings. Throughout the long course of this research journey, significant number of people played a pivotal role in bringing this thesis to fruition. Their names deserve a special mention in this humble expression of gratitude, as the saying goes, "no one who achieves success does so without acknowledging the help of others, the wise and confident acknowledge this help with gratitude".

In the pursuit of any endeavour, earnest and dedicated guidance is the prime component for success. Therefore, my first and foremost expression of immense and deepest appreciation goes to my supervisor ***Dr. Waliur Rahaman****. His patient guidance, consistent advice, meaningful conversations, and practical comments have been crucial in shaping this thesis. I extend my sincerest gratitude to him for providing the foundation for my scientific research journey and being instrumental in the successful completion of the thesis. His dedication, enthusiasm, and passion for research, encouraged me to strive harder in my academic pursuits.*

Sincere gratitude is extended to Dr. Thamban Meloth, Director, NCPOR, for his constructive suggestions, encouragement, and support. I also extend my sincere thanks to Dr. Rahul Mohan for his care and kind words during the journey. Dr. M. Ravichandran, former Director, NCPOR is also kindly acknowledged for all his support. I am sincerely thankful to the departmental research committee members Dr. Sushant S. Naik and Prof. Vishnu M. Matta for their constructive suggestions and support.

This tale of research journey is incomplete without the deep sense of gratitude and heartfelt thanks to my lab colleagues. The bond that I formed with Lathika N. and Mohd Tarique and the teachings and training which I received with many light-hearted moments from them are ever-lasting. I had a great time and received huge support from Pranav S. Prem and Mohammad Nuruzzama. Laboratory support received from Vinita, Kennisia and Ankita is highly acknowledged. Rahul Dey is kindly acknowledged for his help with MATLAB codes, statistical analysis and suggestions.

Acknowledgement and sincere appreciation is owed to all scientists and staff members of the National Centre for Polar and Ocean Research for providing essential academic and administrative support. Recognition is extended to the Ministry of Earth Sciences (MoES), Government of India, for funding through the "PACER-Cryosphere and Climate" project and the University Grants Commission (UGC) for the NET (JRF) fellowship. Special thanks to the Vice-Chancellor, Registrar, Dean, and all staff members of the School of Earth, Ocean and Atmospheric Science at Goa University for their unwavering support.

True friends cheer you in the gloomiest of situations and I have always been blessed to have many who stood by me. A special thanks is owed to Rahul, Tarique, Lathika, Padmasini, Nibedita, Nuruzzama, Pranav for being there and making this journey a pleasant one. I sincerely thank Bhanu, Tariq, Alok, Aritri, Gautami, Ashish, Neha, Pooja and Pallavi whose words of advice helped me to be on the right track. I would also like to extend my thanks to Vishwa Deepak, Shashi, Aditya, Ankit, Siddhi, Pradyumna, Ramanand, Abhinay and Bibhuti for their encouragement and emotional support.

The support and love that one receives from the family is unparalleled and can't be expressed with mere words. I would like to especially mention the love, care and encouragement received from my Nani (grandmother) Mrs. Vimla Devi and Nana ji (grandfather) Late Mr. Rajendra Prasad Rai, aunt Mrs. Abha, my uncle Mr. Anil and Mr. Rajeev. I have always cherished my bond and great friendship with my sister Mrs. Astha and younger ones Dr. Animesh and Dr. Anushtup. My nephew Adriyan is the youngest star among all these mentions. Words are not enough to express how grateful I am to my parents Mrs. Kiran Singh and Mr. Ashok Kumar Singh who have always supported, comforted and motivated me to excel throughout life. Additionally, special heartfelt gratitude is owed to my best friend and life companion Rashmi. Her love, appreciation, understanding, consistent encouragement and unwavering support empowered me to navigate through the challenges.

Priyesh Prabhat

Dedicated to Nani, Ma and Papa.

Table of Contents

List of Tables

List of Figures

Chapter 1

Introduction

Ocean circulation underwent significant changes in geological past and influenced global climate which in turn provides feedback to ocean circulation and maintain a critical balance (Coffin et al., 1992; Dhuime et al., 2015; Hawkesworth et al., 2020). The primary driver of the long term climate and oceanic ocean circulation are the Earth's tectonics and its orbital geometry (De Vleeschouwer et al., 2017; Flower and Kennett, 1994; Laskar et al., 1993). The high frequency climate change (10^4 to 10^5 years) has been attributed to periodic oscillations of Earth's orbital parameters as eccentricity, obliquity, and precession which majorly govern the amount of solar energy received (Laskar et al., 2011; Laskar et al., 1993; Zachos et al., 2001). Climate changes are also modulated by the Earth's boundary conditions defined as the ocean gateways and its bathymetry, continent geography and topography which are primarily controlled by the plate tectonics in million year time scales (Crowley and Burke, 1998; Hodell and Venz-Curtis, 2006; Zachos et al., 2001; Zachos et al., 2008). Throughout the turbulent geological history of the Earth the most recent era is known as the Cenozoic (meaning recent life) era (Berggren et al., 1995; Evernden and Evernden, 1970) (Figure 1.1). This era stretches from 66 million years ago till today and has shaped the Earth's modern geology, geography and climate leading to the evolution of mammals and *Homo sapiens* (Dartnell, 2019; Palmer, 2003). Changes in the Earth climate during Cenozoic has mostly been attributed to the declining atmospheric CO_2 in addition to the changes in the geometry of the ocean-continent tectonic settings (Westerhold et al., 2020a; Zachos et al., 2001). The drawdown of the CO_2 has also been interpreted as a consequence of the tectonic realignment leading to the opening and closing of the ocean gateways and change in the precipitation pattern resulting in enhanced silicate weathering (Kronen Jr, 1998; Steinthorsdottir et al., 2021).

Cenozoic era climate has changed in the several steps from warm Earth with ice free poles to ice capped poles and colder Earth (Pickering, 2000; Zalasiewicz and Williams, 2021). Early Cenozoic is associated with the absence of continental ice, high sea levels, low temperature gradients between the poles and equator, high atmospheric CO_2 and higher global temperatures (Miller et al., 2020; Zachos et al., 2001). Based on the reconstructed temperature conditions Westerhold et al. (2020c) suggest that Warmhouse to Hothouse

condition with 5–10°C warmer than today prevailed from 66 to 34 Ma. Afterwards it transitioned into Coolhouse condition at ~34 Ma and prevailed till mid-Pliocene M2 glaciation (3.3 Ma). The Icehouse climate state, established at Pliocene-Pleistocene transition, was driven by Northern Hemisphere ice sheet waxing and waning. It is important to highlight that most of the inferences of Cenozoic climate are based on the stable isotope records from the carbonate shells of the benthic foraminifera (Evans et al., 2018; Mudelsee et al., 2014; Tiwari et al., 2015; Zachos et al., 2001). These records suggest, the first continuous icesheet in the Antarctica appeared around ~33 Ma (Escutia et al., 2005; Gulick et al., 2017; Rohling et al., 2021) while the first continental ice sheets of the Arctic appeared around the ~5–7 Ma and with permanent polar ice cap since ~2.7 Ma (Rohling et al., 2021; Westerhold et al., 2020a; Zachos et al., 2001). Studies have shown that astronomical forcing is the controlling factor for the shift in the climate. However, major boundary conditions such as oceanic gateways and bathymetry, continental geography and topography are governed by the plate tectonics, and the atmospheric gasses concentration has always impacted the global climate system. The major boundary conditions which shifted the dynamics of the global climate during the Cenozoic include- opening of Tasmania and Drake seaways, rift volcanism of North Atlantic, uplift of Tibet Plateau, closure of Tethys seaway and Central American seaway (CAS), constriction of Indonesian seaway and steep decline in the atmospheric CO_2.

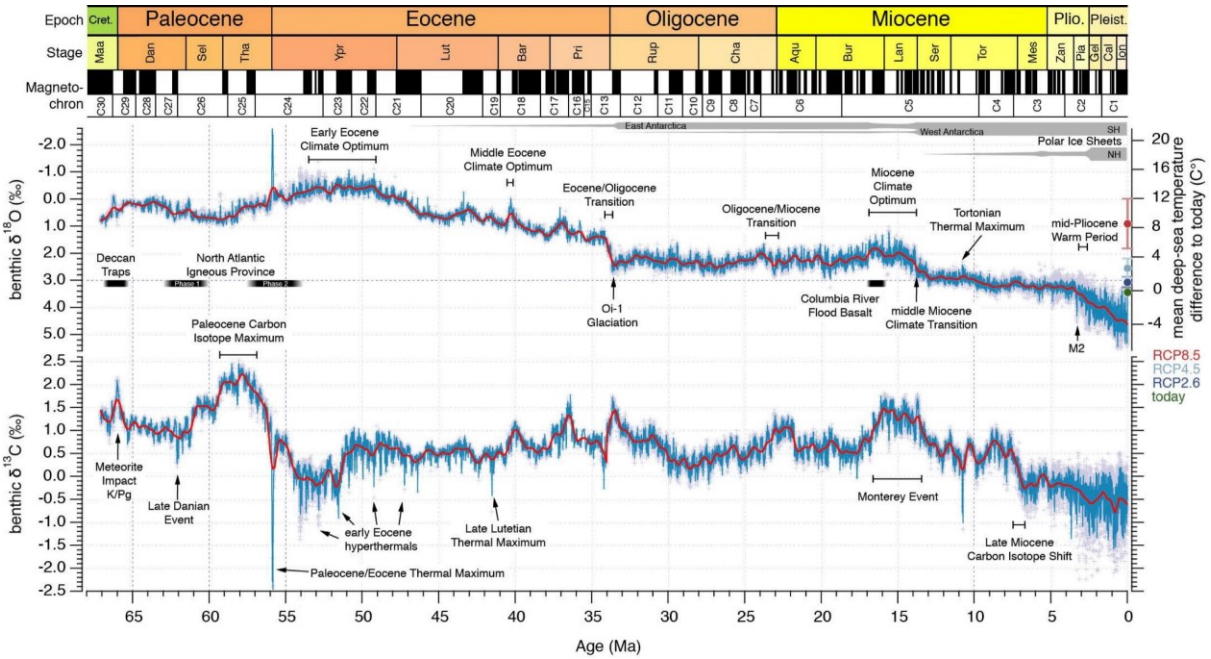

Figure 1.1: Cenozoic global reference benthic foraminifer Oxygen ($\delta^{18}O$) and Carbon ($\delta^{13}C$) isotope dataset from different ocean drilling core sites adopted from Westerhold et al. (2020c). Aqu- Aquitanian; Bur- Burdigalian; Cal- Calabrian; Cha- Chattian; Cret.- Cretaceous; Dan- Danian; Gel- Gelasian; Ion- Ionian; K/Pg- Cretaceous/Paleogene boundary; Lan- Langhian; Lut- Lutetian; M2- first major glacial event in the NH; Maa- Maastrichtian; Mes- Messinian; NH- Northern Hemisphere; Oi-1- the first major glacial period in the Oligocene; Pia- Piacenzian; Pleist.- Pleistocene; Plio.- Pliocene; Pri- Priabonian; Rup- Rupelian; Sel- Selandian; Ser- Serravallian; SH- Southern Hemisphere; Tha- Thanetian; Tor- Tortonian; Ypr- Ypresian; Zan- Zanclean.

Late Cenozoic is marked with global climate shifting into Coolhouse and was later transitioned into icehouse climatic conditions with the final phase of the major tectonic plate reconfiguration at 3.3 Ma. Modern like plate configurations were achieved during the Pliocene-Pleistocene transition, with the closure of the Tethys seaway during the middle Miocene, closure of CAS, and the constriction of the Indonesian seaway during the Pliocene-Pleistocene transition. This interval was followed by a time period of the relative tectonic quiescence during which the climate was dominantly controlled by the orbital forcing. Late Cenozoic interval also saw discernible decline in the atmospheric CO_2 and the global temperature. These change in the boundary conditions lead to permanent east and west Antarctic ice sheet cover. The bipolar ice conditions started existing similar to today with the appearance of the northern hemisphere ice sheets which became permanent since the late Pliocene. Changes in the boundary conditions resulted in the reorganisation of the deep water geometry and the emergence of the Northern and Southern sourced deep water circulation. Studies(Hayashi et al., 2020; Lear et al., 2003; McClymont et al., 2023; Sato et al., 2015; Wei and Peleo-Alampay, 2020) suggests modern like deep water circulation and the climatic conditions established with the cooling of the climate and the strengthening of the Atlantic meridional overturning circulation since the intensification Northern Hemisphere Glaciation (~2.7 Ma).

1.1 Global Ocean Circulation

Global oceans cover 71% of the earth's surface and thus receives most of the incoming solar radiation and plays a key role in the distribution of heat, nutrients and dissolved gases through the movement of the ocean water. The moving Ocean water based on their forcing mechanism can broadly be divided into wind and the buoyancy driven circulation. Wind driven circulation affects the surface of the ocean and results in the formation of the surface currents by the pushing of the surface water by the wind. The direction and extent of surface currents movement is determined by the atmospheric

circulation and the continental landmass present. The buoyancy driven circulation known as the thermohaline circulation (THC; thermo = temperature, halos = salt), is a density driven circulation caused by difference in the temperature and the salinity of the water masses. THC comprises of surface, intermediate, deep and bottom water circulation. Modern THC acts as a conveyor belt and results in global overturning circulation (GOC) pattern (Figure 1.2), driven by deep water mass formation at high latitudes in the sub-polar North Atlantic and circum-Antarctic regions, and the surface water returning from Pacific and Indian and Atlantic Oceans to these regions. At the high latitudes warm water gets modified to cold and dense water which sinks and flows equatorward and upwells in different ocean basins. The down-welled cold and dense water in the high latitude ventilates the deep basins as it acts as a sink for the dissolved gases (CO_2, O_2 etc.) and release them in the upwelling regions acting as the source region for gases like CO_2. The balance of source and sinks of CO_2 modulate atmospheric CO_2 and thus global climate (Anagnostou et al., 2016; Hönisch et al., 2012; Sherwood et al., 2020).. The upwelling GOC brings nutrient rich deep water to the surface which support surface ocean productivity. While the surface waters transports heat (roughly 10^{15} W) to the high latitudes oceans and plays a critical role for the Earth's climate. Deep water formation as a result of the sinking of the water masses is the process closely associated with convection/vertical mixing, is a localised phenomenon and restricted to high latitude oceans. These deep waters mostly spread as deep western boundary currents (DWBC). Deep water formed in the North Atlantic reaches Southern Ocean and gets mixed with recirculated water from the Indian and the Pacific Ocean and the deep water formed in Southern Ocean and form upper and lower cell of the Circumpolar Deep Water (CDW) respectively. In contrast to the sinking, upwelling is not localised. Upwelling of the waters occur in the coastal regions as a result of Coriolis force and the open ocean throughout all the basins due to the buoyancy loss is aided by the wind (Ekman divergence), dominantly in the Antarctic circumpolar region (Talley, 2002; Tomczak and Godfrey, 2003). The THC is closed by the return flow of the upwelling deep waters in the thermocline of the Indian and the Pacific Ocean, and the northward flow of the Antarctic Intermediate water (AAIW) formed as a result of the upwelled deep waters in the Southern Ocean (Talley, 2002). The upwelled deep waters in the Pacific Ocean enters the Indian Ocean via Indonesian throughflow (ITF, Figure 1.2b). From the Indian Ocean these waters enter the Southern and Atlantic Ocean via Agulhas Retroflection and Agulhas leakage off South Africa (Rahmstorf, 2006; You, 2000).

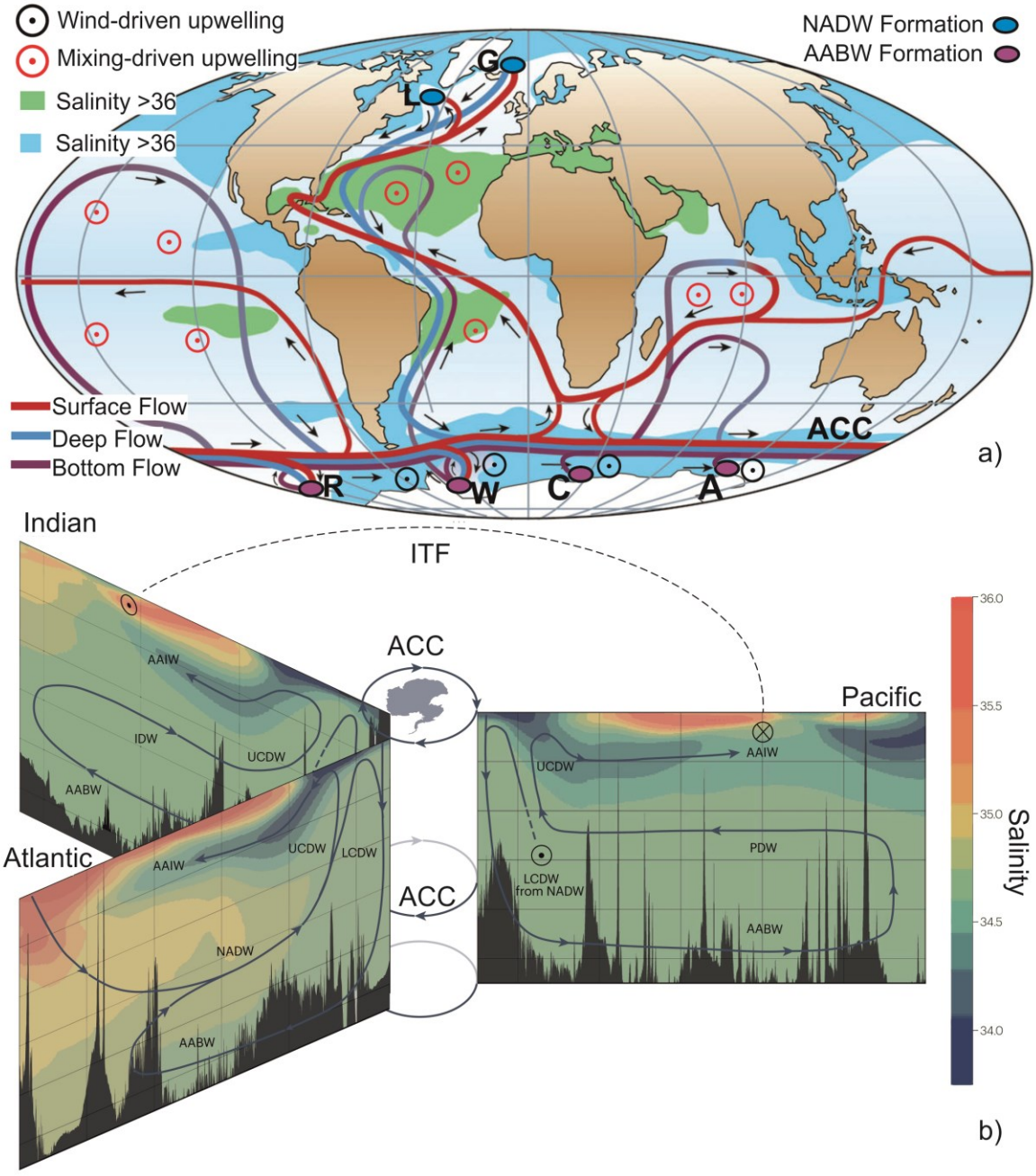

Figure 1.2: Global overturning circulation. a) Simplified sketch of global overturning circulation modified after Rahmstorf (2006). G- Greenland Sea, L- Labrador Sea, R- Ross Sea, W- Weddell Sea, C- Cape Darnley (Prydz Bay), A- Adelie Coast; b) Detailed section profile of global overturning circulation in different ocean basins adopted from Sikes et al. (2023). Arrow indicates the direction of flow. NADW- North Atlantic Deep Water, AABW- Antarctic Bottom Water, ACC- Antarctic Circumpolar Current, AAIW- Antarctic Intermediate Water, IDW- Indian Deep Water, PDW- Pacific Deep Water, UCDW- Upper Circumpolar Deep Water, LCDW- Lower Circumpolar Deep Water, ITF- Indonesian Throughflow. In Southern Ocean as a nexus for the interaction of global ocean water where northern sourced deep water masses upwell to the surface, mix, modify and downwell to re-form bottom and intermediate water.

Formation of deep water in the North Atlantic: Sinking of the surface water in the Labrador Sea and Greenland-Norwegian Sea in the North Atlantic results in the formation of North Atlantic Deep Water (NADW) (Figure 1.2a) (Tomczak and Godfrey, 2003). Ocean basins are filled by NADW in depths ranging from 1000 m to 4000 m. The Arctic Ocean receives water from the precipitation, river runoff, Bering Strait and the North Atlantic current (NAC) through the West Spitsbergen current and the Norwegian Coastal Current, and contributes significantly to NADW formation. The Arctic overflow waters through the Fram Strait compelled by the Coriolis force is transported via East Greenland current. Arctic water after passing through the Fram Strait, mixes with colder and freshened deep waters of the Greenland and the Norwegian Sea and sinks to greater depths after crossing the Greenland-Iceland-Faroe-Scotland Ridge . The deep waters formed in Greenland and the Norwegian Sea is occupies the lower depths (beneath 2000 m) of the NADW. The sinking of the water as a result of the open ocean convection in the Labrador Sea results in less dense water which occupies the upper depths (above 2000 m) of the NADW.

Formation of bottom water in the circum-Antarctic regions: Cold water sinks to form Antarctic Bottom Water (AABW) in the circum-Antarctic regions at the Weddell Sea, Ross Sea, Adelie coast of Wilkes Land and the Prydz Bay (Figure 1.2a). Dense Shelf Water (DSW, precursor of AABW) is formed through brine rejection and heat loss by sea ice formation in the coastal polynyas(Orsi et al., 1999). The open water polynyas formed by the advection of sea ice further from the coast by katabatic winds. The ambient waters entrain in the DSW cascading from the shelf in plumes to form AABW. In addition, open-ocean deep convection may also lead to the production of AABW as observed in the Weddell Sea (Gordon, 2009). AABW formed in the circum-Antarctic region is the densest of the water mass present globally. Topographic features guide the AABW spread, which moves northward in the abyss and fills about one third of the ocean basins (Gupta and England, 2004; Solodoch et al., 2022).

1.1.1 Circulation role in global climate

The interaction between the climate system and the GOC is recognized as a prominent mechanism elucidating historical global climate fluctuations (Broecker, 1998; Curry and Oppo, 2005; Duplessy et al., 1988; Mix et al., 1985). For instance, the Atlantic Meridional Overturning Circulation (AMOC) displays sensitivity to freshwater input in the

subpolar North Atlantic, with AMOC reduction frequently attributed as the primary driver of cooling events in the Northern Hemisphere, such as the Greenland stadial events (Bond et al., 1997; Bond and Lotti, 1995; Broecker, 1998). Alterations in ocean circulation patterns are also proposed to influence oceanic carbon storage and, consequently, atmospheric CO_2 levels, thus serving as a significant feedback mechanism within the global carbon cycle (Anderson et al., 2009).

The persistent rise in global temperatures resulting from anthropogenic activities, is expected to change the responses from the Global Ocean Circulation (GOC) system to heat distribution, nutrient cycling in ocean and effect on ice sheet melting, as discussed by (2014). These responses are poised to have significant implications for human society. Estimates in the previous study show that nearly 90% of the surplus heat in the climate system since the 1970s has been absorbed by the ocean, resulting in widespread oceanic warming, even reaching the ocean's thermocline and other depths (Talley et al., 2016). These signals of anthropogenic warming primarily propagate from the surface to the deep ocean through the formation of NADW and AABW (Kostov et al., 2017; Talley et al., 2016). The slowdown of both AMOC and Sub Antarctic Mode Water Overturning Circulation (SOMOC) in recent decades has been linked to global warming, with its effects projected to intensify in future (Caesar et al., 2018; Talley et al., 2016). Furthermore, the carbon sequestration associated with the creation of NADW and Antarctic Intermediate Water (AAIW) is responsible for storing approximately 30% to 50% of the anthropogenic carbon emissions since the industrial revolution (DeVries et al., 2017; Sabine et al., 2004; Talley et al., 2016). Nevertheless, the variability of these carbon sinks hinges on the climate-GOC feedback, which remains poorly understood (DeVries et al., 2017; Landschützer et al., 2015). To effectively predict future climate changes, comprehending the variations in GOC and their underlying causes is imperative.

However, our quest for this understanding is impeded by the absence of consistent historical documentation of GOC in the recent past. Direct observations of AMOC have only been available since the early 2000s, and a substantial amount of time is required for anthropogenic influences to emerge from the backdrop of natural variability in these observations (Lozier et al., 2019). Furthermore, as of now, there is no direct observations of SOMOC, and our knowledge of its changes primarily relies on data inversion techniques using repeated hydrographic measurements (Talley et al., 2016). Additionally, state-of-the-

art climate models exhibit significant disparities in their projections of AMOC and SOMOC (Abrahamsen et al., 2019; Kostov et al., 2014; Meijers and Sciences, 2014), signifying that our understanding of the circulation physics and the associated boundary condition is incomplete. Therefore, understanding of the past GOC changes under different forcing and boundary conditions such as freshening of the Ocean might help us to understand the GOC-climate feedback in the future warming scenario.

1.1.2 Oceanic gateway changes and its role in deep water circulation

Opening and the closing of the oceanic gateways in the Southern and the Northern hemisphere have facilitated the changes in the circulation pattern of the global basins. In the early Cenozoic a well-developed equatorial circum-global seaway existed known as the Tethys Sea, provided the deep water connections between different ocean basins (Bialik et al., 2019; Lear et al., 2003; Pillot et al., 2022; von der Heydt and Dijkstra, 2006). The Southern Ocean gateways- the Drake Passage and the Tasman Gateway were still closed and Southern Ocean was divided in the two separate basins, the Pacific and the Atlantic-Indian. The Northward movement of the South America and the Indo-Australia plates resulted in the opening of the Southern Ocean and the establishment of the Antarctic Circumpolar Current (ACC). The exact timing for the opening of Southern Ocean is still debated, however it is believed that opening of both the Tasman and the Drake passage started at Eocene-Oligocene boundary and was completely open by the middle Oligocene to Oligocene-Miocene boundary respectively(Barker and Burrell, 1977; Borrelli et al., 2014; Lagabrielle et al., 2009; Lawver and Gahagan, 2003; Livermore et al., 2005; Scher et al., 2015; Sijp et al., 2011). On the other hand, two low latitude gateways the Tethys and the Central American Seaway (CAS) completely closed in the Northern hemisphere. Another low latitude connection between the Pacific and the Indian Ocean, the Indonesian Seaway constricted and shallowed and allowed surface and intermediate waters only to pass through ITF. The closure of the Tethys started with the collision of the Eurasian and the Indo-Australian Plate with the final closure taking place in Middle Miocene (~15 Ma)(Bialik et al., 2019). CAS closure approximates about ~20 Ma since the early Miocene to Pliocene (Molnar, 2008; Montes et al., 2015), which also coincides with the constriction of the Indonesian Seaway (Hall, 2002a; Kuhnt et al., 2004). Northern hemisphere also registered the opening of the three seaways- Greenland-Scotland ridge (GSR), the Fram Strait providing the connection between the Atlantic and the Arctic Oceans, and the Bering Strait – a gateway between the Pacific and the Arctic. Opening of the GSR and the Fram

Strait took place during Oligocene to Late Miocene and Middle Miocene respectively, while the Bering Strait is the most recent one, opened between Pliocene to Pliocene-Pleistocene transition (Brierley et al., 2016; Engen et al., 2008; Gladenkov et al., 2002; Hossain et al., 2021; Poore et al., 2006; Stärz et al., 2017; Uenzelmann-Neben and Gruetzner, 2018).

The changes in the ocean gateways resulted in the bipolar circulation during the late Cenozoic and since then deep water started forming mainly in the high latitudes and exported to the low latitudes. The AABW formation started in the Southern Ocean during the middle Miocene and was enhanced after ~15 Ma due to the growth in the Antarctic ice sheet and has been the densest water mass since the middle Miocene (Flower and Kennett, 1995; Hall et al., 2003). Similarly, in the North Atlantic northern component water (NCW, a deep water- precursor to NADW) started forming since Middle Miocene. However, several studies based on models (Butzin et al., 2011) and geochemical proxies (Billups et al., 2002; Poore et al., 2006) have reported weak NCW formation and its southward export until late Miocene (~6-8 Ma). A compilation of calcium carbonate ($CaCO_3$) records from multiple DSDP and ODP sites in the Atlantic basin has demonstrated increased calcium carbonate sedimentation rates since the late Miocene throughout Atlantic (Keating-Bitonti and Peters, 2019). ODP site 1262 in the South Atlantic at the Walvis Ridge shows an increase in the $CaCO_3$ from ~10% since ~10 Ma and to ~90% during the late Miocene, which became stable thereafter, suggests enhanced export of NCW in the South Atlantic (Zachos et al., 2004). This indicates that carbonate preservation depth started to increase since the past ~10 Ma, which became stable in the late Miocene (~7 Ma) under certain physico-chemical conditions. This evidence suggests that modern-day like vertical structure/configuration of deep water masses in the Atlantic was achieved during the late Miocene. However, these prevailing hypothesis on the forcing factors, mechanisms and timing have not been tested in other global basins and also questioned (Ivanova, 2009; Philander and Fedorov, 2003; Weaver et al., 1999).

The late Cenozoic recorded many paleoceanographic changes, which finally culminated into the intensification of the Northern Hemisphere Glaciation (iNHG). The closure of the Tethys might have triggered the cooling since Middle Miocene, which could have been promoted by the closure of the CAS. Opening of the Southern Ocean gateways resulted in the establishment of the ACC in the circum-Antarctic region. The ACC isolated

the Antarctic and resulted in the cooling of the continent and the development of the east Antarctic ice sheet since the Oligocene and the west Antarctic ice sheet since the middle Miocene.

1.2 Tracer of past ocean circulation

Our understanding of historical ocean-climate dynamics relies significantly on multiple paleocirculation proxies. While conventional hydrographic parameters, such as temperature and salinity, are fundamental to defining water masses, they offer limited insights into water mass formation processes and lack preservation over geological time scale (England and Maier-Reimer, 2001). In contrast, geochemical tracers provide an unique approach to understand the oceanic ventilation processes and surpass the limitations inherent in temperature and salinity measurements (Lynch-Stieglitz and Marchitto, 2006).

Historically, stable carbon isotopes ($\delta^{13}C$) and cadmium/calcium ratios (Cd/Ca) recorded in benthic foraminifera have been the most commonly utilized geochemical tracers for reconstructing deep ocean circulation (Frank, 2002). The $\delta^{13}C$ of deep waters generally exhibits a negative correlation with nutrient (phosphate) concentrations due to the preferential incorporation of ^{12}C into organic matter in surface waters, with subsequent release during remineralisation at depth. However, $\delta^{13}C$ is also influenced by temperature, nutrient availability, and carbonate ion concentration (Broecker and Peng, 1982; Lynch-Stieglitz and Marchitto, 2006). Cd/Ca, on the other hand, positively correlates with nutrient concentration (phosphate and nitrate), but its interpretation is complicated by biogeochemical processes (Lynch-Stieglitz and Marchitto, 2006). Combining these tracers enables the differentiation between low-nutrient (e.g., North Atlantic Deep Water, NADW) and high-nutrient (e.g., North Pacific) deep waters, and indicate past water mass distributions. However, the assessment of water mass mixing through utilising the proxy of $\delta^{13}C$ and Cd/Ca remains challenging, given that neither of the these tracer precisely reflects the nutrient concentrations present in the surrounding deep water (Frank, 2002; Lynch-Stieglitz and Marchitto, 2006).

Stable oxygen isotopes ($\delta^{18}O$) in seawater are determined by fractionation during evaporation and sea ice formation, in addition to the $\delta^{18}O$ content of precipitation and continental runoff (England and Maier-Reimer, 2001; Lynch-Stieglitz and Marchitto, 2006). Consequently, changes in seawater $\delta^{18}O$ recorded in foraminifera can be employed

as a conservative density tracer due to its relationship with seawater temperature and oceanic conditions (e.g., salinity) during calcification (Lynch-Stieglitz et al., 1999; Lynch-Stieglitz et al., 1999). However, temperature and salinity has contrasting impact on $\delta^{18}O$ which poses the challenge while interpreting the data in terms of variability in the temperature, or the salinity. Thus, the data may result in higher uncertainties among key water masses (e.g., NADW and Antarctic Bottom Water, AABW), and interspecies calibration between different calcareous species (Lynch-Stieglitz and Marchitto, 2006).

The utilization of inorganic trace elements, such as neodymium isotopes, as valuable tracers for both modern and historical ocean circulation has gained prominence over the last few decades (Goldstein and Hemming, 2003; Tachikawa et al., 2017; Van de Flierdt et al., 2010). Neodymium isotope systematics provide as excellent medium to be used as the tracer for the water mass reconstruction and to understand the change is the source of the provenance.

1.2.1 Neodymium Isotope Systematics

Neodymium (Nd) as an element belongs to the light rare earth elements of the periodic table and has an atomic number of 60. Nd has seven naturally occurring isotopes: ^{142}Nd (27.1%), ^{143}Nd (12.2%), ^{144}Nd (23.9%), ^{145}Nd (8.3%), ^{146}Nd (17.2%), ^{148}Nd (5.7%), ^{150}Nd (5.6%). Of these isotopes, ^{143}Nd is the radiogenic isotope and is part of the long-lived radiogenic Samarium (Sm)-Nd isotopic systems. ^{147}Sm having a life of 160 billion years, decays radioactively (α-decay) to produce the ^{143}Nd. In the Earth's mantle, during partial melting and/or fractional crystallization of the rocks, Nd being more incompatible preferentially accumulates in the melt fraction, whereas compatible Sm stays in the residuum. Consequently, the rock from this magma (with low Sm/Nd ratio) is depleted in the ^{143}Nd in comparison to the rocks formed as a result of the partial melting at the later stages (having a high Sm/Nd ratio). Commonly, radiogenic ^{143}Nd normalized to the primordial isotopes ^{144}Nd and thus, the $^{143}Nd/^{144}Nd$ isotope ratio of a rock varies as a function of the time and the geological compositions. The $^{143}Nd/^{144}Nd$ isotope ratios are expressed in the ε-notation, which are deviations from CHUR (Chondritic Uniform Reservoir) in the parts per 10,000. $\varepsilon_{Nd} = [(^{143}Nd/^{144}Nd)_{sample}/(^{143}Nd/^{144}Nd)_{CHUR} - 1] \times 10^4$, where CHUR $^{143}Nd/^{144}Nd$ ratio has the value of 0.512638.

Physical and chemical weathering processes contribute to the breakdown of rocks and minerals. Owing to the similar chemical properties and ionic radius of Sm and Nd, most minerals that constitute rocks maintain consistent Sm/Nd ratios. Consequently, the Nd isotope composition of weathered materials and weathering solutions typically closely resembles that of the source rocks and the phenomenon is referred to as congruent weathering. The distribution of Nd isotopes in continental rocks exhibits spatial heterogeneity caused due to variation in Sm/Nd element ratios and formation age of the rocks. In general, ancient continental crusts tend to possess lower $^{147}Sm/^{143}Nd$ ratios and lower ε_{Nd} values, as exemplified by the old-exposed Archean rocks forming the North Atlantic Craton ($\varepsilon_{Nd} \approx -25$), in contrast to more recent mantle-derived rocks, which tend to have higher 147Sm/143Nd ratios and elevated ε_{Nd} values, as observed in the Hawaiian island chain ($\varepsilon_{Nd} \approx +7$) (Robinson et al., 2021).

1.2.2 Neodymium isotopes as a tracer for water mass circulation history

In the conventional framework to explain the distribution of ε_{Nd} in seawater, it is postulated that Nd primarily enters the ocean through fluvial discharge, with a minor contribution originating from the submarine groundwater discharge and the dissolution of atmospheric dust within the surface marine environment (Figure 1.3a) (Frank, 2002; Goldstein and Jacobsen, 1987; Goldstein and Hemming, 2003). It is further proposed that the ε_{Nd} signature of dissolved river water mirrors that of the parent geological formations. Consequently, the ε_{Nd} composition of surface seawater is representative of the geological underpinnings of the adjacent continents. Oceanic circulation mechanisms then transport these localized surface ε_{Nd} characteristics into the profound oceanic realms (Figure 1.3b). With an estimated mean oceanic residence time of Nd in seawater ranging from 360 to 785 years (Arsouze et al., 2009; Pöppelmeier et al., 2022; Rempfer et al., 2012; Tachikawa et al., 2017), ε_{Nd} variations in deep water (Figure 1.2) reflects its shorter residence time compared to the global ocean overturning time (≈ 1500 years) (Broecker and Peng, 1982). This characteristic accounts for the heterogeneous distribution of ε_{Nd} in deep waters. Furthermore, in pelagic seawater, ε_{Nd} can exhibit conservative behaviour, tracking water mass advection and mixing (Goldstein and Hemming, 2003; Hu et al., 2016; Piepgras et al., 1979; Piotrowski et al., 2008; Tachikawa et al., 2017; van de Flierdt et al., 2016). These unique attributes of ε_{Nd} have positioned it as a valuable tool for tracing water mass origins, structures, and mixing, offering critical insights into both contemporary and paleo-ocean circulation (Frank, 2002; Goldstein and Hemming, 2003; Van de Flierdt et al., 2010). An

advantage of dissolved ε_{Nd} in seawater as tracer over carbon isotopes, is that, Nd is not affected by the biological processes (Blaser et al., 2019). However, the above explanation of Nd contribution to the ocean raises an issue referred as the "Nd paradox", a phenomenon characterized by the disparity observed between the residence times of Nd deduced from Nd concentration measurements and those derived from ε_{Nd} values. It asserts that assuming the riverine influx and atmospheric particulate matter as primary contributors to dissolved Nd concentrations, it is evident that the estimated residence time of Nd in the ocean considerably exceeds 1000 years. However, the observed disparities in ε_{Nd} values across different ocean basins suggest that the residence time of Nd must be less than the timescale of global ocean mixing time, which is approximately 1000 years. Otherwise, a more uniform distribution of ε_{Nd} values would be anticipated (Bertram and Elderfield, 1993; Jeandel and Letters, 1993; Tachikawa et al., 2003). The disparity observed in Nd concentrations budget implies the existence of significant sources of Nd not being acknowledged for the contributions and prompted the formulation of the "boundary exchange" hypothesis. This hypothesis suggests that the budget discrepancy reconciliation by introducing exchange fluxes of Nd between seawater and sediments within continental margins. Subsequent computational studies support the hypothesis, indicating that the sedimentary reservoir of Nd may constitute approximately 90% of the total external Nd sources to the ocean (Arsouze et al., 2007; Arsouze et al., 2010; Lacan et al., 2005; Tachikawa et al., 2003). However, to date, the term "boundary exchange" still encompasses geochemical processes that have not been conclusively identified. In recent times, there have been novel investigations into pore water Nd concentrations and ε_{Nd} values, which decipher sedimentary neodymium flux originating from marine sedimentary sources. This flux possesses the capacity to influence the ε_{Nd} composition of bottom waters (Abbott, 2019; Abbott et al., 2015; Abbott et al., 2022). Significantly, these investigations have unveiled that the sedimentary neodymium flux is not restricted solely to coastal margins, as suggested by the boundary exchange hypothesis, but extends into the domain of deep-sea sediments. Hence, before interpreting the archival authigenic ε_{Nd} values in terms of water mass, extent of these processes at the study site must be investigated.

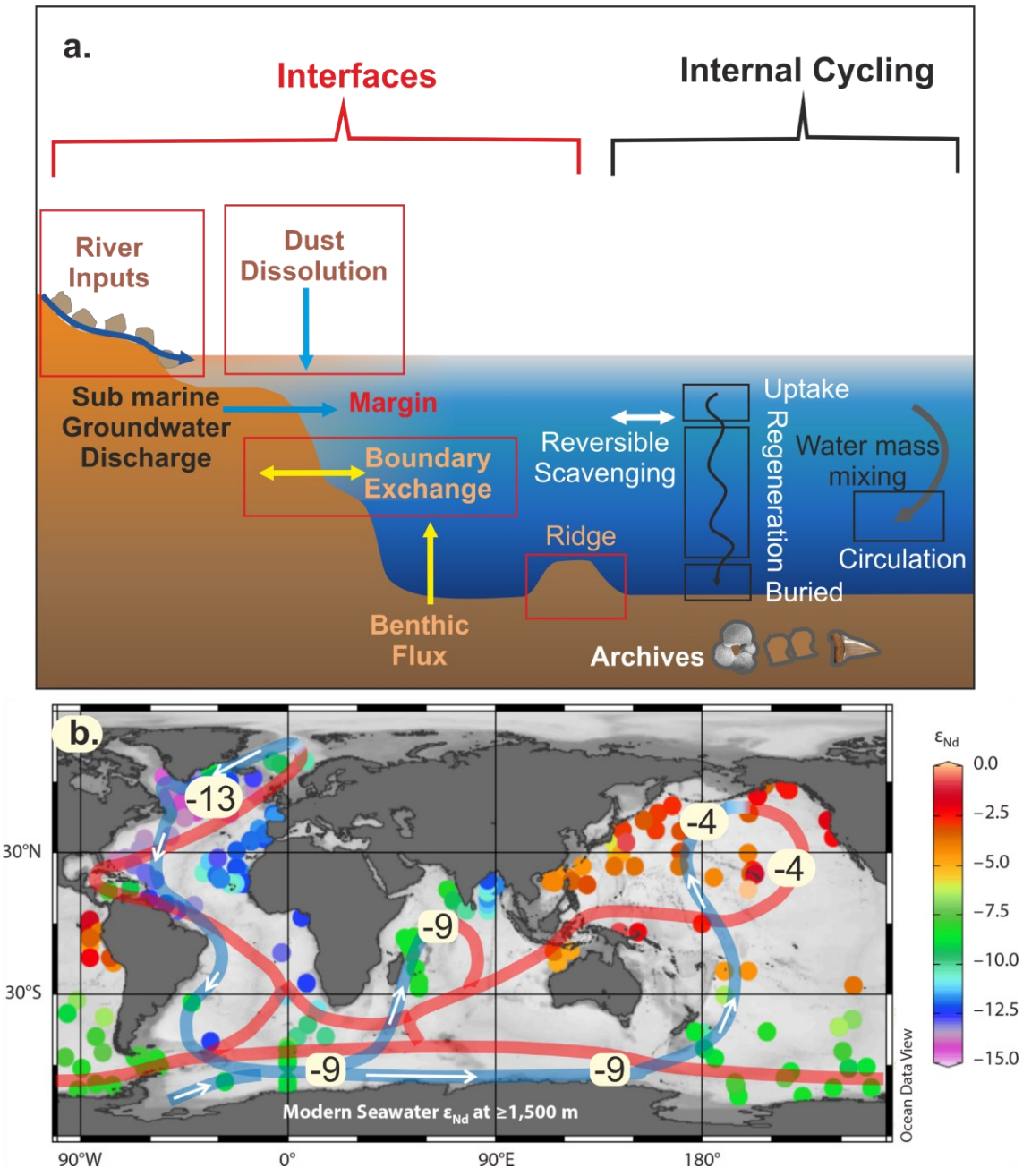

Figure 1.3: Neodymium in Ocean. a) Various sources and processes affecting ocean Neodymium concentration and isotopic composition (figure modified after GEOTRACES http://www.geotraces.org/), b) Distribution of deepwater ε_{Nd} values (Tachikawa et al., 2017), average ε_{Nd} of different ocean basins (Piepgras et al., 1979) are written in white blocks.

In the conceptual framework, NADW emerges as the ε_{Nd} end member with the most negative values (approximately −13 ε_{Nd}) within the global deep ocean (Tachikawa et al., 2017) (Figure 1.3b). This distinction arises from the input of weathered material originating from the ancient continental terrains, notably the Precambrian North American Shield. In

contrast, Pacific Water (PW) exhibits the most positive ε_{Nd} end member values (approximately −4 ε_{Nd}, Figure 1.3b) (Piepgras and Jacobsen, 1988; Tachikawa et al., 2017)due to the influx of younger volcanic materials associated with the Pacific "ring of fire". The ε_{Nd} values of other deep oceanic waters worldwide are regarded as a conservative mixing of these two end members (von Blanckenburg, 1999). For instance, the intermediate ε_{Nd} values characterizing the waters of the Southern Ocean [approximately −8 ε_{Nd} for Antarctic Intermediate Water (AAIW) and Antarctic Bottom Water (AABW), Figure 1.3b] result from this mixing process (Piepgras et al., 1979; Tachikawa et al., 2017).

To employ ε_{Nd} as a tool in paleoceanography, suitable archival materials are imperative. The primary repositories utilized are: iron-manganese nodules, authigenic iron-manganese oxyhydroxides coatings on sediments or on foraminiferal shells, the calcium-hydroxy-fluorapatite, frequently found in fish remains and the deep sea corals (Frank, 2002; Goldstein and Hemming, 2003; Tachikawa et al., 2017; Tachikawa et al., 2014). These archives have their own advantages and limitations and are assumed to passively record the ε_{Nd} composition of bottom waters. studies have shown that foraminifera and fish debris acquire Nd characteristics predominantly after deposition in sediments instead of in the water column (Roberts et al., 2012). These archives have their own advantages and limitations and are assumed to passively record the εNd composition of bottom waters. studies have shown that foraminifera and fish debris acquire Nd characteristics predominantly after deposition in sediments instead of in the water column (Roberts et al., 2012; Tachikawa et al., 2014). Considering the conservativeness and fixed isotopic end member values, measurements of authigenic ε_{Nd} profiles along sediment cores enable us to estimate the fractions of deep water masses at the core site and how these fractions evolved with time (temporal evolution of mixing fractions). For instance, the presence of more positive ε_{Nd} values in the deep South Atlantic during the Last Glacial Maximum (LGM) indicate absence of NADW and complete invasion by Southern Ocean sourced water (SSW) (Piotrowski et al., 2005; Rutberg et al., 2000).

1.3 Antarctic Ice Sheet

Continental-scale ice sheets serve a critical role in controlling in climate dynamics and ocean circulation. The Antarctic ice sheet (AIS) is geographically divided into two the East and the West Antarctic. The East Antarctic Ice Sheet (EAIS) which rests on the topographic high is larger, older and considered to be more stable than the other (DeConto

and Pollard, 2016; Fretwell et al., 2013). The West Antarctic Ice Sheet (WAIS) considered more vulnerable to the climate changes, is smaller of the two and is grounded on the bedrock present below the modern day sea level (Fretwell et al., 2013; Pollard and DeConto, 2009). Modern day Antarctica glaciers stores most of the world's freshwater form of ice sheets. Being the vast reservoir of the fresh water, the whole Antarctic ice sheet mass loss has the potential to raise the sea level by 58.3 m as per the IPCC 2013. It is important to note that contribution of Antarctic to the rise sea level has reached to ~8 millimetres since 1992 under the modern global warming scenario (Golledge et al., 2015; Purkey and Johnson, 2010). As discussed, WAIS is a marine based ice sheet (grounded below sea level) and thus, more vulnerable to the climate changes. WAIS stability is affected both by the warming of the ocean which enhances the ice calving from the bottom and the atmospheric warming which increases the surface melting (Bett et al., 2020; Fyke et al., 2010; Hillenbrand et al., 2017; Joughin and Alley, 2011). Hence under the current global warming scenario WAIS is losing the ice mass balance at a striking pace, which has the potential to raise the global sea level by 5.2 m (DeConto et al., 2021; Pattyn et al., 2018). Over the last decades, the WAIS has been undergoing dramatic mass loss and contributed to present sea-level rise at a faster rate than any other continental ice sheet on Earth (Frezzotti and Orombelli, 2014b; Joughin and Alley, 2011). Model-based simulations predict a complete collapse of the WAIS in the near future that would result in a global sea-level rise of 3.3-4.3 meters (DeConto and Pollard, 2016; Pollard and DeConto, 2009). However, these model predictions have large uncertainties associated with the estimates of timing of the ice sheet collapse and resulting sea-level rise. The IPCC (2007) 4th Assessment Report (Solomon et al., 2007) highlighted that the response of continental ice sheets to climate change and their contribution to global sea-level rise is the largest unknown variable in predicting future sea-level change. The sources of uncertainty could either be due to unaccounted processes/forcing factors in the models or propagation of the large uncertainty associated with the input parameters. In order to improve these model predictions, it is important to improve our knowledge and understanding about past behaviour of the WAIS particularly during geologic times when the climatic conditions were similar to modern day and/or the near distant future.

Studies have suggested that the GOC provides feedback to the climate and vice versa. In turn both the climate and the water circulation have the potential to modulate each other through the feedback mechanism and together both of these can also impact polar ice

sheets (Adkins, 2013; Anderson and Willebrand, 1992). Considering the current mass loss based on the satellite observation, WAIS is considered to be potentially more unstable than the EAIS. The instability of the WAIS arises from its geological foundation, which lies significantly below sea level and deepens inland, reaching depths of approximately 2500 meters below sea level (Fretwell et al., 2013). This geological configuration makes the WAIS susceptible to any initial retreat of the grounding line (the point where the ice sheet meets the ocean) toward deeper ocean water can trigger a cascade of thinning and retreat (Katz et al., 2010; Schoof, 2007). The current mass loss of the WAIS is primarily attributed to the melting of its floating ice shelves due to the intrusion of relatively warm Circumpolar Deep Water (CDW) (Jenkins et al., 2016; Walker et al., 2007; Walker et al., 2013). This intrusion results in substantial thinning of the ice shelves (Pritchard et al., 2012; Rignot and Jacobs, 2002), increased ice flow velocity, and ice discharge, ultimately leading to a rapid retreat of the grounding line. Evidence from multiple proxies, including the magnesium (Mg) to calcium (Ca) ratios in calcareous shells of benthic foraminifera used as a proxy for past bottom-water temperatures, indicates that the CDW played a crucial role in the significant deglaciation events in the Amundsen Sea sector of West Antarctica approximately 10,400 to 7,500 years ago and more recently since the 1940s (Hillenbrand et al., 2017). Initial warnings on the WAIS instability in the past, encompasses sea level reconstructions, sedimentological investigations, and modelling studies. These studies have suggested that the WAIS experienced substantial fluctuations during the Pleistocene and Pliocene epoch (DeConto and Pollard, 2016; Hillenbrand et al., 2009; Holden et al., 2011; Pollard and DeConto, 2009; Scherer et al., 1998; Tigchelaar et al., 2018). However, it is essential to note that most of these investigations provide only indirect evidence of WAIS retreat, underscoring the need for the direct evidence from the close proximity to investigate role of various forcing factors for the evolution during the late Cenozoic and its impact on global sea level. In addition, it is also important to study the WAIS history of the geological intervals e.g. Pliocene and Miocene which are considered to be the climate analogue of near future climate and/or future warmer climate respectively in terms of CO_2 and temperature.

Hence, the study of the evolution of climate and oceanographic conditions during the late Cenozoic becomes important to understand the effects of changing climate on the water circulation and the ice sheet which can change the sea level by several meters. Also, these studies will help to improve the modelling results and provide a cross-check about

proposing the carbon storage in the deep ocean and the stability of the AIS under rising atmospheric CO_2 of current global warming conditions.

1.3.1 Reconstruction of Ice sheet dynamics

A robust method for reconstructing the past variability of ice sheet dynamics involves the analysis of glaciomarine sediment provenance through the utilization of radiogenic isotope dating and fingerprinting techniques (Licht and Hemming, 2017). Glaciogenic material carries the isotopic signature originating from its geological source as is transported from the continent toward the ocean basin by flowing ice or subglacial meltwater. Subsequently, this detrital material is deposited offshore by the action of wind and tidal currents, either through the calving of icebergs laden with detritus or as diamicts (Diekmann and Kuhn, 1999). Isotopic and geochemical examination of the glacially eroded detritus deposited in the ocean provides valuable insights, which are used to gain inputs about the bedrock compositions beneath ice sheets (Pereira, 2018; Pierce et al., 2017) and, in turn, offers a deeper understanding of past ice sheet geometry. This methodology has proven effective in the North Atlantic region. For example, in investigations concerning the origin of Ice-Rafted Debris (IRD) deposited during the late Pleistocene epoch, scientific inquiry has unveiled regions of the Northern Hemisphere ice sheets that experienced substantial destabilization (Downing et al., 2014; Hemming, 2004; Peck et al., 2007). Furthermore, the analysis of isotopic signatures within fine-grained sediment deposits has provided additional insights into historical ice sheet extents (Colville et al., 2011; Farmer et al., 2006; Reyes et al., 2014; Wilson et al., 2018). However, the utilization of isotopic provenance investigations within sedimentary core datasets in the Southern Ocean has been relatively underutilized.

The pioneering efforts to establish a connection between the geochemical origin of contemporary glaciomarine sediments encircling Antarctica and its geological foundations were initially documented by Hemming et al. (2007); Roy et al. (2007); Van de Flierdt et al. (2007); Walter et al. (2000). Subsequent research extended these investigations and further refined the understanding of this linkage, as evidenced by Flowerdew et al. (2012); Pereira (2018); Pierce et al. (2014); Pierce et al. (2011). Over time, the focus of isotopic source tracing studies has predominantly revolved around two key geographical regions: the Ross Sea sector, as documented by Farmer et al. (2006); Licht and Palmer (2013); Licht et al. (2014); Welke et al. (2016); and the Weddell Sea vicinity, as explored through

downcore records, as described by Carter et al. (2017). These studies collectively contribute to the comprehensive understanding of Antarctic sediment provenance.

In the vicinity of Antarctica, the analysis of radiogenic isotopes such as Nd and the Lead (Pb) isotopes in detrital glaciomarine sediments has demonstrated its potential to trace provenance of these sediments and inferred about the past ice-sheet dynamics (Carlson et al., 2021; Pereira, 2018). . Therefore, the radiogenic Sr-Nd-Pb isotope records of sediment cores recovered from the Amundsen Sea Embay shelf, with the well constrained chronology of the WAIS advance, retreat and partial/full collapse events identified based on the sedimentological and geophysical evidenced will enable us to achieve our goals in the present study. The identified facies and prominent layers of ice-rafted debris (IRD) in conjunction with isotope data sets, will help to reconstruct the past glaciological behaviour of the WAIS, especially its first advance to the coast and possible collapse events (Talarico et al., 2011; Williams et al., 2010). The provenance analyses on IRD from the ASE cores will be crucial in identifying a potential WAIS collapse. In a recent study (Wilson et al., 2018) determined the tipping of the east Antarctic ice sheet collapse and suggest that "an Antarctic warming of about 2°C above pre-industrial temperatures for approximately 1,000–2,500 years has been sufficient to cause ice loss beyond that of the modern day or pre-industrial Holocene,". Similar method can be employed in the present study to determine the duration and tipping of point of the temperature rise for the future collapse of WAIS. We expect this method to work in the present study as the WAIS is equally or even more sensitive to climate change than EAIS and thus eroded sediments from various provinces in the hinterland lithologies with distinct isotope signatures associated glacial-interglacial ice sheet dynamics will enables us to determine the boundary conditions.

1.4 Objectives of the thesis

I. To reconstruct the deep water-mass circulation in the Arabian Sea during the late Cenozoic using Neodymium isotope.
II. To decipher the effect of climate and/or tectonics since late Cenozoic on the water mass circulation in the Arabian Sea.
III. To reconstruct the circumpolar deep water-mass circulation in the Amundsen Sea during the late Cenozoic using Neodymium isotope.

IV. To reconstruct the West Antarctic Ice sheet dynamics using detrital neodymium isotope records from the Amundsen Sea Embayment during the Pliocene-Pleistocene.

1.5 Outline of the thesis

Present thesis has been divided into six chapters. The contents of each chapter are as follows:

Chapter 1 presents an introductory and comprehensive overview of the global ocean circulation, its significance within the context of climate dynamics, and an insight of Antarctic ice sheets. Additionally, this chapter introduces Neodymium (Nd) isotope analysis as a valuable tool for reconstructing water mass circulation and comprehending Antarctic ice sheet history. The existing research within this domain, along with identified research gaps, is briefly presented as the driving force behind this study, aligning it with current scientific knowledge and objectives.

Chapter 2 provides an extensive discussion about the study area of the core locations, oceanographic parameters, sampling procedures, analytical methods for the radiogenic Nd and Pb isotopes measurements in core samples and archival resources employed in this research endeavour. This chapter also elucidates the methodologies employed for sample processing, purification via cation exchange column chromatography, and the analytical techniques employed for determining Nd and Pb isotopic compositions.

Chapter 3 delves into a comprehensive examination of the deep water mass structure of the Arabian Sea, employing a down-core investigation of IODP-355 core site U1457, by using the authigenic Nd isotope, extracted from the Fe-Mn coatings of sedimentary layers. The temporal scope of this analysis encompasses the late Miocene through the early Pleistocene epochs. Furthermore, this chapter outlines the timing and mechanisms responsible for the restructuring and transformation of deep water circulation from a Pacific dominated to a modern configuration within the Arabian Sea.

Chapter 4 provides the record of the authigenic Nd isotope composition of the Fe-Mn coatings of the sediment from the core U1532 retrieved during the IODP expedition 379 to the Amundsen Sea. These records provide new insights to assesses the suitability of

the study area, to reconstruct the deep water circulation using authigenic Nd isotope records from the Amundsen Sea.

Chapter 5 describes the radiogenic isotope provenance study of downcore sediments at the core site U1532 in the Amundsen Sea, situated proximal to West Antarctic Ice Sheet (WAIS), spanning the Pliocene-Pleistocene epoch. This chapter discuss about the change in the source of the provenance caused by the variability in the ice sheet dimensions and dynamics during the studied interval.

Chapter 6 highlights the findings of the various chapters of the thesis and synthesises the paleoclimatic and the tectonic changes leading to the restructuring of the water circulation and the variability of the ice sheet and looks ahead to the new research challenges presented by these findings.

Chapter 2

Materials and Method

To achieve the scientific objectives spread through the two different Ocean basins, the present study utilises the two long sediment cores retrieved from the Arabian Sea and the Amundsen Sea. The present chapter provides a comprehensive description of the study area of the core locations, oceanographic settings, sampling procedures, and archival resources employed in this thesis. This chapter also elucidates the methodologies employed for sample processing, methods for extractions of Nd and Pb and their purification via cation exchange column chromatography, and the analytical techniques employed for determining isotopic compositions using mass spectrometry.

The two different core samples used for the present study were retrieved during the International Ocean Discovery Programme (IODP) expedition to the Arabian Sea – IODP 355 and the Amundsen Sea – IODP 379 in the year 2015 and 2019 respectively. Details of the core sites are provided in the following Table 2.1.

Table 2.1**:** Details of the study area.

Region	**Expedition**	**Core Site**	**Latitude**	**Longitude**	**Water Depth**
Arabian Sea	IODP 355	U1457	17°9.94’N	67°55.8’E	3522 m
Amundsen Sea	IODP 379	U1532	68°36.36’S	107°31.50’E	3961 m

2.1 Arabian Sea Site

2.1.1 Regional tectonic and hydrographic settings

Details of the regional tectonic settings of the study area have already been discussed elsewhere. Briefly, the core site U1457 C lies on the western end of NW-SE oriented Laxmi basin in the eastern Arabian Sea (Figure 2.1a). The Laxmi Basin is a depression spanning 200–250 km in width, extending in a northwest–southeast direction parallel to the passive margin of the west coast of India and the Laxmi ridge in the west

(Nair et al., 2021) occupied by the distal fan of the Indus delta. The Laxmi Ridge is considered as a rifted fragment of the Indian continental crust (Bhattacharya et al., 1994; Pandey et al., 2015). The precise age of the rifting event is subject of debate but is likely to precede the emplacement of the Deccan Traps flood basalts in the latest Cretaceous epoch, as indicated by magnetic anomalies analysis (Bhattacharya et al., 1994). Within the axial portion of the Laxmi Basin, a collection of seamounts, including Panikkar and Raman Seamounts, along with Wadia Guyot, collectively constitute what is termed Panikkar Ridge (Krishna et al., 2006). However, these structures do not influence the sedimentary cover within the basin and at Site U1457. The sediments in this region are mostly supplied by the Indus River and a few westward flowing peninsular rivers. The basement of the Laxmi basin is formed by basalt, while the oldest recorded sediments date to the late Palaeocene, while the youngest sediments represent the Holocene. The entire deposition history at this core site reveals major breaks in sedimentations (hiatus). Within our study interval, two hiatuses have been recorded, during the late Miocene (~8.7 Ma) and at the Miocene-Pliocene boundary (~5.5 Ma) (Figure 2.2 Figure 3.4g). The Laxmi basin has also recorded Nataraja Slide – a mass transport complex of gravity slump, transported from further north travelling ~550 km from the offshore Saurashtra region emplaced at ~10.8 Ma triggered possibly due to seismic activity (Calvès et al., 2015; Pandey et al., 2016).

Water mass structure and the oceanographic conditions of the Arabian Sea have already been discussed extensively in previous studies (Goswami et al., 2014; Lathika et al., 2021; Tomczak and Godfrey, 2003; You, 2000). Briefly, the upper water column (Figure 2.1 b, c) in the Arabian Sea up to 1000 m is occupied by the Arabian Sea High Salinity Water (ASHSW, potential temperature 24°C to 28°C, and salinity 35.3 to 36.7), the Persian Gulf Water (PGW, potential temperature 18°C, and salinity 36.8), the Red Sea Water (RSW, potential temperature 11°C, and salinity 36). The ASHSW is formed by excessive evaporation over precipitation of Arabian Sea water and occupies the top 50 to 100 m of the water column. Whereas the PGW and RSW are formed due to spillage of high salinity waters from the Persian Gulf and the Red Sea to the Arabian Sea, respectively. The intermediate water column is occupied by the mixture of ASHSW, PGW, and RSW during their southward flow and is known as the North Indian Intermediate water (NIIW), occupying a depth up to 1500 m. During its southward journey, it mixes with the upwelling polar waters to form the North Indian Deep Water (NIDW). At deeper depths, the Arabian Sea is ventilated from the south by the Modified North Atlantic Deep Water (MNADW,

potential temperature 1.8°C-2.8°C and salinity 34.78 to 34.85) and Antarctic Bottom Water (AABW, potential temperature 0.3°C and salinity 34.5). The MNADW and AABW enter the Madagascar and Mascarene basin as deep western boundary current (DWBC) through the Crozet Basin (30°S and 60°E). After reaching the Somali basin through the narrow Amirante passage, MNADW and AABW enter the Arabian Sea via Owen fracture Zone (Figure 2.1).

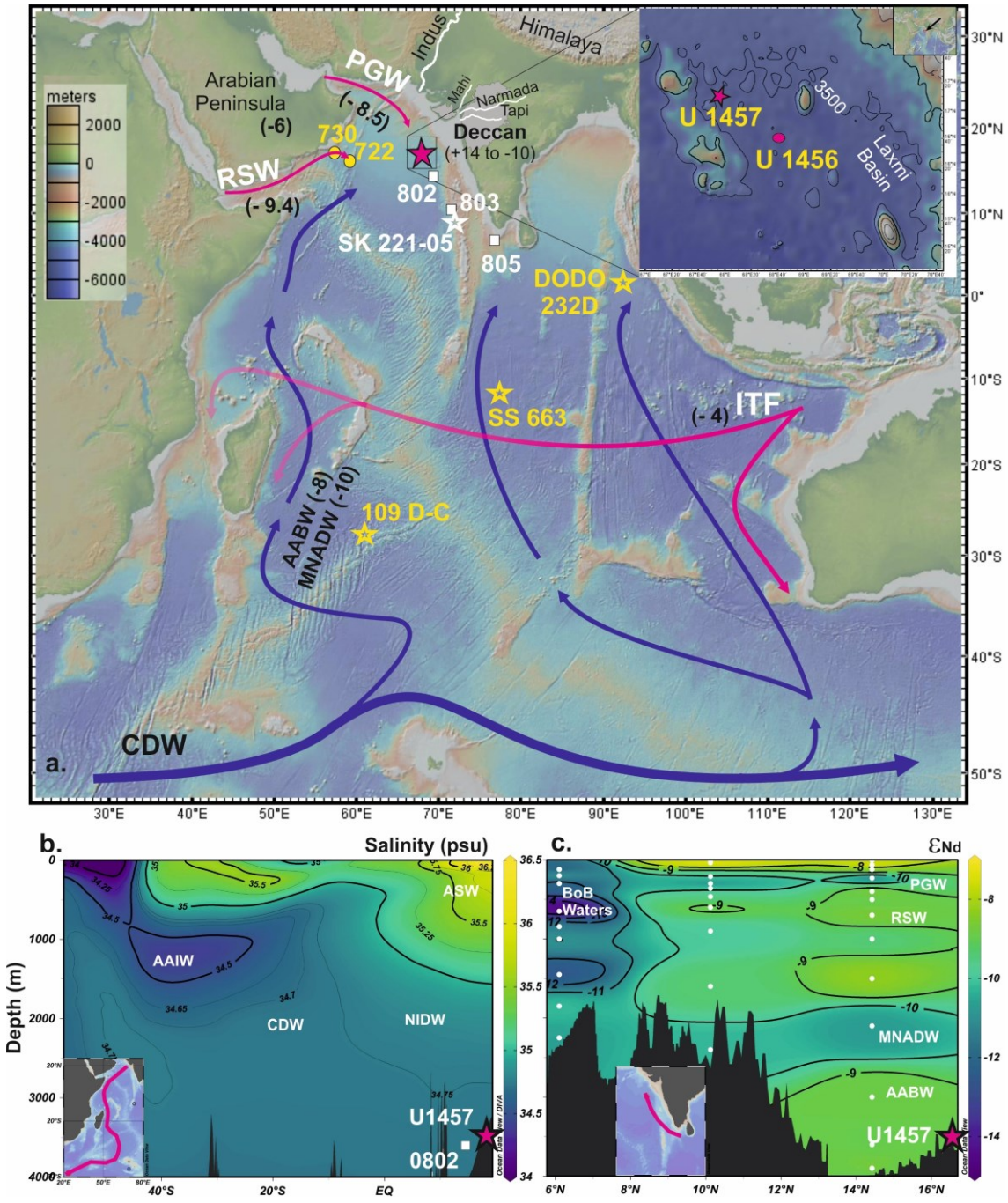

Figure 2.1: Study Area of the Arabian Sea site. Study Area and location of authigenic ε_{Nd} records. (a). Location map with the water mass pathways and their characteristics ε_{Nd}

values. The pink star represents core site (U1457) of the present study. The white square represents the proximal seawater stations 0802, 0803 and 0805 in the Arabian Sea (Goswami et al., 2014). The white star marks the location of sediment core site SK 221-05 (Lathika et al., 2021) used for reconstruction of authigenic ε_{Nd} records in the Arabian Sea. Yellow star marks Fe-Mn crust sites DODO 232D (Frank et al., 2006a), 109 D-C and SS 663 (O'Nions et al., 1998b) from the Indian Ocean. Yellow circle along the Oman coast marks the core site used for the paleo-monsoon reconstructions. Surface water masses are marked by pink lines and blue lines indicate deep water masses. The image in the inset shows the high-resolution bathymetry of the core location. The map was produced using Geomap app (http://www.geomapapp.org); (b) A south-north transect (shown in inset) salinity section representing major water masses of the study area; (c) The ε_{Nd} profile of the water stations present in the Arabian Sea along the south-north transect (shown in inset). The depth-salinity and ε_{Nd} distribution maps were produced using Ocean Data View Software (https://odv.awi.de/). PGW- Persian Gulf Water, RSW- Red Sea Water, ITF- Indonesian Throughflow Water, AAIW- Antarctic intermediate water, NIDW- North Indian Deep Water, CDW- Circumpolar Deep Water, MNADW- Modified North Atlantic deep water, AABW- Antarctic Bottom Water, ASW- Arabian Sea Water (which includes PGW, RSW and Arabian Sea high salinity water), BoB waters- Bay of Bengal waters.

2.1.2 Sediment Core

Sediment core was recovered from the site U1457 C (17°9.95' N, 67°55.81' E, 3522 m) during the IODP 355 expedition in year of 2015 to the eastern Arabian Sea on the western edge of the Laxmi Basin (Figure 2.1a). The core site was drilled on the Indus Delta fan and recovered ~917 m long core with sediment recovery of 48%. The Indus river is the major contributor of sediments to the sampling site, along with the westward flowing Narmada and Tapi rivers. Lithology at the site is affected by the turbidite sequence dominated by dark grey to greenish-grey claystone and light brown to dark grey sand/sandstones. The lower section below 830 m has the occurrence of calcarenite, breccia, and limestone. Occurrences of nannofossil chalk and nannofossil-rich claystone alternate with silty claystone and silty sandstone.

2.1.3 Age models

Study based on calcareous nannofossils and planktonic foraminifers at Site U1457 indicates a temporal span from the early Paleocene to the recent era, with a notable hiatus (~50 million years) observed between lower Paleocene and upper Miocene sediment layers (Pandey et al., 2016). The biostratigraphic analysis conducted at Site U1457 facilitated the identification of three unconformities and a mass transport interval within the Neogene section (Figure 2.2a). Calculations of sedimentation rates at Site U1457 reveal a relatively

consistent rate in the late Miocene at approximately 17 cm/ky, with a hiatus lasting approximately 0.50 million years around 8 Ma. Subsequent to this interruption, sedimentation rates were somewhat lower, averaging around 10 cm/ky for the remainder of the late Miocene. A brief period dominated by slower, hemipelagic sedimentation (~4 cm/ky) is evident between approximately 7.4 and 6 Ma (Figure 2.2a). A hiatus of approximately 2 million years spans the Miocene/Pliocene boundary and early Pliocene. During the late Pliocene to early Pleistocene, the sedimentation rate was around 4 cm/ky. Following another hiatus lasting ~0.45 million years in the early Pleistocene, sedimentation rates increased significantly (~58 cm/ky) for the remainder of this epoch. From the late early Pleistocene to the present, the sedimentation rate gradually decreased, averaging approximately 7 cm/ky (Figure 2.2a) (Pandey et al., 2016; Routledge et al., 2019).

The age model for the present study for site U1457 C is based on the published biostratigraphy as mentioned in Table 2.2 (Figure 2.2b) (Pandey et al., 2016; Routledge et al., 2019).

Table 2.2**:** Biostratigraphic datums used for age depth model for site U1457 C in this study.

Event	Datum	Age (Ma) Indian Ocean Calibrated	References
LO of	*Discoaster brouweri*	1.93	(Pandey et al., 2016)
LO of	*Discoaster pentaradiatus*	2.39	(Pandey et al., 2016)
LO of	*Discoaster surculus*	2.49	(Routledge et al., 2019)
LO of	*Sphenolithus spp.*	3.54	(Routledge et al., 2019)
FO of	*Discoaster tamalis*	4.13	(Routledge et al., 2019)
LO of	*Discoaster quinqueramus*	5.59	(Pandey et al., 2016)
LO of	*Nicklithus amplificus*	5.94	(Routledge et al., 2019)
FO of	*Nicklithus amplificus*	6.7	(Routledge et al., 2019)
FO of	*Amaurolithus spp.*	7.25	(Routledge et al., 2019)
FO of	*Discoaster quinqueramus*	8.12	(Pandey et al., 2016)
LO of	*Minylitha convallis*	8.68	(Pandey et al., 2016)
LO of	*Discoaster bollii*	9.21	(Pandey et al., 2016)
LO of	*Catinaster coalitus*	9.69	(Pandey et al., 2016)
FO of	*Catinaster coalitus*	10.89	(Pandey et al., 2016)

FO- First Occurrence; LO- Last Occurrence; spp.- species

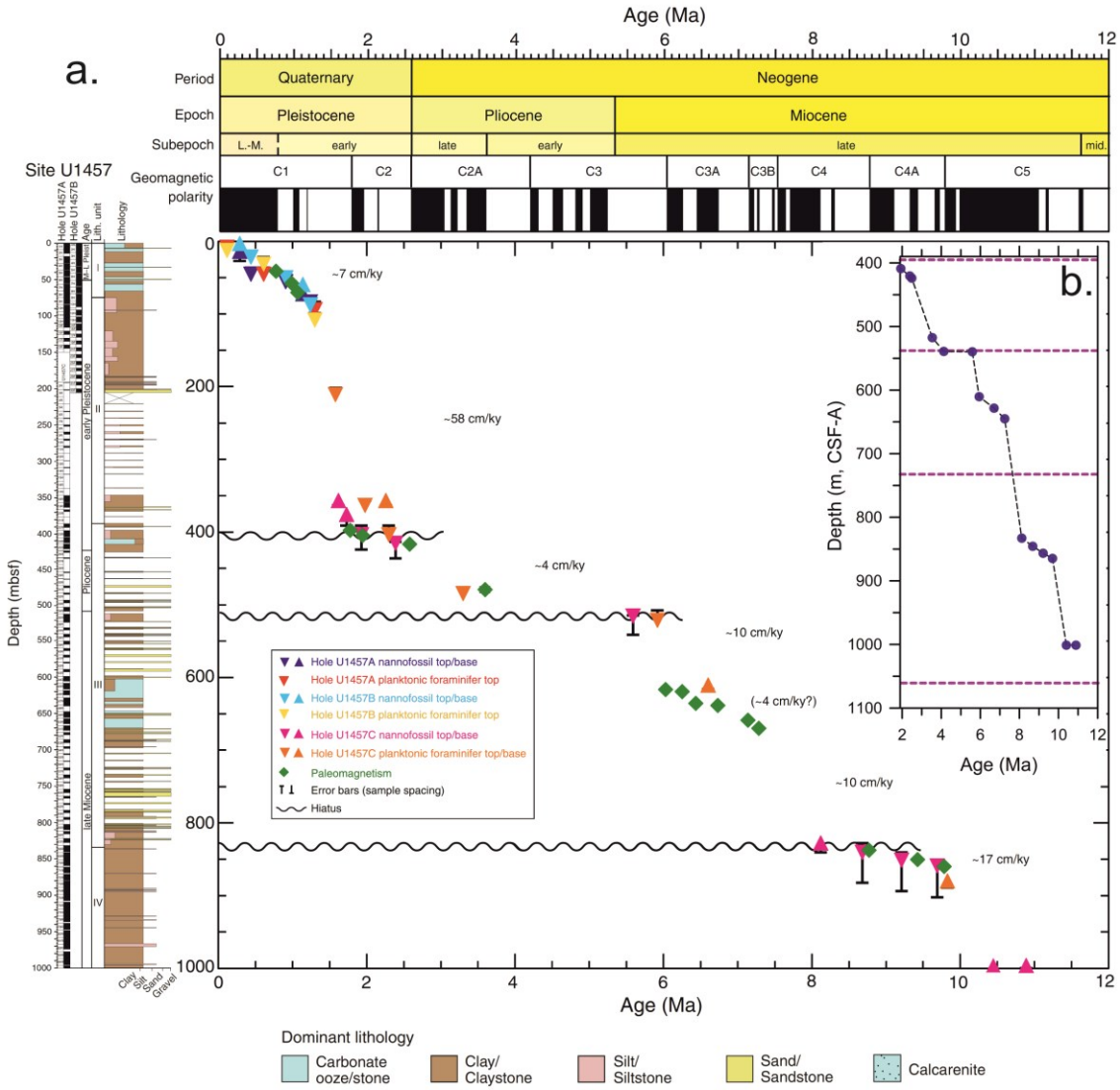

Figure 2.2: Chronology of core site U1457. a) Lithostratigraphic column and age-depth plot for the U1457 site (modified after IODP 355 proceedings site U1457 (Pandey et al., 2016)); b) Age depth model for site U1457 C based on biostratigraphic datums (Table 2.2) used in present study. Dashed lines mark the hiatus.

2.1.4 Sample Preparation

Nd isotopes were measured in the authigenic and detrital phases of the bulk sediments as well as in few fish teeth /debris samples. Neodymium associated with the authigenic phase of the bulk sediment was extracted through acid reductive leaching following the method of Wilson et al. (2013). For the leaching about 3 g of dried sediment sample was powdered and homogenised using Agate mortar and pastel. Homogenised sediment samples were leached with 10 ml of 0.02 M Hydroxylamine Hydrochloride (HH) in 4.4 M acetic acid (pH adjusted to 2) for one hour in a 15 ml centrifuge tube. The sample was then centrifuged at 5000 rpm, and the leachate was decanted carefully without the

transfer of any residue. The same method was employed in a recent study from the South-eastern Arabian Sea (Lathika et al., 2021) with similar regional settings to understand the deep water circulation of the last glacial cycle, which has demonstrated the reliability of the leaching method in extracting the seawater Nd from the bulk sediment. The Nd measured in fish teeth, and foraminifer is considered more robust and reliable than the leachate phase to reconstruct deep water circulation. Due to the lack of foraminifera shells and restricted occurrences in the studied core, we have measured Nd in few handpicked fish teeth/debris samples (n= 10) following the method adopted from Basak et al. (2018a). Fish teeth are phosphatic in nature and they acquire the Nd as result of the postmortem effect once they settle at the seafloor (Frank, 2002; Martin and Scher, 2006a). To get the fish teeth, the samples were first wet sieved >63 mesh size followed by dry sieving between 150 to 250 mesh size. Since fish teeth/debris have the restricted geographical occurrence and less preservation potential, out of 100 wet and dry sieved samples we could get only 10 fish teeth samples along the entire core length of the samples which was analysed. Initially, the fish teeth/debris was cleaned repeatedly by ultrasonication in the Milli-Q followed by the optima grade methanol to remove any detrital particle present. The cleaned samples were then treated with a 1:1 solution of H_2O_2 (30%) to remove the organic matter, followed by dissolution of the fish teeth/debris sample in a 1:1 mixture of HNO_3 and HCl.

To measure Nd in the detrital fraction, the residual material after removing the authigenic phase was first washed by the Milli-Q and was further treated with 0.6 N HCl for the complete removal of carbonates. Subsequently, samples were washed thoroughly with Milli-Q water and dried in the oven at 80° C. Dried samples were ashed at 600°C in a muffle furnace to remove organic matter. ~100 mg powdered, ashed samples were digested in precleaned Teflon vials using HF-HNO_3-HCL mixture at 120°C following the method described in Tripathy et al. (2011) and Subha Anand et al. (2019). Standard Reference Materials BCR-2 and BHVO-2 were also digested along with each batch of the samples.

Dissolved samples (leach, fish teeth/debris and the detrital) were purified by column chromatography and were passed through columns filled with cation-exchange resin Bio-Rad AG50W-X8 (200–400 micron) to separate Rare Earth Elements (REE). Samples were loaded in the 2N HCl medium and the REE fractions were eluted using 6N HCl (Table 2.3, Figure 2.3). REE fractions were then dried and converted to the 0.16N HCl medium and passed through the column containing Eichrom LNspec^{TM} (50 – 100 micron) resin to

separate Nd from the REEs (Pin and Zalduegui, 1997). Nd fraction was eluted using 0.27N HCl and was then dried and converted to HNO_3 medium for the measurement of the isotopic ratios (Table 2.4, Figure 2.4).

Table 2.3: Protocol for the collection of Rare Earth Elements (REEs)

Eluting fraction	**Eluting Reagent**	**Volume (ml)**
Conditioning	2N HCl	10 ml
Sample Loading	2N HCl	1 ml
Fixing	2N HCl	2X1 ml
Rinsing	2N HCl	10ml
Eluting Rb	2N HCl	6 ml
Rinsing	2N HCl	12ml
Eluting Sr	2N HCl	13 ml
Rinsing	6N HCl	6ml
Eluting REEs	6N Hl	10ml

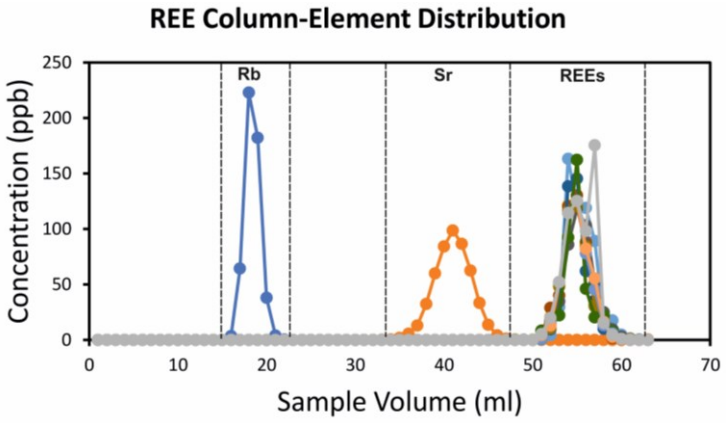

Figure 2.3: REE column- element distribution curve using Bio-Rad AG50W-X8 (200–400 micron) resin.

Table 2.4: Protocol for the collection of Neodymium

Eluting Fraction	**Eluting Reagent**	**Volume (ml)**
Conditioning	0.16N HCl	5 ml
Sample Loading	0.16N HCl	0.5 ml
Fixing	0.16N HCl	0.5 ml
Rejection	0.16N HCl	15 ml
Nd Collection	0.27N HCl	6 ml

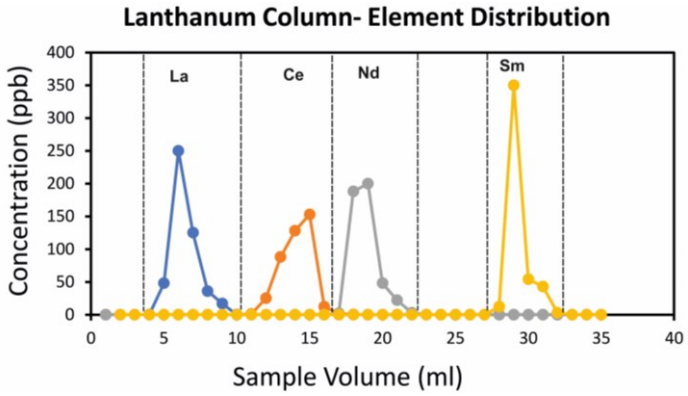

Figure 2.4: Lanthanum column- element distribution curve using Eichrom LNspec^{TM} (50 – 100 micron) resin.

1.1.5 Nd isotope Analysis

Nd isotope ratios were measured using Multi-collector Inductively Coupled Plasma Mass Spectrometer (MC-ICP-MS, Thermo Fischer Scientific, Neptune Plus) at National Centre for Polar and Ocean Research, Goa. The measured $^{143}Nd/^{144}Nd$ ratios were mass-bias corrected using $^{146}Nd/^{144}Nd$ ratio of 0.7219 and normalised to the reported JNdi-1 standard $^{143}Nd/^{144}$ value of 0.512115 (Tanaka et al., 2000). To ensure the quality of measurement, the international standard JNdi-1 was measured at every five samples, and the obtained average ratios were 0.512101 ± 8 ppm (2σ, n= 42) for the leachate, 0.512058 ± 14 (2σ, n= 5) for the fish teeth and 0.512125 ± 9 ppm (2σ, n=6) for the detrital samples. The external reproducibility calculated for each session for the leachate, fish teeth, and detrital samples were 0.06–0.29 ε_{Nd}, 0.28 ε_{Nd}, and 0.14–0.28 ε_{Nd} (2σ) units, respectively. If the internal error (2σ) is larger than the external error, the internal error is reported as the final uncertainty associated with the individual measurements. Several procedural blanks were also processed along with the samples and ascertained an average blank of ~110 pg for the leachate (n=10), 13 pg for the fish teeth (n=1), and 50 pg for the detrital phase (n=2), which are three orders of magnitude lower than the total Nd typically analysed in samples. Hence, no blank correction was applied. Replicates have an average ε_{Nd} variation of ±0.16 (2σ, n= 15, Figure 2.5).

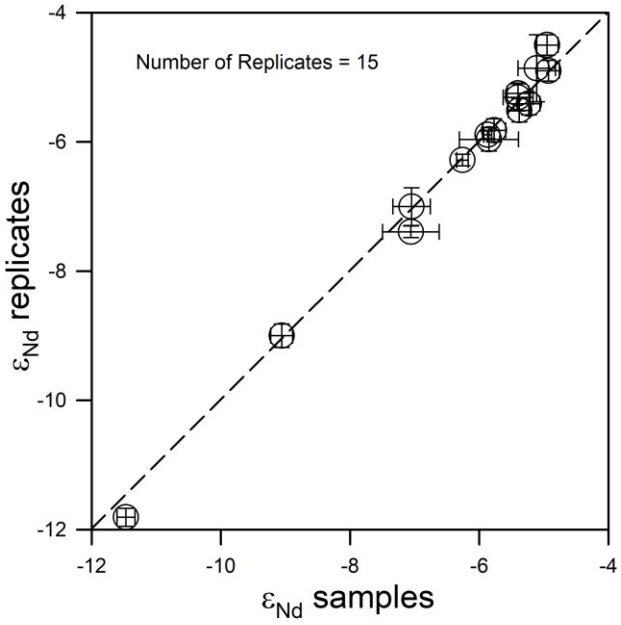

Figure 2.5: Replicate analysis of Nd isotopes. To ascertain the quality of the analysis, Nd isotopes were measured in the replicates and shown in the cross plot. A total of fifteen replicates were analysed, of which most of the Nd isotope data fall on the equiline (1:1)

2.2 Amundsen Sea Site

2.2.1 Regional and hydrographic settings

The Amundsen Sea (AS) is a region bordered by the Ross Sea to the west, the Bellingshausen Sea to the east, the Pacific Ocean to the north, and the West Antarctic Ice Sheet (WAIS) to the south (Figure 2.6). Its basin formation initiated during the Cretaceous period and evolved through a multi-stage rift, progressing from east to west. The final stage of basin development resulted due to ongoing passive margin rift since the Oligocene to Miocene epochs (Jordan et al., 2020). The climatological low-pressure system known as the Amundsen Sea Low plays a crucial role in shaping the region's climate, impacting ocean circulation and facilitating the intrusion of warm marine air masses (Nicolas and Bromwich, 2011).

The continental shelf and rise in the Amundsen Sea have been shaped by the tectonics, surface geological process controlled by the ocean circulation and the ice sheet dynamics. The seafloor adjacent to the continental margin of the AS exhibits distinctive troughs created by the paleo ice streams of the WAIS during the glacial age (Larter et al., 2009). Two of the major troughs, the Pine Island trough in the east and the Dotson-Getz trough in the west AS, have been carved by these ice streams. The tributaries of the

mentioned troughs originate from ice streams/glaciers situated on the innermost ultradeep shelf, reaching depths as profound as 1600 meters below sea level. These tributaries converge at the transition point from the inner to middle shelf (Graham et al., 2009; Larter et al., 2009; Lowe and Anderson, 2002). Both troughs extend toward the outer shelf, gradually shallowing and widening. The shelf configuration encompasses a sizable pre- and syn-rift basin on the midshelf, positioned between the basement exposure on the inner shelf and the submerged basement highs on the outer shelf (Gohl et al., 2013; Hochmuth and Gohl, 2013; Lowe and Anderson, 2002). A subordinate basin within the extensive mid-shelf basin may be linked to movement along an early branch of the West Antarctic Rift System. Ice erosion from the current inner shelf and coastal hinterland has removed a minimum of 4 km of preglacial strata. Evidence of at least five major erosional unconformities signifies phases of notable WAIS advances (Gohl et al., 2013). Prograding sequences and subglacial bedforms on the outer shelf, recovered subglacial tills in cores, and radiocarbon dates on calcareous microfossils and organic matter in overlying sediments suggest the expansion of ground ice to the outer shelf during the Last Glacial Maximum (LGM) and preceding glacial periods (Larter et al., 2014).

The continental rise is characterized by prominent sedimentary deposition centres and sediment drifts, indicative of robust bottom-current activity. Analysis of seismic data from the Amundsen Sea rise proposes the commencement of sediment drift formation in the Eocene/Oligocene (Uenzelmann-Neben et al., 2014; Uenzelmann-Neben and Gohl, 2012). This suggests an enduring bottom-current activity and a cold climate during the late Paleogene, likely influenced by Antarctic Bottom Water originating in the Ross Sea. Seismic records from the entire Marie Byrd Land margin along the continental rise demarcate the base of sediment drifts throughout the Amundsen Sea and into the Ross Sea (Lindeque et al., 2016). These records provide insights into sedimentation processes from preglacial to glacial times, variations in bottom-water circulation, early ice sheet growth, and glacial intensification leading to the present icehouse regime (Uenzelmann-Neben et al., 2014; Uenzelmann-Neben and Gohl, 2012). However, the derivation of stratigraphic age estimates from long-distance seismic correlation with the western Antarctic Peninsula margin and the Ross Sea margin poses limitations to this understanding. Within the Amundsen Sea, numerous sediment drifts have formed as a result of the deposition of suspended sediments, transported by ocean-bottom contour currents. These sediment drifts are separated by deep-sea channels originating at the base of the continental slope and

extending into the abyssal plain. The transportation of sediment downslope in these channels occurs through processes such as turbidity currents, slumps, and other gravity-driven mechanisms, contributing significantly to the accumulation of detritus in the drifts (Dowdeswell et al., 2006; Nitsche et al., 2000).

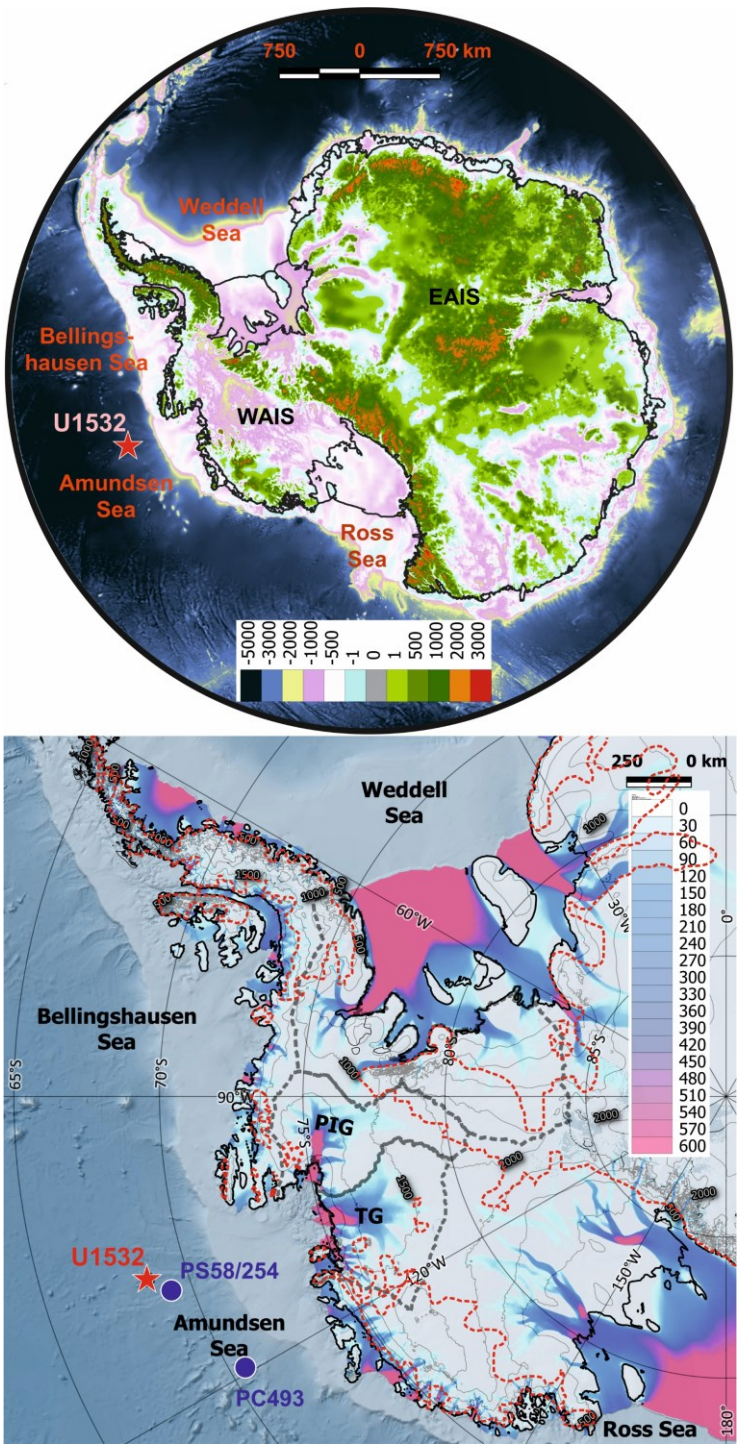

Figure 2.6: Amundsen Sea sector with IODP Expedition 379 drill site U1532 on Resolution Drift (red star). (a) Digital Elevation Map (DEM) of Antarctica (Fretwell et al., 2013). (b) Map showing West Antarctic Ice sheet ice flow rate (m/year) comprising of

Thwaites (TG) and Pine Island glaciers (PIG) basins areas delineated by the grey lines; Purple dot shows the nearby core locations (PC493 and PS58/254) (Pereira, 2018). Colour code represents ice flow rate. Red dashed line marks the ice-sheet extent simulated for the warm Pliocene (DeConto and Pollard, 2016). Base map was prepared Quantarctica (Matsuoka et al., 2021).

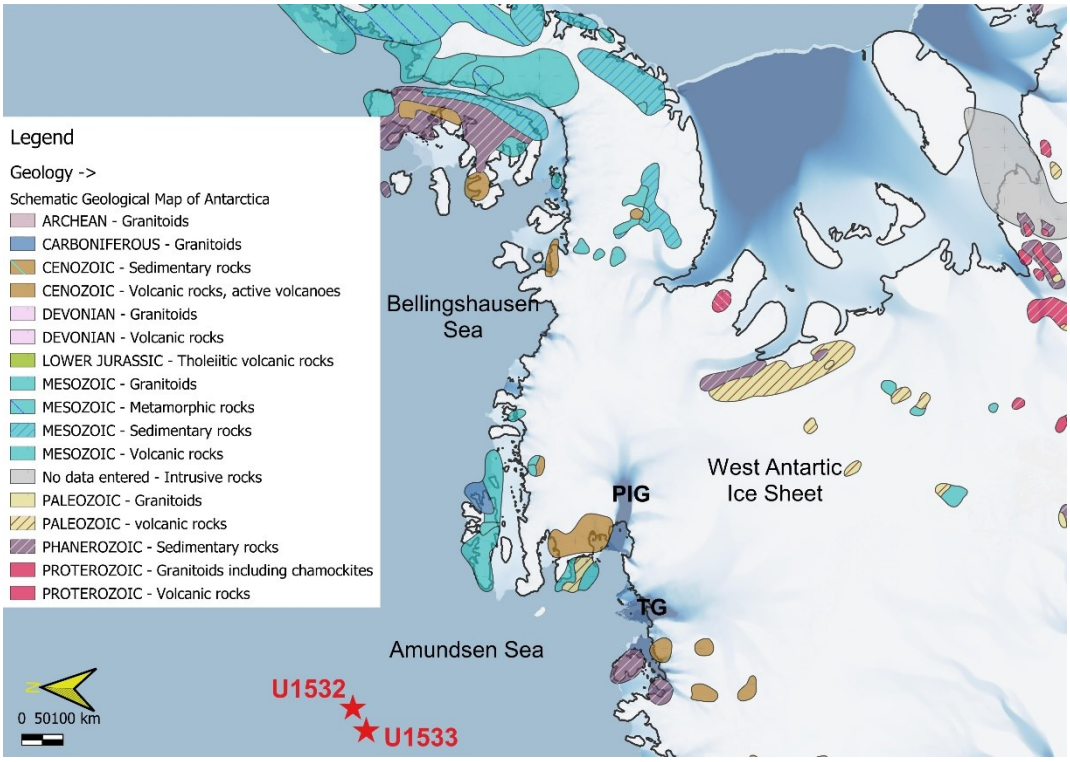

Figure 2.7: Type and age of the rocks exposed in the West Antarctic region. PIG – Pine Island Glacier, TG– Thwaites Glacier. Red Star represents the core sites U1532 and U1533 retrieved during IODP expedition 379. Base map was prepared Quantarctica (Matsuoka et al., 2021).

The Southern Ocean is primarily influenced by the Antarctic Circumpolar Current (ACC), a powerful current, which encircles the Antarctic continent in a clockwise manner and stands out for its ability to blend waters originating from all three major ocean basins (Orsi et al., 1995). The configuration of regional water masses is chiefly regulated by the primary frontal systems associated with the ACC. Across the ACC, there is a noticeable upwelling of Circumpolar Deep Water (CDW) towards the Antarctic landmass, allowing the intrusion of northern deep waters into the Southern Ocean, where they intermingle with surface waters (Orsi et al., 1999; Orsi et al., 1995). In the AS surface waters corresponds to Antarctic Surface Water (AASW) with temperature range from -1.8°C to 1.0°C and salinity values between 33.0 and 33.7 (Smith et al., 1999). These waters undergo freshening and warming due to factors like summer ice melt and heating, leading to the creation of the

spatially and temporally variable temperature and salinity patterns. Positioned below AASW is Winter Water (WW), characterized by a temperature minimum of around -1.5°C and salinities between 33.8 and 34.0. WW represents the end member of AASW (Sievers and Nowlin Jr, 1984) and is generated through winter cooling. Even during the summer, WW retains its temperature-salinity signature from the preceding winter (Smith et al., 1999). However, these characteristics of WW diminish during the austral summer as the upper water column heats up, causing instabilities and mixing with AASW and deeper water masses. Beneath WW lies the CDW, recognized as the most voluminous water mass within the ACC (Sievers and Nowlin Jr, 1988; Sievers and Nowlin Jr, 1984). CDW encompasses a wide spectrum of temperatures and salinities and is encountered in one or more of its variants at all stations within this study. North of the Southern Boundary of the ACC (SBACC), CDW can be categorized into two variants, namely Upper CDW (UCDW) and Lower CDW (LCDW; Figure 2.8), differing in h–S space due to their distinct source regions. UCDW, located at depths between 200 and 400 meters, is characterized by a subsurface temperature maximum, readily distinguished from the underlying temperature minimum of WW. LCDW exhibits a core within the range of 800 to 1000 meters and is distinguished by a salinity maximum, arising from the influence of saline NADW. Nevertheless, in the eastern Pacific sector, this characteristic is somewhat attenuated compared to other regions of the Southern Ocean, as this area is farthest from the NADW influx into the ACC (Whitworth III and Nowlin Jr, 1987). In the AS, CDW has the capacity to intrude significantly into the West Antarctic continental shelf. This water mass typically exhibits modifications in this region, with slightly lower temperatures and salinities resulting from its interaction with the overlying waters (Jacobs, 2004; Jenkins and Jacobs, 2008; Klinck et al., 2004; Smith et al., 1999). Modified RSBW has the potential to constitute the lowermost water mass within the upper continental rise region of the Amundsen Sea(Hellmer et al., 1998; Hellmer, 2004).

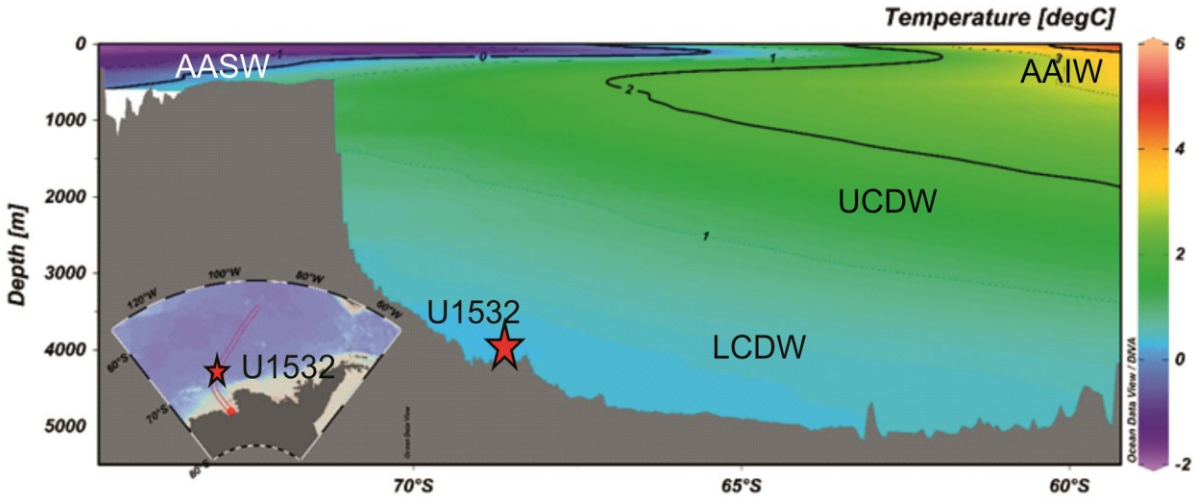

Figure 2.8: Section profile of the water temperature along the section in the Amundsen Sea, eastern Pacific Sector of Southern Ocean. AASW– Antarctic Surface Water, LCDW– Lower circumpolar deep water, UCDW– Lower circumpolar deep water, AAIW– Antarctic intermediate water. Section profile was produced using Ocean Data View Software (https://odv.awi.de/).

2.2.2 Sediment Core

Sediment core was recovered from the site U1532 (68°36.36' S, 107°31.50' E) during the IODP 379 expedition to the Amundsen Sea on the western upper flank of the Resolution Drift, which is located on the continental rise ~270 kilometres north of the Amundsen Sea Embayment shelf edge (Figure 2.6). Site U1532 was drilled at a water depth of 3962 meters with a total core length of 794 meters and a recovery of ~90%. The sedimentary deposits at Site U1532 were categorized into a lithostratigraphic unit consisting of three subunits. These subunits are designated as IA (0–92.6 meters; recent–Pliocene), IB (92.6–400.6 meters; Pliocene), and IC (401.0–787.4 meters; Pliocene–Miocene) (Gohl et al., 2021b). The differentiation of these subunits is primarily based on changes in the facies assemblages within the sediment. The sediments found within the uppermost 150 meters are predominantly unconsolidated, with increasing consolidation observed below this depth. Notably, intervals with carbonate-cemented laminae and thin beds of coarse siltstone and sandstone are present below the 400-meter mark. Some intervals within the stratigraphy exhibit light green, biosilica-rich layers that correspond to higher concentrations of coarse sands and gravels, which are inferred to be indicative of ice-rafted debris (IRD). These intervals also tend to display bioturbation. Certain stratigraphic layers display low to no identifiable diatom debris despite showing characteristics such as low magnetic susceptibility, gamma ray attenuation (GRA) bulk

density, and a greenish colour, which are typically associated with diatomaceous sediments. The absence of diatoms in these layers is interpreted as a result of diagenetic processes leading to the loss of diatoms and other siliceous microfossils. Calcareous microfossils, including foraminifers, calcareous nannofossils, and ostracods, are generally lacking at Site U1532, however they occur in few thin intervals within the Pleistocene section (Gohl et al., 2021b).

2.2.3 Age model

For the present study the cores comprising of single lithostratigraphic unit in which two subunits IA (0 – 92.6 mbsf, Pliocene to recent), IB (92.6 – ~130 mbsf, Pliocene) has been targeted in this study. The age control for the core U1532 is the uses preliminary age-depth model based on the shipboard analysis using magnetostratigraphic polarity zones (Table 2.5), which has been constrained using the biostratigraphy datum age based on radiolarian and diatom ages (Gohl et al., 2021a; Gohl et al., 2021b) (Figure 2.9).

The determination of linear sedimentation rates, as computed between age control points based on magnetostratigraphy, reveals a notable increase in sedimentation rates with depth. In the Pleistocene strata, the sedimentation rates average approximately 2 cm per thousand years (ky), while in the later Miocene to early Pliocene section, they increase substantially to around 24 cm/ky. Notably, the highest sedimentation rates, approximately 61 cm/ky, are observed within the depth interval of approximately 322 to 406 meters, corresponding to subchron C3n.2n with an age range of 4.493 to 4.631 million years. Conversely, the lowest sedimentation rates within the Pliocene section, approximately 10 cm/ky, were calculated for the interval spanning approximately 406 to 422 meters, corresponding to subchron C3n.2r with an age range of 4.631 to 4.799 million years (Table 2.5). This observation may suggest either a temporary reduction in sediment input to the site or the potential existence of a brief hiatus within this specific interval. However, it is worth noting that the presence of a hiatus is not conclusively warranted (Gohl et al., 2021a; Gohl et al., 2021b).

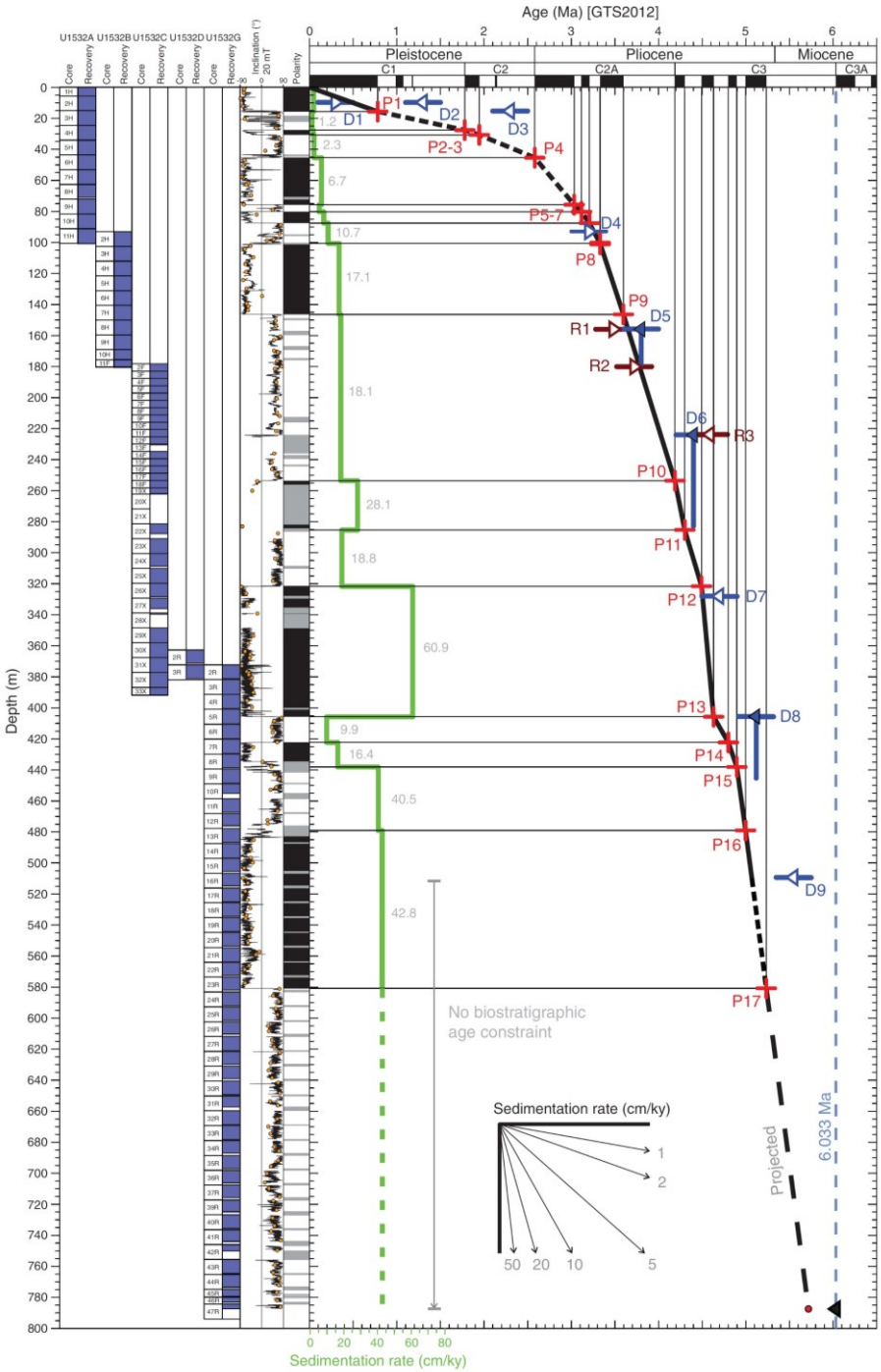

Figure 2.9: Core description and Age-depth model for Site U1532 adopted from proceedings (Gohl et al., 2021b) based on integrated bio-magnetostartigraphy. Paleomagnetic inclination values were obtained from cryogenic magnetometer analysis of archive halves after 20 mT AF demagnetization and cleaning for disturbed sediment intervals. Orange circles = inclination values from discrete sample analysis. Polarity: black = normal, white = reversed, and grey = indeterminate (because of lack of recovery, major sediment disturbance, or other limitations). Blue arrows = tie points for diatom biostratigraphic datums, maroon arrows = radiolarian biostratigraphic datums, red crosses = magnetostratigraphic datums. Open arrows = "younger than" or "older than"

biostratigraphic age constraints, solid arrows = true first appearance datum or last appearance datum. Linear sedimentation rates (green line) are calculated between tie points. Gray numbers = sedimentation rates between each tie point.

Table 2.5: Shipboard key paleomagnetic age data as inferred from correlation of magnetic polarity at Site U1532.

Tie points ID	Magneto stratigraphic tie points	Core, section	Midpoint depth CSF-A(m)	Depth uncertainty CSF-A(m)	Age (Ma)	Sedimentation rates (cm/ka)
		379-U1532A-				
P1	C1n base	3H-1	15.64	0.88	0.781	1.4
P2	C2n top	4H-2	27.6	0.2	1.778	1.9
P3	C2n base	4H-5	30.74	0.1	1.945	2.3
P4	C2An.1n top	6H-2	45.41	0.2	2.581	6.7
P5	C2An.1n base	9H-3	75.71	0.075	3.032	5.4
P6	C2An.2n top	9H-6	80.24	0.075	3.116	8.1
P7	C2An.2n base	10H-4	87.57	0.1	3.207	10.4
P8	C2An.3n top	11H-7	100.35	0.08	3.33	
		379-U1532B-				
P8	C2An.3n top	2H-6	101.03	0.125	3.33	10.7
P9	C2An.3n base	7H-4	146.42	0.125	3.596	17.1
		379-U1532C				
P10	C3n.1n top	18F-1	253.76	0.275	4.187	18.1
P11	C3n.1n base	22X-CC	285.36	4.550	4.300	28.1
P12	C3n.2n top	26X-2	321.68	0.050	4.493	18.8

Further to improve the shipboard chronology of the Pleistocene, we have identified more tie points in the present study based on the correlation between geochemical parameters and global benthic $\delta^{18}O$ curve (LR04) (Lisiecki and Raymo, 2005a) (Figure 2.10). Elemental ratios of (a) Ba/Al, (b) Ba/Rb, (c) PC1 (first principal component) derived from principal component analysis (PCA) of multiple elemental ratios were compared with the LR04 curve (Figure 2.10). In addition to previously determined tie points, nine additional new tie-points were identified based on the excursions in the geochemical parameters and its correspondence with the glacial-interglacial signals in the LR04 $\delta^{18}O$ curve (Figure 2.10). Finally, to generate an age-depth model with an appropriate degree of uncertainty, the MatLab™-based age-depth modelling program Undatable (Lougheed and Obrochta, 2019). The advantage of using Undatable over other available age-depth

modelling programs is that it allows for the input of uncertainties in both age and in depth, and for a series of different types of age control points to be incorporated (Figure 2.11). Undatable was run using 100,000 simulations (Lougheed and Obrochta, 2019). Probability density cloud for uncertainty envelope around the modelled age-depth points was computed using Monte Carlo iterations. Blue and black dotted lines show 1σ and 2σ uncertainty, respectively. Due to more tie points in the Pleistocene interval, the chronology is better constrained to resolve the glacial-interglacial variations with confidence.

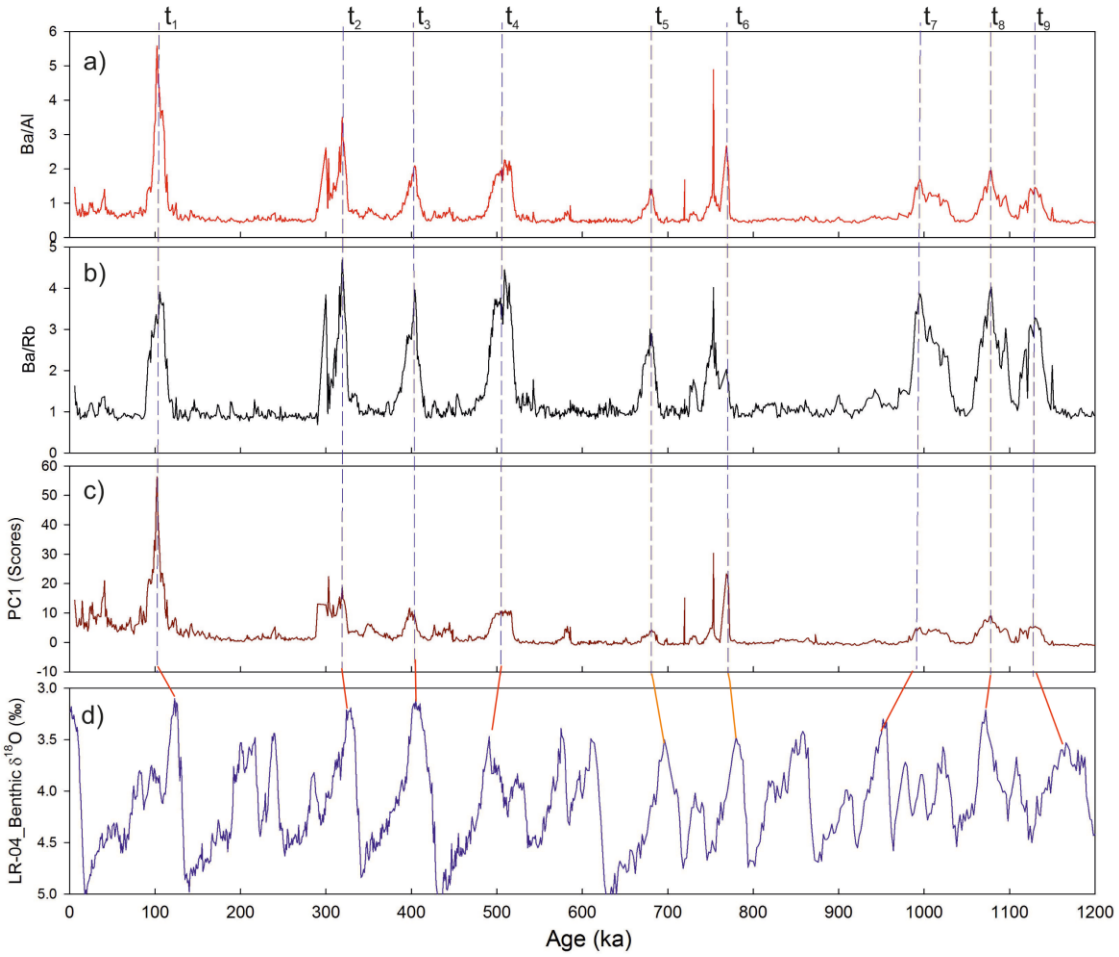

Figure 2.10: Determining tie-points of the Pleistocene glacial-interglacial cycles in U1532 record. To improve the ship based age model, more tie points were determined based on the comparison and tuning of geochemical parameters with respect to the global benthic $\delta^{18}O$ curve (LR04) (Lisiecki and Raymo, 2005b). Elemental ratios of (a) Ba/Al, (b) Ba/Rb, (c) PC1 (first principal component) derived from principal component analysis (PCA) of multiple elemental ratios were compared with (d) global benthic $\delta^{18}O$ record (LR04). The dashed vertical lines indicate interglacial peaks in the $\delta^{18}O$ record and their corresponding matched in the geochemical signals.

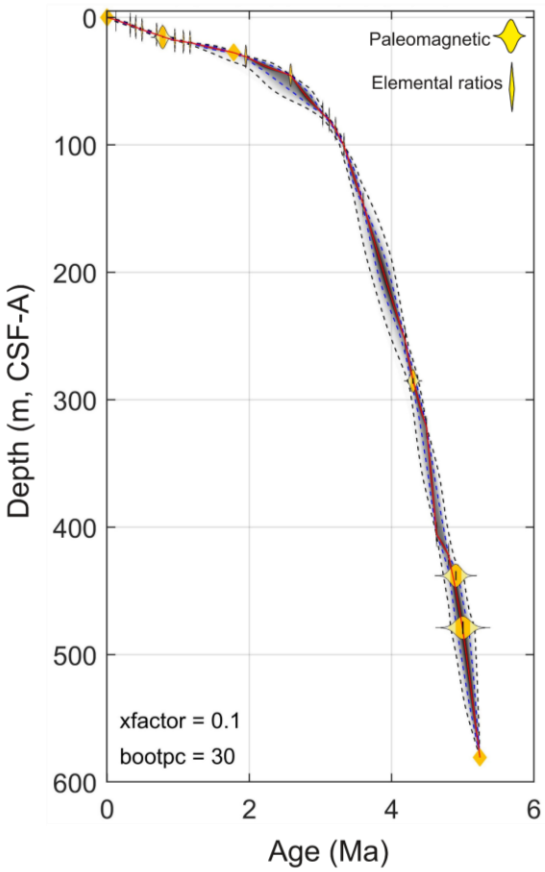

Figure 2.11: Age-depth model was performed using the program Undatable. after including uncertainty in both ages as well as depth intervals. In addition to Biostratigraphic and Paleo-magnetic events, additional tie-points derived from the tuning of the geochemical parameters (Figure 2.10) and benthic $\delta^{18}O$ global curves (LR04) were used for age-depth modelling. The probability density cloud for uncertainty envelope around the modelled age-depth points was computed using Monte Carlo iterations (n=10,000). Blue and black dotted lines show 1σ and 2σ uncertainty, respectively.

2.2.4 Sample Preparation

The chemical reductive leaching method adopted to extract elements from the authigenic Fe-Mn part of sediments, is widely deployed and being used since 1960's (Chester and Hughes, 1967). However, these methods are still under development and may vary from basin to basin depending upon the oceanographic settings and the chemical composition of the sediments. The major concern behind adopting different method is to prevent the dissolution of the non-hydrogenetic components of the sediment. The Arabian Sea samples has high carbonate content and high proportion of the chemically weathered sediment due to its long transport in the hot and humid climate, utilised the smaller volume of solution/sediment sample ratio to restrict the contamination (Lathika et al., 2021; Wilson

et al., 2013). The sediments in the Southern Ocean contain higher proportion of physically weathered detritus, that is more susceptible to chemical reactions during the reductive leaching extraction (Baeyens et al., 2003; Diekmann et al., 2003; Huang et al., 2021). Hence, a leaching method with very short contact time between the sediment and the leaching reagent is more suitable to reduce the contamination from the detritus. Since, during smaller leaching intervals lesser amount of the elements are expected to be leached, hence a chelating ligand are added to prevent re-adsorption of the dissolved authigenic elements (Gutjahr et al., 2007).

Thus, initially we conducted Nd isotopic analysis of acid-reductive leachates, designed to selectively release Fe-Mn oxyhydroxide coatings while preserving detrital sediment phases. We processed approximately 1 gram of bulk sediment using approximately 10 milliliters of 0.005 M Hydroxylamine-Hydrochloride (HH) leachate, containing EDTA and acetic acid at a buffered pH of 4. The leaching procedure, following the protocol established by Blaser et al. (2016) and Gutjahr et al. (2007), lasted for forty minutes. However, in a recent study Huang et al. (2020), refined this method by employing a shorter leaching duration. The comparative analysis of sediments samples subjected to different leaching interval by following the Huang et al. (2020) method revealed that gradual reduction in the contact time between the solvent and sample resulted in slightly less radiogenic ε_{Nd} values (Table 2.6, Figure 2.12).

Table 2.6: Effect of leaching interval on the samples corresponding ε_{Nd} values.

Sample No.	Leaching Time	ε_{Nd} (CSF-A 81.4 m)	ε_{Nd} (CSF-A 99.1 m)	ε_{Nd} (CSF-A 132.46 m)
1	10 sec	-3.66 ± 0.12	-4.98 ± 0.12	-5.57 ± 0.12
2	30 sec	-3.63 ± 0.12	-4.82 ± 0.12	-5.60 ± 0.12
3	1 min	-3.54 ± 0.12	-4.83 ± 0.12	-5.55 ± 0.12
4	5 min	-3.65 ± 0.12	-4.92 ± 0.12	-5.46 ± 0.12
5	10 min	-3.57 ± 0.12	-4.50 ± 0.12	-5.46 ± 0.12
6	15 min	-3.43 ± 0.12	-4.46 ± 0.12	-5.18 ± 0.12
7	30 min	-3.45 ± 0.12	-4.29 ± 0.12	-5.06 ± 0.12

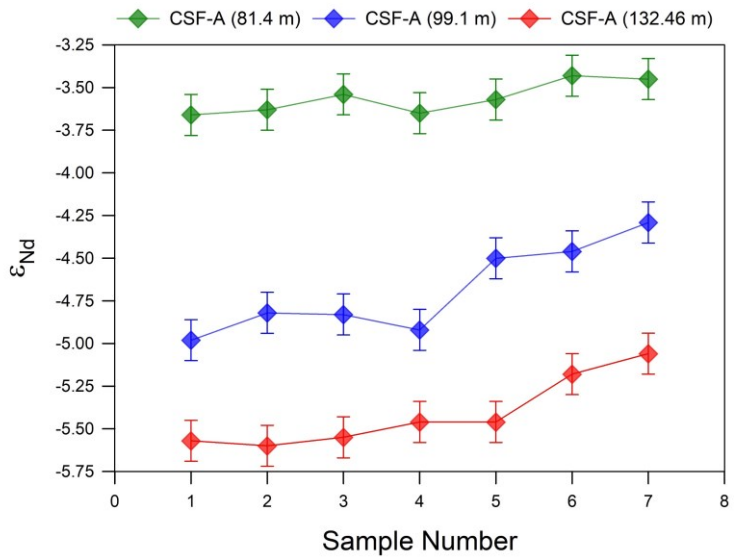

Figure 2.12: Effect of leaching interval. ε_{Nd} profile of samples with respect to their time taken for leaching as mentioned in Table 2.6.

Consequently, we processed our samples in accordance with the Huang et al. (2020) protocol for leaching the authigenic fraction from the bulk sediments. Approximately 0.3 grams of finely powdered and homogenised sediment samples were precisely weighed and subjected for the processing for each measurement. The authigenic fraction of Fe–Mn oxyhydroxides present within the sediment was extracted using a controlled vortexing procedure. This involved agitating the bulk sediment within a solution comprising 0.005M hydroxylamine hydrochloride, 1.5% acetic acid, and 0.003M Na-EDTA, buffered to pH 4 with NaOH, for a maximum duration of 10 seconds. The leachates were subjected to centrifugation, followed by drying, and subsequently dissolved in the concentrated HNO_3 followed by concentrated HCl. After this step, the solutions were dried once more and were taken into 2N HCl prior to column chromatography.

To extract the detrital fraction, the residual material left after removing the authigenic phase was subjected for the 24 hours of the leaching in order to remove all the authigenic components and was further treated with 0.6 N HCl for the complete removal of carbonates. Subsequently, samples were washed thoroughly with Milli-Q water and air dried in the oven at 80° C. Dried samples were then ashed at 600°C in a muffle furnace to remove organic matter. Approximately 50 mg of ashed, homogenised samples were subjected to hotplate digestion in precleaned Teflon vials. Samples underwent dissolution utilizing a solution composed of 2 ml of HF and 1 ml of HNO3, for closed digestion with heating on a hotplate at 120°C for a duration of three to four days, until all observable

particulate matter was absent. Subsequently, the specimens underwent dissolution once more in a 2 ml solution of HCl for a period of two to three days (Pereira et al., 2020; Roy et al., 2007; Wilson et al., 2018). This sequence of steps was reiterated to ensure the thorough digestion of the sample. Further, the samples were dissolved in the 2N HCl, and was divided in two aliquots for the column chromatography of Nd and Pb. Standard Reference Materials BCR-2 and BHVO-2 were also digested along with the samples.

2.2.5 Nd isotope Analysis

Dissolved samples (leach and the detrital) were purified by column chromatography and were passed through columns filled with cation-exchange resin AG50W-X8 (200–400 micron) to separate Rare Earth Elements (REE). Samples were loaded in the 2N HCl medium and the REE fractions were eluted using 6N HCl (Table 2.3). REE fractions were then dried and converted to the 0.16N HCl medium and passed through the column containing Eichrom LNspec^{TM} (50 – 100 micron) resin to separate Nd from the REEs (Table 2.4). Nd fraction was eluted using 0.27N HCl and was then dried and converted to HNO_3 medium for the measurement of the isotopic ratios.

Nd isotope ratios were measured using Multi-collector Inductively Coupled Plasma Mass Spectrometer (Thermo Fischer Scientific, Neptune Plus) at National Centre for Polar and Ocean Research, Goa. Instrumental mass fractionation during Nd isotopic analyses was corrected by normalizing the measured ratio of $^{143}Nd/^{144}Nd$ to $^{146}Nd/^{144}Nd = 0.7219$ using the mass bias correction procedure of Vance and Thirlwall (2002).The measured $^{143}Nd/^{144}Nd$ ratios were normalised to the reported JNdi-1 standard $^{143}Nd/^{144}Nd$ value of 0.512115 (Tanaka et al., 2000). A correction for direct ^{144}Sm interference was also applied, with all samples which was below (<0.1% of the ^{144}Nd signal). To ensure the quality of measurement, the international standard JNdi-1 was matrix matched and measured at every five samples. The obtained average ratios were 0.512115 ± 10 ppm (2σ, n= 90). The external reproducibility calculated for each session was 0.12–0.27 ε_{Nd} (2σ) units based on the repeated measurements of JNdi-1. If the internal error (2σ) is larger than the external error, the internal error is reported as the final uncertainty associated with the individual measurements. Several procedural blanks were also processed along with the samples and ascertained an average blank of ~70 pg for the samples (n=9), which is several orders of magnitude lower than the total Nd typically analysed in samples. Hence, no blank correction was applied. Replicates have an average ε_{Nd} variation of ±0.17 (n= 16). Over the

course of analyses, measurements of rock standard BCR-2 and BHVO-2 processed with the samples gave $^{143}Nd/^{144}Nd$ = 0.512641 ± 0.000010 (2s, n = 7) and $^{143}Nd/^{144}Nd$ = 0.513008 ± 0.000012 (2s, n = 7), in excellent agreement with reported values.

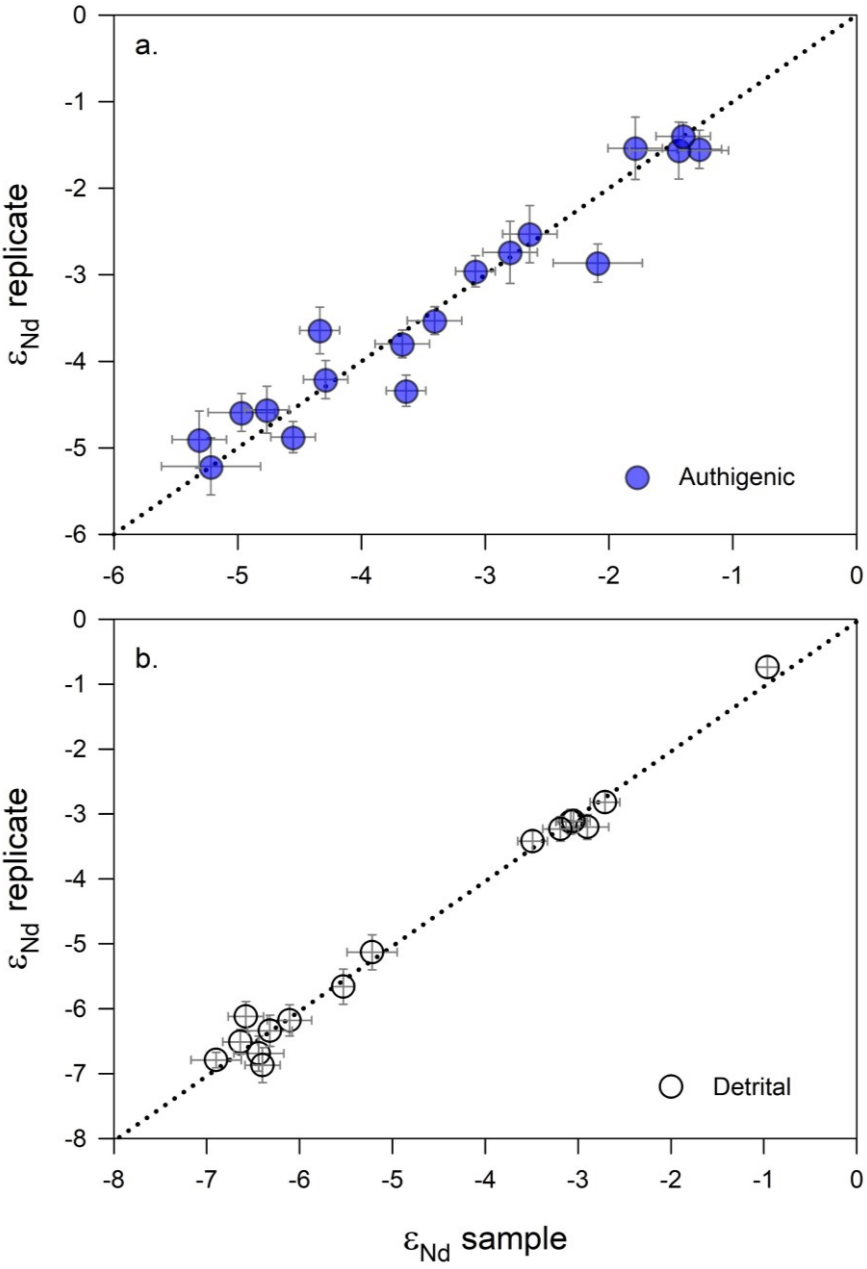

Figure 2.13: Replicate analysis of Nd isotopes. To ascertain the quality of the analysis, Nd isotopes were measured in the replicates and shown in the cross plot. a) authigenic ε_{Nd} (n=18), b) detrital ε_{Nd} (n=16). Dashed line represents the 1:1 equiline.

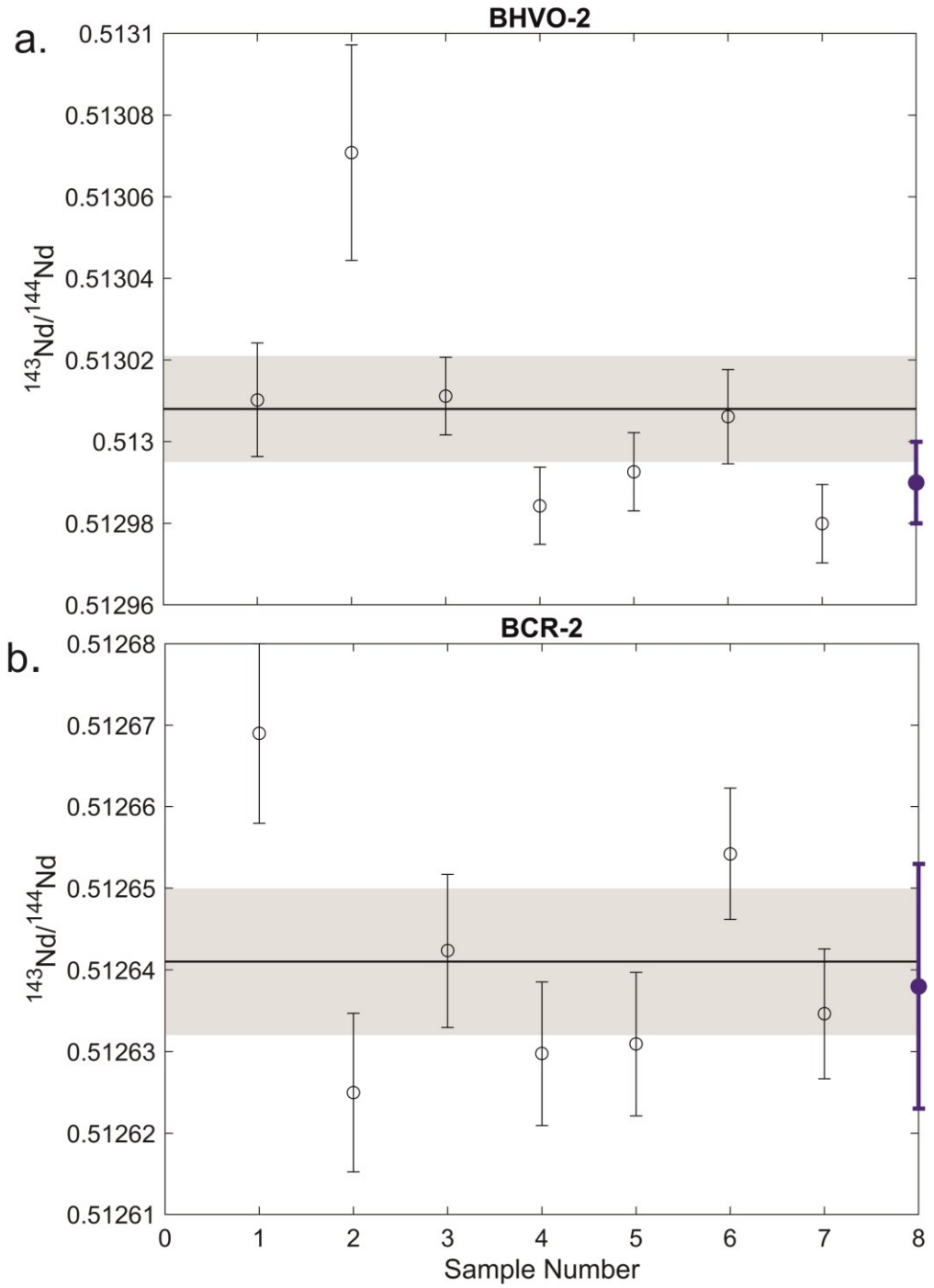

Figure 2.14: $^{143}Nd/^{144}Nd$ ratio of a) BHVO-2 and b) BCR-2 processed with the detrital sample. The black solid line shows the average value 0.5123008 ± 13 ppm (2σ) and 0.512641 ± 9 ppm (2σ) respectively and the grey shading represents 2σ error of the sample. The blue circle represents the reported values of 0.512990 ± 10 ppm (2σ) and 0.512641 ± 15 ppm (2σ) respectively (Weis et al., 2006).

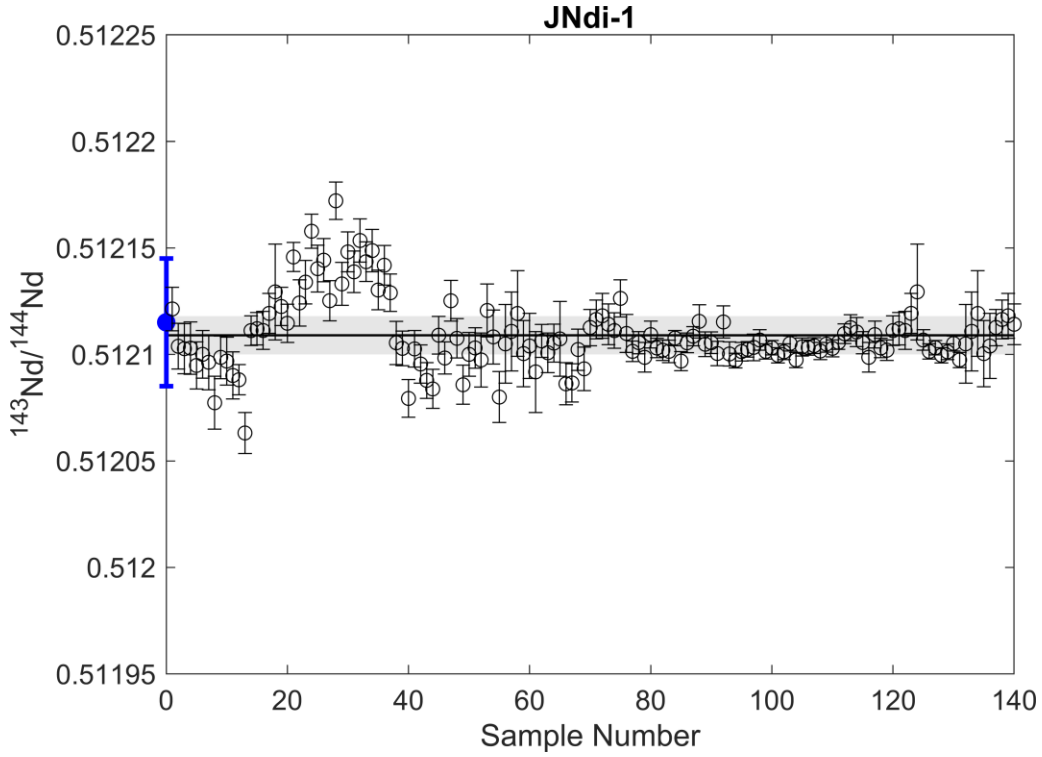

Figure 2.15: Temporal variability of the JNdi-1 $^{143}Nd/^{144}Nd$ ratio. The black solid line shows the average value 0.512109 ± 9 ppm (2σ) and the grey shading represents 2σ error. The blue circle indicates the reported value of 0.512115 ± 30 ppm (2σ) (Tanaka et al., 2000).

2.2.6 Pb isotope Analysis

Pb isotope was analysed in the other aliquot (n=72). The Pb cuts of the dissolved detrital sediment were purified by column chromatography filled with ~80 µL of AG1-X8 resin cleaned with 0.25M HNO_3. Pb aliquot was first dissolved in the 2M HBr and was dried and redissolved into a 300 µl mixture of HNO_3 and HBr (0.5M and 0.2M respectively) to load into the column as a sample. Lead was eluted and collected using 650 µl solution of HNO_3 and HBr mixture having a molarity of 0.5M and 0.03M respectively. The collected Pb fraction was dried and converted to HNO_3 medium for the measurement of the isotopic ratios.

Pb isotopes were measured using a Thermo Scientific Neptune Plus MC-ICP-MS at GEOMAR, Kiel. Mass bias correction during Pb isotope measurements was performed externally using the Tl-doping technique with added NIST997 Tl standard solution. The procedural blanks were ~500 pg which represents less than 0.1% of the sample signal. Blank corrected and uncorrected ratios do not show significant difference and hence blank uncorrected data is reported in this study.

Chapter 3

Onset of modern-like deep water circulation in Indian Ocean caused by Central American Seaway closure

3.1 Introduction

Global Overturning Circulation (GOC) plays a critical role in controlling ocean heat distribution and atmospheric CO_2 levels and thereby influencing global climate (Clark et al., 2002; Elias, 2013; Rahmstorf, 2006). Tectonically driven changes in the ocean-gateways since the late Miocene had a dramatic impact on GOC, such as the closure of the Central American Seaway (CAS) during the late Miocene (Karas et al., 2017; Molnar, 2008) and the Indonesian Throughflow (ITF) during the past 3 to 4 Ma (Hall, 2002b; Kuhnt et al., 2004). These tectonic changes may influence the formation of the northern component water [NCW, a precursor of North Atlantic Deep Water (NADW)] in the North Atlantic and Antarctic Bottom Water (AABW) in the Southern Ocean and their export to the global oceans. These large scale changes in deep water circulation (DWC) might impact global climate through ocean-atmosphere CO_2 and heat exchange and provide feedback to the climate system. The prevailing hypothesis related to the ocean-climate coupling and their feedback through heat and CO_2 exchange since the late Miocene remains untested due to lack of suitable records of formations, export, and distributions of NCW and AABW in global oceans. To the best of our knowledge, these records are mostly from the Pacific and the Atlantic oceans; the majority of these records are either from proximity to the deep water formation regions or oceanic seaways. Hence these records might not necessarily reflect the widespread impact and large scale changes in deep water circulation. Due to the absence of any major deep water formations in the Indian Ocean, it acts only as a host for deep water circulation (NCW and AABW). Further, the northern Indian Ocean is located at one of the terminal ends of the GOC, far away from the deep water formation regions and oceanic seaways. These specific features of the northern Indian Ocean make it an ideal basin to assess large-scale deep water circulation changes in the past associated with tectonics and/or climatic changes and to validate the hypotheses related to ocean-climate couplings and their feedback mechanisms since the late Miocene. Few studies have been carried out in the Indian Ocean to reconstruct past DWC on a longer timescale, based on

authigenic neodymium isotope composition (ε_{Nd}) of sediment cores (Gourlan et al., 2008b; Le Houedec et al., 2012b; Martin and Scher, 2006b) and Fe-Mn crust records (Frank et al., 2006b; O'nions et al., 1998a). These Fe-Mn crusts with growth rate of (1 to 4.3 mm/Ma), are situated at deeper depths (>4000 m) bathed only by AABW and hence, suitable for the reconstruction of AABW only. On the other hand, the existing high-resolution authigenic ε_{Nd} records are either from the intermediate depths of the Central Indian Ocean (Gourlan et al., 2008b; Le Houedec et al., 2012b) or from the Bay of Bengal (BoB) (Gourlan et al., 2008a; Gourlan et al., 2010) (Figure 2.1a, Figure 3.1d). The BoB records are known to be affected by the release of particulate Nd supplied by the Himalayan rivers (Naik et al., 2019; Singh et al., 2012) and hence are not suitable for the reconstruction of DWC. Thus, it is imperative to have records from the regions not affected by such processes and represent large-scale circulation in the Indian Ocean. A recent study (Lathika et al., 2021) has successfully reconstructed the DWC of the last glacial cycle (~136 ka) based on authigenic and foraminifera ε_{Nd} records from the eastern Arabian Sea (SK 221-05, 9°0’32” N, 72°5’32” E; 2700 m water depth) and thus suggests Arabian Sea would be a suitable location for the reconstruction of the past DWC.

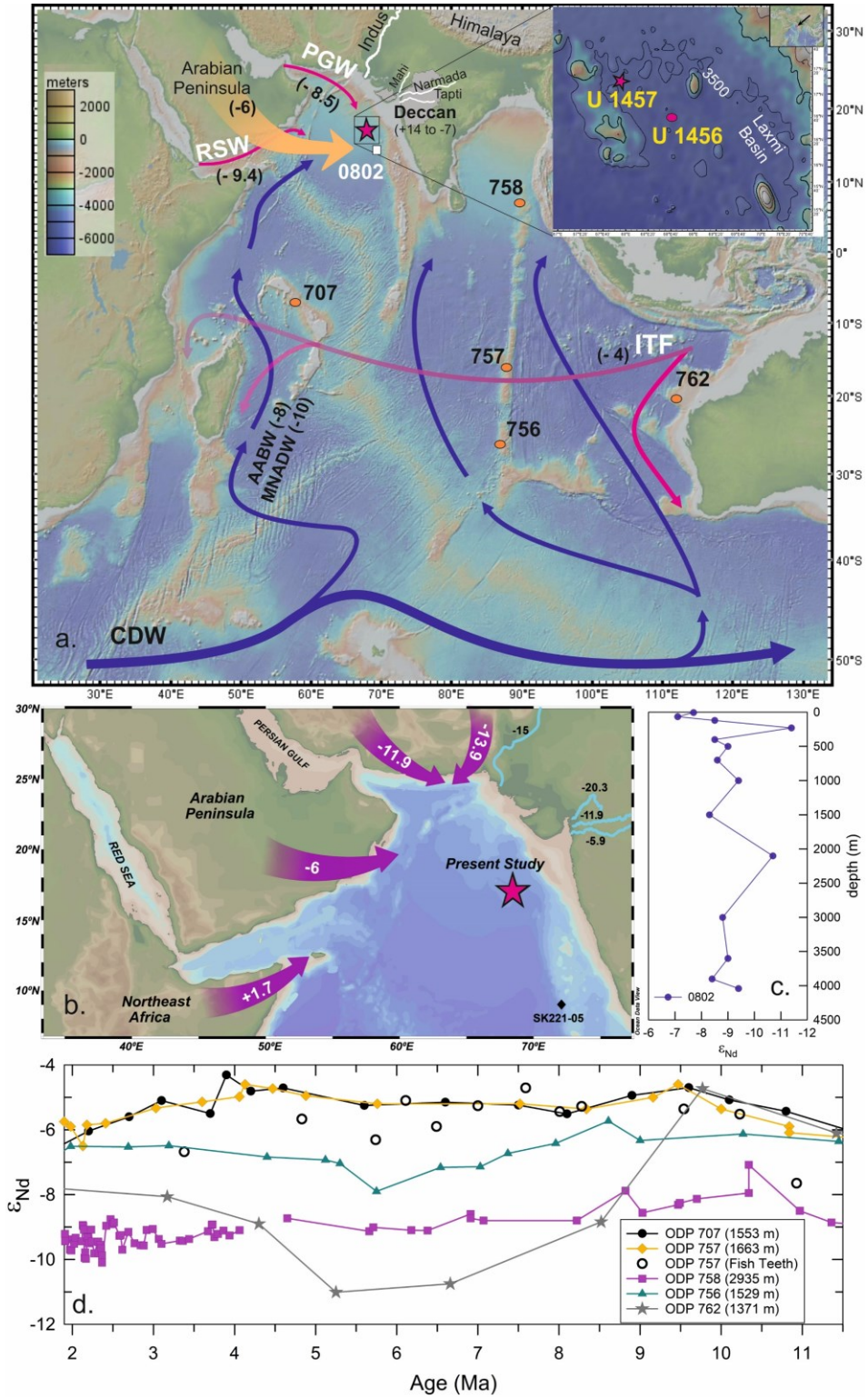

Figure 3.1: Potential sources of Nd with their characteristic ε_{Nd} values and authigenic ε_{Nd} records from the Indian Ocean. (a). Location map with the water mass pathways in the Indian Ocean. The red star marks the present study's location (IODP 355 U1457), while the red circles indicate existing ε_{Nd} records from the Indian Ocean for the studied time interval (ODP sites 707 (Gourlan et al., 2008a), 758 (Gourlan et al., 2008a), 757 (Gourlan et al., 2008a; Martin and Scher, 2006a), 756 (Le Houedec et al., 2012a), 762 (Le Houedec et al.,

2012a)). The yellow square marks the proximal seawater station 0802 (Goswami et al., 2014), whose value has been used for the modern ε_{Nd} values. Surface water masses are indicated by red arrows, whereas blue arrows indicate deep water masses. Orange arrow marks the aeolian dust influx from the Arabian Peninsula. The yellow stars denote the Fe-Mn crust site from the Indian Ocean, DODO 232D (Frank et al., 2006a) SS 663(O'Nions et al., 1998b). ε_{Nd} value of different water masses (given in bracket). PGW- Persian Gulf Water, ITF- Indonesian Throughflow Water, RSW- Red Sea Water, CDW- Circumpolar Deep Water, MNADW- Modified North Atlantic deep water, AABW- Antarctic Bottom Water, ASW- Arabian Sea Water (which includes PGW, RSW and Arabian Sea high salinity water). The image in the inset shows the high-resolution bathymetry of the core location. The base map was produced using online Geomap app (http://www.geomapapp.org); (b) Pink arrow marks the aeolian dust influx from the nearby continents with their ε_{Nd} values given in white (Kumar et al., 2020; Suresh et al., 2021) (Arabian Peninsula -6, Northeast Africa +1.7, Persia -11.9, Thar desert -13.9) along with the rivers ε_{Nd} values which contributes to study site (Goswami et al., 2014). The base map in the Panel b was produced using Ocean Data View Software (https://odv.awi.de/); (c) Modern seawater column ε_{Nd} profile at station 0802 (Goswami et al., 2014); (d) Published authigenic ε_{Nd} records from Indian Ocean ODP 707, 757 and 758 (Gourlan et al., 2008a; Gourlan et al., 2010), ODP 756, 762 (Le Houedec et al., 2012a), Fe-Mn crust record DODO 232D (Frank et al., 2006a) SS 663 (O'Nions et al., 1998b) are compiled; Green open circle represents fish teeth record from ODP 707 (Martin and Scher, 2006a).

In the present study, we have generated ε_{Nd} record from the Arabian Sea at the core site U1457C (17°9.95' N, 67°55.81' E, 3522 m) and reconstructed the DWC record of the Indian Ocean for the interval between the late Miocene to early Pleistocene (11.3 to 1.98 Ma). According to the modern hydrographic settings, the core site is presently bathed by Lower Circumpolar Deep Water (LCDW) with a higher proportion of AABW (Figure 2.1) (Goswami et al., 2014). Thus, the ε_{Nd} record at this core site would be able to capture large scale changes in the production and export of deep water masses in the late Miocene associated with tectonic and climatic changes. This will enable us to understand how the Indian Ocean DWC responded to these events in the past and evolved to the modern-like deep water circulation system.

3.2 Result

Nd isotope compositions were measured in the authigenic fraction of the bulk sediments (authigenic ε_{Nd}) and a few fish teeth/debris samples (n = 10) in a sediment core recovered from the IODP site U1457 C from the eastern Arabian Sea (Figure 3.2, Table 3.1). In addition, Nd isotope composition was also measured in selected residual detrital

fraction (detrital ε_{Nd}) of the same samples (Figure 3.4g) to examine the diagenetic overprinting on the authigenic ε_{Nd}. The fish teeth ε_{Nd} is considered to be more robust and reliable (Basak et al., 2018a) than leachate ε_{Nd} as a proxy for past water mass circulation due to the possibility of partial dissolution of detrital Nd during the leaching of bulk sediments, which can alter the authigenic ε_{Nd} signature (Abbott, 2019; Abbott et al., 2015; Haley et al., 2017a). The agreement between the fish teeth and leachate ε_{Nd} values (Figure 3.2a Figure 3.3) gives us confidence that the leachate ε_{Nd} is not affected by the partial dissolution of detrital Nd during the leaching. Due to restricted occurrences of fish teeth and foraminifera in the present core, ε_{Nd} was measured in the leach fraction to generate a high resolution record.

The authigenic ε_{Nd} record shows a narrow range from -6.5 to -4.5 with an average value of -5.5 ± 1 during the late Miocene interval (11.3 to 8.3 Ma). Thereafter, it shows a progressive shift towards less radiogenic values except for the three distinct excursions of more radiogenic values with similar magnitude (-5.5 ± 0.5) during the intervals of 7.4 to 6 Ma, ~3.5 Ma, and 2.5 to 2 Ma (Figure 3.2a). The observed range in the authigenic ε_{Nd} record between -9 and -4.5 at the U1457 site is much higher than the earlier reports from the north-eastern Arabian Sea and the equatorial Indian Ocean (EIO) (-9 to -6.5) during the late Quaternary glacial-interglacial periods (Lathika et al., 2021; Piotrowski et al., 2009). The overall trend in the authigenic ε_{Nd} profile excluding these three excursions shows a progressive shift from more radiogenic values (-5.5 ± 1) prior to ~9 Ma to less radiogenic values (-8.7 ± 0.11) during the Miocene-Pliocene transition (~6 Ma) (Figure 3.2a). These less radiogenic values are similar to that of the average value of the late Holocene -8.8 ± 0.2 (Lathika et al., 2021) and modern deep water -9 ± 0.4 (Goswami et al., 2014) reported from the Arabian Sea (Figure 3.1c) and thus indicating that the authigenic ε_{Nd} record has remained stable at the modern value (~ -9) since the Miocene-Pliocene transition (~6 Ma). The detrital ε_{Nd} measured in selected samples (n=16), ranges from -12 to -5.7 (Figure 3.4f, Table 3.1), are consistent with the reported range (-12.6 to -5.3) (Clift et al., 2019b; Dailey et al., 2019) from this core (Figure 3.4f).

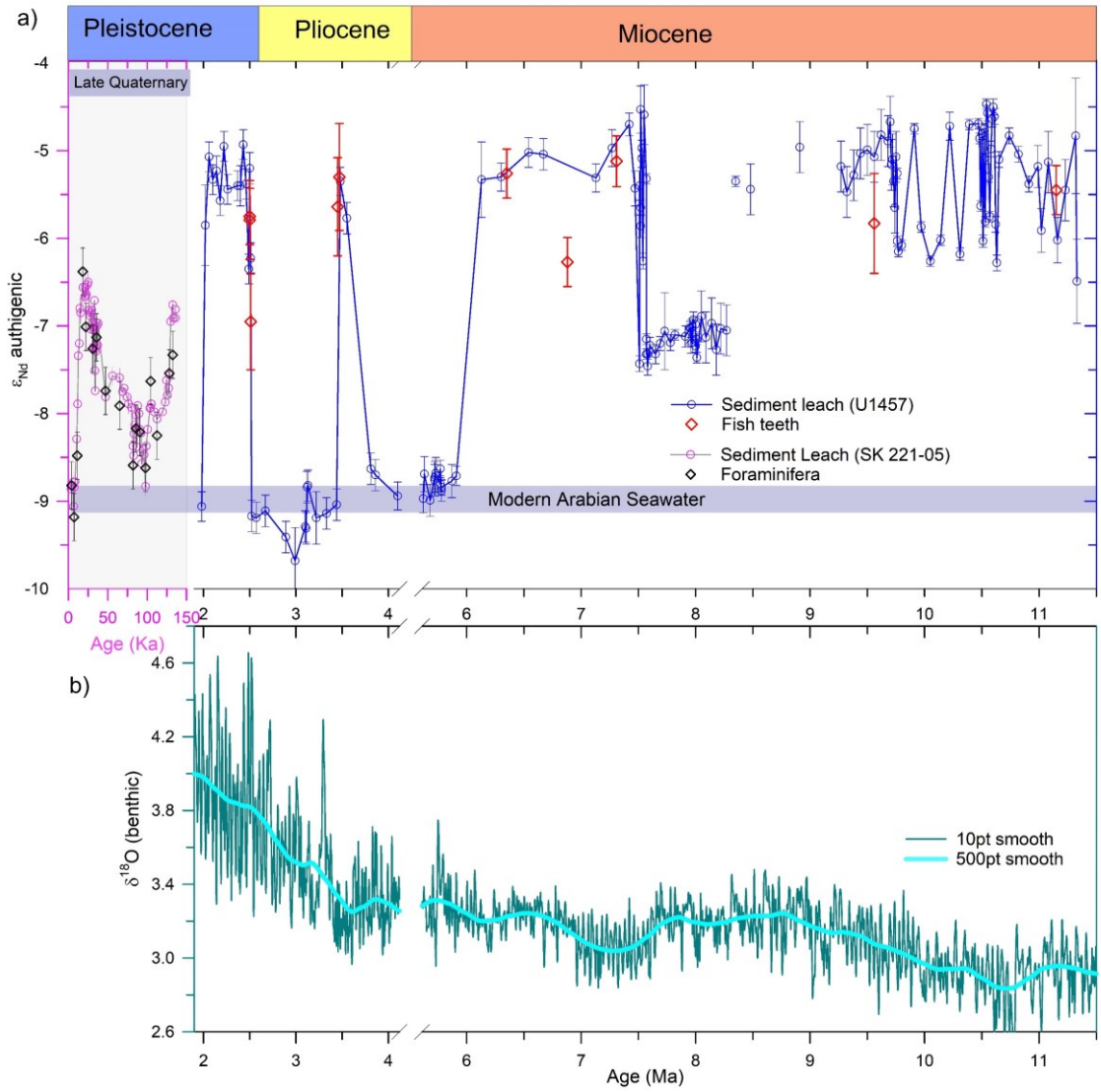

Figure 3.2: Authigenic and detrital ε_{Nd} records from the Arabian Sea. (a) Authigenic ε_{Nd} record of site U1457 (water depth 3522 m) covering a time span of 1.9 to 11.3 Ma (blue line), the late Quaternary record (pink line) is from site SK 221-05 (water depth 2700 m) (Lathika et al., 2021). The blue horizontal bar represents the modern-day deep water ε_{Nd} value for the Arabian Sea. (b) Global benthic $\delta^{18}O$ record (Westerhold et al., 2020b). Error bar represents external error (2σ) of the ε_{Nd} measurements.

Table 3.1: Neodymium isotopic composition of IODP 355, site U1457 C

CSF(m)	Age (Ma)	$^{143}Nd/^{144}Nd$	ε_{Nd}	error ε_{Nd} (2σ)
Authigenic ε_{Nd}				
405.10	1.98	0.512174	-9.06	0.17
405.10R		0.512177	-9.00	0.18
406.10	2.02	0.512338	-5.85	0.46
406.10R		0.512332	-5.96	0.18

407.10	2.06	0.512378	-5.07	0.17
408.08	2.10	0.512365	-5.33	0.17
409.04	2.14	0.512370	-5.23	0.17
409.04R		0.512361	-5.41	0.17
410.04	2.18	0.512353	-5.57	0.17
411.00	2.22	0.512384	-4.95	0.17
411.00R		0.512407	-4.50	0.16
412.05	2.26	0.512359	-5.44	0.17
414.80	2.37	0.512361	-5.40	0.17
414.80R		0.512369	-5.25	0.16
415.80	2.40	0.512361	-5.40	0.23
415.80R		0.512366	-5.31	0.21
416.82	2.43	0.512385	-4.93	0.17
416.82R		0.512387	-4.90	0.16
417.82	2.46	0.512362	-5.38	0.17
417.82R		0.512356	-5.51	0.18
418.82	2.49	0.512313	-6.35	0.17
419.82	2.50	0.512371	-5.20	0.18
420.83	2.51	0.512318	-6.23	0.18
421.83	2.52	0.512168	-9.17	0.18
425.50	2.57	0.512167	-9.19	0.18
434.98	2.67	0.512171	-9.11	0.18
454.66	2.89	0.512155	-9.41	0.18
463.30	2.99	0.512142	-9.68	0.38
473.00	3.10	0.512162	-9.29	0.18
474.00	3.11	0.512161	-9.31	0.18
475.00	3.12	0.512185	-8.84	0.18
475.69	3.13	0.512186	-8.82	0.18
483.71	3.22	0.512167	-9.19	0.30
493.60	3.33	0.512170	-9.14	0.18
503.10	3.44	0.512175	-9.04	0.18
507.10	3.48	0.512364	-5.35	0.16
512.80	3.55	0.512342	-5.77	0.18
512.80R		0.512340	-5.82	0.18
522.73	3.81	0.512196	-8.63	0.18
531.24	3.86	0.512192	-8.70	0.18
533.20	4.10	0.512180	-8.94	0.16
540.90	5.62	0.512178	-8.97	0.16
541.90	5.63	0.512193	-8.69	0.20
551.70	5.68	0.512177	-8.99	0.18
560.30	5.72	0.512191	-8.73	0.18
561.29	5.72	0.512189	-8.76	0.18
562.31	5.73	0.512193	-8.68	0.18
563.31	5.73	0.512192	-8.71	0.18

570.00	5.77	0.512187	-8.80	0.09
571.00	5.77	0.512196	-8.63	0.10
572.00	5.78	0.512183	-8.88	0.12
573.02	5.78	0.512185	-8.84	0.09
590.40	5.87	0.512188	-8.77	0.19
600.10	5.91	0.512191	-8.71	0.11
609.80	6.13	0.512365	-5.33	0.43
613.81	6.30	0.512366	-5.30	0.16
619.50	6.54	0.512381	-5.02	0.17
622.49	6.67	0.512380	-5.04	0.18
629.20	7.13	0.512366	-5.31	0.16
633.20	7.27	0.512383	-4.97	0.21
638.77	7.42	0.512397	-4.70	0.13
648.60	7.47	0.512360	-5.43	0.20
657.30	7.51	0.512257	-7.43	0.09
658.30	7.51	0.512361	-5.40	0.17
659.25	7.52	0.512338	-5.86	0.13
660.26	7.52	0.512348	-5.65	0.09
661.26	7.52	0.512406	-4.53	0.27
662.26	7.53	0.512377	-5.09	0.10
663.28	7.53	0.512383	-4.97	0.09
664.28	7.54	0.512317	-6.26	0.09
664.28R		0.512316	-6.28	0.09
667.00	7.55	0.512403	-4.59	0.34
670.00	7.57	0.512365	-5.32	0.06
671.00	7.57	0.512271	-7.15	0.06
672.00	7.57	0.512263	-7.32	0.06
672.98	7.58	0.512263	-7.32	0.06
673.65	7.58	0.512255	-7.46	0.10
677.70	7.60	0.512268	-7.22	0.09
687.40	7.65	0.512263	-7.32	0.11
697.14	7.69	0.512269	-7.20	0.08
706.80	7.73	0.512276	-7.06	0.44
706.80R		0.512259	-7.39	0.09
716.49	7.78	0.512269	-7.19	0.09
726.20	7.82	0.512274	-7.10	0.06
745.60	7.91	0.512273	-7.12	0.12
754.30	7.95	0.512278	-7.02	0.07
755.30	7.96	0.512269	-7.20	0.11
756.30	7.96	0.512277	-7.03	0.10
757.3	7.97	0.512279	-7.01	0.10
758.30	7.97	0.512269	-7.19	0.12
759.26	7.98	0.512283	-6.93	0.09
763.96	8.00	0.512280	-6.98	0.09

765.00	8.00	0.512268	-7.23	0.07
765.97	8.01	0.512272	-7.15	0.06
767.00	8.01	0.512261	-7.36	0.06
774.58	8.05	0.512285	-6.89	0.29
784.40	8.09	0.512273	-7.13	0.29
794.10	8.14	0.512281	-6.97	0.29
803.80	8.18	0.512265	-7.27	0.29
813.50	8.22	0.512277	-7.03	0.29
823.20	8.27	0.512277	-7.05	0.29
823.20R		0.512279	-7.00	0.29
832.90	8.35	0.512364	-5.35	0.06
842.58	8.48	0.512359	-5.44	0.29
851.30	8.91	0.512383	-4.96	0.29
852.30	9.27	0.512373	-5.18	0.29
853.30	9.32	0.512357	-5.47	0.29
854.30	9.38	0.512367	-5.28	0.29
855.30	9.44	0.512380	-5.03	0.29
856.29	9.50	0.512382	-4.99	0.29
857.31	9.56	0.512378	-5.07	0.29
858.31	9.62	0.512391	-4.82	0.29
859.28	9.68	0.512387	-4.89	0.29
861.00	9.70	0.512399	-4.67	0.29
861.98	9.71	0.512374	-5.16	0.29
863.00	9.72	0.512377	-5.10	0.29
864.00	9.73	0.512364	-5.35	0.29
865.00	9.74	0.512349	-5.65	0.29
866.00	9.75	0.512378	-5.07	0.29
867.00	9.76	0.512368	-5.26	0.06
868.00	9.76	0.512329	-6.03	0.06
869.00	9.77	0.512323	-6.15	0.06
871.70	9.80	0.512326	-6.08	0.06
884.40	9.91	0.512394	-4.75	0.06
891.10	9.97	0.512337	-5.87	0.06
891.10R		0.512336	-5.89	0.06
900.80	10.05	0.512317	-6.26	0.06
910.50	10.14	0.512330	-6.02	0.06
920.28	10.22	0.512396	-4.72	0.16
929.90	10.31	0.512321	-6.18	0.07
939.60	10.39	0.512397	-4.70	0.06
948.30	10.47	0.512398	-4.69	0.06
949.30	10.48	0.512389	-4.86	0.06
950.30	10.49	0.512350	-5.63	0.06
951.30	10.50	0.512391	-4.81	0.06
952.30	10.51	0.512329	-6.03	0.07

953.30	10.52	0.512394	-4.75	0.06
954.30	10.52	0.512377	-5.09	0.06
955.30	10.53	0.512340	-5.81	0.06
956.30	10.54	0.512409	-4.47	0.06
957.30	10.55	0.512404	-4.57	0.09
958.00	10.56	0.512366	-5.30	0.06
959.00	10.57	0.512343	-5.75	0.06
961.00	10.58	0.512383	-4.98	0.09
962.00	10.59	0.512400	-4.64	0.09
963.00	10.60	0.512408	-4.50	0.09
964.00	10.61	0.512401	-4.61	0.09
965.00	10.62	0.512339	-5.84	0.09
966.00	10.63	0.512316	-6.28	0.09
968.70	10.65	0.512376	-5.10	0.09
978.40	10.74	0.512390	-4.83	0.09
988.10	10.82	0.512379	-5.04	0.09
997.83	10.91	0.512362	-5.38	0.09
1007.20	10.99	0.512372	-5.18	0.24
1011.14	11.02	0.512335	-5.91	0.25
1017.23	11.08	0.512375	-5.13	0.35
1026.50	11.16	0.512329	-6.02	0.26
1034.40	11.23	0.512359	-5.45	0.35
1044.59	11.32	0.512391	-4.83	0.66
1045.43	11.33	0.512305	-6.49	0.48
Fish Teeth/Debris ε_{Nd}				
419.34	2.50	0.512341	-5.79	0.45
419.74	2.50	0.512343	-5.75	0.32
420.34	2.51	0.512282	-6.95	0.55
504.2	3.45	0.512349	-5.64	0.56
506.34	3.47	0.512366	-5.30	0.61
614.8	6.35	0.512375	-5.12	0.28
628.2	7.09	0.512317	-6.27	0.28
650.6	7.48	0.512376	-5.11	0.29
650.6R		0.512389	-4.86	0.52
857.31	9.56	0.512339	-5.83	0.57
1025.89	11.15	0.512359	-5.45	0.28
Detrital ε_{Nd}				
405.1	1.98	0.512024	-11.97	0.14
407.1	2.06	0.512246	-7.64	0.14
413.01	2.30	0.512275	-7.08	0.14
420.83	2.51	0.512193	-8.68	0.14
463.3	2.99	0.512019	-12.08	0.14
512.8	3.55	0.512218	-8.20	0.14
541.9	5.63	0.512050	-11.47	0.14

541.9R		0.512033	-11.81	0.14
600.1	5.91	0.512037	-11.72	0.14
609.8	6.13	0.512241	-7.73	0.14
657.3	7.51	0.512112	-10.26	0.14
669	7.56	0.512232	-7.92	0.14
671	7.57	0.512120	-10.11	0.14
853.3	9.32	0.512194	-8.65	0.14
861.98	9.71	0.512158	-9.35	0.14
939.6	10.39	0.512219	-8.17	0.14
1035.4	11.24	0.512344	-5.74	0.28

CSF-A - core depth below seafloor; R - represents replicate analysis.

3.3 Discussion

We have conducted a detailed assessment to test the fidelity of the authigenic ε_{Nd} record as a proxy for past deep water circulation in this oceanographic setting at the core site. This was conducted at two stages, i.e., (i) investigated the possible detrital dissolution during the leaching for the extraction of authigenic Nd from the bulk sediments and (ii) examined whether the authigenic Nd extracted from the bulk sediment recorded the deep water signature. A recent study from the South-eastern Arabian Sea (Lathika et al., 2021) (Figure 3.2a) has shown an excellent agreement between authigenic ε_{Nd} of the leachate and foraminifera (Figure 3.2a, Figure 3.3). The fish teeth/debris ε_{Nd} data of the present core combined with the foraminifera ε_{Nd} record of SK 221-05 from the South-eastern Arabian Sea (Lathika et al., 2021) with their corresponding leachate ε_{Nd} values show an excellent agreement over longer time scales ranging from the late Miocene to the Holocene (Figure 3.2a, Figure 3.3). A similar study in the BoB (Naik et al., 2019) shows that authigenic ε_{Nd} data extracted from bulk sediments using different leaching methods are similar to that of fish teeth and cleaned/uncleaned foraminifera within their analytical uncertainty. This close agreement between the ε_{Nd} data of different archives suggests insignificant partial dissolution during the leaching process regardless of the methods used. Based on the present study and demonstration in earlier studies (Lathika et al., 2021; Naik et al., 2019), we rule out the possibility of significant detrital dissolution during the leaching.

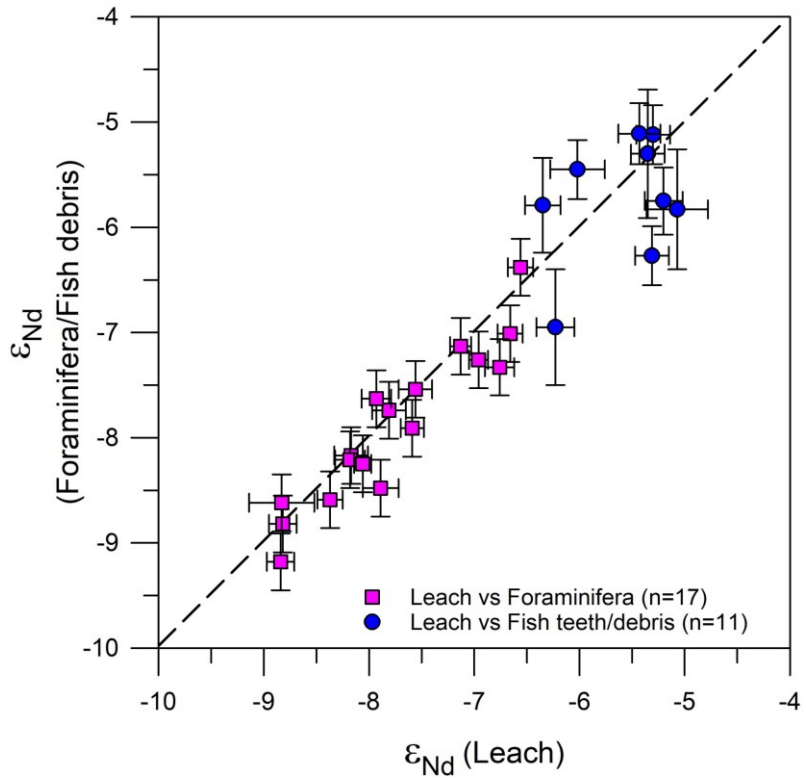

Figure 3.3: Assessing fidelity of authigenic ε_{Nd} records. Cross plot of the ε_{Nd} of leach versus corresponding ε_{Nd} fish teeth/debris (present study) and ε_{Nd} foraminifera published record from Lathika et al. (2021) and ε_{Nd} of leach vs ε_{Nd} fish teeth/debris (present study). Dashed line represents 1:1 equiline. Error bar represents external error (2σ) of the ε_{Nd} measurements.

Modern water column Nd isotope study in the eastern Arabian Sea has demonstrated that deep water ε_{Nd} signature primarily reflects the water mass mixing of AABW and NADW without significant contributions from other sources (Goswami et al., 2014). In the subsequent study, Lathika et al. (2021) successfully reconstructed the DWC history of the last glacial cycle (~136 ka) based on combined authigenic and foraminifera ε_{Nd} records from the eastern Arabian Sea. This suggests that the extracted authigenic ε_{Nd} at the U1457 core site records the past deep water ε_{Nd} signature and hence can be used to reconstruct the past deep water circulation in the western Indian Ocean. However, contributions from other potential sources to the past deep water ε_{Nd} variability must be investigated before interpreting this record in terms of deep water circulation.

3.3.1 Factors contributed to the past authigenic ε_{Nd} variability at the U1457 core site

A study (Goswami et al., 2014) on dissolved Nd isotope in the Eastern Arabian Sea water column has identified potential sources, their characteristic ε_{Nd} signatures and quantified their contributions to the water column at various depths. The potential sources are (i) chemical weathering fluxes from nearby continents supplied by the westward-flowing rivers, (ii) aeolian dust deposition, and (iii) water mass mixing/circulations. Dissolved ε_{Nd} data of the water column station 0802 (14.42 °N, 69.42 °E) (Figure 3.1c) (Goswami et al., 2014) from the proximity to our core site have demonstrated that deep water ε_{Nd} values at the similar core depth primarily reflect mixing of AABW (85%) and NADW (10–15%) (Goswami et al., 2014). Further, reconstruction of past deep water circulation from the eastern Arabian Sea (Lathika et al., 2021) suggests that the composition of the Holocene and the inter-glacials water mass fractions were similar to that of modern-day, however, it changed to ~100% AABW during the glacials. It is noteworthy that the radiogenic values observed in our record (ε_{Nd} = -4.5) are even more radiogenic than the glacial values (ε_{Nd} = -6.5) when the northern Indian Ocean was completely occupied by AABW (Lathika et al., 2021). The radiogenic values (-6.5 to -4.5) in the older intervals (11.3 to ~8.3 Ma) do not show any significant correlation with the detrital ε_{Nd} values. In contrast, there is a good correspondence between authigenic and detrital values in the later intervals, particularly during the periods of radiogenic excursions Ca. 7.4 to 6 Ma, at ~3.5 Ma, and 2.5 to 2 Ma (Figure 3.4f, g). The correspondence between the authigenic and detrital ε_{Nd} values could be due to diagenetic overprinting of radiogenic material supplied by the Tapi River draining through Deccan basalts characterised by more radiogenic Nd (Goswami et al., 2012), alteration of deep water through boundary exchange processes and/or partial dissolution of dust transported from north-east Africa and Arabian Peninsula. Since the core site U1457 is far from the continental margin and situated at a deeper depth of 3522 m, the possibility of boundary exchange processes for contributing radiogenic ε_{Nd} values could be ruled out. Monsoonal precipitation influences sediment discharge and weathering fluxes from the Himalayan rivers, i.e., Indus and westward-flowing peninsular rivers such as Narmada, Tapi, and Mahi (Figure 2.1a). The Nd isotopic composition of seawater might be influenced by the release of particulate Nd due to huge supply of sediments as it has been demonstrated in the BoB (Naik et al., 2019; Singh et al., 2012) and Andaman Sea (Rashid et al., 2019). However, a similar study in the Arabian Sea water

column (Goswami et al., 2014) and authigenic ε_{Nd} record (Lathika et al., 2021) from the Arabian Sea did not show any evidence for such release of particulate Nd altering deep water ε_{Nd} signature. Though there are divergent views on the evolution of the south-west Indian monsoon, the most recent study based on multi-proxy records from the study area suggests a weak monsoon during our studied interval, which intensified after ~3 Ma (Khim et al., 2019; Tripathi et al., 2017). It is noteworthy that more radiogenic values in the authigenic ε_{Nd} profile coincide with the period of lower sedimentation rates (Pandey et al., 2016) (Figure 3.4g) and lower chemical weathering intensity (Clift et al., 2019a) during the interval ~6 Ma to 7.7 Ma, ruling out the possibility of enhanced weathering and erosion fluxes from the Deccan rivers. It is rather intriguing to note that these excursions of more radiogenic ε_{Nd} values coincide with the higher percentage of total nitrogen (TN%) and total organic carbon (TOC%) (Khim et al., 2019), indicating higher productivity (Figure 3.4d,e). These intervals of higher productivity further coincide with the increase in C_4 plant abundance based on $\delta^{13}C$ (foreland) record of organic carbon (Quade et al., 1989), indicating stronger aridity (Figure 3.4c). Further, an increase in *G. bulloides* abundance (Figure 3.4a,b) indicates enhanced upwelling driven by stronger wind conditions (Gupta et al., 2015; Huang et al., 2007). These compelling evidences based on multi-proxy records clearly suggest increased aridity over the potential dust source regions coupled with stronger wind favoured enhanced dust supply to the Arabian Sea during these excursions.

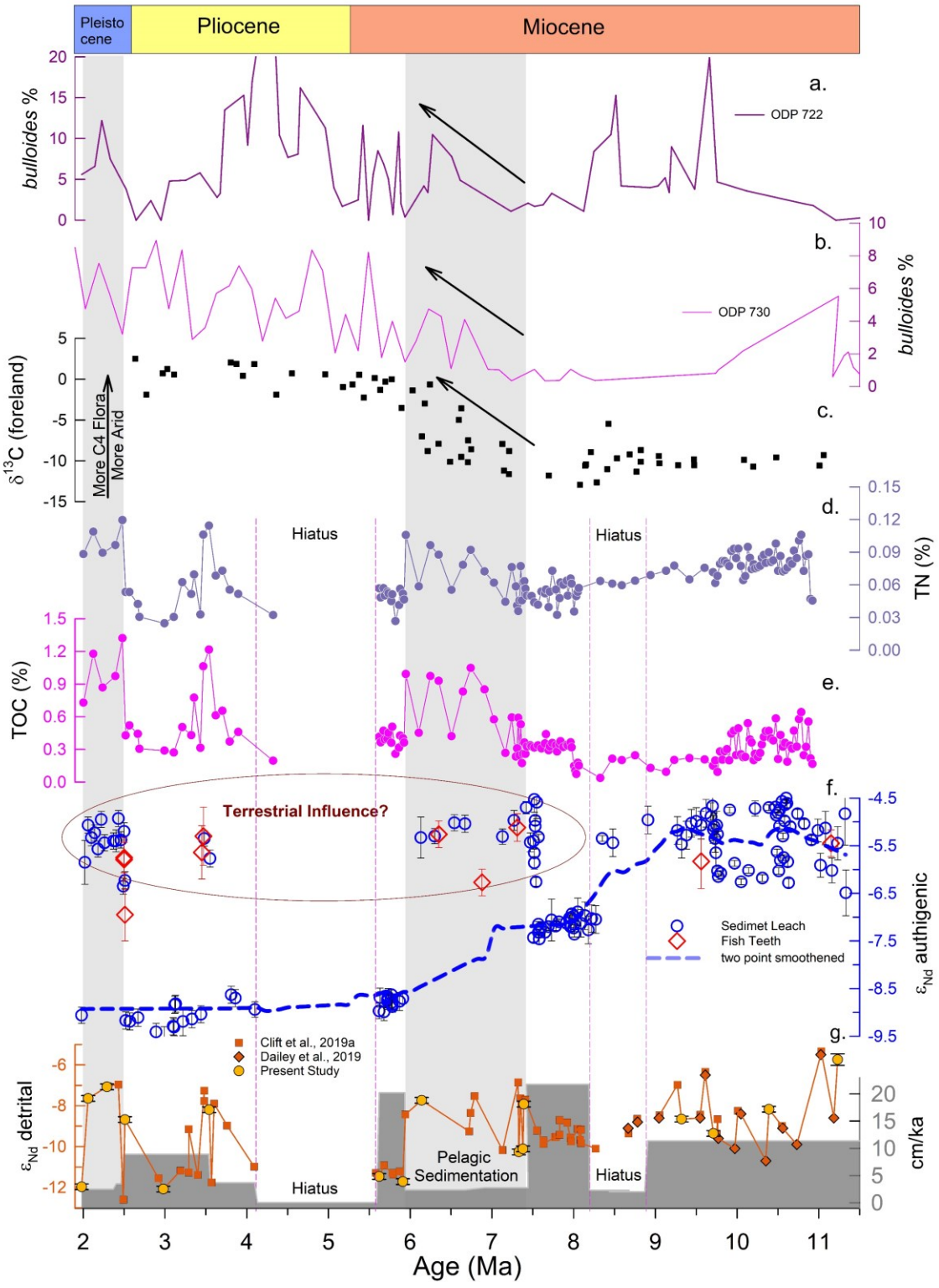

Figure 3.4: Multi-proxy records and their comparison with the authigenic ε_{Nd} record. (a, b) bulloides % from the Oman Coast, Arabian Sea (ODP 722 (Huang et al., 2007), ODP 730 (Gupta et al., 2015)), (c) $\delta^{13}C$ from foreland Pakistan Siwalik (Quade et al., 1989), (d) Total Nitrogen (TN, weight %) record from Site U1457 (Khim et al., 2019), (e) Total organic carbon (TOC, weight %) record from Site U1457 (Khim et al., 2019), (f) Authigenic ε_{Nd} record of site U1457 (present study), the solid dark blue line represents the two-point

smoothened data to show the trend, (g) Sedimentation rate (cm/ka) (Pandey et al., 2016; Routledge et al., 2019) and detrital ε_{Nd} record (present study and published record (Clift et al., 2019b; Dailey et al., 2019)). Error bar represents external error (2σ) of the ε_{Nd} measurements.

Therefore, the dust supply became the dominant fraction of the total sediment over the riverine supply during periods of lower sedimentation rates. The atmospheric dust deposition over the sea surface and release of Nd from aeolian dust can influence the isotopic composition of dissolved Nd (Le Houedec et al., 2012a). The dust-derived ε_{Nd} contributing to surface water at two sampling stations, 0802 and 0803 (Figure 2.1a), were estimated to be -6.1 ± 2.2 and -5.3 ± 1.9, respectively (Goswami et al., 2014). These values are consistent with the reported values of major dust sources supplying to the Arabian Sea (Kumar et al., 2020; Suresh et al., 2021) (Figure 3.1b). Hence, we suggest that enhanced dust supply due to strong aridity could contribute to more radiogenic Nd and produce an agreement between detrital and authigenic ε_{Nd} (Figure 3.5c). Therefore, we infer that these three radiogenic excursions resulted from the enhanced dust supply due to strong aridity over the continents and reduced river sediment supply that made the dust a dominant fraction of the terrigenous input. In conclusion, the radiogenic excursions resulted from enhanced dust supply and/or diagenetic overprinting and hence do not reflect water mass signature.

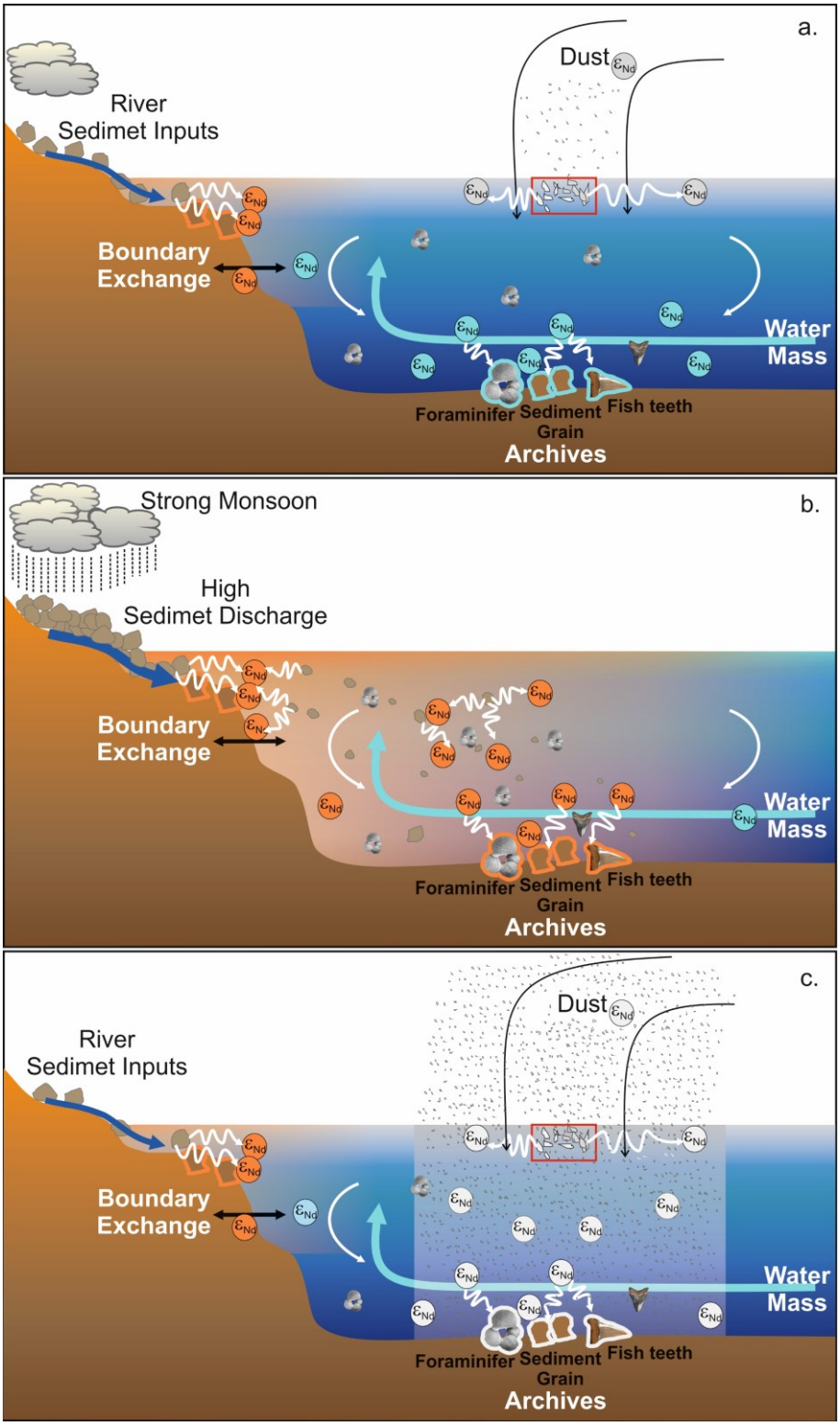

Figure 3.5: An illustration of how deep water acquires ε_{Nd} values in different scenarios and archived its signature in the authigenic phase. (a) This figure shows how various archives such as authigenic Fe-Mn coatings on the foraminifera, sediment grains and fish teeth/debris deposited in the open ocean acquire deep seawater ε_{Nd} signature. The influence of other processes/sources, such as dissolution/desorption of particulate Nd from the dust deposition (shown by grey tinge) and river-borne sediment are restricted within the top few

hundred meters in the seawater column (Goswami et al., 2014) under moderate aeolian and riverine input. The impact of boundary exchange process is restricted to shelf area. (b) During high sediment discharge from rivers due to strong precipitation, river particles may interact with the water column and alter its ε_{Nd} values. This altered ε_{Nd} gets deposited as the authigenic coating of the archives. This scenario has been reported from the BoB (Naik et al., 2019), while the Arabian Sea is not affected by such process (Goswami et al., 2014; Lathika et al., 2021); (c) During high eolian dust deposition, dust can alter deep water ε_{Nd} signature through the dissolution and/or diagenetic processes. This altered authigenic values will be recorded in all the archives as shown in the panel. The observed radiogenic excursion in the present study could be attributed to this process. Blue arrow – river inputs, cyan arrow – seawater circulation, curved white arrow – water mass mixing. Orange circle- ε_{Nd} leached from the river sediments to the water column, cyan circle- ε_{Nd} of the water mass, grey circle- ε_{Nd} leached from the dust particles to the water column.

Excluding these extremely radiogenic values, the smoothed curve (blue dashed line, Figure 3.4f) based on two points running average can be interpreted in terms of changes in the deep water circulations. This curve shows a systematic shift from more radiogenic ε_{Nd} values during the late Miocene to less radiogenic values during the Miocene-Pliocene transition. This observation indicates a major change/reorganisation in the deep water circulation in the Indian Ocean, and we expect similar observations in other ε_{Nd} records elsewhere in the Indian Ocean. However, unfortunately, there is no ε_{Nd} record available from the Indian Ocean at a similar depth range (Figure 3.1d). Alternate proxy records such as the benthic $\delta^{13}C$ records have been extensively used to reconstruct the evolution of past water mass circulations despite several caveats attached to its application as a water mass circulation proxy (Billups et al., 2002; Lear et al., 2003). The benthic $\delta^{13}C$ records from the Indian Ocean (Bolton et al., 2022; Gupta et al., 2004; Gupta et al., 2015; Huang et al., 2007) shows a major negative shift between ~8 to 6.5 Ma, is consistent with the global benthic $\delta^{13}C$ records (Westerhold et al., 2020b) (Figure 3.6b), referred as "late Miocene carbon isotope shift" which has been attributed to the change in the terrestrial vegetation pattern from C_3 to C_4 plants and increase in the weathering inputs to global oceans (Du et al., 2022a). Since the north Indian Ocean is among the most biologically productive basin and receives a huge amount of weathering fluxes from the Himalayan and Peninsular rivers, the benthic $\delta^{13}C$ would be largely affected by these processes and thus cannot be directly used as a proxy for water mass circulation. On the contrary, the $\delta^{18}O$ (benthic) record does not show a substantial shift in the values since the establishment of the West Antarctic ice sheet during the middle Miocene to late Pliocene (Westerhold et al., 2020b) (Figure 1.1). The

AABW formation enhanced after ~15.5 Ma due to the growth in the Antarctic ice sheet (Hall et al., 2003), and has been the densest water mass since the middle Miocene (Flower and Kennett, 1995). However, the benthic $\delta^{18}O$ record does not show concomitant changes with the global deep water circulation changes during the late Miocene. This indicates that the deep water mass circulation changes were decoupled from the Antarctic ice sheet evolution during the late Miocene.

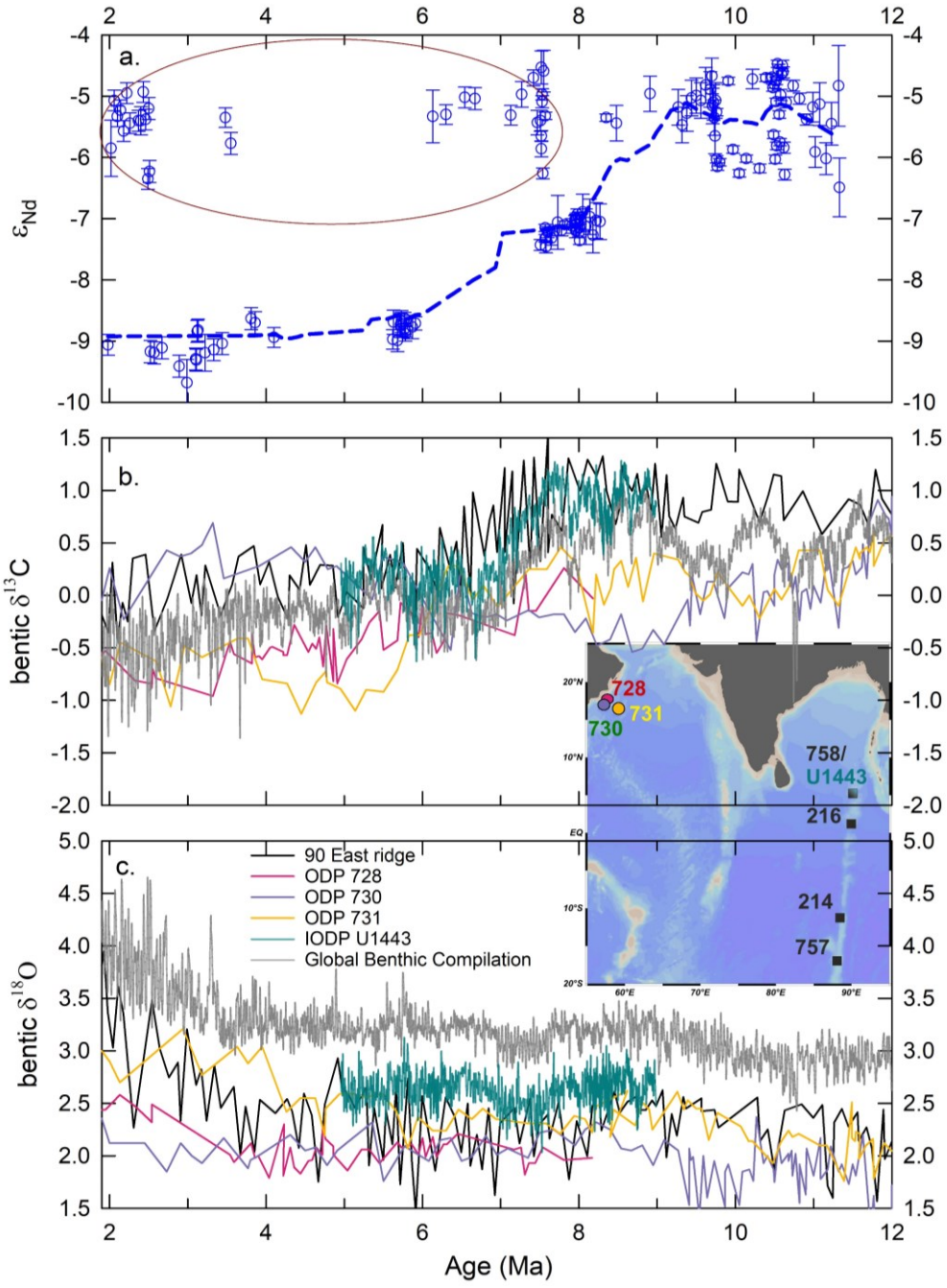

Figure 3.6: Comparison of the authigenic ε_{Nd} record with the benthic carbon and oxygen isotope records from the Indian Ocean. (a) The authigenic ε_{Nd} record from IODP site U1457

(present study); (b) benthic $\delta^{13}C$ isotope record from the Arabian Sea (Gupta et al., 2015; Huang et al., 2007), 90 East ridge (Bolton et al., 2022; Gupta et al., 2004) in the eastern Indian Ocean, global benthic compilation (Westerhold et al., 2020b); (c) benthic $\delta^{18}O$ isotope record from the Arabian Sea (Gupta et al., 2015; Huang et al., 2007), 90 East ridge (Bolton et al., 2022; Gupta et al., 2004) in the eastern Indian Ocean, global benthic compilation (Westerhold et al., 2020b). Error bar represents external error (2σ) of the ε_{Nd} measurements.

The authigenic ε_{Nd} record shows a discernible declining trend from more radiogenic values (-5.5 ± 1) during the late Miocene (11.3 to ~9 Ma Ma) to less radiogenic values (-9 ± 0.5) during the Miocene-Pliocene transition, similar to that of the late Holocene and modern deep water in the Arabian Sea (Goswami et al., 2014; Lathika et al., 2021). The radiogenic ε_{Nd} values in the older intervals can be explained either by introducing additional deep water masses with more radiogenic ε_{Nd} signature or by major changes/re-organisation of deep water circulation that modified the end-member ε_{Nd} values of AABW and NADW. The Indian Ocean Fe-Mn crust records (109 D-C, water depth 5700 m, SS-663, water depth 5300 m, and DODO-232D, water depth 4119 m) (Frank et al., 2006a; O'Nions et al., 1998b) bathed by AABW in the modern time show uniform ε_{Nd} values within a narrow range (-8 ± 1) during the interval between ~2 to 16 Ma (Figure 3.7). This implies that the ε_{Nd} values of AABW in the Indian Ocean were stable at around the modern-day value (-8 ± 1) for the entire interval.

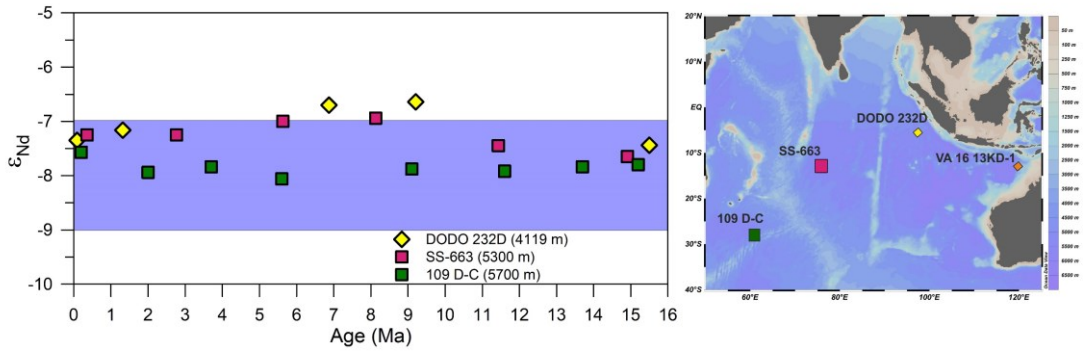

Figure 3.7: Deepwater Fe-Mn crust ε_{Nd} records (Frank et al., 2006; O'Nions et al., 1998) from the Indian Ocean and their locations. Blue shading represents the modern day ε_{Nd} value of the AABW.

Further, the authigenic ε_{Nd} records from the Angola basin, the Fe-Mn Crust DS43 (Reynolds et al., 1999) record (water depth 1990 m, bathed by upper NADW), and the

sediment core ODP 1262 (Thomas and Via, 2007) (water depth 4755 m, bathed by lower NADW), oscillated between -13 and -11 during our studied interval (Figure 3.8). These values are consistent with the modern NADW ε_{Nd} range reported from the Angola basin (Figure 3.8). This also indicates that the ε_{Nd} value of the NCW was within the range of modern-day ε_{Nd} value of the NADW. The radiogenic values observed in the U1457 record (-4.5 to -6.5) during the older intervals (~11.3 to ~9 Ma) were higher than the modern deep water values and even higher than the Quaternary glacial-interglacial ranges (Lathika et al., 2021). These radiogenic ε_{Nd} values in the Indian Ocean cannot be explained in terms of mixing of these two water masses alone (AABW and NCW, ε_{Nd} end members stable and less radiogenic) and therefore hints at the possibility of major reorganisation in the deep water circulation in the southern ocean that modified to more radiogenic deep water ε_{Nd} signature exported to the Indian Ocean.

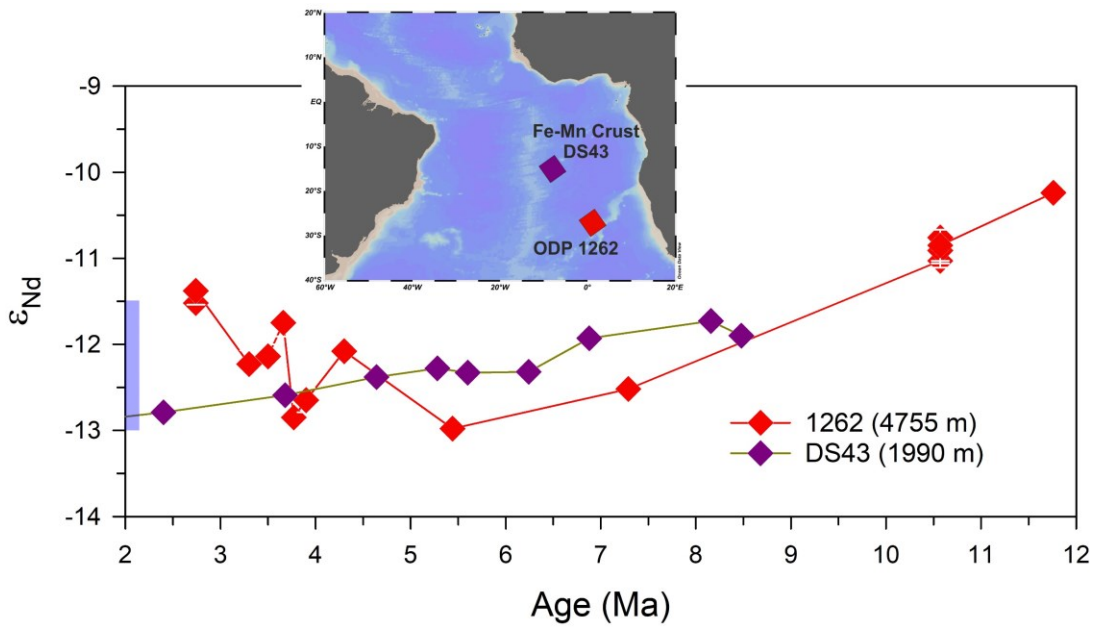

Figure 3.8: Evolution of northern component of water (NCW) based on the authigenic ε_{Nd} records from Fe-Mn Crust DS43 (Reynolds et al., 1999) and ODP Site 1262 (Thomas and Via, 2007). The blue bar represents the modern ε_{Nd} value of NADW from the Angola basin (Rahlf et al., 2020).

The published records from the Arabian Sea (Lathika et al., 2021), equatorial Indian Ocean (Piotrowski et al., 2009), and South Atlantic (Dausmann et al., 2017) have revealed that the glacial values of CDW were modified to more radiogenic values (-6.5 ± 0.5) due to reduced export of NADW to the Southern Ocean and enhanced supply of the Pacific Deep Water (PDW) (Lathika et al., 2021; Piotrowski et al., 2009). The present tectonic

configuration of the Arabian Sea has been stable since the closure of the Tethys Sea at ~14 Ma ago (Bialik et al., 2019). Therefore, the possibility of any tectonically driven regional circulation changes within the Indian Ocean during our study interval (11.3 to ~2 Ma) could be ruled out. Among all the major water masses in the global ocean, Pacific water is characterised by the most radiogenic ε_{Nd} values (-3.5 ± 0.5) (Howe et al., 2016; Yu et al., 2020). Therefore, the only possibility that can explain such radiogenic values of the deep Indian Ocean water is, the export of the Pacific water into the Indian Ocean. In the modern oceanographic setting, the Pacific water is exported to the Indian Ocean via two pathways, the Indonesian Throughflow (ITF) as surface water mass and the Southern Ocean as deep water mass (PDW). The Pacific water entering through the ITF is fresh and shallow water mass and hence cannot penetrate deeper depths up to ~ 3500 m to alter the deep water ε_{Nd} signature at the present core site. Thus, we rule out the possibility of the Pacific water influence through the ITF to alter the deep water ε_{Nd}. Other possibility is the export of PDW to the Southern Ocean and mixing with CDW as recirculated Pacific Deep Water (rPDW). Previous studies of the last glacial cycle suggest that the rPDW occupied the deeper depth during the glacial period due to the shoaling/reduced export of NCW to the Southern Ocean (Lathika et al., 2021; Piotrowski et al., 2009). Therefore, the enhanced contribution of rPDW to the Southern Ocean could make the CDW more radiogenic, and the export of this water mass to the northern Indian Ocean could produce such radiogenic ε_{Nd} values.

3.3.2 Forcing factors and mechanisms for the late Miocene circulation changes

Several studies based on models (Butzin et al., 2011) and geochemical proxies (Billups et al., 2002; Poore et al., 2006) have reported weak NCW with reduced southward export during the late Miocene (Figure 3.9d). The NCW export to the Southern Ocean was reduced due to weaker Atlantic Meridional Overturning Circulation (AMOC) caused by a higher influx of fresh and warm Pacific water into the mid-latitude Atlantic Ocean through the Central American Seaway (CAS) (Nisancioglu et al., 2003; Sepulchre et al., 2014). Therefore, given the timing of the changes observed in the authigenic ε_{Nd} record, constriction and shoaling of the CAS could be the most likely cause for the reduced influx of the Pacific water into the Atlantic Ocean and strengthening of NCW production after 9.5 Ma (Billups et al., 2002; Kirillova et al., 2019; Newkirk and Martin, 2009). The less radiogenic shift of ε_{Nd} records from the Caribbean Sea has been interpreted as the reduced

influx and advection of Pacific water into the north Atlantic as a result of progressive closure and shoaling of the CAS after 9.5 Ma (Kirillova et al., 2019; Newkirk and Martin, 2009). This conclusion was further supported by the model results (Butzin et al., 2011). Our observations of deep water circulation changes in the western Indian Ocean are consistent with the tectonically driven changes in the Pacific-Atlantic gateways, i.e., closure of the CAS (Figure 3.9a). Therefore, the more radiogenic values oscillating between -4.5 to -6.5 during the interval of 11.3 to ~9 Ma could result from reduced export of NCW, compensated by the enhanced contribution of rPDW into the CDW. These evidences indicate that the CDW exported to the Arabian Sea comprised of a higher percentage of rPDW with more radiogenic ε_{Nd}. Subsequently, the authigenic ε_{Nd} values gradually became less radiogenic during the interval of ~9 to 6 Ma with the progressive closure of CAS and thereafter became stable at -9 ± 0.2, similar to the late Holocene (-8.8 ± 0.2) (Lathika et al., 2021) and modern deep water values (-9 ± 0.4) (Goswami et al., 2014) (Figure 3.2a, Figure 3.1c). Therefore, we suggest that the progressive closure of CAS and thereby strengthening of AMOC after ~9 Ma enhanced the export of NCW to the Indian Ocean and attained modern deep water ε_{Nd} value during the Miocene-Pliocene transition. The late Miocene cooling (Herbert et al., 2016) of sea surface temperature at higher latitudes (Figure 3.9b) might contribute to the increase in NCW formation and its density through brine rejection. Thus, the increased salinity along with the decrease in the bottom water temperature (Billups and Scheiderich, 2012; Lear et al., 2015) (Figure 3.9c) indicates the evolution of the density driven water mass mixing proportion of the deep water circulation in the study area and corroborates our conclusion. Further, the suggestions of enhanced production and export of the NCW to the Southern Ocean since the late Miocene based on benthic $\delta^{13}C$ records (Billups et al., 2002; Butzin et al., 2011; Poore et al., 2006) and stable NCW formation during the final phase of the closure of CAS (Bell et al., 2015) (4.7 Ma and afterward) are consistent with the finding in the present study.

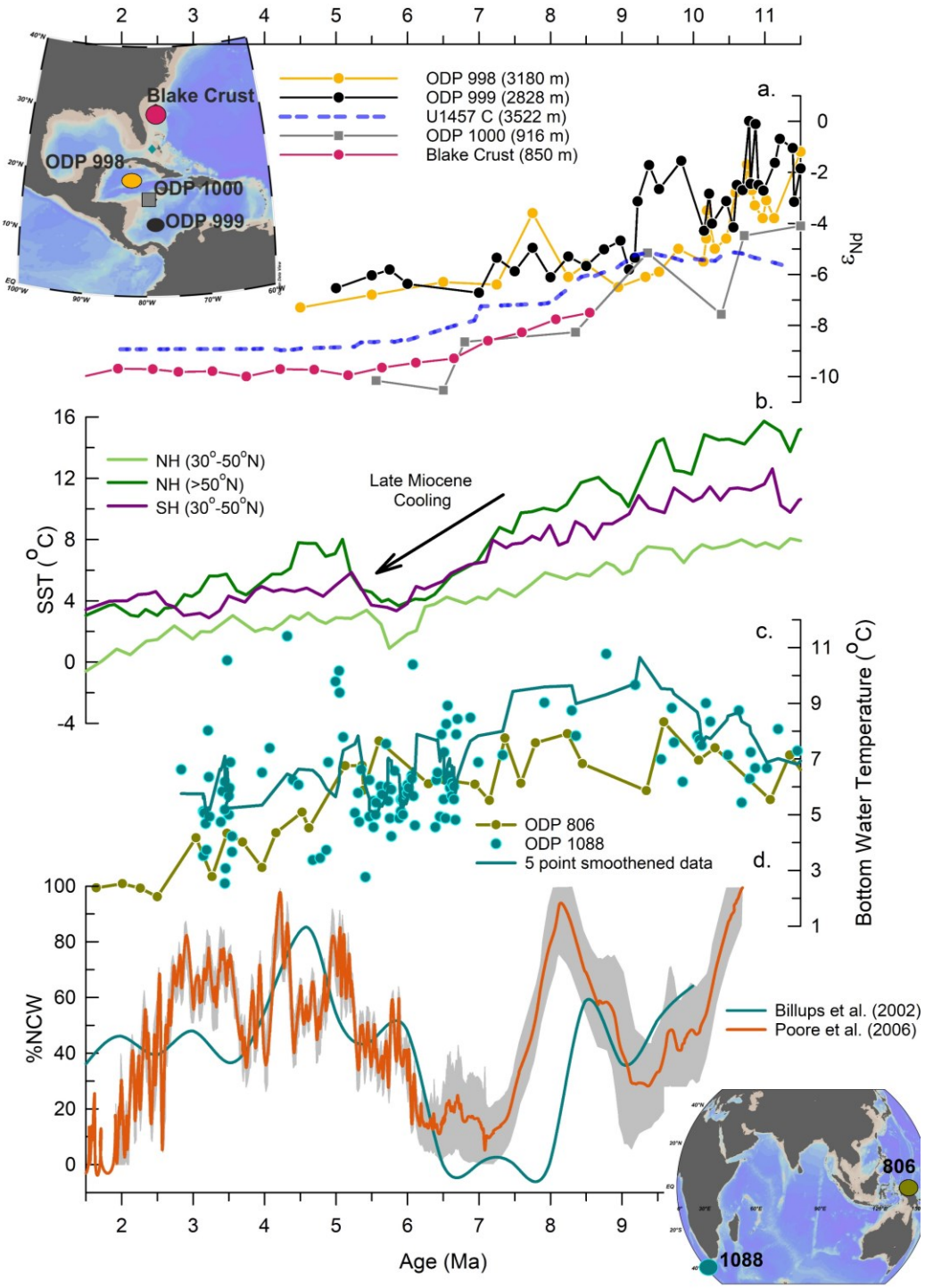

Figure 3.9: Evolution of deep water circulation since the late Miocene. (a) ε_{Nd} record from the Caribbean Sea, Atlantic Ocean ODP 998, 999 (Newkirk and Martin, 2009), ODP 1000 (Kirillova et al., 2019), Blake Fe-Mn Crust (Reynolds et al., 1999); (b) Sea surface temperature (SST) for the subtropical and high latitude northern hemisphere (NH) and southern hemisphere (SH) (Herbert et al., 2016); (c) bottom water temperature based on Mg/Ca paleothermometry (Billups and Scheiderich, 2012; Lear et al., 2015); (d) %NCW (Billups et al., 2002; Poore et al., 2006) estimation based on benthic $\delta^{13}C$. Grey envelope represents the error band on the %NCW record (Poore et al. (2006)).

Due to the cessation of significant deep-water exchange with the Pacific and the Atlantic Ocean through the CAS, the South Atlantic seafloor started bathing in NADW, which caused the deepening of the lysocline, carbonate compensation depth (CCD) and enhanced the carbonate preservation (Moore et al., 1978; Van Andel, 1975; Zachos et al., 2004). A recent compilation of calcium carbonate ($CaCO_3$) records from multiple DSDP and ODP sites in the Atlantic basin has demonstrated increased calcium carbonate sedimentation rates since the late Miocene throughout Atlantic (Keating-Bitonti and Peters, 2019) (Figure 3.10c). One of the sites (ODP 1262) in the South Atlantic at the Walvis Ridge shows an increase in the $CaCO_3$ from ~10% since ~10 Ma and to ~90% during the late Miocene and became stable thereafter (Figure 3.10b) and suggested enhanced NCW in the South Atlantic (Zachos et al., 2004). This change in $CaCO_3$ (weight %) at site 1262 is coeval with the shift in ε_{Nd} values toward less radiogenic signature (Thomas and Via, 2007) reported from the same site (Figure 3.8). This indicates that carbonate preservation depth started to increase since the past ~10 Ma, which became stable in the late Miocene (~7 Ma) under certain physico-chemical conditions. This evidence suggests that modern-day like vertical structure/configuration of deep water masses in the Atlantic was achieved during the late Miocene. The ε_{Nd} based reconstruction of DWC is consistent with the changes in lysocline and CCD in the Atlantic and thus corroborates our conclusion.

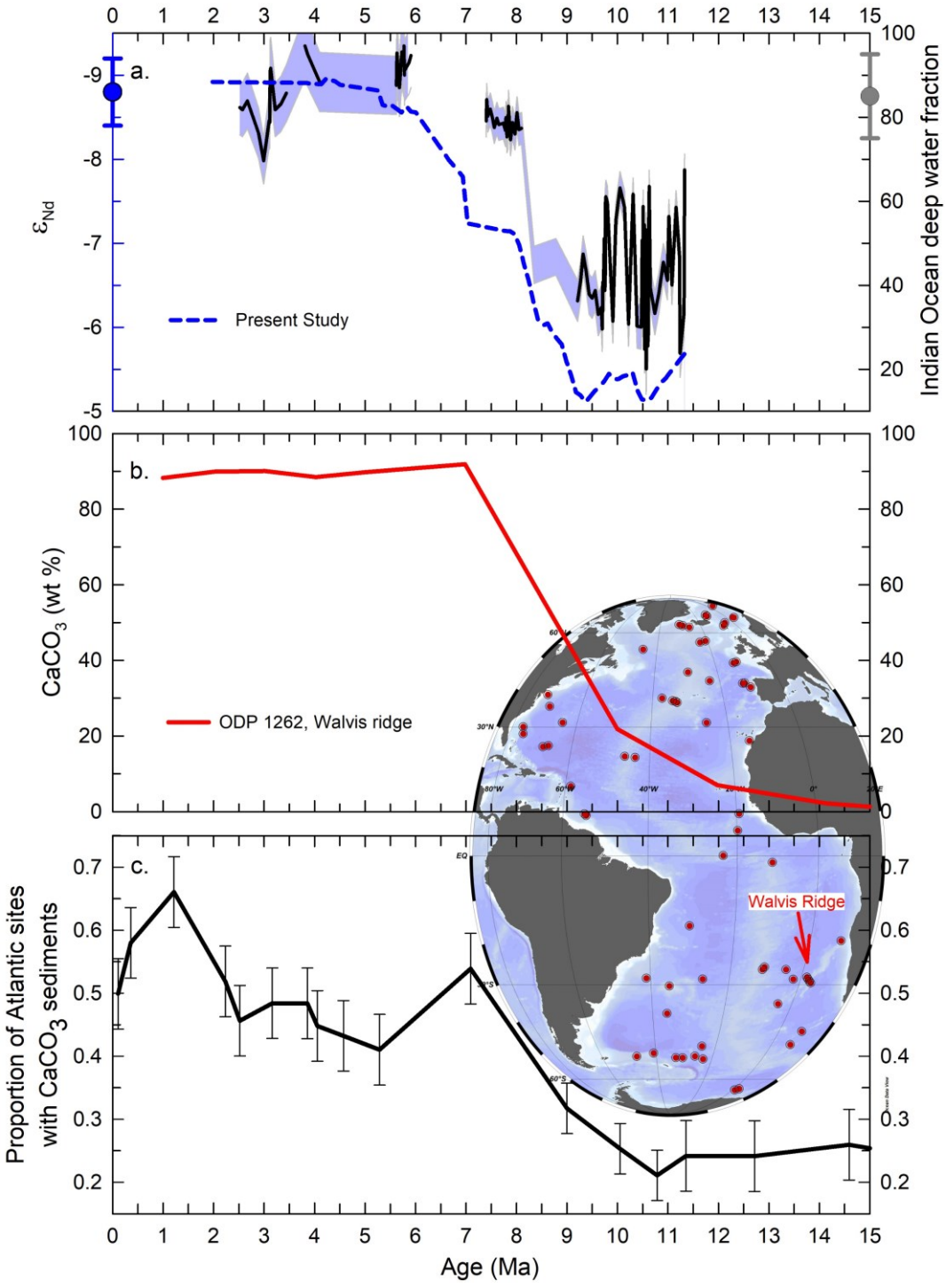

Figure 3.10: Role of deep water circulation in carbonate chemistry. (a) Authigenic ε_{Nd} record (two-point smoothened, blue line) of site U1457 and its corresponding Indian Ocean deep water fractions (black line with grey error envelope) with their modern-day values plotted on their respective axis (filled circle); (b) calcium carbonate weight percentage (wt %) for site ODP 1262 (water depth 4769 m) (Zachos et al. 2004); (c) proportion $CaCO_3$ sediments from the DSDP and ODP sites (sites shown in map) in the Atlantic Ocean.

The deep water circulation changes driven by the tectonic forcing that contributed to the gradual shift from more radiogenic to less radiogenic ε_{Nd} values in the Indian Ocean are illustrated in three stages (Figure 3.11). The first stage before ~9 Ma (Figure 3.11a) depicts a wider opening in the CAS, indicating more influx of Pacific water to the North Atlantic that resulted in weaker AMOC and reduced NCW export to the Southern Ocean. In the absence of NCW at deeper depths in the Southern Ocean, rPDW mixed with AABW and exported to the north-western Indian Ocean from the lower cell of the CDW (Figure 3.11d). This circulation pattern changed with the progressive constriction of the CAS after ~9 Ma (stage 2), as depicted in Figure 3.11b, where a gradual reduction in Pacific water influx into the North Atlantic resulted in enhanced formation of NCW and its southward export (Figure 3.11b). During the later phase (~6 Ma, stage 3), CAS shoaled to a critical depth leading to reduced advection of the Pacific water in the Atlantic. This led to the strengthening of AMOC, which resulted in the enhanced formation and southward export of the NCW (Figure 3.11c). Enhanced export of NCW to the Southern Ocean replaced rPDW from the lower cell of the CDW as rPDW shoaled due to its lower density compared to NCW and joined the upper cell of the CDW (Figure 3.11e). Thus, after ~9 Ma, there was a gradual reduction in the rPDW component to LCDW, while AABW and NCW became the main component of the LCDW. This transition from the Pacific-dominated deep water circulation system to the AABW-NCW dominated circulation system in the Indian Ocean was gradual and finally stabilized at a modern-like circulation system during the Miocene-Pliocene transition at ~6 Ma.

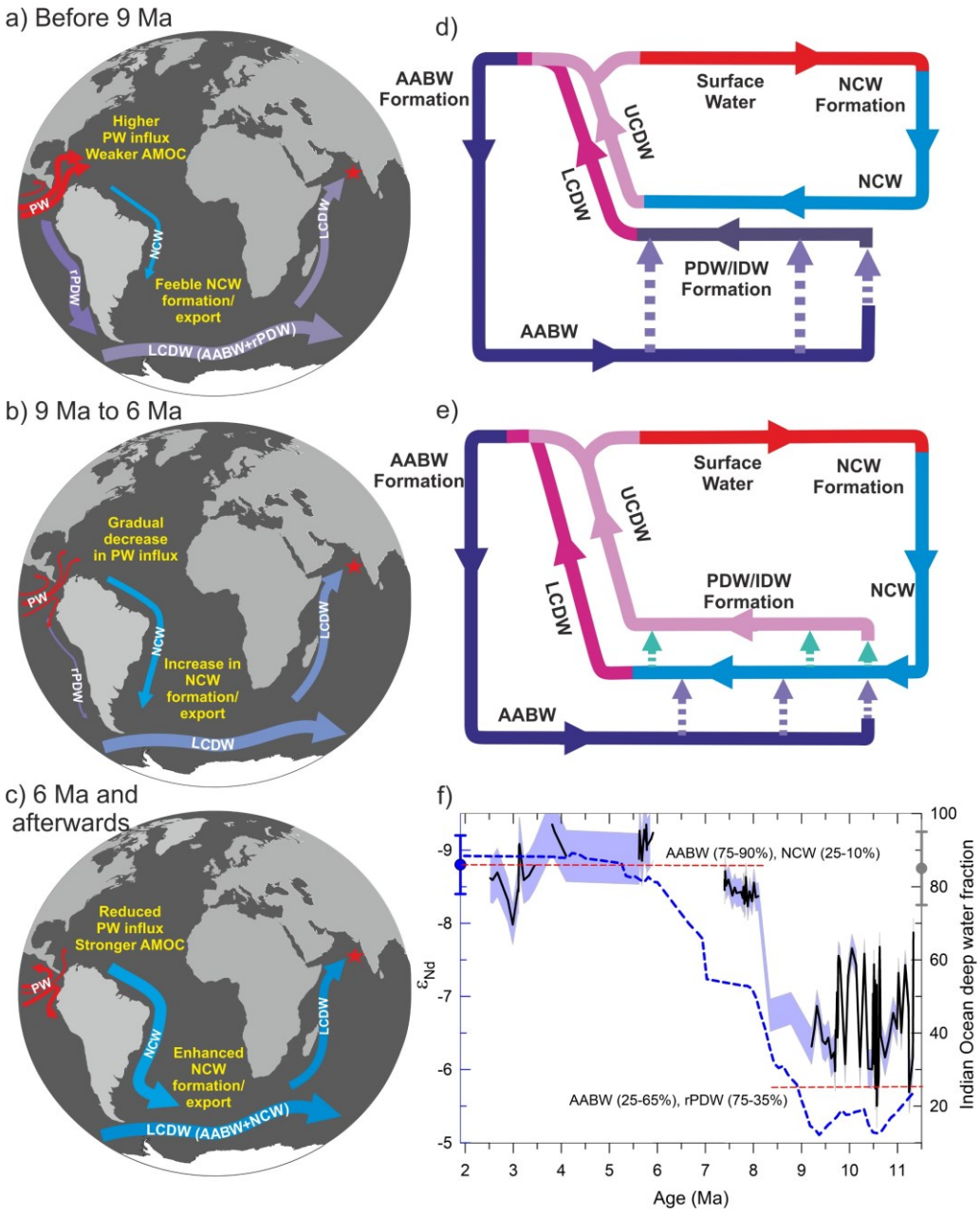

Figure 3.11: Constriction and shoaling of the CAS and its widespread impact on deep water circulation in three different stages. (a). Stage 1 (before ~9 Ma): large influx of fresh PW into the north Atlantic Ocean resulted in weaker AMOC and reduced formation and export of NCW to the Southern Ocean, as a result AABW mixed with rPDW to form the LCDW; (b) Stage 2 (~9 Ma to 6 Ma): gradual decrease in the PW influx to the North Atlantic and increase in the NCW formation and export to the Southern Ocean; (c) Stage 3 (after ~6 Ma): reduced export of PW into the north Atlantic and subsequent strengthening of NCW formation and enhanced export (as a result of stronger AMOC) to the Southern Ocean resulted in LCDW being formed by the mixture of AABW and NCW, while the rPDW formed the upper cell of the CDW owing to its lesser density than NCW similar to modern time; these schematic shows circulation cell structure (d) during the reduced NCW formation and its export to the Southern Ocean; e). enhanced NCW formation and export

to the Southern Ocean; f). authigenic ε_{Nd} record (two-point smoothened, blue line) of site U1457 and its corresponding Indian Ocean deep water fractions (black line with grey error envelope) with their modern-day values plotted on their respective axis. Horizontal red dotted lines show the contribution range of water masses at time interval before ~9 Ma (AABW and rPDW) and after ~9 Ma (AABW and NCW). PW - Pacific water; NCW - Northern component water; AABW - Antarctic bottom water; rPDW - recirculated Pacific deep water; PDW - Pacific deep water; IDW - Indian deep water; CDW - Circumpolar deep water; LCDW - Lower circumpolar deep water; UCDW - Upper circumpolar deep water.

We have quantified the proportion of each water mass (AABW, NCW, and rPDW) using the binary mixing model for different time intervals. It is important to mention that in the mixing calculation, fraction estimates are critically dependent on how accurately the end member values were constrained. The end-member compositions might undergo significant changes over the studied interval, therefore, we have considered dynamic end-members for specific intervals with an uncertainty that will accommodate the variability and changes in the end-member values.

To quantify the fractional contributions of each water mass during the studied interval in the Arabian Sea, we have done Nd isotope mass balance calculation following the method of Rahaman et al. (2020). The calculation is based on the assumption that the Nd isotope behaves quasi-conservatively. We have divided our record into two stages, and the water mass fractions of each stage are calculated separately. In the first stage (11.3 to ~9 Ma), the end member water masses taken are the AABW and PDW. In the second stage (~8 Ma onwards), mixing calculation is done considering the AABW and the NADW as the end members. The end-member composition of water masses for each stage is calculated using the following binary mixing equation. The uncertainty associated with the estimates was calculated using the Monte-Carlo error propagation method (Rahaman et al., 2020).

$$\varepsilon_{Nd_{\mathrm{M}}} = \frac{\varepsilon_{Nd_A} * C_A * f_A + \varepsilon_{Nd_B} * C_B * f_B}{C_A * f_A + C_B * f_B} \qquad Eq\ (1)$$

$$f_A + f_B = 1 \qquad Eq\ (2)$$

The %A ε_{Nd} = f_A*100 is the relative contribution of the water mass A to the Arabian Sea, and %B ε_{Nd} = 100 - %A ε_{Nd} is the relative contribution of water mass B to the Arabian Sea. Here C_A and C_B represent the concentration of Nd in the water mass A and B,

respectively. $\varepsilon_{Nd\ M}$ is the value of Nd isotope compositions of sediment leach from the Arabian Sea, and ε_{NdA} and ε_{NdB} are the end-members of the water mass A and B, respectively. The f_A and f_B represent the fractions of the water mass A and B. The details of end-member water masses and their end-member values used in both stages are provided in the Table 3.2.

Table 3.2: Water masses and their characteristic Nd isotope compositions in modern ocean

	ε_{Nd}	[Nd]	reference
NADW	-13.5±0.5	17.5±1	(Howe et al., 2016; Yu et al., 2020)
AABW	-8.5±0.5	25.1±1	(Howe et al., 2016; Yu et al., 2020)
PDW	-3.5±0.5	35±1	(Howe et al., 2016; Yu et al., 2020)

Since authigenic ε_{Nd} record shows similar value to that of the modern and interglacial periods since ~6 Ma, and thus, semi-quantitative estimate of fractional contribution shows that deep water composition was stable at modern-like deep water composition comprises of 85 to 90% AABW and 10 to 15% NCW, since the Miocene-Pliocene transition. On the contrary, the DWC was dominated by the southern sourced AABW with a significant fraction of PDW (50 ± 10%) during the older intervals (11.3 to ~9 Ma) (Figure 3.11f).

The late Miocene evolution trend of the deep water circulation shows a clear shift from the Pacific-dominated deep circulation system to the Atlantic influenced deep water circulation in the Indian Ocean with the strengthening of AMOC during the Miocene-Pliocene transition. Our finding suggests a profound and widespread impact of the late Miocene CAS closure on the evolution of ocean deep water circulation and validates the so called “Panama Closure Hypothesis”.

Chapter 4

Pliocene-Pleistocene authigenic Nd isotope records from the Amundsen Sea: Role of deep water circulation versus lithogenic influence

4.1 Introduction

It is believed that the transient West Antarctic Ice Sheet (WAIS) emerged about 34 million years ago, coinciding with the inception of ice sheets in East Antarctica, however, it became permanent since the middle Miocene (Westerhold et al., 2020a; Zachos et al., 2001). Seismic profiles in the central Ross Sea, correlated with dated horizons at Deep Sea Drilling Project Site 270, reveal glacial unconformities, indicating occurrences of an extensive grounded marine ice sheet within the Ross Sea embayment since the Early Miocene (Lindeque et al., 2016). However, the WAIS has always been considered more vulnerable to retreat or collapse under warmer atmospheric and oceanographic forcing due to predominantly marine based ice sheets and the retrograde bed structure of the WAIS region (Fretwell et al., 2013; Gudmundsson et al., 2012; Oppenheimer, 1998). During the warmest periods of the Pliocene (3.3–3.0 Ma), Earth's average surface temperature was approximately 2–3 °C warmer than the present, atmospheric pCO2 levels were around 400 ppm, and equator-to-pole temperature gradients were less pronounced (Westerhold et al., 2020a). Model based studies have suggested that during the Pliocene warmth, the predominantly marine-based WAIS had a reduced extent compared to modern (Figure 4.1d) (DeConto and Pollard, 2016; Naish et al., 2009; Pollard and DeConto, 2009), with global sea levels estimated to have been 5–40 m higher than present, converging mostly around 20–25 m (Miller et al., 2020; Rohling et al., 2021). The subsequent cooling, leading to the onset of significant Northern Hemispheric glaciation at around 2.7 Ma, has been attributed to various forcing factors such as declining pCO2, changes in orbital forcing, tectonic influences, changing oceanic physico-chemical condition resulting in increased stratification in the northern high latitudes, and reduced zonal gradient of sea surface temperature (SST) gradients in the equatorial Pacific Ocean (Westerhold et al., 2020a; Zachos et al., 2001) (Ferrari et al., 2014). However, relative roles of various forcing in modulating WAIS during the Pliocene–Pleistocene transition remains understudied.

The modern day Southern Ocean is acknowledged as a region sensitive to climate variations and exhibit a more rapid warming trend compared to lower latitudes (Figure 4.1a, b) (Böning et al., 2008; Gao et al., 2021; Gille, 2008). This accelerated warming phenomenon is primarily attributed to the strengthening of the circumpolar westerlies, which has been hypothesised to intensify the upwelling rate (Le Quéré et al., 2007; Meredith et al., 2016) of warm circumpolar deep water (CDW) and facilitate the transport of CDW onto the Antarctic continental shelves (Arneborg et al., 2012; Bai et al., 2022; Dinniman et al., 2012; Morrison et al., 2020; Spence et al., 2014; Thoma et al., 2008). This influx of oceanic heat onto the continental shelf due to CDW intrusion leads to an augmented basal ice shelf melt rate, contributing to increased freshwater input to the shelf regions (Figure 4.1c) (Adusumilli et al., 2020; Paolo et al., 2015; Pritchard et al., 2012; Rignot et al., 2013; Rintoul et al., 2016). Consequently, this process results in the reduction of the density of dense shelf water (DSW), the suppression of Antarctic bottom water (AABW) formation (Williams et al., 2016), and has profound implications for the global thermohaline circulation (Lumpkin and Speer, 2007; Marshall and Speer, 2012). A key focus in understanding the impact of CDW on ice sheet dynamics lies in the Amundsen Sea, a region that had received relatively limited scientific attention until the last decade. Ice streams in the Amundsen Sea basin drain a substantial portion of the WAIS, which is currently experiencing an unprecedented rate of ice mass loss. The changes in the ice sheet mass balance in the Amundsen Sea sector of the WAIS are primarily driven by the ongoing oceanic and atmospheric warming and significant alterations in circulation patterns within these systems. This underscores the critical role of the Amundsen Sea in the broader context of understanding ice sheet dynamics and their response to contemporary climate change. Since the heat carrying CDW entrains the Amundsen Sea Embayment through deeper troughs and results in basal melting, the variability in the CDW ε_{Nd} in the past can help us understand the different constituents of the CDW and may help to understand the past WAIS variability caused due to the ocean forcing. According to Adkins (2013), in the contemporary Antarctic region, the primary heat source for ice shelf melting is the Circumpolar Deep Water, a modified form of North Atlantic Deep Water. This water, responsible for ice shelf melting, undergoes freshening during the process. Despite this freshening, its cold temperature allows it to remain sufficiently dense, making it a key contributor to the formation of Antarctic Bottom Water, which fills the ocean's deepest regions. Throughout the ice age, a cooling or "shutdown" of North Atlantic Deep Water

occurred, leading to the production of colder and saltier Antarctic Bottom Water, resulting in an overall cooler ocean (Headly and Severinghaus, 2007). Conversely, the cooling of Circumpolar Deep Water would have diminished the melting beneath Antarctic ice shelves. Consequently, a combination of warming North Atlantic Deep Water and changes in wind patterns may play a significant role in the retreat of the East and West Antarctic Ice Sheets during the post-glacial period by reintroducing warm waters to ice-shelf grounding lines.

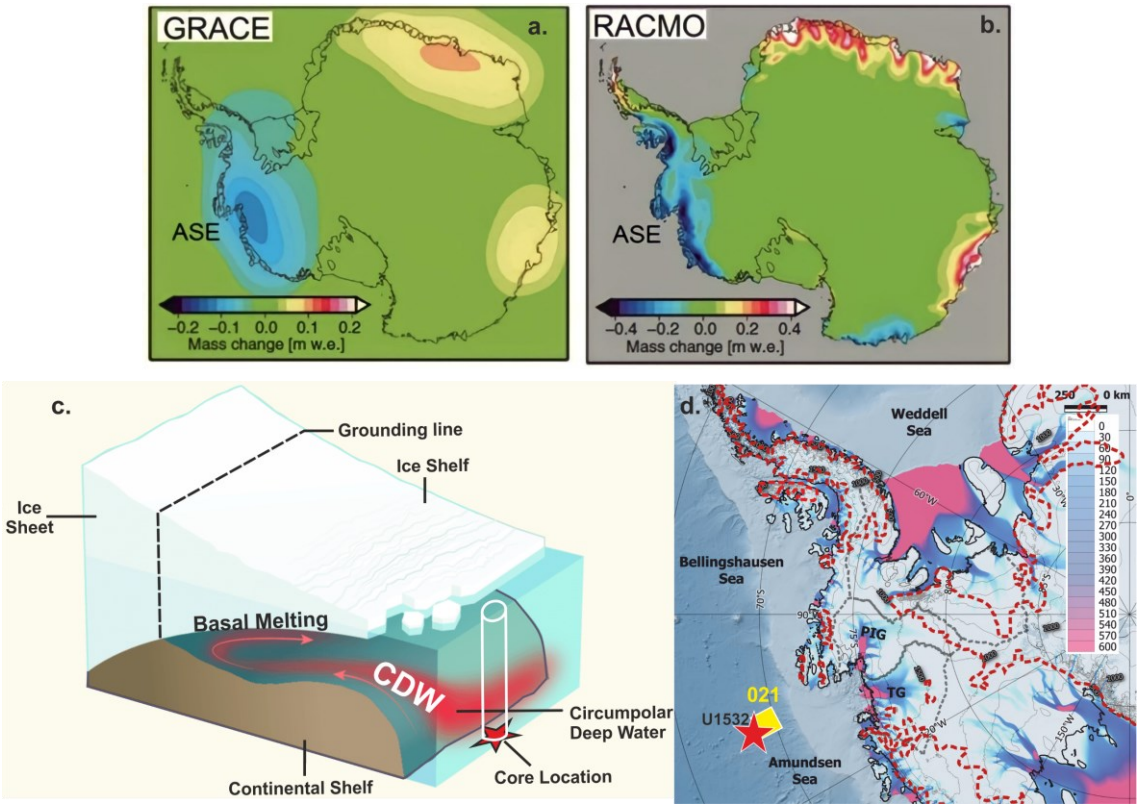

Figure 4.1: Antarctic ice sheet mass balance reduction. a, b) Mass loss of Antarctic ice is quantified by GRACE satellite and RACMO model (https://www.projects.science.uu.nl/iceclimate/models/racmo.php) for the period (1979 - 2010); c) Schematic of the incursion of Circumpolar Deep Water (CDW) in the Amundsen Sea Embayment through the shelf. CDW is warmer (2–3 °C) than the Shelf water and thus, results in the increased basal melting and the possible retreat of the grounding; d) map showing the core location (site U1532, red star) and the water station (021, yellow square). Red dotted line in the panel d) shows model derived Antarctic ice sheet extent for the Pliocene.

Thus, the reconstruction of the deep water mass circulation in the Amundsen Sea region of the WAIS from site U1532 retrieved during the IODP expedition 379 (Figure 2.6) can reveal the response of the Ice Sheet with respect to the changing water mass

constituents of the CDW onto the embayment leading to the higher basal melting causing the collapse or the retreat of the ice sheet in the past.

4.2 Results

The investigated data within the temporal range from the recent past to 4.6 million years ago (Ma) exhibit a variation in ε_{Nd} values ranging approximately from ~-4.5 (± 1) to ~-2 (± 1). It is noteworthy that the recorded minimum radiogenic ε_{Nd} value of -8 (± 0.27) is deemed an outlier, which may be attributed to analytical factors (Figure 4.2, Table 4.1). Authigenic ε_{Nd} values remained less radiogenic from 4.6 to 3.3 Ma, which subsequently shifts gradually towards the radiogenic value of approximately ~-2 (± 1). Authigenic ε_{Nd} values remained stable towards more radiogenic values in the late Pliocene and Pleistocene. Throughout the studied temporal span, the authigenic ε_{Nd} records, considered indicative of water mass values, do not exhibit any co-variability with the trajectory of benthic $\delta^{18}O$. The latter is well-established for its role in capturing climatic variations.

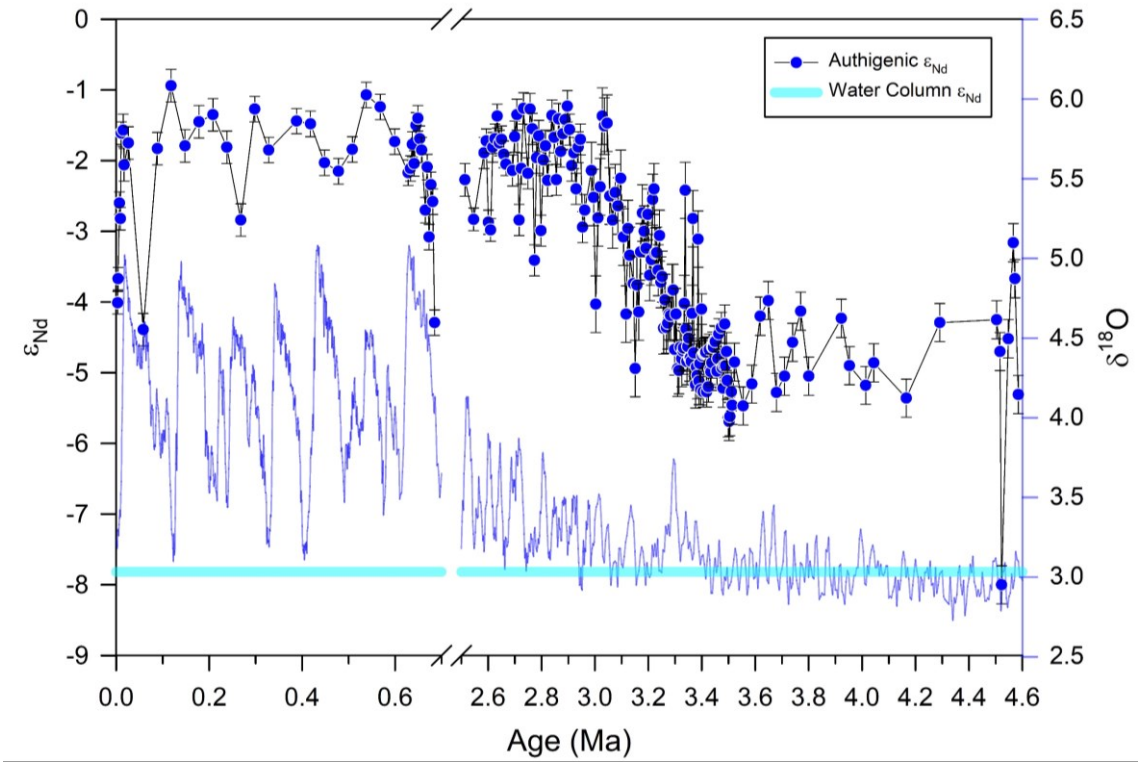

Figure 4.2: Authigenic ε_{Nd} record from the site U1532 and $d^{18}O$ (benthic) record for the site 1532. The cyan colour band represents the modern day water column ε_{Nd} value for depth > 3500 m.

Table 4.1: Authigenic Neodymium isotope record from the IODP 379 site U1532.

Top depth CSF-A (m)	Bottom depth CSF-A (m)	$^{143}Nd/^{144}Nd$	ε_{Nd}	Error (2σ)
0.02	0.04	0.5124324	-4.01	0.16
0.08	0.1	0.5124499	-3.67	0.16
0.12	0.14	0.5125047	-2.6	0.16
0.15	0.17	0.5124934	-2.82	0.16
0.24	0.26	0.5125555	-1.61	0.16
0.28	0.3	0.5125575	-1.57	0.23
0.46	0.48	0.5125324	-2.06	0.23
1.1	1.12	0.5125483	-1.75	0.23
1.71	1.73	0.5124130	-4.39	0.23
2.3	2.32	0.5125442	-1.83	0.23
2.9	2.92	0.5125898	-0.94	0.23
3.5	3.52	0.5125462	-1.79	0.23
4.1	4.12	0.5125637	-1.45	0.23
4.7	4.72	0.5125688	-1.35	0.23
5.3	5.32	0.5125452	-1.81	0.23
5.9	5.92	0.5124924	-2.84	0.23
6.5	6.52	0.5125729	-1.27	0.18
7.7	7.72	0.5125432	-1.85	0.18
8.3	8.32	0.5125642	-1.44	0.18
8.9	8.92	0.5125621	-1.48	0.18
9.5	9.52	0.5125339	-2.03	0.18
10.1	10.12	0.5125278	-2.15	0.18
10.7	10.72	0.5125437	-1.84	0.18
11.3	11.32	0.5125831	-1.07	0.18
11.92	11.94	0.5125744	-1.24	0.18
12.5	12.52	0.5125493	-1.73	0.18
12.6	12.62	0.5125268	-2.17	0.18
12.68	12.7	0.5125298	-2.11	0.18
12.76	12.78	0.5125473	-1.77	0.18
12.84	12.86	0.5125334	-2.04	0.18
12.92	12.94	0.5125611	-1.5	0.18
13	13.02	0.5125662	-1.4	0.18
13.08	13.1	0.5125514	-1.69	0.18
13.15	13.17	0.5125432	-1.85	0.18
13.32	13.34	0.5124996	-2.7	0.18
13.4	13.42	0.5125309	-2.09	0.18
13.48	13.5	0.5124801	-3.08	0.18
13.56	13.58	0.5125180	-2.34	0.18

13.64	13.66	0.5125057	-2.58	0.18
13.72	13.74	0.5124181	-4.29	0.18
43.8	43.82	0.5125216	-2.27	0.23
44.55	44.57	0.5124929	-2.83	0.16
45.65	45.67	0.5125411	-1.89	0.22
46.2	46.22	0.5125498	-1.72	0.17
46.75	46.77	0.5124909	-2.87	0.17
47.3	47.32	0.5124852	-2.98	0.16
47.85	47.87	0.5125452	-1.81	0.21
48.4	48.42	0.5125514	-1.69	0.21
48.95	48.97	0.5125678	-1.37	0.17
49.5	49.52	0.5125483	-1.75	0.18
50.05	50.07	0.5125509	-1.7	0.19
50.6	50.62	0.5125401	-1.91	0.19
51.15	51.17	0.5125329	-2.05	0.16
52.8	52.82	0.5125283	-2.14	0.22
53.35	53.37	0.5125529	-1.66	0.22
53.9	53.92	0.5125688	-1.35	0.22
54.45	54.47	0.5124924	-2.84	0.22
55	55.02	0.5125298	-2.11	0.22
55.55	55.57	0.5125734	-1.26	0.22
56.65	56.67	0.5125262	-2.18	0.22
57.2	57.22	0.5125729	-1.27	0.22
57.75	57.77	0.5125585	-1.55	0.22
58.3	58.32	0.5124632	-3.41	0.22
58.85	58.87	0.5125375	-1.96	0.22
59.4	59.42	0.5125534	-1.65	0.22
59.95	59.97	0.5124847	-2.99	0.22
60.5	60.52	0.5125360	-1.99	0.22
61.05	61.07	0.5125462	-1.79	0.22
61.6	61.62	0.5125211	-2.28	0.22
62.7	62.72	0.5125683	-1.36	0.22
63.25	63.27	0.5125524	-1.67	0.22
63.8	63.82	0.5125216	-2.27	0.22
64.35	64.37	0.5125657	-1.41	0.22
64.9	64.92	0.5125421	-1.87	0.22
65.45	65.47	0.5125550	-1.62	0.22
66	66.02	0.5125652	-1.42	0.22
66.55	66.57	0.5125749	-1.23	0.22
67.1	67.12	0.5125580	-1.56	0.22
67.65	67.67	0.5125319	-2.07	0.22

68.2	68.22	0.5125411	-1.89	0.22
68.75	68.77	0.5125150	-2.4	0.22
69.3	69.32	0.5125452	-1.81	0.22
69.85	69.87	0.5125509	-1.7	0.22
70.4	70.42	0.5124873	-2.94	0.22
70.95	70.97	0.5124996	-2.7	0.22
72.6	72.62	0.5125283	-2.14	0.4
73.15	73.17	0.5125088	-2.52	0.4
73.7	73.72	0.5124314	-4.03	0.4
74.25	74.27	0.5124939	-2.81	0.4
74.8	74.82	0.5125165	-2.37	0.4
75.35	75.37	0.5125678	-1.37	0.4
75.9	75.92	0.5125606	-1.51	0.4
76.45	76.47	0.5125626	-1.47	0.4
77	77.02	0.5125098	-2.5	0.4
77.55	77.57	0.5124924	-2.84	0.4
78.1	78.12	0.5125124	-2.45	0.4
78.65	78.67	0.5125027	-2.64	0.4
79.2	79.22	0.5125227	-2.25	0.4
79.75	79.77	0.5124801	-3.08	0.4
80.3	80.32	0.5124242	-4.17	0.4
80.85	80.87	0.5124863	-2.96	0.4
81.4	81.42	0.5124668	-3.34	0.4
82.5	82.52	0.5124463	-3.74	0.4
83.05	83.07	0.5123848	-4.94	0.4
83.6	83.62	0.5124452	-3.76	0.4
84.15	84.17	0.5124258	-4.14	0.4
84.7	84.72	0.5124693	-3.29	0.4
85.25	85.27	0.5124975	-2.74	0.4
85.8	85.82	0.5124842	-3	0.36
86.35	86.37	0.5124719	-3.24	0.36
86.9	86.92	0.5124965	-2.76	0.36
87.45	87.47	0.5124524	-3.62	0.36
88	88.02	0.5124637	-3.4	0.36
88.55	88.57	0.5125073	-2.55	0.36
89.1	89.12	0.5125150	-2.4	0.36
89.65	89.67	0.5124683	-3.31	0.36
90.2	90.22	0.5124688	-3.3	0.36
90.75	90.77	0.5124560	-3.55	0.36
91.3	91.32	0.5124811	-3.06	0.36
91.85	91.87	0.5124473	-3.72	0.36

92.4	92.42	0.5124514	-3.64	0.36
92.95	92.97	0.5124140	-4.37	0.36
93.5	93.52	0.5124345	-3.97	0.36
94.05	94.07	0.5124145	-4.36	0.36
94.6	94.62	0.5124176	-4.3	0.36
95.15	95.17	0.5124242	-4.17	0.36
95.7	95.72	0.5124232	-4.19	0.36
96.25	96.27	0.5124417	-3.83	0.36
96.8	96.82	0.5124417	-3.83	0.36
97.35	97.37	0.5123986	-4.67	0.36
97.9	97.92	0.5124242	-4.17	0.36
98.55	98.57	0.5123848	-4.94	0.4
99.1	99.12	0.5123832	-4.97	0.33
99.65	99.67	0.5124001	-4.64	0.33
100.2	100.22	0.5123919	-4.8	0.4
100.75	100.77	0.5123976	-4.69	0.33
101.3	101.32	0.5123996	-4.65	0.33
101.85	101.87	0.5124319	-4.02	0.4
102.4	102.42	0.5125139	-2.42	0.4
102.95	102.97	0.5124135	-4.38	0.33
103.5	103.52	0.5123899	-4.84	0.33
104.05	104.07	0.5124006	-4.63	0.33
104.6	104.62	0.5124068	-4.51	0.33
105.15	105.17	0.5123924	-4.79	0.33
105.7	105.72	0.5123924	-4.79	0.33
106.25	106.27	0.5123899	-4.84	0.33
106.8	106.82	0.5124247	-4.16	0.4
107.35	107.37	0.5124934	-2.82	0.4
107.9	107.92	0.5123960	-4.72	0.33
109	109.02	0.5123730	-5.17	0.33
109.55	109.57	0.5123858	-4.92	0.33
110.1	110.12	0.5123796	-5.04	0.33
110.65	110.67	0.5124786	-3.11	0.4
111.2	111.22	0.5123755	-5.12	0.33
111.75	111.77	0.5123883	-4.87	0.33
112.3	112.32	0.5123694	-5.24	0.22
112.85	112.87	0.5124278	-4.1	0.22
113.4	113.42	0.5123940	-4.76	0.22
113.95	113.97	0.5123678	-5.27	0.22
114.5	114.52	0.5123955	-4.73	0.22
115.05	115.07	0.5123960	-4.72	0.22

115.6	115.62	0.5123965	-4.71	0.22
116.15	116.17	0.5123678	-5.27	0.22
117.25	117.27	0.5123714	-5.2	0.22
117.8	117.82	0.5123986	-4.67	0.22
118.35	118.37	0.5123842	-4.95	0.22
118.9	118.92	0.5123822	-4.99	0.22
119.45	119.47	0.5123889	-4.86	0.22
120	120.02	0.5124001	-4.64	0.22
120.55	120.57	0.5124001	-4.64	0.22
121.1	121.12	0.5124047	-4.55	0.22
121.65	121.67	0.5124042	-4.56	0.22
123.3	123.32	0.5123919	-4.8	0.22
123.85	123.87	0.5124099	-4.45	0.22
124.95	124.97	0.5123817	-5	0.22
125.5	125.52	0.5124145	-4.36	0.22
126.05	126.07	0.5123853	-4.93	0.27
126.6	126.62	0.5123704	-5.22	0.27
127.15	127.17	0.5123868	-4.9	0.27
127.7	127.72	0.5124171	-4.31	0.27
128.25	128.27	0.5123868	-4.9	0.27
128.8	128.82	0.5123971	-4.7	0.27
129.35	129.37	0.5123760	-5.11	0.27
129.9	129.92	0.5123489	-5.64	0.27
130.45	130.47	0.5123463	-5.69	0.27
131	131.02	0.5123499	-5.62	0.27
131.93	131.95	0.5123678	-5.27	0.27
132.46	132.48	0.5123581	-5.46	0.27
133.98	134	0.5123894	-4.85	0.27
139.48	139.5	0.5123576	-5.47	0.27
145.04	145.06	0.5123735	-5.16	0.27
150.48	150.5	0.5124227	-4.2	0.27
155.98	156	0.5124340	-3.98	0.27
161.48	161.5	0.5123673	-5.28	0.27
166.98	167	0.5123791	-5.05	0.27
172.48	172.5	0.5124037	-4.57	0.27
177.98	178	0.5124263	-4.13	0.27
183.48	183.5	0.5123791	-5.05	0.27
205.48	205.5	0.5124212	-4.23	0.27
210.98	211	0.5123868	-4.9	0.27
221.98	222	0.5123725	-5.18	0.27
227.48	227.5	0.5123889	-4.86	0.27

249.48	249.5	0.5123632	-5.36	0.27
282.88	282.9	0.5124181	-4.29	0.27
328	328.02	0.5124201	-4.25	0.27
335.6	335.62	0.5123971	-4.7	0.27
339.4	339.42	0.5122238	-8.08	0.27
354.6	354.62	0.5124063	-4.52	0.27
366	366.02	0.5124760	-3.16	0.27
369.8	369.82	0.5124499	-3.67	0.27
377.4	377.42	0.5123658	-5.31	0.27

4.3 Discussion

The modern day Southern Ocean water column exhibits ε_{Nd} values in the range of approximately -7 to -9, which is in accordance with its role within the global Thermohaline Circulation (THC) system as a well-mixed intermediate region with significant contributions from North Atlantic Deep Water (NADW, ε_{Nd} = -13) and Pacific Deep Water (PDW, ε_{Nd} = -4) (Goldstein and Hemming, 2003; Stichel et al., 2012; Tachikawa et al., 2017; van de Flierdt et al., 2016; von Blanckenburg and Nägler, 2001). The ε_{Nd} distribution beneath the pycnocline in the deep Atlantic Ocean reflects patterns analogous to conservative water mass tracers, such as salinity, signifying the mixing of NADW with Antarctic Bottom Water (AABW, ε_{Nd} = -8) and Antarctic Intermediate Water (AAIW, ε_{Nd} = -8). In instances where the mixture contains a higher proportion of NADW, the ε_{Nd} values become more negative along the present-day western Atlantic boundary current (Lambelet et al., 2016; Wu et al., 2022), which is why this behaviour is described as "quasi-conservative". A study by Carter et al. (2012) has shown homogeneity in CDW with ε_{Nd} value of -8.7 in the eastern Pacific Sector of the Southern Ocean (Figure 4.3). The water station 021 (69°13'S, 106°40'E, water depth 4218 m) close to the study area has the ε_{Nd} value of -7.7 ± 0.1 from water depth 3009 to 4208 meters (Figure 4.4). Contrary to this, the present study, throughout the core does not show any ε_{Nd} value less radiogenic than -5.6 (other than single -8 value) during the studied interval (Figure 4.2). Authigenic ε_{Nd} record from the studied core site is not close to the modern day water column study and, hence cannot be considered as the true representative of past deep water circulation values in the region. It is important to understand that the reconstructions of past circulation patterns are influenced by the inherent limitations of the proxies used. Hence, it becomes intriguing to

understand the processes affecting the authigenic Nd values extracted from the sediment core samples.

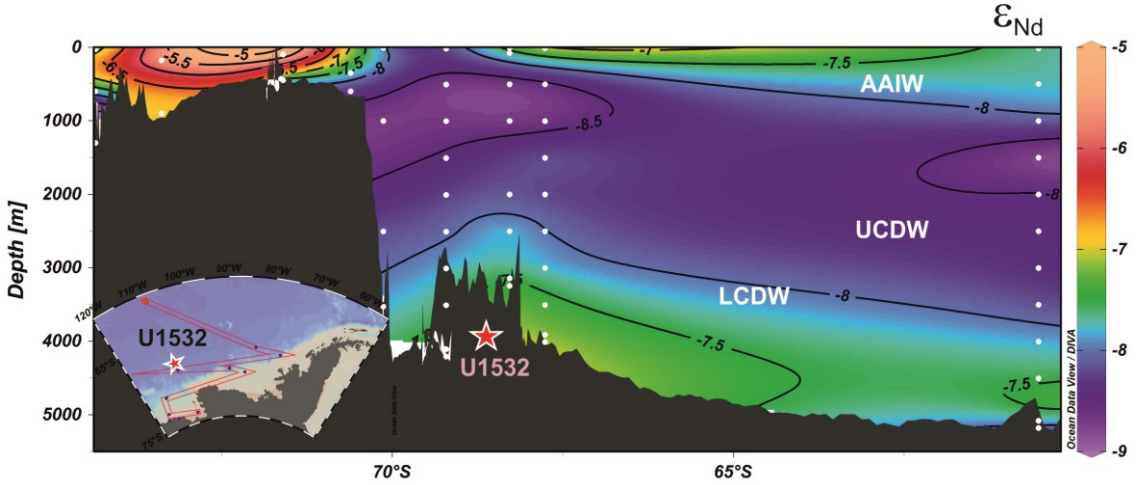

Figure 4.3: Section profile of modern day water column ε_{Nd} record along east Pacific sector of the Southern Ocean.

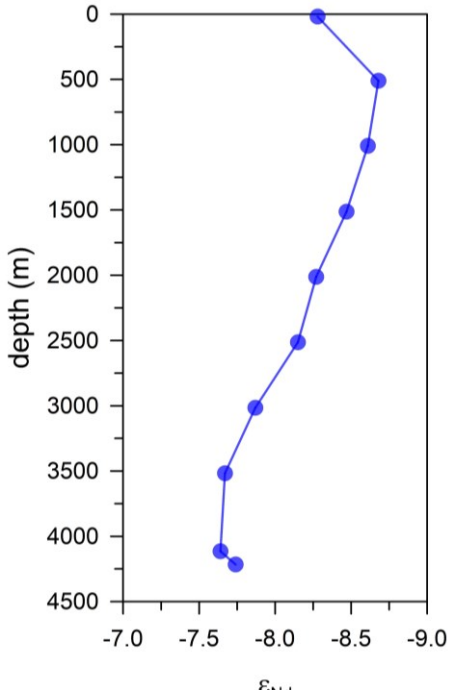

Figure 4.4: Modern day water column ε_{Nd} record from the water station 021 (69°13'S, 106°40'E, water depth 4218 m) close to present study site U1532 (Figure 4.1d).

The use of Nd-isotopes in ocean authigenic precipitates as a potential application relies on the assumption that their sub-pycnocline ocean distribution in the past was analogous to that of conservative tracers like salinity (Frank, 2002; Goldstein and

Hemming, 2003; Tachikawa et al., 2017; von Blanckenburg and Nägler, 2001; Wu et al., 2022). In the scenario where ε_{Nd} behaves conservatively in bottom water, primarily altered by water mass mixing only. Consequently, the ε_{Nd} signature of bottom water serves as a tracer for water mass mixing, revealing the water mass's origin based on its neodymium fingerprint (Frank, 2002). Additionally, in this scenario, the ε_{Nd} composition of bottom water dictates the authigenic ε_{Nd}, which remains unchanged during diagenesis (Figure 4.5a). Pore water ε_{Nd} inherits its signature from bottom water ε_{Nd}, and under ambient conditions, there is no active interaction between sediment and fluid. In the absence of reactive sediment phases, the sediment functions solely as a sink for Nd, with no benthic source at these locations. This scenario forms the basis of using Nd isotope as tracer for the past water circulation and can be considered as the **classical model**.

Given the exclusive dependence of authigenic ε_{Nd} on the origin of the overlying water mass in classical scenario, it can be entirely decoupled from the local detrital ε_{Nd} record. This decoupling may elucidate the observed homogeneity in the CDW in the eastern Pacific sector of the Southern Ocean (approximately at -8.7) away from the shelf regions, where Nd isotope acts non-conservatively (Figure 4.3) (Carter et al., 2012). Interestingly, for the regions away from the shelf (station 021, 022), over the same transect, a more radiogenic detrital ε_{Nd} is evident (Du et al., 2022b; Robinson et al., 2021; Roy et al., 2007). Thus, if the classical scenario prevails, it is expected that authigenic ε_{Nd} should consistently match with bottom water ε_{Nd} values (-8 to -9), irrespective of detrital composition, and will change only upon the intrusion of a different water mass into the region (Abbott et al., 2022). Thus, the variations in the authigenic ε_{Nd} recorded reflects the changes in the water mass mixing during the ocean circulation (Basak et al., 2018b; Blaser et al., 2019; Frank, 2002; Huck et al., 2016), and bottom water ε_{Nd} and detrital ε_{Nd} values can easily be decoupled.

However, the interpretation of ε_{Nd} records in terms of deep water circulation as depicted in the classical model has encountered two significant challenges. The first challenge, referred as "the paleo- Nd concentration problem", pertains to the absence of constraints on past Nd-concentrations ([Nd]) in the end-members of global THC water masses. The absence of constraints/information can influence Nd-isotope ratios at intermediate locations (Pöppelmeier et al., 2022). Attempts are being made to overcome this issue by utilising the Bayesian approach (Yehudai et al., 2023). The study based on

this approach contemplates that the significant alterations in the Nd-concentrations are unlikely to exert considerable influence on the Nd-isotope ratios. This suggests that, with appropriately chosen locations, Nd-isotope ratios effectively capture deep water signature, thereby substantiating their utility in reconstructing past ocean circulation. The second challenge arises from the fact that while ocean observations demonstrate that Nd-isotopes approximately adhere to conservative mixing in the contemporary oceans (Frank, 2002; Goldstein and Hemming, 2003; Stichel et al., 2012; Tachikawa et al., 2017; van de Flierdt et al., 2016; Wu et al., 2022), non-conservative processes can introduce alterations to the Nd-isotope signatures along the flow paths of water masses (Haley et al., 2014; Jeandel and Oelkers, 2015; Johannesson et al., 2007; Lacan et al., 2005; Tachikawa et al., 2017). The contribution of Rare Earth Elements (REEs), including Nd, from seabed sediments to the ocean at the water-sediment interface is a critical factor that aids in addressing the second issue, is referred to as "boundary processes" occurring in the uppermost seabed layer. Two primary processes, namely "benthic flux" and "boundary exchange" (Wilson et al., 2013), have been extensively studied in this context. Benthic flux has the capacity to alter both the concentration ([Nd]) and ε_{Nd} of local bottom water (Abbott et al., 2015; Jeandel and Sciences, 2016). This occurs as porewaters, rich in dissolved Nd, migrate upwards from sediment porewater into the bottom waters. The ε_{Nd} of these porewaters differs from that of bottom waters due to Nd release through processes such as desorption from particles, reduction of authigenic phases, or dissolution of detrital particles. Boundary exchange, on the other hand, is characterized by the transfer of elements from seabed sediments into interacting seawater through particle dissolution, concomitant with the simultaneous removal of elements present in the seawater through boundary scavenging (Arsouze et al., 2009; Lacan et al., 2005). This process has the potential to modify the ε_{Nd} in bottom water without causing a significant alteration in [Nd]. Understanding these input mechanisms is crucial for resolving the complexities of boundary processes at the water-sediment interface in marine environments. Considerably, the precise mechanism underlying the modification of Nd isotopic ratios remains unresolved. The boundary exchange processes are considered to effective near the continental margin, and on the contrary, present study site is located far from the margin. Hence, the possibility of such processes affecting the ε_{Nd} values throughout the cored interval is ruled out.

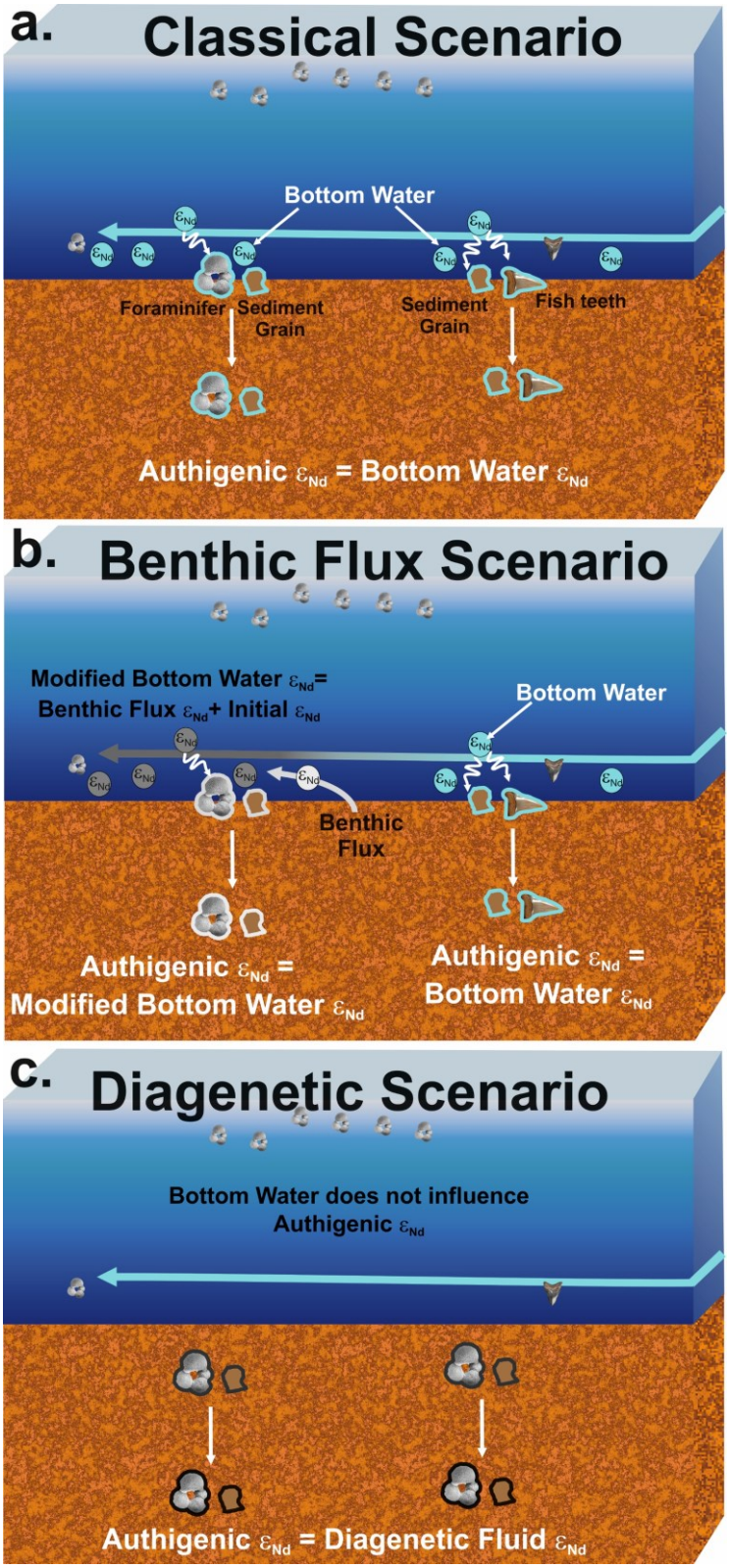

Figure 4.5: Processes affecting authigenic ε_{Nd} record. a) Classical model scenario- archives acquire bottom water ε_{Nd} signature, which is does not get affected during the diagenetic processes and records authigenic ε_{Nd} is equal to true bottom water ε_{Nd}; b) Benthic flux model scenario- archives acquire bottom water ε_{Nd} signature where benthic flux is not effective, which suggests authigenic ε_{Nd} is equal to true bottom water ε_{Nd}. While along the

flow where benthic flux is modifying the bottom water archives record authigenic ε_{Nd} record of the modified bottom water with the neodymium isotopic composition from the benthic flux; c) Diagenetic model suggests that the archives acquire authigenic ε_{Nd} within the sediment column during the process of the diagenesis. The elements dissolved in the interstitial space water form the authigenic coating of the archives as a result of the interaction of the reactive component of the sediment with the water.

In the context of **benthic flux**, the composition of bottom water undergoes substantial modification due to a non-conservative behaviour of ε_{Nd} in the bottom water, as discussed by Abbott et al. (2015) and Abbott (2019). This flux involves the introduction of elements into the bottom water through a diffusive process, moving from higher concentrations of elements in the pore water to lower concentrations elements in the bottom water, either at the study location or earlier along the water mass's flow path (Abbott et al., 2015; Haley et al., 2017b; Haley et al., 2014; Jeandel and Oelkers, 2015; Jeandel and Sciences, 2016). The resulting authigenic ε_{Nd} record in this scenario is dependent on the magnitude and isotopic compositions of the benthic flux, as well as the exposure time of a water mass to that flux (Figure 4.5b). As the bottom water is continually influenced by sediments during its movement, the ε_{Nd} at any specific location is also influenced by the water mass's flow path and speed, which is inversely related to exposure time (Abbott et al., 2015; Haley et al., 2017b). The degree of coupling between authigenic ε_{Nd} and detrital ε_{Nd} is contingent upon the local benthic flux (both in magnitude and εNd) and the flow path. A strong local benthic flux, can lead to coupling between authigenic and the detrital values, making authigenic ε_{Nd} more closer to detrital ε_{Nd}. Conversely, strong circulation or a weak local benthic flux may show decoupling between the authigenic and detrital values ε_{Nd} (Abbott et al., 2016; Haley et al., 2017b; Tachikawa et al., 2017).

The authigenic ε_{Nd} signal observed at present study site U1532 consistently exhibits a radiogenic authigenic ε_{Nd} values compared to the detrital ε_{Nd} signal over the entire studied interval except for few depth intervals (Figure 4.6). The authigenic core top values (ε_{Nd} = -4) are less radiogenic than the core top detrital value (ε_{Nd} = ~-3; Figure 4.6a, Table 4.1, Table 5.1), however it is higher than the modern day CDW value by ~4 ε_{Nd} unit and is similar to the PDW ε_{Nd} values. The presence of PDW at deeper depths is not suggested due to the lower density of the water mass asserted by the physico-chemical conditions. The detrital values display an increasing trend similar to the authigenic values, implying a certain degree of coupling between them (Figure 4.6). Nevertheless, the contemporary ε_{Nd} value of seawater at station 021 (Carter et al., 2012), recorded in the water depth range of

approximately 3000 to 4000 m (in proximity to the sediment-water interface), is documented as -7.7 ± 0.1 (Figure 4.4). This modern water mass ε_{Nd} value, closely resembles the modern Circumpolar Deep Water (CDW) value, and is less radiogenic than both the detrital surface sediment values (~-3 ε_{Nd}) reported in the region (Roy et al., 2007; Simões Pereira et al., 2020) and the detrital core top value from our current study. This comparative analysis implies that while benthic flux may influence the bottom water mass in the region, however, it alone cannot account for the radiogenic values recorded in our study.

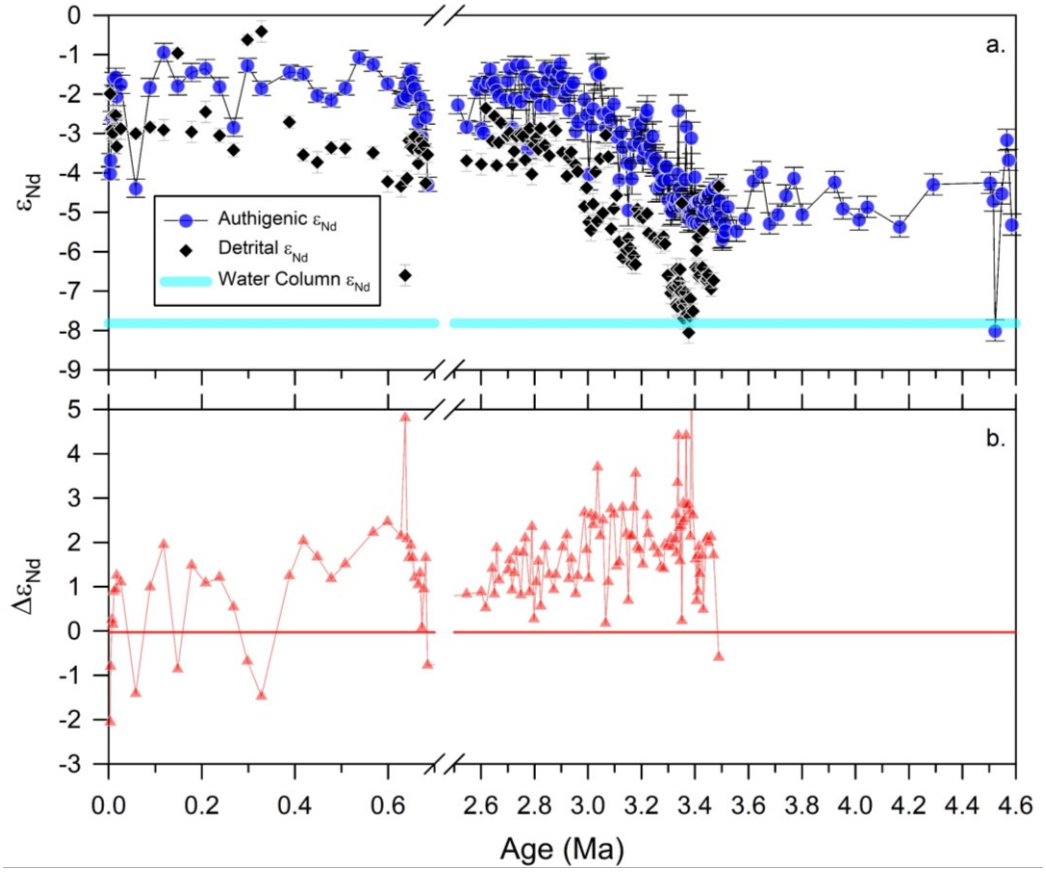

Figure 4.6: a) Authigenic and the detrital ε_{Nd} record from the core site U1532 (present study). The cyan colour band represents the modern day water column ε_{Nd} value for depth > 3500 m; b) $\Delta\varepsilon_{Nd}$, difference of authigenic ε_{Nd} to that of detrital ε_{Nd}. The solid orange line at zero marks authigenic values more radiogenic than detrital, if $\Delta\varepsilon_{Nd} > 0$ and less radiogenic, if $\Delta\varepsilon_{Nd} > 0$.

4.3.1 Process affecting the authigenic ε_{Nd} record at the present study site.

The other possibility that could affect the authigenic values lies in the sediment column during the diagenesis of the sediments. In the **diagenetic model**, the authigenic ε_{Nd} is solely influenced by the surrounding sediments and does not encapsulate the ε_{Nd} of bottom water (Figure 4.5c). This approach aligns with the recent studies finding that the

Nd concentration in bottom water is frequently 1 to 2 orders of magnitude lower than that of pore water (Abbott et al., 2022). Notably, pore water contains less than 0.001% of the total Nd reservoir in sediments (Abbott et al., 2015; Abbott et al., 2016; Du et al., 2016; Haley et al., 2014), rendering the bottom water chemical composition inconsequential in a sediment-dominated system. Study based on the pore water ε_{Nd} profiles (Abbott et al., 2015; Abbott et al., 2022) indicate that at 1 cm sediment depth, the ε_{Nd} of the pore water is different than that of the overlying bottom water and closely resembles the values recorded in deeper pore water (8–12 cm). These findings indicates that early diagenetic processes drive the alteration of authigenic values without substantial burial. Consequently, even in the upper layers (top few cm) of the sediment column, the ε_{Nd} of authigenic phases can mirror the sedimentary ε_{Nd}. Thus, this model suggests for changes in the authigenic phases throughout diagenesis, as a result of the encompassing dissolution-precipitation cycles, growth of secondary mineral phases, and as a result of the replacement of primary phase of the precipitates (Abbott, 2019; Skinner et al., 2019).

Hence following the ongoing discussion, the authigenic ε_{Nd} record of the present study could be explained exclusively by acquiring the authigenic phases within the sediment column during the diagenesis process. Consequently, authigenic ε_{Nd} record of present study was acquired within the sediment column as a function of the reactivity of the sediment components during the diagenesis. Hence, authigenic ε_{Nd} values represent a reactivity-weighted average ε_{Nd} of the detrital fraction instead of the bottom water signature. The reactive components of the detrital fragments interact with the water present in the interstitial spaces of the sediments. Thus, the variability in the authigenic records can be attributed to the reactive components of the detrital part and their partial dissolution in the interstitial fluid. Clay minerals like kaolinite, chlorite, illite and volcanic glasses are more susceptible to dissolution and could contribute to the more radiogenic values to the interstitial waters present in the sediments (Wang et al., 2022). With time, more and more REE's may dissolve and become part of the solution which gets precipitated as the authigenic fraction on the detrital grains and can contribute towards the more radiogenic values. This explains the robust association between authigenic ε_{Nd} and detrital ε_{Nd} mostly covarying with discernible increasing trends. While bottom water is not considered to influence the authigenic record in this scenario, it is anticipated that the pore water undergoes significant alteration, given that a reactive sediment column is likely to elevate Nd concentrations in the pore water. This condition is similar to the modern water column

studies which record less radiogenic Nd values close to CDW which are also less radiogenic than the surface sediment values in the surrounding region (Carter et al., 2012). The authigenic ε_{Nd} value of the top part of the present sediment core (2-4 cm and 8-10 cm) is less radiogenic (-4 and -3.6 ε_{Nd}) than the core top detrital (-2 and -2.9 ε_{Nd}, Figure 4.6a,b). There is a possibility that with more time provided within the interstitial fluid to dissolve and exchange the ε_{Nd} values, it may become radiogenic with time. The occasional peaks and troughs apart from the general trend in the authigenic values may be contributed to the ice rafted debris associated with the calving ice sheets.

The above discussion implies that the changes in the authigenic ε_{Nd} values are reflected as the variable influence of detrital fraction signature. Also, a similar trend is visible in the downcore ε_{Nd} values of the authigenic and detrital fraction as both show an increasing trend towards the radiogenic values since 3.3 Ma onwards (Figure 4.6). This change in the authigenic ε_{Nd} values, thus, reflects the change in the source of the sediments being deposited at the core site, instead of the bottom water composition.

The uncertainties associated with the influence of seafloor cycling on the chemical behaviour of trace and rare earth elements and their isotopes in the water column remain understudied (Homoky et al., 2016). Several preliminary investigations suggests detrital contributions to authigenic phases in isotope systems like chromium (Frank et al., 2020; Janssen et al., 2021), nickel (Gueguen and Rouxel, 2021), and iron (Abadie et al., 2017). (Jeandel and Oelkers, 2015) underscore the significance of sediment dissolution in the water column on the surface or during the diagenesis on ocean chemistry and global element cycles. Therefore, it is crucial to examine and differentiate the impacts of sediment geochemical properties, such as composition, reactivity, and resulting benthic flux, as well as local environmental conditions, from the variations occurring due to changes in ocean circulation, specifically in terms of water mass mixing. Present investigation assesses the impact of lithogenic factors on the archives of marine authigenic ε_{Nd} , within the sedimentary column during the diagenesis. It is important to highlight that, similar lithogenic influences may be recorded in the authigenic ε_{Nd} values of fish teeth/debris and foraminifera, if the environment is characterized by a strong correlations/coupling between authigenic and the detrital ε_{Nd}. Although authigenic ε_{Nd} aligns well with assertions to trace the changes in past ocean circulation pattern, care must be taken while interpreting authigenic ε_{Nd} solely. Therefore, present study suggests that sediment characteristics and

detrital signature should be integrated before interpreting the reconstruction of past ocean circulation from the Amundsen Sea setting or other similar oceanic settings around Antarctica.

Chapter 5

Investigating Provenance Changes in Amundsen Sea Sediments: Implication for West Antarctic Ice Sheet Dynamics

5.1 Introduction

The West Antarctic Ice Sheet (WAIS), largely a marine-based (grounding line is below sea level) and therefore highly sensitive to climatic and oceanographic changes (Joughin and Alley, 2011). Over the last decades, the WAIS has been undergoing dramatic mass loss due to subglacial melting and contributed to present sea-level rise at a faster rate than any other continental ice sheet on Earth (Frezzotti and Orombelli, 2014a; Joughin and Alley, 2011). Model-based simulations predict a complete collapse/retreat of the WAIS in near future that may result in a global sea-level rise to 3.3-4.3 meters (DeConto and Pollard, 2016; Pollard and DeConto, 2009). However, these model predictions differ for both the past and future ice sheet stability and have large uncertainties associated with the estimates of timing of the collapse of the ice sheet and resulting sea-level rise (Dolan et al., 2018). Therefore, these numerical model-based projections require validation. An alternative approach based on geological evidence from proximal WAIS margins can be utilized to constrain ice sheet sensitivity to climate forcing(s), particularly during geologic past, when climate conditions were similar to modern day and/or the near distant future. Arguably the best analogue in the recent Earth's history for near-future global climate is the Pliocene with as temporal span from 5.33–2.58 Ma, experienced 2-3°C higher global mean temperatures (Dowsett et al., 2009) and the atmospheric CO_2 concentrations ranged between 350 and 450 ppm, which is 25–60% higher than the pre-industrial levels (de la Vega et al., 2020; Foster et al., 2017; Pagani et al., 2010; Seki et al., 2010). This epoch underwent a gradual shift from relatively warmer climates in the Pliocene to cooler conditions in the early Pleistocene. This particular interval of Pliocene-Pleistocene climate transition represents a crucial focal point for exploring ice sheet behaviour due to comparable ice sheet boundary conditions of modern day and near future in terms of atmospheric CO_2 level, sea surface temperature and sea-level (Cook et al., 2013; Wilson et al., 2018). Reconstructions of past WAIS dimension and configuration in the past will enable us to evaluate ice sheet models that aim to forecast future behaviour and assess the

potential contribution from the WAIS collapse to global sea-level rise. Though, few attempts have been made earlier based on sediment cores retrieved from the western Ross Sea under the Antarctic Drilling (ANDRILL) project, however, the ANDRILL results (Naish et al., 2009) does not representative of the WAIS in the Amundsen Sea sector where most extreme melting and maximum mass loss are taking place today (Figure 2.6b) (Turner et al., 2017). The Amundsen Sea Embayment (ASE) in the West Antarctica holds significant importance for monitoring the stability of the ice sheet (Figure 2.6). The continental ice sheet in this region is presently experiencing accelerated loss, resulting in the swift retreat of Pine Island, Thwaites, and adjacent glaciers (Rignot et al., 2019; Turner et al., 2017). Numerical model based studies hypothesise, Amundsen Sea sector to be a potential precursor for substantial retreat or even collapse for major WAIS during the most intense warm intervals of the Pliocene-Pleistocene epoch over the past 5 Ma (DeConto and Pollard, 2016; Pollard and DeConto, 2009). However, geological evidence for a collapse, widespread retreat or even smaller dimensions of it during the Late Quaternary, remains primarily indirect, relying predominantly on far-field data, such as sea-level records (Dutton et al., 2015). Direct geological evidences from ice-proximal records to the WAIS are limited.

In this study, we present a novel dataset that constrains the dynamics of the WAIS in the Amundsen Sea sector throughout the late Pliocene and Pleistocene epochs. Present analysis relies on sedimentological and geochemical data derived from a marine sediment core site U1532 (68°36.683′S, 107°31.500′W, 3961.5 m water depth) retrieved during IODP Expedition 379 in 2019 (Figure 2.6) (Gohl and the Expedition, 2021). This site is expected to have documented the processes intricately linked to past WAIS dynamics, specifically through sediment deposition subsequent to downslope transportation via deep-sea channels. Additionally, influence of bottom currents may be observed during the transport and deposition of the sediments. For the present study, only the Site U1532 has been considered because of its higher sedimentation rates (Figure 5.1e), thus providing higher temporal resolution (Gohl and the Expedition, 2021).

To constrain the effects of extended warming on the variability of the WAIS, a comprehensive record has been generated encompassing late Pliocene to Pleistocene continental erosion patterns, utilizing detrital marine sediment provenance data obtained from IODP Site U1532. This study utilises the radiogenic isotope composition of the

neodymium [$^{143}Nd/^{144}Nd$, expressed as ε_{Nd}, which is the deviation from the measured $^{143}Nd/^{144}Nd$ ratios of the Chondritic Uniform Reservoir (CHUR) in parts per ten thousand] and lead isotope ratio ($^{208}Pb/^{204}Pb$ and $^{208}Pb/^{207}Pb$) to trace sediment provenance. These isotopic signatures of the bulk sediments are relatively conservative during transportation and deposition, reflecting a mixture of contributing sources. The principles behind using Nd and Pb isotopes in bulk detrital sediment as a tracer for sediment provenance are derived from the fact that different geological sources have distinct isotopic compositions from where sediments are derived without significantly altering their isotope compositions. The isotopic variability arises due to differences in the geological history and mineralogical characteristics of the source regions. Among various combinations of Pb isotope ratios, we have used $^{208}Pb/^{204}Pb$ and $^{208}Pb/^{207}Pb$ ratios as they show coherent signal and discernible trend that are consistent with the ε_{Nd} record (Figure 5.1a, b, c). It is important to highlight that the Pleistocene interglacials and the Pliocene erosional history of the east Antarctica and ice sheet variability from the East Antarctic Ice Sheet (EAIS) were successfully reconstructed using detrital ε_{Nd} records from the Adélie Land sector of East Antarctica (Cook et al., 2013; Wilson et al., 2018). These studies have demonstrated that most extreme changes in the locus of glacial erosion were linked to coastal versus inland erosion due to retreat and expansion of EAIS during the late Pleistocene G-I cycles. Distinct sediment sourcing associated with the growth and retreat of the ice sheet margin and multiple collapse events clearly establish a close link between ice sheet dynamics and erosion.

5.2 Results

The detrital ε_{Nd} record in the bulk sample at IODP Site U1532 (Table 5.1) shows a distinct shift from the less radiogenic values (-7±1) during the late Pliocene to more radiogenic Pleistocene values (-3±1) (Figure 5.1a). It is noteworthy to highlight that except three anomalous data points, all the detrital ε_{Nd} values were stable at -3±1 in the entire Pleistocene glacial-interglacial (G-I) cycles. The detrital Pb isotope records ($^{208}Pb/^{204}Pb$ and $^{207}Pb/^{208}Pb$) also followed similar trend with higher ratios during the late Pliocene and lower ratios in the Pleistocene (Figure 5.1b). A previous report of detrital ε_{Nd} records in fine fractions (<63 μm) from two core sites, i.e. PC493a (0 to 1102 ka) and PS58/254 (0 to 1106 ka) (Pereira, 2018) in close proximity to our core sites show almost uniform values during the Pleistocene which are consistent with our ε_{Nd} record (Figure 5.1a). The overall trend (loess fit, a non-parametric fit, Figure 5.1a) derived from the compiled ε_{Nd} records of these

three core sites clearly demonstrate a gradual but distinct shift from less radiogenic Pliocene sediments to more radiogenic Pleistocene sediments and afterward largely invariant sediment sourcing in the entire Pleistocene. It is noteworthy that the physical properties, lithological and bulk geochemistry parameters also show discernible changes and a consistent pattern with the trend in the radiogenic isotope profiles particularly during the Pliocene-Pleistocene transition (Figure 5.1); higher sedimentation rates (~50 cm/ka) (Figure 5.1f), lower reflectance (Figure 5.1e) and higher total organic carbon and nitrogen (TOC/TN) (Figure 5.1d) during the warm Pliocene coincide with the less radiogenic ε_{Nd} values compared to the Pleistocene.

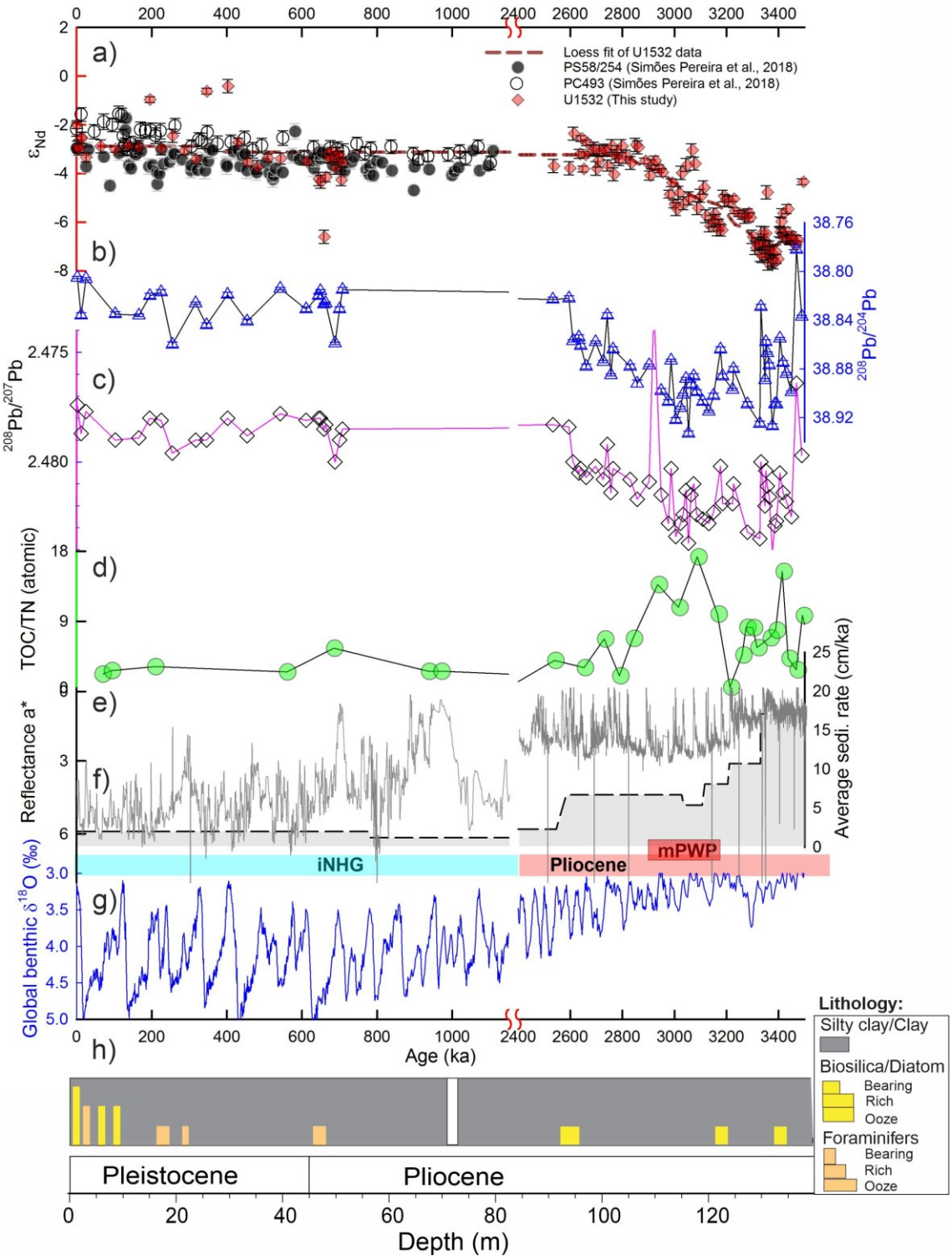

Figure 5.1: Late Pliocene and Pleistocene records from Amundsen Sea embayment U1532. (a) Bulk detrital sediment Nd isotopes (ε_{Nd}) (error bars are 2 σ external reproducibility) record from IODP Site U1532 (this study) together with earlier published records of bulk detrital (<63 μm fraction) from the core sites PC493 (Lat: 71°08′W, Long: 119°55S) and PS58/254 (Lat: 69°19′W, Long: 108°27′S) (Pereira, 2018), (b) Bulk detrital sediment Pb isotope record from the site U1532. (c) Ratio of total organic carbon and nitrogen percentage (TOC/TN). (d) Sediment reflectance a*. (e) Average sedimentation rates. (f)

Global benthic $\delta^{18}O$ (LR04) curve (Lisiecki and Raymo, 2005b). Colour bank indicates climate transitions; iNHG-intensification of northern hemispheric glaciations and mPWP-mid Pliocene warmth period. (g) Lithological log (Gohl et al., 2021b) of U1532A,B.

Table 5.1: Neodymium isotope record of detrital sediments from IODP 379, site U1532

Top depth CSF-A (m)	Bottom depth CSF-A (m)	$^{143}Nd/^{144}Nd$	ε_{Nd}	Error (2σ)
0.02	0.04	0.5125360	-1.99	0.16
0.08	0.1	0.5124893	-2.9	0.23
0.12	0.14	0.5124898	-2.89	0.27
0.15	0.17	0.5124842	-3	0.23
0.24	0.26	0.5125083	-2.53	0.23
0.28	0.3	0.5125078	-2.54	0.23
0.46	0.48	0.5124673	-3.33	0.19
1.1	1.12	0.5124904	-2.88	0.27
1.71	1.73	0.5124842	-3	0.12
2.3	2.32	0.5124924	-2.84	0.12
2.9	2.92	0.5124888	-2.91	0.27
3.5	3.52	0.5125888	-0.96	0.12
4.1	4.12	0.5124863	-2.96	0.27
4.7	4.72	0.5125124	-2.45	0.27
5.3	5.32	0.5124816	-3.05	0.18
5.9	5.92	0.5124627	-3.42	0.18
6.5	6.52	0.5126062	-0.62	0.12
7.7	7.72	0.5126170	-0.41	0.27
8.3	8.32	0.5124991	-2.71	0.16
8.9	8.92	0.5124565	-3.54	0.16
9.5	9.52	0.5124468	-3.73	0.27
10.1	10.12	0.5124658	-3.36	0.16
10.7	10.72	0.5124647	-3.38	0.23
11.92	11.94	0.5124591	-3.49	0.16
12.5	12.52	0.5124217	-4.22	0.27
12.6	12.62	0.5124155	-4.34	0.27
12.76	12.78	0.5122997	-6.6	0.27
12.84	12.86	0.5124258	-4.14	0.19
12.92	12.94	0.5124750	-3.18	0.18
13	13.02	0.5124658	-3.36	0.19
13.08	13.1	0.5124647	-3.38	0.19
13.15	13.17	0.5124801	-3.08	0.16
13.32	13.34	0.5124452	-3.76	0.27

13.4	13.42	0.5124627	-3.42	0.23
13.48	13.5	0.5124755	-3.17	0.23
13.56	13.58	0.5124683	-3.31	0.23
13.64	13.66	0.5124196	-4.26	0.23
13.72	13.74	0.5124565	-3.54	0.19
44.55	44.57	0.5124488	-3.69	0.27
46.75	46.77	0.5124442	-3.78	0.27
47.85	47.87	0.5125170	-2.36	0.27
49.5	49.52	0.5124745	-3.19	0.19
50.05	50.07	0.5125068	-2.56	0.12
50.6	50.62	0.5124427	-3.81	0.12
51.15	51.17	0.5124724	-3.23	0.12
51.7	51.72	0.5124980	-2.73	0.12
53.35	53.37	0.5124816	-3.05	0.23
53.9	53.92	0.5124852	-2.98	0.27
54.45	54.47	0.5124437	-3.79	0.28
55	55.02	0.5124611	-3.45	0.28
55.55	55.57	0.5124806	-3.07	0.23
56.65	56.67	0.5124832	-3.02	0.23
57.2	57.22	0.5124806	-3.07	0.23
57.75	57.77	0.5124499	-3.67	0.23
58.85	58.87	0.5124909	-2.87	0.27
59.4	59.42	0.5124314	-4.03	0.27
59.95	59.97	0.5124693	-3.29	0.27
60.5	60.52	0.5124781	-3.12	0.27
61.05	61.07	0.5124637	-3.4	0.27
61.6	61.62	0.5124909	-2.87	0.27
62.7	62.72	0.5124688	-3.3	0.27
63.8	63.82	0.5124555	-3.56	0.27
64.9	64.92	0.5124934	-2.82	0.27
65.45	65.47	0.5124883	-2.92	0.27
67.1	67.12	0.5124596	-3.48	0.12
68.2	68.22	0.5124288	-4.08	0.19
68.75	68.77	0.5124524	-3.62	0.19
69.3	69.32	0.5124601	-3.47	0.19
70.4	70.42	0.5124432	-3.8	0.16
70.95	70.97	0.5124350	-3.96	0.16
72.6	72.62	0.5123894	-4.85	0.16
73.15	73.17	0.5124135	-4.38	0.16
73.7	73.72	0.5123689	-5.25	0.16
74.25	74.27	0.5123581	-5.46	0.27

74.8	74.82	0.5123924	-4.79	0.27
75.35	75.37	0.5124345	-3.97	0.27
75.9	75.92	0.5123704	-5.22	0.27
76.45	76.47	0.5124514	-3.64	0.27
77	77.02	0.5123807	-5.02	0.27
77.55	77.57	0.5124822	-3.04	0.27
78.1	78.12	0.5124540	-3.59	0.27
78.65	78.67	0.5123602	-5.42	0.27
79.2	79.22	0.5123863	-4.91	0.27
79.75	79.77	0.5124037	-4.57	0.27
80.3	80.32	0.5123432	-5.75	0.27
81.4	81.42	0.5123227	-6.15	0.24
82.5	82.52	0.5123325	-5.96	0.24
83.05	83.07	0.5123478	-5.66	0.24
83.6	83.62	0.5123350	-5.91	0.24
84.15	84.17	0.5123145	-6.31	0.24
84.7	84.72	0.5123248	-6.11	0.24
85.25	85.27	0.5123140	-6.32	0.24
85.8	85.82	0.5123858	-4.92	0.24
86.35	86.37	0.5123766	-5.1	0.24
87.45	87.47	0.5123745	-5.14	0.22
89.1	89.12	0.5123801	-5.03	0.12
89.65	89.67	0.5123545	-5.53	0.12
91.85	91.87	0.5123484	-5.65	0.12
93.5	93.52	0.5123432	-5.75	0.12
94.6	94.62	0.5123422	-5.77	0.27
95.7	95.72	0.5123499	-5.62	0.18
96.25	96.27	0.5123407	-5.8	0.18
97.35	97.37	0.5122997	-6.6	0.27
98.55	98.57	0.5122766	-7.05	0.27
99.1	99.12	0.5122843	-6.9	0.27
100.2	100.22	0.5122843	-6.9	0
100.75	100.77	0.5122617	-7.34	0.27
101.3	101.32	0.5123079	-6.44	0.27
101.85	101.87	0.5122592	-7.39	0.27
102.4	102.42	0.5122863	-6.86	0.27
102.95	102.97	0.5122920	-6.75	0.27
103.5	103.52	0.5123073	-6.45	0.27
104.05	104.07	0.5122781	-7.02	0.27
104.6	104.62	0.5123935	-4.77	0.27
105.15	105.17	0.5122648	-7.28	0.27

105.7	105.72	0.5122433	-7.7	0.27
106.25	106.27	0.5122592	-7.39	0.27
106.8	106.82	0.5122776	-7.03	0.27
107.35	107.37	0.5122663	-7.25	0.27
107.9	107.92	0.5122494	-7.58	0.27
109	109.02	0.5122253	-8.05	0.27
109.55	109.57	0.5122463	-7.64	0.27
110.1	110.12	0.5122689	-7.2	0.27
110.65	110.67	0.5121402	-9.71	0.27
111.75	111.77	0.5122530	-7.51	0.19
113.4	113.42	0.5123099	-6.4	0.19
113.95	113.97	0.5123320	-5.97	0.19
114.5	114.52	0.5123073	-6.45	0.19
115.05	115.07	0.5123494	-5.63	0.19
115.6	115.62	0.5122976	-6.64	0.19
116.15	116.17	0.5123002	-6.59	0.19
117.8	117.82	0.5123099	-6.4	0.19
118.35	118.37	0.5123581	-5.46	0.19
120	120.02	0.5122940	-6.71	0.19
120.55	120.57	0.5122925	-6.74	0.19
121.1	121.12	0.5122956	-6.68	0.19
121.65	121.67	0.5123007	-6.58	0.19
123.3	123.32	0.5122822	-6.94	0.19
124.95	124.97	0.5122930	-6.73	0.19
128.25	128.27	0.5124155	-4.34	0.12
128.8	128.82	0.5123971	-4.7	0.27
129.35	129.37	0.5123760	-5.11	0.27
129.9	129.92	0.5123489	-5.64	0.27
130.45	130.47	0.5123463	-5.69	0.27
131	131.02	0.5123499	-5.62	0.27
131.93	131.95	0.5123678	-5.27	0.27
132.46	132.48	0.5123581	-5.46	0.27
133.98	134	0.5123894	-4.85	0.27
139.48	139.5	0.5123576	-5.47	0.27
145.04	145.06	0.5123735	-5.16	0.27
150.48	150.5	0.5124227	-4.2	0.27
155.98	156	0.5124340	-3.98	0.27
161.48	161.5	0.5123673	-5.28	0.27
166.98	167	0.5123791	-5.05	0.27
172.48	172.5	0.5124037	-4.57	0.27
177.98	178	0.5124263	-4.13	0.27

183.48	183.5	0.5123791	-5.05	0.27
205.48	205.5	0.5124212	-4.23	0.27
210.98	211	0.5123868	-4.9	0.27
221.98	222	0.5123725	-5.18	0.27
227.48	227.5	0.5123889	-4.86	0.27
249.48	249.5	0.5123632	-5.36	0.27
282.88	282.9	0.5124181	-4.29	0.27
328	328.02	0.5124201	-4.25	0.27
335.6	335.62	0.5123971	-4.7	0.27
339.4	339.42	0.5122238	-8.08	0.27
354.6	354.62	0.5124063	-4.52	0.27
366	366.02	0.5124760	-3.16	0.27
369.8	369.82	0.5124499	-3.67	0.27
377.4	377.42	0.5123658	-5.31	0.27

Table 5.2 Lead (Pb) isotope record of detrital sediments from IODP 379, site U1532

Average depth CSF-A (m)	$^{208}Pb/^{204}Pb$	2σ	$^{208}Pb/^{207}Pb$	2σ
0.03	38.773	0.0020	2.4753	0.000034
0.09	38.805	0.0015	2.4774	0.000020
0.25	38.836	0.0017	2.4787	0.000028
0.47	38.806	0.0013	2.4777	0.000024
1.72	38.835	0.0018	2.4790	0.000024
2.91	38.836	0.0015	2.4789	0.000037
3.51	38.820	0.0016	2.4780	0.000022
4.11	38.817	0.0016	2.4781	0.000023
4.71	38.860	0.0016	2.4796	0.000028
5.91	38.826	0.0011	2.4790	0.000026
6.51	38.844	0.0018	2.4790	0.000039
7.71	38.819	0.0017	2.4780	0.000030
8.91	38.841	0.0015	2.4788	0.000031
10.71	38.814	0.0015	2.4778	0.000031
11.93	38.831	0.0016	2.4781	0.000029
12.51	38.820	0.0018	2.4780	0.000028
12.61	38.816	0.0014	2.4780	0.000020
12.77	38.827	0.0014	2.4785	0.000036
12.85	38.826	0.0014	2.4783	0.000037
13.33	38.859	0.0013	2.4800	0.000028
13.57	38.831	0.0017	2.4790	0.000027
13.73	38.815	0.0016	2.4785	0.000030
44.56	38.823	0.0017	2.4783	0.000035
46.76	38.822	0.0016	2.4784	0.000022
47.86	38.857	0.0014	2.4800	0.000028
49.51	38.854	0.0017	2.4805	0.000031
50.06	38.861	0.0016	2.4803	0.000026

51.71	38.878	0.0020	2.4807	0.000026
54.46	38.858	0.0014	2.4802	0.000037
56.66	38.874	0.0014	2.4808	0.000030
57.76	38.836	0.0020	2.4792	0.000033
58.86	38.885	0.0015	2.4814	0.000028
59.41	38.864	0.0017	2.4803	0.000025
63.81	38.878	0.0018	2.4808	0.000021
65.46	38.892	0.0026	2.4817	0.000033
68.21	38.877	0.0014	2.4809	0.000027
69.31		0.0019	2.4728	0.000026
70.96	38.898	0.0017	2.4815	0.000029
72.61	38.907	0.0017	2.4828	0.000027
73.16	38.873	0.0014	2.4803	0.000031
74.26	38.922	0.0017	2.4834	0.000024
75.36	38.912	0.0010	2.4828	0.000022
75.91	38.901	0.0013	2.4824	0.000022
76.46	38.888	0.0013	2.4813	0.000031
77.01	38.933	0.0020	2.4837	0.000026
77.56	38.893	0.0018	2.4815	0.000025
78.11	38.886	0.0016	2.4810	0.000030
78.66	38.899	0.0019	2.4824	0.000022
79.76	38.907	0.0018	2.4826	0.000023
81.41	38.915	0.0014	2.4828	0.000025
83.06	38.902	0.0016	2.4823	0.000029
85.26	38.864	0.0018	2.4802	0.000026
85.81	38.886	0.0015	2.4819	0.000027
89.11	38.897	0.0014	2.4819	0.000027
89.66	38.880	0.0018	2.4810	0.000031
95.71	38.909	0.0018	2.4832	0.000026
100.76	38.925	0.0018	2.4835	0.000025
101.31	38.829	0.0016	2.4800	0.000036
104.06	38.889	0.0012	2.4820	0.000027
104.61	38.858	0.0019	2.4804	0.000027
105.71	38.867	0.0014	2.4811	0.000026
106.81	38.877	0.0016	2.4816	0.000026
109.01	38.927	0.0018	2.4841	0.000025
110.66	38.909	0.0021	2.4829	0.000039
111.76	38.909	0.0017	2.4827	0.000028
113.96	38.855	0.0014	2.4805	0.000023
116.16	38.875	0.0017	2.4814	0.000029
118.36	38.884	0.0014	2.4818	0.000039
121.66	38.899	0.0013	2.4825	0.000027
124.96	38.782	0.0020	2.4764	0.000036
128.26	38.837	0.0014	2.4797	0.000020

5.3 Discussion

The prominent shift observed in the radiogenic isotope profiles (Figure 5.1a, b, c) could result from (i) mineralogical and grain size sorting, (ii) sediment dispersal and transport associated with ocean currents and/or (iii) changes in sediment provenance and erosion regime associated with ice-sheet dynamics. Previous studies have investigated the potential role of grain-size effects based on the detrital ε_{Nd} measurements in the bulk and fine fraction (<63 μm) of samples collected from the Pacific margin of West Antarctica (Wang et al., 2022) and detrital ε_{Nd} measurements in the sediment core samples from the site U1361A (Wilson et al., 2018) and proximal core sites PS58/254 and PC493 (Pereira, 2018). These results did not show any significant difference between bulk and fine fractions thus ruling out the potential effects of mineralogical or grain size sorting on the isotope compositions.

Sediment transport by coastal currents could shift the sediment provenance from the west Antarctic Peninsula and the Ross Sea sector. At the extreme southern periphery of the Southern Ocean, a slender westward-flowing circulation feature, denoted as the Antarctic Slope Current (ASC), forms at the juncture of the Antarctic continental slope and the continental shelf (Thompson et al., 2018). The strength of the ASC could change the sediment transport from the west Antarctic Peninsula. However, we argue against such changes in the sediment transports by the ASC. Recent study demonstrates that the westerly winds in the southern hemisphere have shifted poleward in the recent decades under continued anthropogenic forcing (Abell et al., 2021). The observed warming is associated with a diminished Antarctic Slope Front and attenuated coastal currents. Drawing a parallel to a similar scenario during the warm Pliocene, westerlies underwent a poleward shift and consequently, diminished the role of coastal currents in transporting sediments to the core site. On the contrary, we expect significant changes in the structure, position and strength in ASC during the Pleistocene glacial-interglacial periods and thereby associated changes in the sediment transport. However, we observed invariant sediment sources during the entire Pleistocene G-I cycles. Further, sortable silt mean grain size (10 – 63 μm) measured in U1532 shows no co-variation with detrital Nd and Pb isotope records (Figure 5.2), which indicates that sediment transport associated with the ocean bottom currents did not play significant role in driving the radiogenic Nd and Pb isotope variations. These lines of

evidences indicate that ocean currents play less vital role compared to downslope transport of the sediments from hinterland erosion in driving the radiogenic isotope variations.

5.3.1 Sediment sources and their characteristics isotope signatures

Based on the above discussion, the prominent shift in the radiogenic isotope profiles can only be explained by the changes in the hinterland continental erosion with distinct isotope signatures. West Antarctic geology in the vicinity to the core site encompasses lithologies of diverse range and ages.

Pine Island Glacier (PIG) and Thwaites Glacier (TG) are two major ice streams responsible for draining around 32% of the WAIS into Pine Island Bay (PIB) within the southeastern Amundsen Sea Embayment (Figure 2.6b). These glaciers, collectively termed as the "weak underbelly" of the WAIS (Simões Pereira et al., 2020), represent the most vulnerable section prone to rapid collapse. To enable effective geochemical tracing of these crucial glaciers in the Amundsen Sea, we have employed radiogenic isotopes of Nd (ε_{Nd}) and Pb ($^{208}Pb/^{204}Pb$ and $^{208}Pb/^{207}Pb$ ratios) data of the surface sediments and hinterland lithologies from the literature (Carlson et al., 2021; Simões Pereira et al., 2020). By compiling the available ε_{Nd} data, a distinct demarcation becomes apparent in the detritus signatures delivered by the PIG and TG, notably near the ice-shelf of both the ice-stream systems and across various grain sizes and proxies explored. Detritus transported by PIG is distinguished by its lower ε_{Nd} values (~ −9), while TG exhibits higher ε_{Nd} values (~−4) (Simões Pereira et al., 2020). However, within the PIG, we observe significant variability; it shows a progressive trend towards radiogenic Nd moving westward (eastern PIB: ε_{Nd} = −8.3 to −6.7; central PIB: ε_{Nd} = −6.0 to −5.9; western PIB: ε_{Nd} = −5.1 to −2.3) (Robinson et al., 2021). The distinctive provenance of detritus from PIG and TG is confidently identified due to the analysis of sediment samples recovered in close proximity to the grounding line, including sub-ice shelf areas. Based on Nd and Pb isotope data, Carlson et al. (2021), have categorized five distinct geochemical provinces: the Ross Sea (RS), Amundsen West (AW), Amundsen East (AE), Bellingshausen Sea (BS), and Antarctic Peninsula (AP) (Figure 5.2e, f). The endmember values of these geochemical provinces are provided Table 5.3. We observe some overlap in Nd isotope compositions between the AP and AW and western PIG and TG (Figure 5.2a, b), however, they can be distinguished with Pb isotope constrain (Figure 5.2c, d). The endmembers value of the Bellingshausen Sea (BS) and Amundsen East (AE) exhibit similar ε_{Nd} values but AE shows higher Pb isotope

ratios. In contrast, the Antarctic Peninsula (AP) and Amundsen West (AW) show the lowest Pb isotope ratios and the highest ε_{Nd} values. Among sources, the Ross Sea sediments are clearly distinct with the lowest values of ε_{Nd} and the highest values of $^{208}/^{207}$Pb (Figure 5.2). Employing both Nd and Pb isotopes, we aim to identify potential source regions for IODP Site U1532.

Table 5.3: The endmember values of the geochemical provinces.

Region	**^{206}Pb/^{204}Pb**	**^{207}Pb/^{204}Pb**	**^{208}Pb/^{204}Pb**	**^{208}Pb/^{207}Pb**	**ε_{Nd}**
AP	18.857±0.126	15.649±0.013	38.726±0.108	2.475±0.005	-1.08±2.5
BS	18.759±0.001	15.632±0.001	38.688±0.002	2.475±0.005	-5.82
AE	18.887±0.022	15.651±0.002	38.787±0.020	2.478±0.001	-4.42±1.5
AW	18.920±0.049	15.656±0.003	38.786±0.077	2.477±0.005	-0.10±1.3
RS	18.932±0.050	15.672±0.005	39.045±0.116	2.491±0.008	-11.43±0.4

AP-Antarctic Peninsula, BS-Bellingshausen Sea, AE, AW -Amundsen Sea East and West, RS-Ross Sea. These data is taken from the Carlson et al. (2021) and Pereira et al. (2020).

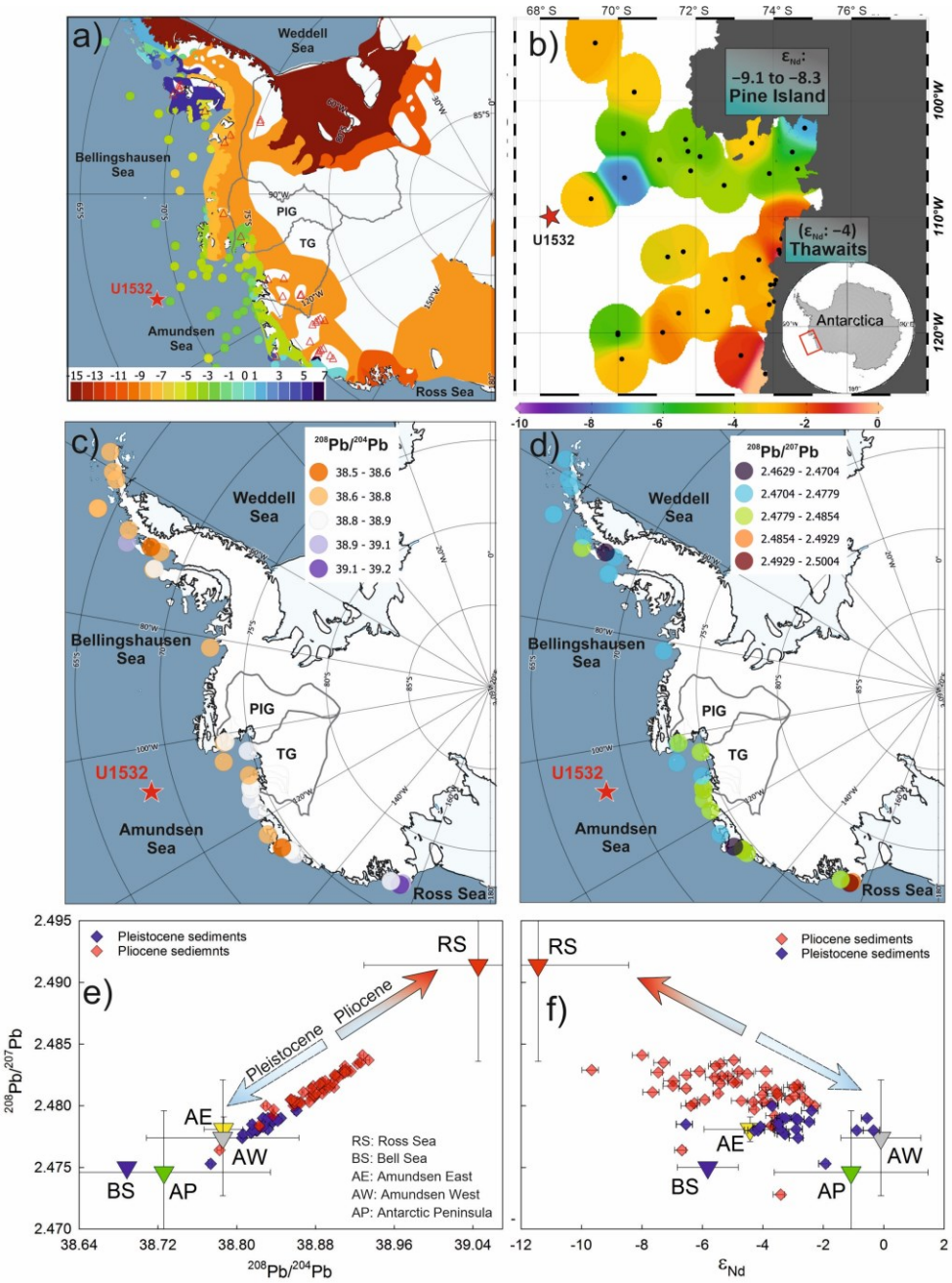

Figure 5.2: Sediment provenances and their Nd and Pb isotope compositions. (a) Detrital ε_{Nd} signature of surface sediments (Robinson et al., 2021) in proximal margin of west Antarctica and hinterland lithology. Star represents core site U1532. (b) Close insight of surface ε_{Nd} distribution in the Amundsen Sea Embayment (Robinson et al., 2021). (c, d) Pb isotope distributions in surface sediments along the coastal regions of the west Antarctica and Antarctic Peninsula are shown in these panels. The Pb isotope data is taken from Carlson et al. (2021). To trace sediment provenance using detrital Nd and Pb isotope records during the late Pliocene and late Pleistocene, our Nd and Pb isotope data are plotted in the cross plot between detrital (e) $^{208}Pb/^{204}Pb$ and $^{208}Pb/^{207}Pb$ ratios and (e) ε_{Nd} and $^{208}Pb/^{207}Pb$ ratios in the present core U1532. The Pliocene and Pleistocene core records of Pb and Nd isotopes plotted in red and blue colours respectively. Filled coloured inverted triangles

indicate major sources of sediments such as Ross Sea, Bell Sea, Amundsen Sea West and East and Antarctic Peninsula. The trends in the distributions in the mixing plots show higher contributions from the Ross Sea during the Pliocene whereas higher contributions from the other sources.

The PIG and TG are the two major ice streams draining in the Amundsen Sea Embayment (ASE) and further, supply glaciogenic detritus to the core sites (Figure 2.6b). Radiogenic isotope fingerprints of fine grained detritus can provide knowledge about the provenance signatures of glaciogenic detritus sourced from the major ice streams. A previous study conducted in the ASE suggests that the glacially eroded detritus transported offshore by PIG is characterised by lower ε_{Nd} value (~-9) and distinct from the sediments supplied by the TG (~-4, Figure 5.2) (Pereira et al., 2020). Therefore, the shift in the ε_{Nd} and Pb record (Figure 5.1a, b, c; Figure 5.3) during the Pliocene-Pleistocene climate transition may indicates change in the sediment provenance. The glacial detritus to the core site is mainly sourced from the PIG and TG, however, contribution from other adjacent glacial basins during different configuration of the WAIS can not be ruled out (Figure 5.2). Detrital Nd and Pb isotope composition of the surface sediments (Carlson et al., 2021) along the coastal regions of west Antarctica shows five distinct provinces such as East and West Amundsen Sea (AW, AE), Antarctic Peninsula (AP), Bell Sea (BS) and Ross Sea (RS) (Figure 5.2). The Pb and Nd isotope data of the present core U1532 in $^{208Pb}/^{204}Pb$ vs. $^{208}Pb/^{207}Pb$ and ε_{Nd} vs. $^{208}Pb/^{207}Pb$ space shows binary mixing between the Amundsen Sea and the Ross Sea (Figure 5.2c, d) with distinct pattern; the Pliocene sediments tending towards the RS whereas the Pleistocene sediments are clustered around the AW. Higher sedimentation with extremely less radiogenic ε_{Nd} value (~ -9) indicates large scale retreat of the ice sheet from the PIG to the hinterland basin of the RS. The large variations in TOC/TN ratio suggests input of both the terrestrial and the marine-derived matter, with a higher ratio indicating a greater contribution of terrestrial or regenerated organic matter(Meyers, 1994). Higher sedimentation rates during the Pliocene warm period together with higher TOC/TN suggests enhanced erosion from the hinterland continent due to extended warming and supply of more terrestrial sediments from the interior of WAIS region. A seismic study at the present core site U1532 identified buried grounding zone wedges which suggests an extended ice-sheet retreat, or potential collapse, during a prolonged Pliocene warm period from ~4.2–3.2 Ma (Gohl et al., 2021a) further corroborate our conclusion. Massive ice sheet melting resulted in large ice free area in hinterland glacier basins exposed for more erosion and supply of sediments in downstream. Such

configuration of the WAIS is consistent with the numerical model simulation for the Pliocene (DeConto and Pollard, 2016). This situation gradually changed with the expansion of the WAIS when entered in the Pleistocene cold climate. The Pleistocene expansion of the ice sheet restricted sediment supply by almost fivefold compared to the Pliocene as reflected in sedimentation records (Figure 5.1f). The shift in the erosion pattern and reduced erosion fluxes during the transition from the Pliocene warm climate to Pleistocene cold climate suggests expansion of the WAIS over the PIG and Ross Ice Shelf that reduced erosion and thus reduced sediment supply to downstream.

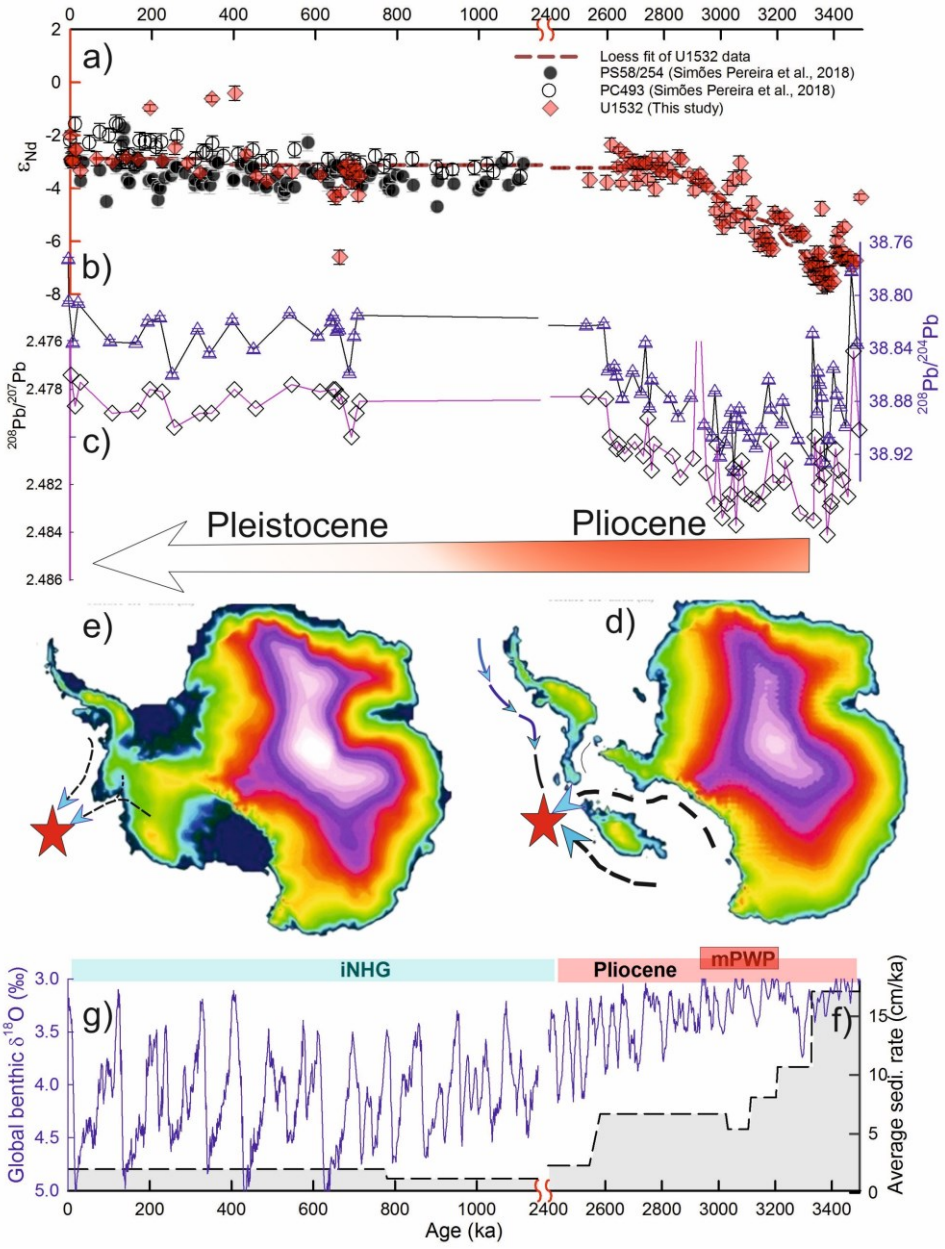

Figure 5.3: Inferring West Antarctic ice-sheet dynamics and extent from past erosion record. (a) Bulk detrital ε_{Nd} record from the core site U1532 (red colour diamond) is

compiled with the previously published records of fine fractions (<63 μm) of the detrital ε_{Nd} records (Pereira, 2018) from the two core sites PC493 and PS58/254 in the close proximity. (b, c) Pb isotope records ($^{208}Pb/^{204}Pb$ and $^{208}Pb/^{207}Pb$ ratios) of the present core site U1532. (d, e) Model derived (Pollard and DeConto, 2009) ice sheet extent of the Antarctic ice sheet during the Pliocene and Pleistocene. Arrow along the coast indicates Antarctic coastal current. Red star represent core site U1532. The schematic with model based ice-sheet geometry (Pollard and DeConto, 2009) depict possible sediment sources to the core sites during the Pliocene-Pleistocene climate transition. (f) Records of sedimentation rate at the present core site U1532. (g) Global benthic $\delta^{18}O$ curve (LR04) (Lisiecki and Raymo, 2005b)

5.3.2 Ice sheet dynamics in controlling erosion pattern during the Pliocene-Pleistocene interval

The major sources of glacial detritus supplied to the core sites are PIG, TG and adjacent basins (Figure 5.2). It is noteworthy that most of the Pliocene sediments tend towards the RS whereas the Pleistocene sediments are clustered around the AW. The close insight in the hinterland lithologies feeding the majority sediments to AW is primarily from the PIG and TG. The ε_{Nd} value of the PIG and TW are quite distinct and shows that modern sediments in the AW are primarily dominated by TG. The ε_{Nd} values of the RS sediments and PIG are quite close; therefore, we suggest that the Pliocene sediments could be contributed by the PIG and RS (Figure 5.3e). Higher sedimentation with extremely less radiogenic ε_{Nd} value (~ -9) indicates large scale retreat of the ice sheet from the eastern PIG to the hinterland basin of the RS. Such configuration of the WAIS is consistent with the numerical model simulation for the Pliocene (DeConto and Pollard, 2016).

The dramatic shift in the erosion regime and reduced erosion fluxes during the transition from the Pliocene warm climate to Pleistocene cold climate suggests a higher extent of the WAIS which restricted erosion processes over the hinterland glacier basins. The PIG basin area is mostly interior compared to the TG with reference to the modern day ice sheet margin. Therefore, due to the increase in the ice sheet extent, the erosion processes and the sediment delivery to the downstream Amundsen Sea were restricted due to the extensive ice cover. Sediments deposited at three sites (U1532, PC493 and PS58/254) show similar Nd isotopic compositions indicating uniform sediment provenance in the hinterland or sediment provenance did not undergo significant changes during the entire Pleistocene. However, distinct Nd isotope signatures of the Pine Island (ε_{Nd} ~-9) and Thwaites (ε_{Nd} ~-4) basins clearly indicates stable sediment provenance (Figure 5.3).

Thus, sediments deposited at three sites (U1532, PC493 and PS58/254) show similar ε_{Nd} values despite distinct isotope signatures of the sources clearly indicate stable erosion (Figure 5.3a, b, c), . Therefore, our observation of the Pleistocene stable erosion based on three records (Figure 5.1a, b, c) does not support large scale retreat or collapse of the WAIS and contribution to sea level change during the Pleistocene. Our finding is also consistent with the previous reports based on geomorphology and cosmogenic nuclides study from the southern Ellsworth Mountains (Hein et al., 2016) and glacio-marine sediment records from the West Antarctic continental margin in the Amundsen Sea (Hillenbrand et al., 2002).

In conclusion, we support the hypothesis of WAIS stability during the Late Pleistocene, characterised by lack of ice retreat towards the interior of the continent. With regard to glacial-interglacial ice sheet dynamics between the WAIS and EAIS during the Pleistocene, broader consensus based on modelling studies and geological records is that EAIS underwent significant changes with several collapse events during the super interglacials. The ice-sheet model prediction for the Pliocene is consistent with our proposition, however, contradicts the predictions for the Pleistocene interglacials (DeConto and Pollard, 2016).

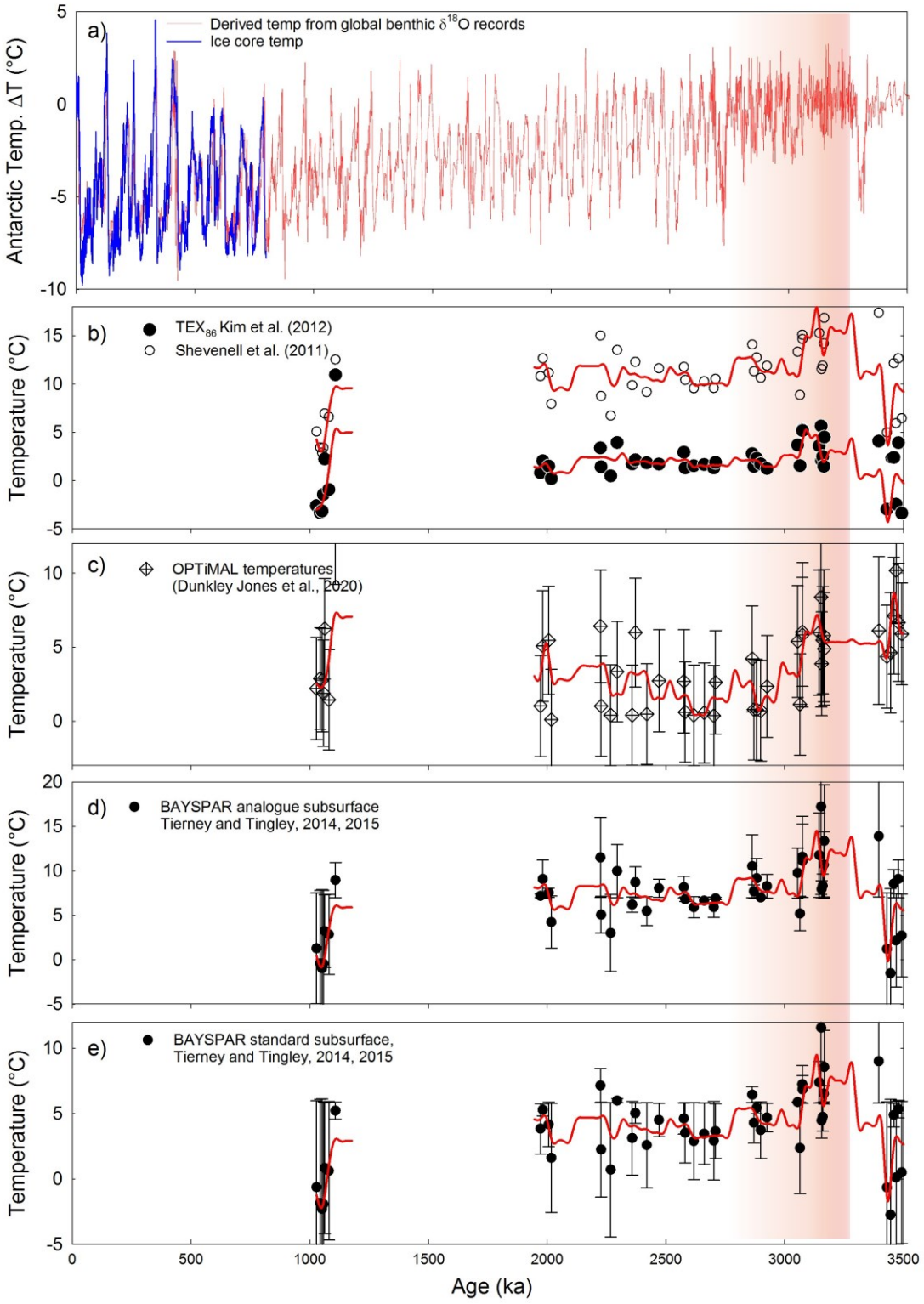

Figure 5.4: Multi-proxy derived temperature records to assess sensitivity of WAIS dynamics. (a) Antarctic ice core derived temperature anomaly record (blue curve) (Jouzel et al., 2007). Reconstructed temperature based the on the relationship between deep-sea temperature (TW) and Antarctic temperature ($\Delta T_w \approx 0.25\ \Delta T_{EDC}$) (Rohling et al., 2021). (b) Shevenell et al. (2011) (standard error of ±2.5°C) and TEX_{86} Kim et al. (2012) (error of ±2.8°C). d) BAYSPAR Standard SubT (Tierney and Tingley, 2014, 2015) and e) BAYSPAR

Analogue SubT (Tierney and Tingley, 2014, 2015) (errors displayed are ^{90}th percentile confidence intervals). The red colour shade indicates temperature drop during the Pliocene-Pleistocene transition which are consistent in all the records.

5.3.3 Antarctic Temperature records of the late Pliocene to Pleistocene

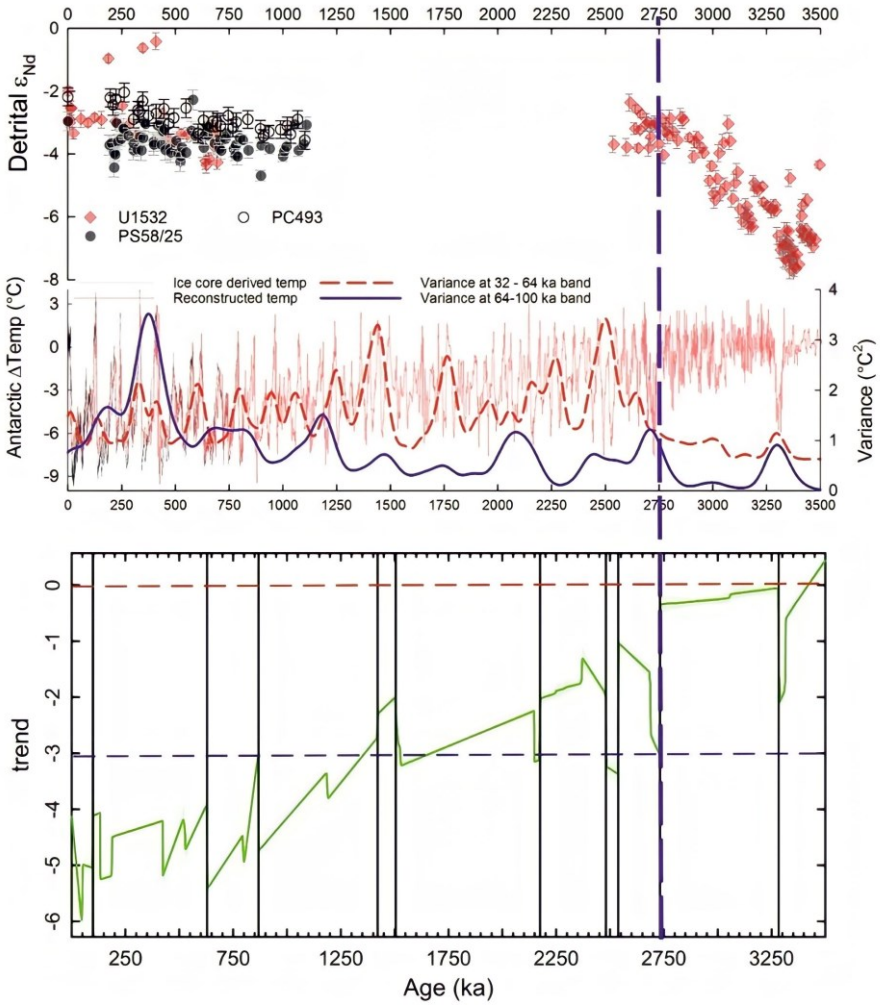

Figure 5.5: Determining sensitivity of the west Antarctic ice sheet dynamics to temperature change. (a) Detrital ε_{Nd} record is compared to the Antarctic temperature. The variance in the temperature record shows abrupt changes at ~ 40 bands. (b) Abrupt changes in the temperature time series were detected using a MATLAB based Bayesian model averaging time-series decomposition algorithm (BEAST) (Zhao et al., 2019). This algorithm offers robust method to detect abrupt change points and nonlinear trend in the Antarctic temperature record. The vertical dashed blue line indicates an abrupt change at 2.75 Ma which coincides with the period when the erosion became stable, sharp increase in temperature variance at ~40 and drop in temperature by ~3°C with respect to the pre-industrial temperature.

To determine the sensitivity of the WAIS to temperature change and the tipping points that underpin the growth of ice sheet during the epoch of Pliocene-Pleistocene climate transition, a high-resolution temperature record is imperative. In a recent study, deep-sea temperature (Tw) was reconstructed based on the deep-sea foraminiferal oxygen isotope ($\delta^{18}O$) records (Rohling et al., 2021) and subsequently validated through a rigorous comparison with the independently ascertained variations in Antarctic temperature at the European Project for Ice Coring in Antarctica (EPICA) Dome C (EDC) site (Jouzel et al., 2007) (Figure 5.4a). The comparison shows a remarkable concurrence between the reconstructed Tw and T_{EDC}, with a scaling relationship approximated as $\Delta Tw \approx 0.25\ \Delta T_{EDC}$. Thus, we have employed this relationship beyond the limit of the ice core temperature record (~800 ka), to reconstruct Antarctic temperatures up to the late Pliocene (~3.5 Ma). Further, near-field records of upper-ocean temperatures from the Ross Sea (Duncan et al., 2022) using glycerol dialkyl glycerol tetraethers (GDGTs) and OPTiMAL machine-learning-based temperature calibration shows an excellent consistency among all these temperature records (Figure 5.4b, c, d, e). All the temperature records elucidate a key pattern of cooling of 1 - 3°C amidst the Pliocene-Pleistocene transition (Duncan et al., 2022) which coincides with the expansion of marine ice sheets. This phenomenon aligned with the prevailing cold orbital conditions and reduced atmospheric carbon dioxide levels (~400 – 280 ppm) (Figure 5.6, Figure 5.7).

To detect changes in the temperature record and its concomitant changes in the ice sheet dynamics and the configuration, a MATLAB based Bayesian model decomposition algorithm (BEAST) was performed on reconstructed high resolution temperature record Tw (Figure 5.5). This algorithm offers robust method to detect abrupt change points and nonlinear trend in the Antarctic temperature record. This analysis has detected abrupt cooling at 2.75 Ma which coincides with the sharp increase in temperature variance at ~40 ka paced by orbital changes (obliquity) and drop in temperature by ~3°C with respect to the pre-industrial temperature.

5.3.4 Role of forcing factors in modulating Pliocene-Pleistocene WAIS dynamics

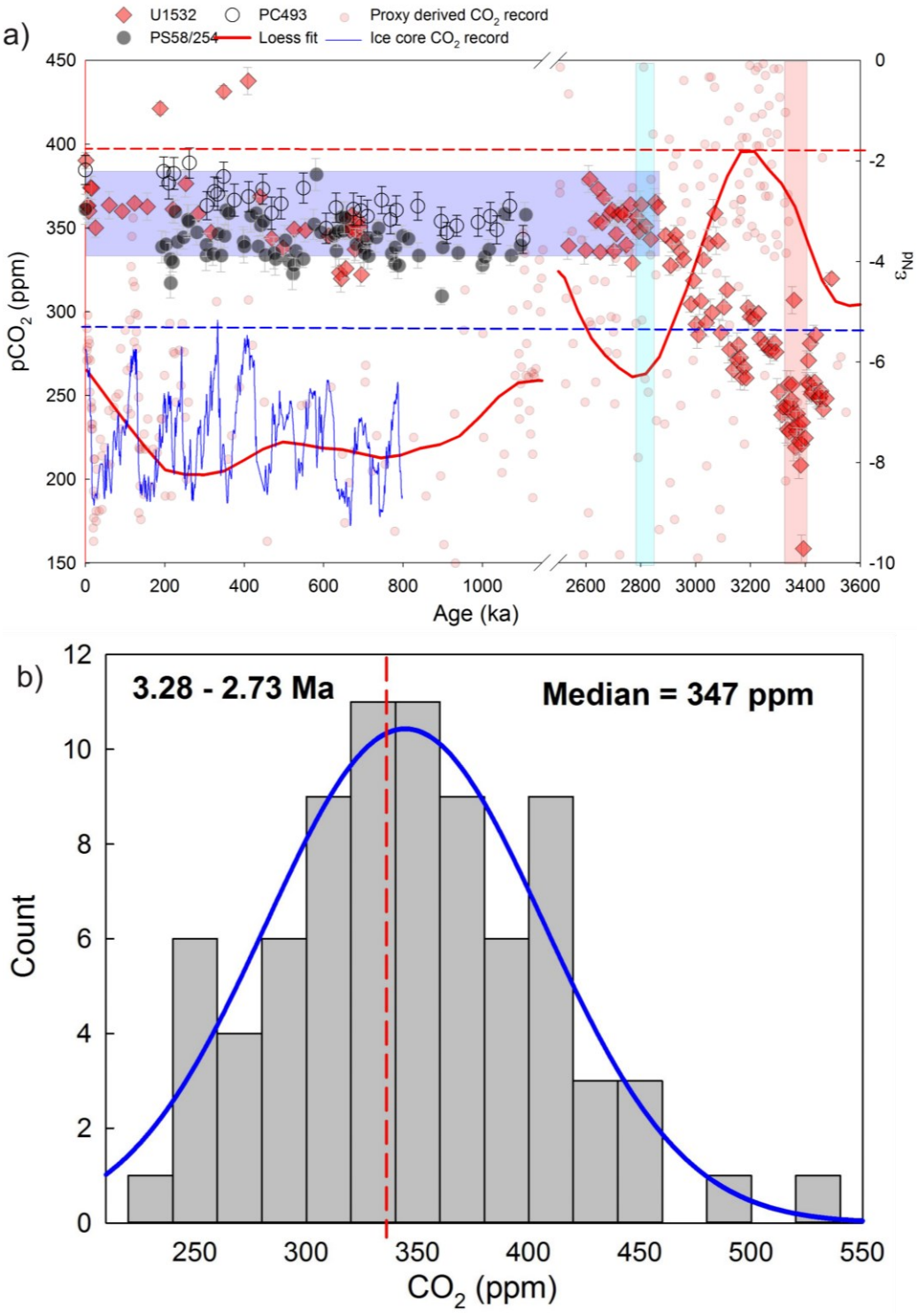

Figure 5.6: Role of atmospheric CO2 driven radiative forcing. (a) Comparison of detrital ε_{Nd} record of U1532 with atmospheric CO_2 record. Red filled circle represent boron isotope of the planktic foraminifera derived CO_2 record (Foster et al., 2017) whereas the blue colour curve represent Antarctic ice core derived CO_2 record of the late Pleistocene (Jouzel et al.,

2007). Dashed blue line indicate pre-industrial CO2 level (~280 ppm) whereas the red coloured dashed horizontal line indicates the maximum CO2 level during the Pliocene (~400 ppm) when the detrital ε_{Nd} shows extremely less radiogenic values. (b) Median value of atmospheric CO_2 level during the Pliocene-Pleistocene climate transition (3.28 – 2.73).

The change point detection analysis in the temperature record revealed persistent cooling trend in west Antarctic temperature (1 – 3° C) between 3.25 Ma to 2.75 Ma (Figure 5.7) due to the onset of glacial-interglacial cycles paced by the orbital forcing (at ~40 ka obliquity band) and drawdown of atmospheric CO_2 from ~400 to 280 ppm (Foster et al., 2017). This resulted in massive change in the WAIS dimension from smaller extent during the Pliocene to a more extensive and stable ice sheet during the Pleistocene despite large variations in temperature (+4 to -8 °C) and atmospheric CO_2 during the glacial-interglacial cycles (~180 to 280 ppm). This observation is consistent with the previous reports from the Ross Ice Shelf based on the ANDRILL sediment core records recovered from beneath the Ross Sea Ice Shelf, that 40-ka cyclic variations in ice-sheet extent is linked to the cycles in insolation influenced by shift in the Earth's obliquity during the Pliocene (Naish et al., 2009). The Pliocene records from the proximity of the WAIS margin in the Amundsen Sea and the Ross Sea clearly provide direct evidence for orbitally induced oscillations in the WAIS.

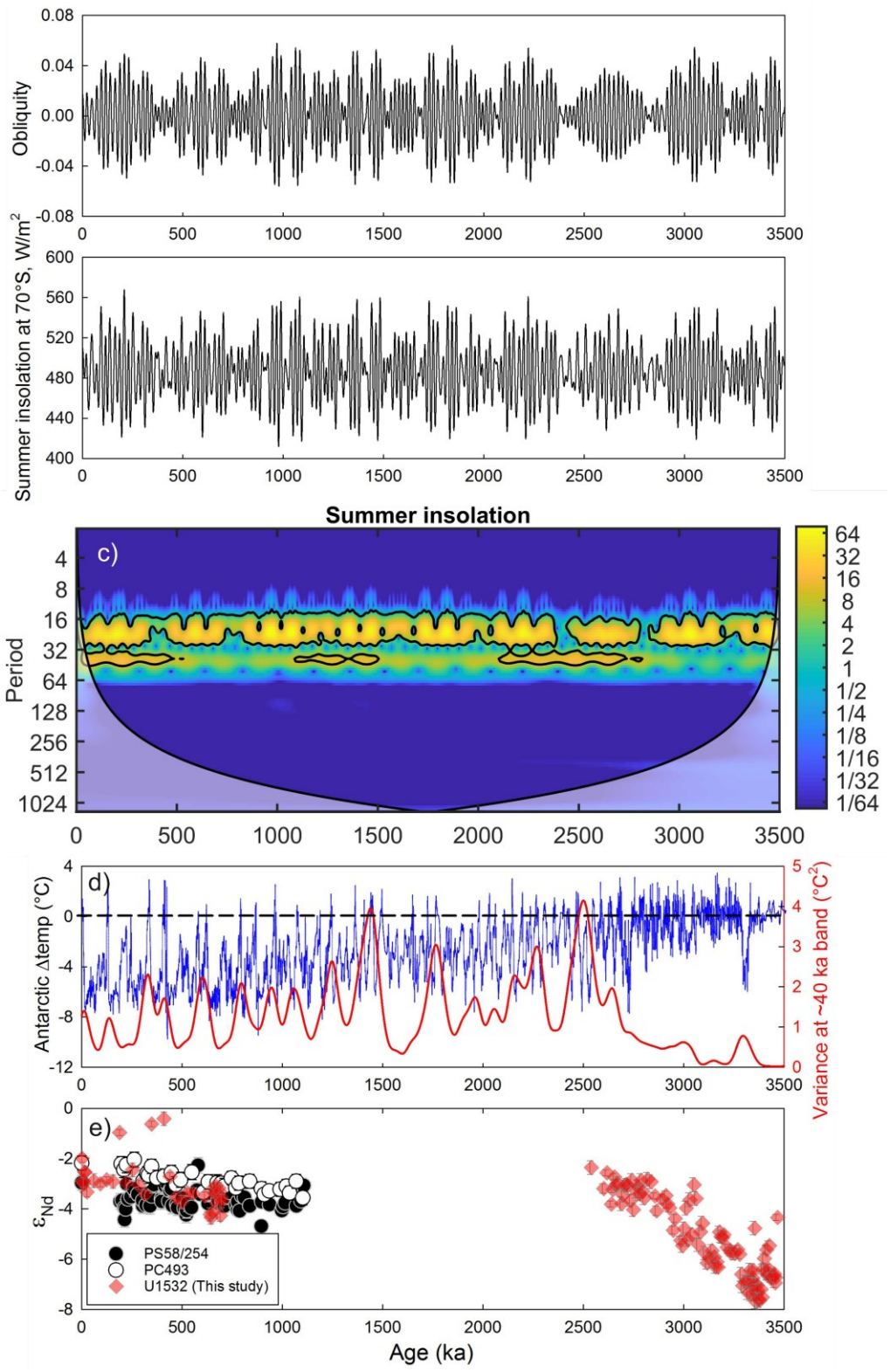

Figure 5.7: Role of orbital forcing in modulating Antarctic temperature. (a) Obliquity (Laskar et al., 2004), (b) summer insolation at 70°S, (c) wavelet analysis of summer insolation which shows how the frequency of the summer insolation was evolved, (d) Antarctic surface temperature with respect to pre-industrial era and (e) detrital ε_{Nd} records.

The tipping points for the east Antarctic Ice sheet collapse was determined based on the comparison of the extreme changes in the erosion pattern and temperature records (Wilson et al., 2018), however, our study does not show any significant changes even during late Pleistocene super interglacial (e.g. last interglacial period) including MIS 5, 9 and 11 when temperature was 2 -3°C higher than pre-industrial and ~280 ppm of atmospheric CO_2 for the duration of 2-6 ka. This suggests that these extreme super interglacial conditions were not sufficient for the collapse of the WAIS which is on contrary to the previous reports (Scherer et al., 1998) based on the sedimentological records from the Ross Sea Embayment. Further, our observation of stable WAIS in Pleistocene is in contrast to the reports from the East Antarctic ice sheet (Wilson et al., 2018) which suggests ice sheet thinning and retreat proximal to the Wilkes Subglacial Basin during the warm late Pleistocene intervals. Our finding has come as a surprise in the context of present-day mass loss of west Antarctica and mass gain of the east Antarctic ice sheet. Therefore, we suggest that present mass loss of the WAIS might not be part of the long-term climate cycle, it might rather be a recent phenomenon resulting from the concomitant changes in the atmospheric circulation and changes in the incursion strength and pattern of the circumpolar deep water circulation.

Our isotopic data places new constraints on forcing for the dynamics from the large scale retreat to expanded WAIS during the late Pliocene greenhouse conditions coincide with persistent cooling of 1-3 °C in the west Antarctic temperature resulting from the onset of glacial and interglacial cycles paced orbital forcing and the potential drawdown of atmospheric CO_2. On the contrary, we observe stable ice sheet in the entire Pleistocene despite large glacial-interglacial variations in temperature and atmospheric CO_2. Our observation supports the model results for the reduced WAIS during warm Pliocene, while the existence of stable WAIS during the Pleistocene (e.g. last Interglacial) contradicts model simulations and questions earlier suggestion of WAIS contribution to the Pleistocene sea level change. In the context of present day rapid mass loss from the west Antarctic ice sheet and mass gain of the east Antarctic ice sheet, our finding has come as a surprise as it has been believed that West Antarctic ice sheet is more vulnerable than the east Antarctic ice sheet. Our findings suggest that the tipping point for the stability of WAIS lies within oceanic and atmospheric conditions of the Pliocene-Pleistocene transition. These findings have significant implications for understanding the future ice sheet behaviour and its contribution to sea level rise in a warming world.

Chapter 6

Synthesis and future perspective

This thesis dwells into the application of the radiogenic Neodymium isotopic composition (ε_{Nd}) in the authigenic fraction of marine sediments to understand the changes in circulation patterns of deep and bottom water masses in two different basins and the processes affecting these records. The residual phase called "detrital fraction" ε_{Nd} record was used to decipher the sediment provenance and to reconstruct past erosion associated with the West Antarctic icesheet dynamics. The primary objectives of the study are to (i) reconstruct deep water circulation in the Arabian Sea using authigenic ε_{Nd} records; (ii) examine the potential of authigenic ε_{Nd} record as proxy for deepwater circulations and to reconstruct past CDW in the Amundsen Sea; (iii) reconstruct past erosion pattern from the Amundsen Sea region and to reconstruct the past West Antarctic Ice sheet (WAIS) dynamics. This study investigates the role of tectonics and climate in controlling the deep water circulation and changes. Further, in this study an attempt has been made to reconstruct the dimension of the WAIS and dynamics during the Pliocene and Pleistocene glacial-interglacial variations; some of the intervals are considered to be the near future climate analogues. This chapter consolidates the key insights derived from the present investigation and outlines prospective research directions that can extend and complement the findings outlined here.

6.1 Reconstruction of late Miocene deep water circulation in the Arabian Sea using authigenic ε_{Nd} record.

This investigation presents a novel authigenic ε_{Nd} record derived from the authigenic fraction of sediments retrieved from the deep northwestern Indian Ocean, covering the temporal span between the Late Miocene (approximately 11 Ma) and the early Pleistocene (~2 Ma). The observed gradual transition in ε_{Nd} values, shifting from radiogenic to less radiogenic values, is attributed to an escalating influence of North Component Water (NCW, a proto-North Atlantic Deep Water, NADW) and a concurrent reduction in the contribution from Pacific Deep Water (PDW) within the circumpolar deep water (CDW) during the period spanning 9 to 6 Ma. The alterations in the proportional input of NCW and PDW to the deep water enveloping the northwestern Indian Ocean are elucidated by the

ongoing closure of the Central American Seaway (CAS) throughout this interval. Subsequent to this progressive seaway closure, it is inferred that stable, modern-like environmental conditions were established after 6 Ma. The change in the geometry of the PDW and NADW component in the CDW resulted due to strengthening AMOC as a result of the constriction of CAS which was also aided by the global late Miocene cooling. This study finding suggests a profound and widespread impact of the late Miocene CAS closure on the evolution of ocean deep water circulation and validates the so called "Panama Closure Hypothesis".

6.2 Assessing the fidelity of authigenic ε_{Nd} records from the Amundsen Sea as a proxy for past CDW

Present study investigates the variability in the authigenic ε_{Nd} records in terms of deep water circulation. However, these authigenic ε_{Nd} records are far radiogenic than the modern CDW values from the Amundsen Sea and thus, analyses the processes affecting these authigenic ε_{Nd} records. This study explains the lithogenic effects on marine authigenic ε_{Nd} archives, directly within the sediment column during the diagenesis process as a process affecting the authigenic records. The authigenic ε_{Nd} record of present study was acquired within the sediment column as a function of the reactivity of the sediment components during the diagenesis. Hence, authigenic ε_{Nd} record represents a reactivity-weighted average ε_{Nd} values of the detrital fraction instead of the bottom water signature. The reactive components of the detrital fragments interact with the water present in the interstitial spaces of the sediments. Thus, the variability in the authigenic records has been attributed to the reactive components of the detrital part and their partial dissolution in the interstitial fluid. This study implies that the changes in the authigenic ε_{Nd} values is reflected as variable contributions of detrital Nd fraction instead of the bottom-deep water Nd. Also, the downcore ε_{Nd} values of the authigenic and detrital fraction shows similar trend towards the radiogenic values since 3.3 Ma onwards. This change in the authigenic ε_{Nd} values, thus, reflects the change in the source of the sediments being deposited at the core site, instead of the bottom water composition. Hence, present study also establishes that the region is not suitable for the reconstructions of past deep water circulation studies using the Neodymium isotope records.

6.3 Detrital ε_{Nd} records from the Amundsen Sea to decipher sediment provenance and to reconstruct past erosion associated WAIS dynamics

Present study provides new sedimentological and geochemical constraints from a sedimentary drill site located in close proximity to modern day rapidly retreating ice margin of the West Antarctic. The detrital ε_{Nd} record reveals a distinct shift in sediment provenance associated with ice sheet dynamics tracing the transition from a highly dynamic and smaller ice sheet during the warm Pliocene to a stable and near-modern extension in the Pleistocene, despite large glacial-interglacial (G-I) variations in mean global temperature (+4 to -10 °C) and atmospheric CO_2 levels (~180 – 280 ppm). The observation of a stable Pleistocene ice sheet is contrary to model results and questions the contribution of the WAIS to Pleistocene sea level change. This massive expansion of ice sheet coincides with a persistent cooling resulted from onset of orbitally paced G-I cycles and atmospheric CO_2 drawdown and thus suggests that the tipping point for the stability of WAIS lies within oceanic-atmospheric conditions during the Pliocene-Pleistocene transition. These findings have significant implications for predicting future ice sheet behaviour and its contribution to sea level rise in a warming world.

6.4 Scope for future research

The findings presented in the investigation of authigenic ε_{Nd} values from the North-west Indian Ocean offers a compelling basis for future research endeavours focused on understanding the intricate dynamics of ocean circulation and tectonic evolution during late Miocene Earth's history. The coherence observed between ε_{Nd} records of the active (North Atlantic) and passive (Indian) basins in the present study will serve as a vital cross-validation tool to evaluate modelling outcomes, especially in the context of model-driven proposals for carbon storage in the deep ocean – a subject of perpetual interest. The high-resolution authigenic ε_{Nd} records from sediment cores retrieved from the deeper depths of Atlantic and Indian Ocean, along the flow path of NADW and CDW, will provide a more comprehensive understanding of the changes in overturning circulations. The intermediate depth authigenic ε_{Nd} records from sites close to CAS in the Pacific Ocean will help us understand the role of CAS closure on the water circulation in the Pacific. Pacific ocean records combined with records from the Atlantic and Indian Ocean will shed the light upon

the physico-chemical condition of the water masses leading to the late Miocene carbonate crash in the different ocean basins.

Neodymium isotopes are considered as a reliable tracer for past water mass circulation. However, present and previous studies have highlighted the complications of authigenic Nd isotope records as a tracer for past ocean circulation, which has been attributed to the reactivity of the detrital component during diagenesis. Hence, it is important to integrate both sediment properties and detrital isotope record with the authigenic ε_{Nd} records to enhance the accuracy of reconstructions. Therefore, a new geochemical tool(s), independent of the productivity and lithogenic influence, is needed to reconstruct the past water mass circulation variabilities in the Southern Ocean as it is the source region for the production of AABW. Further, sea surface temperature and bottom water temperature records from the Amundsen Sea Shelf are essential to understand the retreat in the grounding line of ice sheets, due to the upwelling of the modified CDW during the warmer intervals. A high temporal resolution record for the change in the sediment provenance is required to understand the variability in the WAIS during the peak glacial-interglacial cycles of Pleistocene. Future studies must work towards obtaining long sediment core record from the continental shelf area of the WAIS region, covering the middle Miocene, which will provide us the complete history of ice sheet dynamics from the region. The deduced forcing mechanisms for the melting of the ice sheets from the different regions must be synthesised together and should be incorporated in the numerical modelling studies for the better and precise prediction of the Earth's future under warmer conditions.

References

2014. Technical Summary, in: Intergovernmental Panel on Climate, C. (Ed.), Climate Change 2013 – The Physical Science Basis: Working Group I Contribution to the Fifth Assessment Report of the Intergovernmental Panel on Climate Change. Cambridge University Press, Cambridge, pp. 31-116.

Abadie, C., Lacan, F., Radic, A., Pradoux, C., Poitrasson, F.J.P.o.t.N.A.o.S., 2017. Iron isotopes reveal distinct dissolved iron sources and pathways in the intermediate versus deep Southern Ocean. 114, 858-863.

Abbott, A.N., 2019. A benthic flux from calcareous sediments results in non-conservative neodymium behavior during lateral transport: A study from the Tasman Sea. Geology 47, 363-366.

Abbott, A.N., Haley, B.A., McManus, J., 2015. Bottoms up: Sedimentary control of the deep North Pacific Ocean's εNd signature. Geology 43, 1035-1035.

Abbott, A.N., Haley, B.A., McManus, J.J.E., Letters, P.S., 2016. The impact of sedimentary coatings on the diagenetic Nd flux. 449, 217-227.

Abbott, A.N., Löhr, S.C., Payne, A., Kumar, H., Du, J.J.G.e.C.A., 2022. Widespread lithogenic control of marine authigenic neodymium isotope records? Implications for paleoceanographic reconstructions. 319, 318-336.

Abell, J.T., Winckler, G., Anderson, R.F., Herbert, T.D., 2021. Poleward and weakened westerlies during Pliocene warmth. Nature 589, 70-75.

Abrahamsen, E.P., Meijers, A.J., Polzin, K.L., Naveira Garabato, A.C., King, B.A., Firing, Y.L., Sallée, J.-B., Sheen, K.L., Gordon, A.L., Huber, B.A.J.N.C.C., 2019. Stabilization of dense Antarctic water supply to the Atlantic Ocean overturning circulation. 9, 742-746.

Adkins, J.F.J.P., 2013. The role of deep ocean circulation in setting glacial climates. 28, 539-561.

Adusumilli, S., Fricker, H.A., Medley, B., Padman, L., Siegfried, M.R.J.N.g., 2020. Interannual variations in meltwater input to the Southern Ocean from Antarctic ice shelves. 13, 616-620.

Anagnostou, E., John, E.H., Edgar, K.M., Foster, G.L., Ridgwell, A., Inglis, G.N., Pancost, R.D., Lunt, D.J., Pearson, P.N.J.N., 2016. Changing atmospheric CO2 concentration was the primary driver of early Cenozoic climate. 533, 380-384.

Anderson, D.L., Willebrand, J.J.R.o.P.i.P., 1992. Recent advances in modelling the ocean circulation and its effects on climate. 55, 1.

Anderson, R., Ali, S., Bradtmiller, L., Nielsen, S., Fleisher, M., Anderson, B., Burckle, L.J.s., 2009. Wind-driven upwelling in the Southern Ocean and the deglacial rise in atmospheric CO2. 323, 1443-1448.

Arneborg, L., Wåhlin, A., Björk, G., Liljebladh, B., Orsi, A.J.N.G., 2012. Persistent inflow of warm water onto the central Amundsen shelf. 5, 876-880.

Arsouze, T., Dutay, J.-C., Lacan, F., Jeandel, C.J.B., 2009. Reconstructing the Nd oceanic cycle using a coupled dynamical–biogeochemical model. 6, 2829-2846.

Arsouze, T., Dutay, J.-C., Lacan, F., Jeandel, C.J.C.G., 2007. Modeling the neodymium isotopic composition with a global ocean circulation model. 239, 165-177.

Arsouze, T., Treguier, A.-M., Peronne, S., Dutay, J.-C., Lacan, F., Jeandel, C.J.O.S., 2010. Modeling the Nd isotopic composition in the North Atlantic basin using an eddy-permitting model. 6, 789-797.

Baeyens, W., Monteny, F., Leermakers, M., Bouillon, S.J.A., Chemistry, B., 2003. Evalution of sequential extractions on dry and wet sediments. 376, 890-901.

Bai, Y., Zhao, L., Xiao, J., Lin, S.J.A.O.S., 2022. Contraction and warming of Antarctic Bottom Water in the Amundsen Sea. 41, 68-79.

Barker, P., Burrell, J.J.M.g., 1977. The opening of Drake passage. 25, 15-34.

Basak, C., Fröllje, H., Lamy, F., Gersonde, R., Benz, V., Anderson, R.F., Molina-Kescher, M., Pahnke, K., 2018a. Breakup of last glacial deep stratification in the South Pacific. Science 359, 900.

Basak, C., Fröllje, H., Lamy, F., Gersonde, R., Benz, V., Anderson, R.F., Molina-Kescher, M., Pahnke, K.J.S., 2018b. Breakup of last glacial deep stratification in the South Pacific. 359, 900-904.

Bell, D.B., Jung, S.J.A., Kroon, D., Hodell, D.A., Lourens, L.J., Raymo, M.E., 2015. Atlantic Deep-water Response to the Early Pliocene Shoaling of the Central American Seaway. Scientific reports 5, 12252.

Berggren, W.A., Kent, D.V., Swisher, C.C., Aubry, M.-P., 1995. A revised Cenozoic geochronology and chronostratigraphy.

Bertram, C., Elderfield, H.J.G.e.C.A., 1993. The geochemical balance of the rare earth elements and neodymium isotopes in the oceans. 57, 1957-1986.

Bett, D.T., Holland, P.R., Naveira Garabato, A.C., Jenkins, A., Dutrieux, P., Kimura, S., Fleming, A.J.J.o.G.R.O., 2020. The impact of the Amundsen Sea freshwater balance on ocean melting of the West Antarctic Ice Sheet. 125, e2020JC016305.

Bhattacharya, G., Chaubey, A., Murty, G., Srinivas, K., Sarma, K., Subrahmanyam, V., Krishna, K.J.E., Letters, P.S., 1994. Evidence for seafloor spreading in the Laxmi Basin, northeastern Arabian Sea. 125, 211-220.

Bialik, O.M., Frank, M., Betzler, C., Zammit, R., Waldmann, N.D., 2019. Two-step closure of the Miocene Indian Ocean Gateway to the Mediterranean. Scientific reports 9, 8842.

Billups, K., Channell, J.E.T., Zachos, J., 2002. Late Oligocene to early Miocene geochronology and paleoceanography from the subantarctic South Atlantic. Paleoceanography 17, 4-1-4-11.

Billups, K., Scheiderich, K., 2012. A Synthesis of Late Oligocene through Miocene Deep Sea Temperatures as Inferred from Foraminiferal Mg/Ca Ratios, Carbonate Systems during the Oligocene–Miocene Climatic Transition, pp. 1-16.

Blaser, P., Lippold, J., Gutjahr, M., Frank, N., Link, J.M., Frank, M.J.C.G., 2016. Extracting foraminiferal seawater Nd isotope signatures from bulk deep sea sediment by chemical leaching. 439, 189-204.

Blaser, P., Pöppelmeier, F., Schulz, H., Gutjahr, M., Frank, M., Lippold, J., Heinrich, H., Link, J., Hoffmann, J., Szidat, S.J.G.e.C.A., 2019. The resilience and sensitivity of Northeast Atlantic deep water εNd to overprinting by detrital fluxes over the past 30,000 years. 245, 79-97.

Bolton, C.T., Gray, E., Kuhnt, W., Holbourn, A.E., Lübbers, J., Grant, K., Tachikawa, K., Marino, G., Rohling, E.J., Sarr, A.C., Andersen, N., 2022. Secular and orbital-scale variability of equatorial Indian Ocean summer monsoon winds during the late Miocene. Clim. Past 18, 713-738.

Bond, G., Showers, W., Cheseby, M., Lotti, R., Almasi, P., DeMenocal, P., Priore, P., Cullen, H., Hajdas, I., Bonani, G.J.s., 1997. A pervasive millennial-scale cycle in North Atlantic Holocene and glacial climates. 278, 1257-1266.

Bond, G.C., Lotti, R.J.s., 1995. Iceberg discharges into the North Atlantic on millennial time scales during the last glaciation. 267, 1005-1010.

Böning, C.W., Dispert, A., Visbeck, M., Rintoul, S., Schwarzkopf, F.U.J.N.G., 2008. The response of the Antarctic Circumpolar Current to recent climate change. 1, 864-869.

Borrelli, C., Cramer, B.S., Katz, M.E.J.P., 2014. Bipolar Atlantic deepwater circulation in the middle-late Eocene: Effects of Southern Ocean gateway openings. 29, 308-327.

Brierley, C.M., Fedorov, A.V.J.E., Letters, P.S., 2016. Comparing the impacts of Miocene–Pliocene changes in inter-ocean gateways on climate: Central American Seaway, Bering Strait, and Indonesia. 444, 116-130.

Broecker, W.S., Peng, T.-H., 1982. Tracers in the Sea. Lamont-Doherty Geological Observatory, Columbia University Palisades, New York.

Broecker, W.S.J.P., 1998. Paleocean circulation during the last deglaciation: a bipolar seesaw? 13, 119-121.

Butzin, M., Lohmann, G., Bickert, T., 2011. Miocene ocean circulation inferred from marine carbon cycle modeling combined with benthic isotope records. Paleoceanography 26.

Caesar, L., Rahmstorf, S., Robinson, A., Feulner, G., Saba, V.J.N., 2018. Observed fingerprint of a weakening Atlantic Ocean overturning circulation. 556, 191-196.

Calvès, G., Huuse, M., Clift, P.D., Brusset, S.J.E., Letters, P.S., 2015. Giant fossil mass wasting off the coast of West India: the Nataraja submarine slide. 432, 265-272.

Carlson, A.E., Beard, B.L., Hatfield, R.G., Laffin, M., 2021. Absence of West Antarctic-sourced silt at ODP Site 1096 in the Bellingshausen Sea during the last interglaciation: Support for West Antarctic ice-sheet deglaciation. Quaternary Science Reviews 261, 106939.

Carter, A., Riley, T.R., Hillenbrand, C.-D., Rittner, M.J.E., Letters, P.S., 2017. Widespread Antarctic glaciation during the late Eocene. 458, 49-57.

Carter, P., Vance, D., Hillenbrand, C., Smith, J., Shoosmith, D.J.G.e.C.A., 2012. The neodymium isotopic composition of waters masses in the eastern Pacific sector of the Southern Ocean. 79, 41-59.

Chester, R., Hughes, M.J.C.g., 1967. A chemical technique for the separation of ferro-manganese minerals, carbonate minerals and adsorbed trace elements from pelagic sediments. 2, 249-262.

Clark, P.U., Pisias, N.G., Stocker, T.F., Weaver, A.J.J.N., 2002. The role of the thermohaline circulation in abrupt climate change. 415, 863-869.

Clift, P.D., Kulhanek, D.K., Zhou, P., Bowen, M.G., Vincent, S.M., Lyle, M., Hahn, A., 2019a. Chemical weathering and erosion responses to changing monsoon climate in the Late Miocene of Southwest Asia. Geological Magazine, 1-17.

Clift, P.D., Zhou, P., Stockli, D.F., Blusztajn, J., 2019b. Regional Pliocene exhumation of the Lesser Himalaya in the Indus drainage. Solid Earth 10, 647-661.

Coffin, M.F., Gahagan, L.M., Lawver, L.A., Lee, T.-Y., Rosencrant, E.J.U.o.T.I.f.G.T.R., 1992. Atlas of Mesozoic/Cenozoic reconstructions (200 Ma to Present Day)(PLATES Project, Progress Report No. 01-0192).

Colville, E.J., Carlson, A.E., Beard, B.L., Hatfield, R.G., Stoner, J.S., Reyes, A.V., Ullman, D.J.J.S., 2011. Sr-Nd-Pb isotope evidence for ice-sheet presence on southern Greenland during the Last Interglacial. 333, 620-623.

Cook, C.P., van de Flierdt, T., Williams, T., Hemming, S.R., Iwai, M., Kobayashi, M., Jimenez-Espejo, F.J., Escutia, C., González, J.J., Khim, B.-K., McKay, R.M., Passchier, S., Bohaty, S.M., Riesselman, C.R., Tauxe, L., Sugisaki, S., Galindo, A.L., Patterson, M.O., Sangiorgi, F., Pierce, E.L., Brinkhuis, H., Klaus, A., Fehr, A., Bendle, J.A.P., Bijl, P.K., Carr, S.A., Dunbar, R.B., Flores, J.A., Hayden, T.G.,

Katsuki, K., Kong, G.S., Nakai, M., Olney, M.P., Pekar, S.F., Pross, J., Röhl, U., Sakai, T., Shrivastava, P.K., Stickley, C.E., Tuo, S., Welsh, K., Yamane, M., 2013. Dynamic behaviour of the East Antarctic ice sheet during Pliocene warmth. Nature Geoscience 6, 765-769.

Crowley, T.J., Burke, K., 1998. Tectonic boundary conditions for climate reconstructions. Oxford University Press, USA.

Curry, W.B., Oppo, D.W.J.P., 2005. Glacial water mass geometry and the distribution of δ13C of ΣCO2 in the western Atlantic Ocean. 20.

Dailey, S., Clift, P., K. Kulhanek, D., Blusztajn, J., Routledge, C., Calves, G., O'Sullivan, P., Jonell, T., Pandey, D., Andò, S., Coletti, G., Zhou, P., Li, Y., E. Neubeck, N., A.P. Bendle, J., Aharonovich, S., Griffith, E., Gurumurthy, G.P., Hahn, A., Zhaojie, Y.U., 2019. Large-scale mass wasting on the Miocene continental margin of western India. GSA Bulletin.

Dartnell, L., 2019. Origins: How the Earth shaped human history. Random House.

Dausmann, V., Frank, M., Gutjahr, M., Rickli, J., 2017. Glacial reduction of AMOC strength and long-term transition in weathering inputs into the Southern Ocean since the mid-Miocene: Evidence from radiogenic Nd and Hf isotopes. Paleoceanography 32, 265-283.

de la Vega, E., Chalk, T.B., Wilson, P.A., Bysani, R.P., Foster, G.L., 2020. Atmospheric CO2 during the Mid-Piacenzian Warm Period and the M2 glaciation. Scientific reports 10, 11002.

De Vleeschouwer, D., Vahlenkamp, M., Crucifix, M., Pälike, H.J.G., 2017. Alternating Southern and Northern Hemisphere climate response to astronomical forcing during the past 35 my. 45, 375-378.

DeConto, R.M., Pollard, D., 2016. Contribution of Antarctica to past and future sea-level rise. Nature 531, 591-597.

DeConto, R.M., Pollard, D., Alley, R.B., Velicogna, I., Gasson, E., Gomez, N., Sadai, S., Condron, A., Gilford, D.M., Ashe, E.L.J.N., 2021. The Paris Climate Agreement and future sea-level rise from Antarctica. 593, 83-89.

DeVries, T., Holzer, M., Primeau, F.J.N., 2017. Recent increase in oceanic carbon uptake driven by weaker upper-ocean overturning. 542, 215-218.

Dhuime, B., Wuestefeld, A., Hawkesworth, C.J.J.N.G., 2015. Emergence of modern continental crust about 3 billion years ago. 8, 552-555.

Diekmann, B., Fälker, M., Kuhn, G.J.S., 2003. Environmental history of the south-eastern South Atlantic since the Middle Miocene: Evidence from the sedimentological records of ODP Sites 1088 and 1092. 50, 511-529.

Diekmann, B., Kuhn, G.J.M.G., 1999. Provenance and dispersal of glacial–marine surface sediments in the Weddell Sea and adjoining areas, Antarctica: ice-rafting versus current transport. 158, 209-231.

Dinniman, M.S., Klinck, J.M., Hofmann, E.E.J.J.o.C., 2012. Sensitivity of circumpolar deep water transport and ice shelf basal melt along the West Antarctic Peninsula to changes in the winds. 25, 4799-4816.

Dolan, A.M., de Boer, B., Bernales, J., Hill, D.J., Haywood, A.M., 2018. High climate model dependency of Pliocene Antarctic ice-sheet predictions. Nature communications 9, 2799.

Dowdeswell, J., Evans, J., Ó Cofaigh, C., Anderson, J.J.G.S.o.A.B., 2006. Morphology and sedimentary processes on the continental slope off Pine Island Bay, Amundsen Sea, West Antarctica. 118, 606-619.

Downing, G.E., Hemming, S.R., Jost, A., Roy, M.J.G.S., London, Special Publications, 2014. 40Ar/39Ar hornblende provenance clues about Heinrich event 3 (H3). 378, 245-263.

Dowsett, H.J., Robinson, M.M., Foley, K.M., 2009. Pliocene three-dimensional global ocean temperature reconstruction. Climate of the Past 5, 769-783.

Du, J., Haley, B.A., Mix, A.C.J.G.e.C.A., 2016. Neodymium isotopes in authigenic phases, bottom waters and detrital sediments in the Gulf of Alaska and their implications for paleo-circulation reconstruction. 193, 14-35.

Du, J., Tian, J., Ma, W., 2022a. The Late Miocene Carbon Isotope Shift driven by synergetic terrestrial processes: A box-model study. Earth and Planetary Science Letters 584, 117457.

Du, Z., Yang, J., Wang, L., Wang, N., Svensson, A., Zhang, Z., Ma, X., Liu, Y., Wang, S., Xu, J.J.E.S.S.D., 2022b. A database of radiogenic Sr–Nd isotopes at the “three poles”. 14, 5349-5365.

Duncan, B., McKay, R., Levy, R., Naish, T., Prebble, J.G., Sangiorgi, F., Krishnan, S., Hoem, F., Clowes, C., Dunkley Jones, T., Gasson, E., Kraus, C., Kulhanek, D.K., Meyers, S.R., Moossen, H., Warren, C., Willmott, V., Ventura, G.T., Bendle, J., 2022. Climatic and tectonic drivers of late Oligocene Antarctic ice volume. Nature Geoscience 15, 819-825.

Duplessy, J., Shackleton, N., Fairbanks, R., Labeyrie, L., Oppo, D., Kallel, N.J.P., 1988. Deepwater source variations during the last climatic cycle and their impact on the global deepwater circulation. 3, 343-360.

Dutton, A., Carlson, A.E., Long, A.J., Milne, G.A., Clark, P.U., DeConto, R., Horton, B.P., Rahmstorf, S., Raymo, M.E., 2015. Sea-level rise due to polar ice-sheet mass loss during past warm periods. Science 349, aaa4019.

Elias, S., 2013. Encyclopedia of Quaternary science. Newnes.

Engen, Ø., Faleide, J.I., Dyreng, T.K.J.T., 2008. Opening of the Fram Strait gateway: A review of plate tectonic constraints. 450, 51-69.

England, M.H., Maier-Reimer, E.J.R.o.G., 2001. Using chemical tracers to assess ocean models. 39, 29-70.

Escutia, C., De Santis, L., Donda, F., Dunbar, R., Cooper, A., Brancolini, G., Eittreim, S.J.G., Change, P., 2005. Cenozoic ice sheet history from East Antarctic Wilkes Land continental margin sediments. 45, 51-81.

Evans, D., Badger, M.P., Foster, G.L., Henehan, M.J., Lear, C.H., Zachos, J.C.J.N.c., 2018. No substantial long-term bias in the Cenozoic benthic foraminifera oxygen-isotope record. 9, 2875.

Evernden, J.F., Evernden, R.K.S.J.G.S.o.A., Special Paper, 1970. The Cenozoic time scale. 124, 71-90.

Farmer, G.L., Licht, K., Swope, R.J., Andrews, J.J.E., Letters, P.S., 2006. Isotopic constraints on the provenance of fine-grained sediment in LGM tills from the Ross Embayment, Antarctica. 249, 90-107.

Ferrari, R., Jansen, M.F., Adkins, J.F., Burke, A., Stewart, A.L., Thompson, A.F.J.P.o.t.N.A.o.S., 2014. Antarctic sea ice control on ocean circulation in present and glacial climates. 111, 8753-8758.

Flower, B.P., Kennett, J.P., 1995. Middle Miocene deepwater paleoceanography in the southwest Pacific: Relations with East Antarctic Ice Sheet development. 10, 1095-1112.

Flower, B.P., Kennett, J.P.J.P., palaeoclimatology, palaeoecology, 1994. The middle Miocene climatic transition: East Antarctic ice sheet development, deep ocean circulation and global carbon cycling. 108, 537-555.

Flowerdew, M.J., Tyrrell, S., Riley, T.R., Whitehouse, M.J., Mulvaney, R., Leat, P.T., Marschall, H.R.J.C.G., 2012. Distinguishing East and West Antarctic sediment sources using the Pb isotope composition of detrital K-feldspar. 292, 88-102.

Foster, G.L., Royer, D.L., Lunt, D.J., 2017. Future climate forcing potentially without precedent in the last 420 million years. Nature communications 8, 14845.

Frank, A.B., Klaebe, R.M., Löhr, S., Xu, L., Frei, R.J.G.e.C.A., 2020. Chromium isotope composition of organic-rich marine sediments and their mineral phases and implications for using black shales as a paleoredox archive. 270, 338-359.

Frank, M., Whiteley, N., van de Flierdt, T., Reynolds, B.C., O'Nions, K., 2006a. Nd and Pb isotope evolution of deep water masses in the eastern Indian Ocean during the past 33 Myr. Chemical Geology 226, 264-279.

Frank, M., Whiteley, N., van de Flierdt, T., Reynolds, B.C., O'Nions, K.J.C.G., 2006b. Nd and Pb isotope evolution of deep water masses in the eastern Indian Ocean during the past 33 Myr. 226, 264-279.

Frank, M.J.R.o.g., 2002. Radiogenic isotopes: Tracers of past ocean circulation and erosional input. 40, 1-1-1-38.

Fretwell, P., Pritchard, H.D., Vaughan, D.G., Bamber, J.L., Barrand, N.E., Bell, R., Bianchi, C., Bingham, R., Blankenship, D.D., Casassa, G.J.T.c., 2013. Bedmap2: improved ice bed, surface and thickness datasets for Antarctica. 7, 375-393.

Frezzotti, M., Orombelli, G., 2014a. Glaciers and ice sheets: current status and trends. Rendiconti Lincei 25, 59-70.

Frezzotti, M., Orombelli, G.J.R.L., 2014b. Glaciers and ice sheets: current status and trends. 25, 59-70.

Fyke, J.G., Carter, L., Mackintosh, A., Weaver, A.J., Meissner, K.J.J.J.o.C., 2010. Surface melting over ice shelves and ice sheets as assessed from modeled surface air temperatures. 23, 1929-1936.

Gao, H., Liang, B., Shao, Z.J.A.O.R., 2021. A global climate analysis of wave parameters with a focus on wave period from 1979 to 2018. 111, 102652.

Gille, S.T.J.J.o.C., 2008. Decadal-scale temperature trends in the Southern Hemisphere ocean. 21, 4749-4765.

Gladenkov, A.Y., Oleinik, A.E., Marincovich Jr, L., Barinov, K.B.J.P., Palaeoclimatology, Palaeoecology, 2002. A refined age for the earliest opening of Bering Strait. 183, 321-328.

Gohl, K., Denk, A., Eagles, G., Wobbe, F.J.T., 2013. Deciphering tectonic phases of the Amundsen Sea Embayment shelf, West Antarctica, from a magnetic anomaly grid. 585, 113-123.

Gohl, K., Uenzelmann-Neben, G., Gille-Petzoldt, J., Hillenbrand, C.-D., Klages, J.P., Bohaty, S.M., Passchier, S., Frederichs, T., Wellner, J.S., Lamb, R., Leitchenkov, G., Scientists, I.E., 2021a. Evidence for a Highly Dynamic West Antarctic Ice Sheet During the Pliocene. Geophysical Research Letters 48, e2021GL093103.

Gohl, K., Wellner, J., Klaus, A., Expedition 379 Scientists, 2021b. Amundsen Sea West Antarctic Ice Sheet History, Proceedings of the International Ocean Discovery Program, Expedition 379. International Ocean Discovery Program, College Station, TX , USA.

Gohl, K.W.J.S.K.A., the Expedition, S., 2021. Amundsen Sea West Antarctic Ice Sheet History. Proceedings of the International Ocean Discovery Program. International Ocean Discovery Program, College Station, TX.

Goldstein, S.J., Jacobsen, S.B.J.C.G.I.G.s., 1987. The Nd and Sr isotopic systematics of river-water dissolved material: Implications for the sources of Nd and Sr in seawater. 66, 245-272.

Goldstein, S.L., Hemming, S.R.J.T.o.g., 2003. Long-lived isotopic tracers in oceanography, paleoceanography, and ice-sheet dynamics. 6, 625.

Golledge, N.R., Kowalewski, D.E., Naish, T.R., Levy, R.H., Fogwill, C.J., Gasson, E.G.J.N., 2015. The multi-millennial Antarctic commitment to future sea-level rise. 526, 421-425.

Gordon, A.L.J.O.c., 2009. Bottom water formation. 263, 269.

Goswami, V., Singh, S.K., Bhushan, R., 2014. Impact of water mass mixing and dust deposition on Nd concentration and ε Nd of the Arabian Sea water column. Geochimica et Cosmochimica Acta 145, 30-49.

Goswami, V., Singh, S.K., Bhushan, R., Rai, V.K., 2012. Temporal variations in87Sr/86Sr and εNdin sediments of the southeastern Arabian Sea: Impact of monsoon and surface water circulation. Geochemistry, Geophysics, Geosystems 13, n/a-n/a.

Gourlan, A.T., Meynadier, L., Allègre, C.J., 2008a. Tectonically driven changes in the Indian Ocean circulation over the last 25 Ma: Neodymium isotope evidence. Earth and Planetary Science Letters 267, 353-364.

Gourlan, A.T., Meynadier, L., Allègre, C.J., Tapponnier, P., Birck, J.-L., Joron, J.-L., 2010. Northern Hemisphere climate control of the Bengali rivers discharge during the past 4 Ma. Quaternary Science Reviews 29, 2484-2498.

Gourlan, A.T., Meynadier, L., Allègre, C.J.J.E., Letters, P.S., 2008b. Tectonically driven changes in the Indian Ocean circulation over the last 25 Ma: Neodymium isotope evidence. 267, 353-364.

Graham, A.G., Larter, R.D., Gohl, K., Hillenbrand, C.-D., Smith, J.A., Kuhn, G.J.Q.S.R., 2009. Bedform signature of a West Antarctic palaeo-ice stream reveals a multi-temporal record of flow and substrate control. 28, 2774-2793.

Gudmundsson, G., Krug, J., Durand, G., Favier, L., Gagliardini, O.J.T.C., 2012. The stability of grounding lines on retrograde slopes. 6, 1497-1505.

Gueguen, B., Rouxel, O.J.C.G., 2021. The Nickel isotope composition of the authigenic sink and the diagenetic flux in modern oceans. 563, 120050.

Gulick, S.P., Shevenell, A.E., Montelli, A., Fernandez, R., Smith, C., Warny, S., Bohaty, S.M., Sjunneskog, C., Leventer, A., Frederick, B.J.N., 2017. Initiation and long-term instability of the East Antarctic Ice Sheet. 552, 225-229.

Gupta, A.K., Singh, R.K., Joseph, S., Thomas, E., 2004. Indian Ocean high-productivity event (10–8 Ma): Linked to global cooling or to the initiation of the Indian monsoons? Geology 32, 753.

Gupta, A.K., Yuvaraja, A., Prakasam, M., Clemens, S.C., Velu, A., 2015. Evolution of the South Asian monsoon wind system since the late Middle Miocene. Palaeogeography, Palaeoclimatology, Palaeoecology 438, 160-167.

Gupta, A.S., England, M.H.J.J.o.p.o., 2004. Evaluation of interior circulation in a high-resolution global ocean model. Part I: Deep and bottom waters. 34, 2592-2614.

Gutjahr, M., Frank, M., Stirling, C.H., Klemm, V., Van de Flierdt, T., Halliday, A.N.J.C.G., 2007. Reliable extraction of a deepwater trace metal isotope signal from Fe–Mn oxyhydroxide coatings of marine sediments. 242, 351-370.

Haley, B.A., Du, J., Abbott, A.N., McManus, J., 2017a. The Impact of Benthic Processes on Rare Earth Element and Neodymium Isotope Distributions in the Oceans. 4.

Haley, B.A., Du, J., Abbott, A.N., McManus, J.J.F.i.M.S., 2017b. The impact of benthic processes on rare earth element and neodymium isotope distributions in the oceans. 4, 426.

Haley, B.A., Frank, M., Hathorne, E., Pisias, N.J.G.e.C.A., 2014. Biogeochemical implications from dissolved rare earth element and Nd isotope distributions in the Gulf of Alaska. 126, 455-474.

Hall, I.R., McCave, I.N., Zahn, R., Carter, L., Knutz, P.C., Weedon, G.P., 2003. Paleocurrent reconstruction of the deep Pacific inflow during the middle Miocene: Reflections of East Antarctic Ice Sheet growth. 18.

Hall, R., 2002a. Cenozoic geological and plate tectonic evolution of SE Asia and the SW Pacific: computer-based reconstructions, model and animations. Journal of Asian Earth Sciences 20, 353-431.

Hall, R.J.J.o.A.e.s., 2002b. Cenozoic geological and plate tectonic evolution of SE Asia and the SW Pacific: computer-based reconstructions, model and animations. 20, 353-431.

Hawkesworth, C.J., Cawood, P.A., Dhuime, B., 2020. The Evolution of the Continental Crust and the Onset of Plate Tectonics. 8.

Hayashi, T., Yamanaka, T., Hikasa, Y., Sato, M., Kuwahara, Y., Ohno, M., 2020. Latest Pliocene Northern Hemisphere glaciation amplified by intensified Atlantic meridional overturning circulation. Communications Earth & Environment 1, 25.

Headly, M.A., Severinghaus, J.P.J.J.o.G.R.A., 2007. A method to measure Kr/N2 ratios in air bubbles trapped in ice cores and its application in reconstructing past mean ocean temperature. 112.

Hein, A.S., Woodward, J., Marrero, S.M., Dunning, S.A., Steig, E.J., Freeman, S.P.H.T., Stuart, F.M., Winter, K., Westoby, M.J., Sugden, D.E., 2016. Evidence for the stability of the West Antarctic Ice Sheet divide for 1.4 million years. Nature communications 7, 10325.

Hellmer, H., Jacobs, S.S., Jenkins, A., 1998. Oceanic erosion of a floating Antarctic glacier in the Amundsen Sea.

Hellmer, H.H.J.G.R.L., 2004. Impact of Antarctic ice shelf basal melting on sea ice and deep ocean properties. 31.

Hemming, S., Van de Flierdt, T., Goldstein, S., Franzese, A., Roy, M., Gastineau, G., Landrot, G.J.G., Geophysics, Geosystems, 2007. Strontium isotope tracing of terrigenous sediment dispersal in the Antarctic Circumpolar Current: implications for constraining frontal positions. 8.

Hemming, S.R.J.R.o.G., 2004. Heinrich events: Massive late Pleistocene detritus layers of the North Atlantic and their global climate imprint. 42.

Herbert, T.D., Lawrence, K.T., Tzanova, A., Peterson, L.C., Caballero-Gill, R., Kelly, C.S., 2016. Late Miocene global cooling and the rise of modern ecosystems. Nature Geoscience 9, 843-847.

Hillenbrand, C.-D., Fütterer, D.K., Grobe, H., Frederichs, T., 2002. No evidence for a Pleistocene collapse of the West Antarctic Ice Sheet from continental margin sediments recovered in the Amundsen Sea. Geo-Marine Letters 22, 51-59.

Hillenbrand, C.-D., Kuhn, G., Frederichs, T.J.Q.S.R., 2009. Record of a Mid-Pleistocene depositional anomaly in West Antarctic continental margin sediments: an indicator for ice-sheet collapse? 28, 1147-1159.

Hillenbrand, C.-D., Smith, J.A., Hodell, D.A., Greaves, M., Poole, C.R., Kender, S., Williams, M., Andersen, T.J., Jernas, P.E., Elderfield, H.J.N., 2017. West Antarctic Ice Sheet retreat driven by Holocene warm water incursions. 547, 43-48.

Hochmuth, K., Gohl, K.J.G.S., London, Special Publications, 2013. Glaciomarine sedimentation dynamics of the Abbot glacial trough of the Amundsen Sea Embayment shelf, West Antarctica. 381, 233-244.

Hodell, D.A., Venz-Curtis, K.A.J.G., Geophysics, Geosystems, 2006. Late Neogene history of deepwater ventilation in the Southern Ocean. 7.

Holden, P., Edwards, N., Wolff, E.W., Valdes, P.J., Singarayer, J.S.J.J.o.Q.S., 2011. The Mid-Brunhes event and West Antarctic ice sheet stability. 26, 474-477.

Homoky, W.B., Weber, T., Berelson, W.M., Conway, T.M., Henderson, G.M., Van Hulten, M., Jeandel, C., Severmann, S., Tagliabue, A.J.P.T.o.t.R.S.A.M., Physical, Sciences, E., 2016. Quantifying trace element and isotope fluxes at the ocean–sediment boundary: a review. 374, 20160246.

Hönisch, B., Ridgwell, A., Schmidt, D.N., Thomas, E., Gibbs, S.J., Sluijs, A., Zeebe, R., Kump, L., Martindale, R.C., Greene, S.E.J.s., 2012. The geological record of ocean acidification. 335, 1058-1063.

Hossain, A., Knorr, G., Jokat, W., Lohmann, G.J.a., 2021. Opening of the Fram Strait led to the establishment of a modern-like three-layer stratification in the Arctic Ocean during the Miocene. 7, 1-12.

Howe, J.N., Piotrowski, A.M., Noble, T.L., Mulitza, S., Chiessi, C.M., Bayon, G., 2016. North Atlantic Deep Water Production during the Last Glacial Maximum. Nature communications 7, 11765.

Hu, R., Noble, T.L., Piotrowski, A.M., McCave, I.N., Bostock, H.C., Neil, H.L.J.E., Letters, P.S., 2016. Neodymium isotopic evidence for linked changes in Southeast Atlantic and Southwest Pacific circulation over the last 200 kyr. 455, 106-114.

Huang, H., Gutjahr, M., Eisenhauer, A., Kuhn, G.J.N.c., 2020. No detectable Weddell Sea Antarctic bottom water export during the last and penultimate glacial maximum. 11, 424.

Huang, H., Gutjahr, M., Kuhn, G., Hathorne, E.C., Eisenhauer, A.J.G., Geophysics, Geosystems, 2021. Efficient extraction of past seawater Pb and Nd isotope signatures from Southern Ocean sediments. 22, e2020GC009287.

Huang, Y., Clemens, S.C., Liu, W., Wang, Y., Prell, W.L., 2007. Large-scale hydrological change drove the late Miocene C4 plant expansion in the Himalayan foreland and Arabian Peninsula. Geology 35, 531.

Huck, C.E., van de Flierdt, T., Jiménez-Espejo, F.J., Bohaty, S.M., Röhl, U., Hammond, S.J.J.G., Geophysics, Geosystems, 2016. Robustness of fossil fish teeth for seawater neodymium isotope reconstructions under variable redox conditions in an ancient shallow marine setting. 17, 679-698.

Ivanova, E., 2009. The global thermohaline paleocirculation. Springer Science & Business Media.

Jacobs, S.S.J.A.S., 2004. Bottom water production and its links with the thermohaline circulation. 16, 427-437.

Janssen, D.J., Rickli, J., Abbott, A.N., Ellwood, M.J., Twining, B.S., Ohnemus, D.C., Nasemann, P., Gilliard, D., Jaccard, S.L.J.E., letters, p.s., 2021. Release from biogenic particles, benthic fluxes, and deep water circulation control Cr and δ53Cr distributions in the ocean interior. 574, 117163.

Jeandel, C., Oelkers, E.H.J.C.G., 2015. The influence of terrigenous particulate material dissolution on ocean chemistry and global element cycles. 395, 50-66.

Jeandel, C.J.E., Letters, P.S., 1993. Concentration and isotopic composition of Nd in the South Atlantic Ocean. 117, 581-591.

Jeandel, C.J.P.T.o.t.R.S.A.M., Physical, Sciences, E., 2016. Overview of the mechanisms that could explain the 'Boundary Exchange'at the land–ocean contact. 374, 20150287.

Jenkins, A., Dutrieux, P., Jacobs, S., Steig, E.J., Gudmundsson, G.H., Smith, J., Heywood, K.J.J.O., 2016. Decadal ocean forcing and Antarctic ice sheet response: Lessons from the Amundsen Sea. 29, 106-117.

Jenkins, A., Jacobs, S.J.J.o.G.R.O., 2008. Circulation and melting beneath George VI ice shelf, Antarctica. 113.

Johannesson, K.H., Burdige, D.J.J.E., Letters, P.S., 2007. Balancing the global oceanic neodymium budget: Evaluating the role of groundwater. 253, 129-142.

Jordan, T.A., Riley, T.R., Siddoway, C.S.J.N.R.E., Environment, 2020. The geological history and evolution of West Antarctica. 1, 117-133.

Joughin, I., Alley, R.B., 2011. Stability of the West Antarctic ice sheet in a warming world. Nature Geoscience 4, 506-513.

Jouzel, J., Masson-Delmotte, V., Cattani, O., Dreyfus, G., Falourd, S., Hoffmann, G., Minster, B., Nouet, J., Barnola, J.M., Chappellaz, J., Fischer, H., Gallet, J.C., Johnsen, S., Leuenberger, M., Loulergue, L., Luethi, D., Oerter, H., Parrenin, F., Raisbeck, G., Raynaud, D., Schilt, A., Schwander, J., Selmo, E., Souchez, R., Spahni, R., Stauffer, B., Steffensen, J.P., Stenni, B., Stocker, T.F., Tison, J.L., Werner, M., Wolff, E.W., 2007. Orbital and Millennial Antarctic Climate Variability over the Past 800,000 Years. Science 317, 793-796.

Karas, C., Nürnberg, D., Bahr, A., Groeneveld, J., Herrle, J.O., Tiedemann, R., Demenocal, P.B.J.S.R., 2017. Pliocene oceanic seaways and global climate. 7, 39842.

Katz, R.F., Worster, M.G.J.P.o.t.R.S.A.M., Physical, Sciences, E., 2010. Stability of ice-sheet grounding lines. 466, 1597-1620.

Keating-Bitonti, C.R., Peters, S.E., 2019. Influence of increasing carbonate saturation in Atlantic bottom water during the late Miocene. Palaeogeography, Palaeoclimatology, Palaeoecology 518, 134-142.

Khim, B.-K., Lee, J., Ha, S., Park, J., Pandey, D.K., Clift, P.D., Kulhanek, D.K., Steinke, S., Griffith, E.M., Suzuki, K., Xu, Z., 2019. Variations in δ13C values of

sedimentary organic matter since late Miocene time in the Indus Fan (IODP Site 1457) of the eastern Arabian Sea. Geological Magazine, 1-10.

Kim, J.-H., Crosta, X., Willmott, V., Renssen, H., Bonnin, J., Helmke, P., Schouten, S., Sinninghe Damsté, J.S., 2012. Holocene subsurface temperature variability in the eastern Antarctic continental margin. Geophysical Research Letters 39.

Kirillova, V., Osborne, A.H., Störling, T., Frank, M., 2019. Miocene restriction of the Pacific-North Atlantic throughflow strengthened Atlantic overturning circulation. Nature communications 10, 4025.

Klinck, J.M., Hofmann, E.E., Beardsley, R.C., Salihoglu, B., Howard, S.J.D.S.R.P.I.T.S.i.O., 2004. Water-mass properties and circulation on the west Antarctic Peninsula Continental Shelf in Austral Fall and Winter 2001. 51, 1925-1946.

Kostov, Y., Armour, K.C., Marshall, J.J.G.R.L., 2014. Impact of the Atlantic meridional overturning circulation on ocean heat storage and transient climate change. 41, 2108-2116.

Kostov, Y., Marshall, J., Hausmann, U., Armour, K.C., Ferreira, D., Holland, M.M.J.C.D., 2017. Fast and slow responses of Southern Ocean sea surface temperature to SAM in coupled climate models. 48, 1595-1609.

Krishna, K., Gopala Rao, D., Sar, D.J.T., 2006. Nature of the crust in the Laxmi Basin (14–20 N), western continental margin of India. 25.

Kronen Jr, J.D., 1998. Marine sedimentary deposits at different temporal and spatial scales: Investigation of repetitive systems influenced by climate and sea level. University of Hawai'i at Manoa.

Kuhnt, W., Holbourn, A., Hall, R., Zuvela, M., Käse, R.J.C.-O.I.w.E.A.M.S.G.M., 2004. Neogene history of the Indonesian throughflow. 149, 299-320.

Kumar, A., Suresh, K., Rahaman, W., 2020. Geochemical characterization of modern aeolian dust over the Northeastern Arabian Sea: Implication for dust transport in the Arabian Sea. Science of The Total Environment 729, 138576.

Lacan, F., Jeandel, C.J.E., Letters, P.S., 2005. Neodymium isotopes as a new tool for quantifying exchange fluxes at the continent–ocean interface. 232, 245-257.

Lagabrielle, Y., Goddéris, Y., Donnadieu, Y., Malavieille, J., Suarez, M.J.E., Letters, P.S., 2009. The tectonic history of Drake Passage and its possible impacts on global climate. 279, 197-211.

Lambelet, M., Van De Flierdt, T., Crocket, K., Rehkämper, M., Kreissig, K., Coles, B., Rijkenberg, M.J., Gerringa, L.J., de Baar, H.J., Steinfeldt, R.J.G.e.C.A., 2016. Neodymium isotopic composition and concentration in the western North Atlantic Ocean: Results from the GEOTRACES GA02 section. 177, 1-29.

Landschützer, P., Gruber, N., Haumann, F.A., Rödenbeck, C., Bakker, D.C., Van Heuven, S., Hoppema, M., Metzl, N., Sweeney, C., Takahashi, T.J.S., 2015. The reinvigoration of the Southern Ocean carbon sink. 349, 1221-1224.

Larter, R.D., Anderson, J.B., Graham, A.G., Gohl, K., Hillenbrand, C.-D., Jakobsson, M., Johnson, J.S., Kuhn, G., Nitsche, F.O., Smith, J.A.J.Q.S.R., 2014. Reconstruction of changes in the Amundsen Sea and Bellingshausen sea sector of the West Antarctic ice sheet since the last glacial maximum. 100, 55-86.

Larter, R.D., Graham, A.G., Gohl, K., Kuhn, G., Hillenbrand, C.-D., Smith, J.A., Deen, T.J., Livermore, R.A., Schenke, H.-W.J.G., 2009. Subglacial bedforms reveal complex basal regime in a zone of paleo–ice stream convergence, Amundsen Sea embayment, West Antarctica. 37, 411-414.

Laskar, J., Fienga, A., Gastineau, M., Manche, H.J.A., Astrophysics, 2011. La2010: a new orbital solution for the long-term motion of the Earth. 532, A89.

Laskar, J., Joutel, F., Boudin, F.J.A., Astrophysics , v., no. 1-2, p. 522-533., 1993. Orbital, precessional, and insolation quantities for the Earth from-20 Myr to+ 10 Myr. 270, 522-533.

Laskar, J., Robutel, P., Joutel, F., Gastineau, M., Correia, A.C.M., Levrard, B., 2004. A long-term numerical solution for the insolation quantities of the Earth. A&A 428, 261-285.

Lathika, N., Rahaman, W., Tarique, M., Gandhi, N., Kumar, A., Thamban, M., 2021. Deep water circulation in the Arabian Sea during the last glacial cycle: Implications for paleo-redox condition, carbon sink and atmospheric CO2 variability. Quaternary Science Reviews 257, 106853.

Lawver, L.A., Gahagan, L.M.J.P., Palaeoclimatology, Palaeoecology, 2003. Evolution of Cenozoic seaways in the circum-Antarctic region. 198, 11-37.

Le Houedec, S., Meynadier, L., Allègre, C.J., 2012a. Nd isotope systematics on ODP Sites 756 and 762 sediments reveal major volcanic, oceanic and climatic changes in South Indian Ocean over the last 35Ma. Earth and Planetary Science Letters 327-328, 29-38.

Le Houedec, S., Meynadier, L., Allègre, C.J.J.E., Letters, P.S., 2012b. Nd isotope systematics on ODP Sites 756 and 762 sediments reveal major volcanic, oceanic and climatic changes in South Indian Ocean over the last 35 Ma. 327, 29-38.

Le Quéré, C., Rodenbeck, C., Buitenhuis, E.T., Conway, T.J., Langenfelds, R., Gomez, A., Labuschagne, C., Ramonet, M., Nakazawa, T., Metzl, N.J.s., 2007. Saturation of the Southern Ocean CO2 sink due to recent climate change. 316, 1735-1738.

Lear, C.H., Coxall, H.K., Foster, G.L., Lunt, D.J., Mawbey, E.M., Rosenthal, Y., Sosdian, S.M., Thomas, E., Wilson, P.A., 2015. Neogene ice volume and ocean temperatures: Insights from infaunal foraminiferal Mg/Ca paleothermometry. 30, 1437-1454.

Lear, C.H., Rosenthal, Y., Wright, J.D., 2003. The closing of a seaway: ocean water masses and global climate change. Earth and Planetary Science Letters 210, 425-436.

Licht, K., Palmer, E.J.Q.S.R., 2013. Erosion and transport by Byrd Glacier, Antarctica during the last glacial maximum. 62, 32-48.

Licht, K.J., Hennessy, A.J., Welke, B.M.J.A.S., 2014. The U-Pb detrital zircon signature of West Antarctic ice stream tills in the Ross embayment, with implications for Last Glacial Maximum ice flow reconstructions. 26, 687-697.

Lindeque, A., Gohl, K., Henrys, S., Wobbe, F., Davy, B.J.P., Palaeoclimatology, Palaeoecology, 2016. Seismic stratigraphy along the Amundsen Sea to Ross Sea continental rise: a cross-regional record of pre-glacial to glacial processes of the West Antarctic margin. 443, 183-202.

Lisiecki, L., Raymo, M., 2005a. Lisiecki, L. E. & Raymo, M. E. A Pliocene-Pleistocene stack of 57 globally distributed benthic 18O records. Paleoceanography 20, PA1003. Paleoceanography 20.

Lisiecki, L.E., Raymo, M.E., 2005b. A Pliocene-Pleistocene stack of 57 globally distributed benthic δ18O records. Paleoceanography 20.

Livermore, R., Nankivell, A., Eagles, G., Morris, P.J.E., Letters, P.S., 2005. Paleogene opening of Drake passage. 236, 459-470.

Lougheed, B.C., Obrochta, S.P., 2019. A Rapid, Deterministic Age-Depth Modeling Routine for Geological Sequences With Inherent Depth Uncertainty. Paleoceanography and Paleoclimatology 34, 122-133.

Lowe, A.L., Anderson, J.B.J.Q.S.R., 2002. Reconstruction of the West Antarctic ice sheet in Pine Island Bay during the Last Glacial Maximum and its subsequent retreat history. 21, 1879-1897.

Lozier, M.S., Li, F., Bacon, S., Bahr, F., Bower, A.S., Cunningham, S., de Jong, M.F., de Steur, L., deYoung, B., Fischer, J.J.S., 2019. A sea change in our view of overturning in the subpolar North Atlantic. 363, 516-521.

Lumpkin, R., Speer, K.J.J.o.P.O., 2007. Global ocean meridional overturning. 37, 2550-2562.

Lynch-Stieglitz, J., Curry, W.B., Slowey, N.J.N., 1999. Weaker Gulf Stream in the Florida straits during the last glacial maximum. 402, 644-648.

Lynch-Stieglitz, J., Marchitto, T.J.T.o.g., 2006. Tracers of past ocean circulation. 6, 433-451.

Lynch-Stieglitz, J., Curry, W.B., Slowey, N.J.P., 1999. A geostrophic transport estimate for the Florida Current from the oxygen isotope composition of benthic foraminifera. 14, 360-373.

Marshall, J., Speer, K.J.N.g., 2012. Closure of the meridional overturning circulation through Southern Ocean upwelling. 5, 171-180.

Martin, E.E., Scher, H., 2006a. A Nd isotopic study of southern sourced waters and Indonesian Throughflow at intermediate depths in the Cenozoic Indian Ocean. Geochemistry, Geophysics, Geosystems 7, n/a-n/a.

Martin, E.E., Scher, H.J.G., Geophysics, Geosystems, 2006b. A Nd isotopic study of southern sourced waters and Indonesian throughflow at intermediate depths in the Cenozoic Indian Ocean. 7.

Matsuoka, K., Skoglund, A., Roth, G., de Pomereu, J., Griffiths, H., Headland, R., Herried, B., Katsumata, K., Le Brocq, A., Licht, K.J.E.M., Software, 2021. Quantarctica, an integrated mapping environment for Antarctica, the Southern Ocean, and sub-Antarctic islands. 140, 105015.

McClymont, E.L., Ho, S.L., Ford, H.L., Bailey, I., Berke, M.A., Bolton, C.T., De Schepper, S., Grant, G.R., Groeneveld, J., Inglis, G.N., Karas, C., Patterson, M.O., Swann, G.E.A., Thirumalai, K., White, S.M., Alonso-Garcia, M., Anand, P., Hoogakker, B.A.A., Littler, K., Petrick, B.F., Risebrobakken, B., Abell, J.T., Crocker, A.J., de Graaf, F., Feakins, S.J., Hargreaves, J.C., Jones, C.L., Markowska, M., Ratnayake, A.S., Stepanek, C., Tangunan, D., 2023. Climate Evolution Through the Onset and Intensification of Northern Hemisphere Glaciation. 61, e2022RG000793.

Meijers, A.J.P.T.o.t.R.S.A.M., Physical, Sciences, E., 2014. The Southern Ocean in the coupled model intercomparison project phase 5. 372, 20130296.

Meredith, M.P., Ducklow, H.W., Schofield, O., Wåhlin, A., Newman, L., Lee, S.J.D.S.R.P.I.T.S.i.O., 2016. The interdisciplinary marine system of the Amundsen Sea, Southern Ocean: Recent advances and the need for sustained observations. Elsevier, pp. 1-6.

Meyers, P.A., 1994. Preservation of elemental and isotopic source identification of sedimentary organic matter. Chemical Geology 114, 289-302.

Miller, K.G., Browning, J.V., Schmelz, W.J., Kopp, R.E., Mountain, G.S., Wright, J.D.J.S.a., 2020. Cenozoic sea-level and cryospheric evolution from deep-sea geochemical and continental margin records. 6, eaaz1346.

Mix, A.C., Fairbanks, R.G.J.E., Letters, P.S., 1985. North Atlantic surface-ocean control of Pleistocene deep-ocean circulation. 73, 231-243.

Molnar, P.J.P., 2008. Closing of the Central American Seaway and the Ice Age: A critical review. 23.

Montes, C., Cardona, A., Jaramillo, C., Pardo, A., Silva, J., Valencia, V., Ayala, C., Pérez-Angel, L., Rodriguez-Parra, L., Ramirez, V.J.S., 2015. Middle Miocene closure of the Central American seaway. 348, 226-229.

Moore, T.C., Tj, H.v.A., Sancetta, C., Pisias, N., 1978. Cenozoic Hiatuses in Pelagic Sediments. Micropaleontology 24, 113-138.

Morrison, A., Hogg, A.M., England, M.H., Spence, P.J.S.A., 2020. Warm Circumpolar Deep Water transport toward Antarctica driven by local dense water export in canyons. 6, eaav2516.

Mudelsee, M., Bickert, T., Lear, C.H., Lohmann, G.J.R.o.G., 2014. Cenozoic climate changes: A review based on time series analysis of marine benthic δ18O records. 52, 333-374.

Naik, S.S., Basak, C., Goldstein, S.L., Naidu, P.D., Naik, S.N., 2019. A 16-kyr Record of Ocean Circulation and Monsoon Intensification From the Central Bay of Bengal. Geochemistry, Geophysics, Geosystems 20, 872-882.

Nair, N., Pandey, D.K., Pandey, A., Prerna, R., 2021. Seismic stratigraphy and the sedimentation history in the Laxmi Basin of the eastern Arabian Sea: Constraints from IODP Expedition 355. Geoscience Frontiers 12, 101111.

Naish, T., Powell, R., Levy, R., Wilson, G., Scherer, R., Talarico, F., Krissek, L., Niessen, F., Pompilio, M., Wilson, T., Carter, L., DeConto, R., Huybers, P., McKay, R., Pollard, D., Ross, J., Winter, D., Barrett, P., Browne, G., Cody, R., Cowan, E., Crampton, J., Dunbar, G., Dunbar, N., Florindo, F., Gebhardt, C., Graham, I., Hannah, M., Hansaraj, D., Harwood, D., Helling, D., Henrys, S., Hinnov, L., Kuhn, G., Kyle, P., Läufer, A., Maffioli, P., Magens, D., Mandernack, K., McIntosh, W., Millan, C., Morin, R., Ohneiser, C., Paulsen, T., Persico, D., Raine, I., Reed, J., Riesselman, C., Sagnotti, L., Schmitt, D., Sjunneskog, C., Strong, P., Taviani, M., Vogel, S., Wilch, T., Williams, T., 2009. Obliquity-paced Pliocene West Antarctic ice sheet oscillations. Nature 458, 322-328.

Newkirk, D.R., Martin, E.E., 2009. Circulation through the Central American Seaway during the Miocene carbonate crash. Geology 37, 87-90.

Nicolas, J.P., Bromwich, D.H.J.J.o.C., 2011. Climate of West Antarctica and influence of marine air intrusions. 24, 49-67.

Nisancioglu, K.H., Raymo, M.E., Stone, P.H., 2003. Reorganization of Miocene deep water circulation in response to the shoaling of the Central American Seaway. Paleoceanography 18.

Nitsche, F.O., Cunningham, A.P., Larter, R.D., Gohl, K.J.M.G., 2000. Geometry and development of glacial continental margin depositional systems in the Bellingshausen Sea. 162, 277-302.

O'nions, R., Frank, M., von Blanckenburg, F., Ling, H.-F.J.E., Letters, P.S., 1998a. Secular variation of Nd and Pb isotopes in ferromanganese crusts from the Atlantic, Indian and Pacific Oceans. 155, 15-28.

O'Nions, R.K., Frank, M., von Blanckenburg, F., Ling, H.F., 1998b. Secular variation of Nd and Pb isotopes in ferromanganese crusts from the Atlantic, Indian and Pacific Oceans. Earth and Planetary Science Letters 155, 15-28.

Oppenheimer, M.J.N., 1998. Global warming and the stability of the West Antarctic Ice Sheet. 393, 325-332.

Orsi, A.H., Johnson, G.C., Bullister, J.L.J.P.i.O., 1999. Circulation, mixing, and production of Antarctic Bottom Water. 43, 55-109.

Orsi, A.H., Whitworth III, T., Nowlin Jr, W.D.J.D.S.R.P.I.O.R.P., 1995. On the meridional extent and fronts of the Antarctic Circumpolar Current. 42, 641-673.

Pagani, M., Liu, Z., LaRiviere, J., Ravelo, A.C., 2010. High Earth-system climate sensitivity determined from Pliocene carbon dioxide concentrations. Nature Geoscience 3, 27-30.

Palmer, D., 2003. Prehistoric past revealed: the four billion year history of life on Earth. Univ of California Press.

Pandey, A., Pandey, D.K.J.G., Geodynamics, 2015. Mechanism of crustal extension in the Laxmi Basin, Arabian Sea. 6, 409-422.

Pandey, D.K., Clift, P.D., Kulhanek, D.K., Scientists, a.t.E., 2016. Site U1457. Proceedings of the International Ocean Discovery Program 355, 1-49.

Paolo, F.S., Fricker, H.A., Padman, L.J.S., 2015. Volume loss from Antarctic ice shelves is accelerating. 348, 327-331.

Pattyn, F., Ritz, C., Hanna, E., Asay-Davis, X., DeConto, R., Durand, G., Favier, L., Fettweis, X., Goelzer, H., Golledge, N.R.J.N.c.c., 2018. The Greenland and Antarctic ice sheets under 1.5 C global warming. 8, 1053-1061.

Peck, V.L., Hall, I.R., Zahn, R., Grousset, F., Hemming, S., Scourse, J.J.Q.S.R., 2007. The relationship of Heinrich events and their European precursors over the past 60 ka BP: a multi-proxy ice-rafted debris provenance study in the North East Atlantic. 26, 862-875.

Pereira, P.S., 2018. Insights Into West Antarctica's Geology and Late Pleistocene Ice Sheet Behaviour from Isotopic Sedimentary Provenance Studies. Imperial College London.

Pereira, P.S., van de Flierdt, T., Hemming, S.R., Frederichs, T., Hammond, S.J., Brachfeld, S., Doherty, C., Kuhn, G., Smith, J.A., Klages, J.P.J.C.G., 2020. The geochemical and mineralogical fingerprint of West Antarctica's weak underbelly: Pine Island and Thwaites glaciers. 550, 119649.

Philander, S.G., Fedorov, A.V.J.P., 2003. Role of tropics in changing the response to Milankovich forcing some three million years ago. 18.

Pickering, K.T.J.B.r.t.g.c.T.l., 2000. The Cenozoic world. 145, 20-34.

Piepgras, D.J., Jacobsen, S.B.J.G.e.C.A., 1988. The isotopic composition of neodymium in the North Pacific. 52, 1373-1381.

Piepgras, D.J., Wasserburg, G., Dasch, E.J.E., Letters, P.S., 1979. The isotopic composition of Nd in different ocean masses. 45, 223-236.

Pierce, E., Hemming, S., Williams, T., Van de Flierdt, T., Thomson, S., Reiners, P., Gehrels, G., Brachfeld, S., Goldstein, S.J.E.-S.R., 2014. A comparison of detrital U–Pb zircon, 40Ar/39Ar hornblende, 40Ar/39Ar biotite ages in marine sediments off East Antarctica: Implications for the geology of subglacial terrains and provenance studies. 138, 156-178.

Pierce, E.L., van de Flierdt, T., Williams, T., Hemming, S.R., Cook, C.P., Passchier, S.J.E., Letters, P.S., 2017. Evidence for a dynamic East Antarctic ice sheet during the mid-Miocene climate transition. 478, 1-13.

Pierce, E.L., Williams, T., Van De Flierdt, T., Hemming, S.R., Goldstein, S.L., Brachfeld, S.A.J.P., 2011. Characterizing the sediment provenance of East Antarctica's weak underbelly: The Aurora and Wilkes sub-glacial basins. 26.

Pillot, Q., Donnadieu, Y., Sarr, A.C., Ladant, J.B., Suchéras-Marx, B.J.P., Paleoclimatology, 2022. Evolution of Ocean circulation in the North Atlantic Ocean during the Miocene: impact of the Greenland ice sheet and the Eastern Tethys Seaway. 37, e2022PA004415.

Pin, C., Zalduegui, J.S., 1997. Sequential separation of light rare-earth elements, thorium and uranium by miniaturized extraction chromatography: Application to isotopic analyses of silicate rocks. Analytica Chimica Acta 339, 79-89.

Piotrowski, A.M., Banakar, V.K., Scrivner, A.E., Elderfield, H., Galy, A., Dennis, A., 2009. Indian Ocean circulation and productivity during the last glacial cycle. Earth and Planetary Science Letters 285, 179-189.

Piotrowski, A.M., Goldstein, S.L., Hemming, S.R., Fairbanks, R.G.J.S., 2005. Temporal relationships of carbon cycling and ocean circulation at glacial boundaries. 307, 1933-1938.

Piotrowski, A.M., Goldstein, S.L., Sidney, R.H., Fairbanks, R.G., Zylberberg, D.R.J.E., Letters, P.S., 2008. Oscillating glacial northern and southern deep water formation from combined neodymium and carbon isotopes. 272, 394-405.

Pollard, D., DeConto, R.M., 2009. Modelling West Antarctic ice sheet growth and collapse through the past five million years. Nature 458, 329-332.

Poore, H.R., Samworth, R., White, N.J., Jones, S.M., McCave, I.N., 2006. Neogene overflow of Northern Component Water at the Greenland-Scotland Ridge. Geochemistry, Geophysics, Geosystems 7, n/a-n/a.

Pöppelmeier, F., Lippold, J., Blaser, P., Gutjahr, M., Frank, M., Stocker, T.F.J.Q.s.r., 2022. Neodymium isotopes as a paleo-water mass tracer: A model-data reassessment. 279, 107404.

Pritchard, H., Ligtenberg, S.R., Fricker, H.A., Vaughan, D.G., van den Broeke, M.R., Padman, L.J.N., 2012. Antarctic ice-sheet loss driven by basal melting of ice shelves. 484, 502-505.

Purkey, S.G., Johnson, G.C.J.J.o.C., 2010. Warming of global abyssal and deep Southern Ocean waters between the 1990s and 2000s: Contributions to global heat and sea level rise budgets. 23, 6336-6351.

Quade, J., Cerling, T.E., Bowman, J.R., 1989. Development of Asian monsoon revealed by marked ecological shift during the latest Miocene in northern Pakistan. Nature 342, 163-166.

Rahaman, W., Smik, L., Köseoğlu, D., N, L., Tarique, M., Thamban, M., Haywood, A., Belt, S.T., Knies, J., 2020. Reduced Arctic sea ice extent during the mid-Pliocene Warm Period concurrent with increased Atlantic-climate regime. Earth and Planetary Science Letters 550, 116535.

Rahlf, P., Hathorne, E., Laukert, G., Gutjahr, M., Weldeab, S., Frank, M., 2020. Tracing water mass mixing and continental inputs in the southeastern Atlantic Ocean with dissolved neodymium isotopes. Earth and Planetary Science Letters 530, 115944.

Rahmstorf, S., 2006. Thermohaline Ocean Circulation.

Rashid, H., Gourlan, A.T., Marche, B., Sheppard, K., Khélifi, N., 2019. Changes in Indian Summer Monsoon Using Neodymium (Nd) Isotopes in the Andaman Sea During the Last 24,000 years. Earth Systems and Environment 3, 241-253.

Rempfer, J., Stocker, T.F., Joos, F., Dutay, J.C.J.J.o.G.R.O., 2012. Sensitivity of Nd isotopic composition in seawater to changes in Nd sources and paleoceanographic implications. 117.

Reyes, A.V., Carlson, A.E., Beard, B.L., Hatfield, R.G., Stoner, J.S., Winsor, K., Welke, B., Ullman, D.J.J.N., 2014. South Greenland ice-sheet collapse during marine isotope stage 11. 510, 525-528.

Reynolds, B.C., Frank, M., O'Nions, R.K., 1999. Nd- and Pb-isotope time series from Atlantic ferromanganese crusts: implications for changes in provenance and paleocirculation over the last 8 Myr. Earth and Planetary Science Letters 173, 381-396.

Rignot, E., Jacobs, S., Mouginot, J., Scheuchl, B.J.S., 2013. Ice-shelf melting around Antarctica. 341, 266-270.

Rignot, E., Jacobs, S.S.J.S., 2002. Rapid bottom melting widespread near Antarctic ice sheet grounding lines. 296, 2020-2023.

Rignot, E., Mouginot, J., Scheuchl, B., van den Broeke, M., van Wessem, M.J., Morlighem, M., 2019. Four decades of Antarctic Ice Sheet mass balance from 1979–2017. Proceedings of the National Academy of Sciences 116, 1095.

Rintoul, S.R., Silvano, A., Pena-Molino, B., van Wijk, E., Rosenberg, M., Greenbaum, J.S., Blankenship, D.D.J.S.A., 2016. Ocean heat drives rapid basal melt of the Totten Ice Shelf. 2, e1601610.

Roberts, N.L., Piotrowski, A.M., Elderfield, H., Eglinton, T.I., Lomas, M.W.J.G.e.C.A., 2012. Rare earth element association with foraminifera. 94, 57-71.

Robinson, S., Ivanovic, R., van de Flierdt, T., Blanchet, C.L., Tachikawa, K., Martin, E.E., Cook, C.P., Williams, T., Gregoire, L., Plancherel, Y., Jeandel, C., Arsouze, T., 2021. Global continental and marine detrital εNd: An updated compilation for use in understanding marine Nd cycling. Chemical Geology 567, 120119.

Rohling, E.J., Yu, J., Heslop, D., Foster, G.L., Opdyke, B., Roberts, A.P., 2021. Sea level and deep-sea temperature reconstructions suggest quasi-stable states and critical transitions over the past 40 million years. Science Advances 7, eabf5326.

Routledge, C.M., Kulhanek, D.K., Tauxe, L., Scardia, G., Singh, A.D., Steinke, S., Griffith, E.M., Saraswat, R., 2019. A revised chronostratigraphic framework for International Ocean Discovery Program Expedition 355 sites in Laxmi Basin, eastern Arabian Sea. Geological Magazine, 1-18.

Roy, M., van de Flierdt, T., Hemming, S.R., Goldstein, S.L.J.C.G., 2007. 40Ar/39Ar ages of hornblende grains and bulk Sm/Nd isotopes of circum-Antarctic glacio-marine sediments: Implications for sediment provenance in the southern ocean. 244, 507-519.

Rutberg, R.L., Hemming, S.R., Goldstein, S.L.J.N., 2000. Reduced North Atlantic Deep Water flux to the glacial Southern Ocean inferred from neodymium isotope ratios. 405, 935-938.

Sabine, C.L., Feely, R.A., Gruber, N., Key, R.M., Lee, K., Bullister, J.L., Wanninkhof, R., Wong, C., Wallace, D.W., Tilbrook, B.J.s., 2004. The oceanic sink for anthropogenic CO2. 305, 367-371.

Sato, M., Makio, M., Hayashi, T., Ohno, M., 2015. Abrupt intensification of North Atlantic Deep Water formation at the Nordic Seas during the late Pliocene climate transition. 42, 4949-4955.

Scher, H.D., Whittaker, J.M., Williams, S.E., Latimer, J.C., Kordesch, W.E., Delaney, M.L.J.N., 2015. Onset of Antarctic Circumpolar Current 30 million years ago as Tasmanian Gateway aligned with westerlies. 523, 580-583.

Scherer, R.P., Aldahan, A., Tulaczyk, S., Possnert, G., Engelhardt, H., Kamb, B., 1998. Pleistocene Collapse of the West Antarctic Ice Sheet. Science 281, 82-85.

Schoof, C.J.J.o.G.R.E.S., 2007. Ice sheet grounding line dynamics: Steady states, stability, and hysteresis. 112.

Seki, O., Foster, G.L., Schmidt, D.N., Mackensen, A., Kawamura, K., Pancost, R.D., 2010. Alkenone and boron-based Pliocene pCO2 records. Earth and Planetary Science Letters 292, 201-211.

Sepulchre, P., Arsouze, T., Donnadieu, Y., Dutay, J.-C., Jaramillo, C., Le Bras, J., Martin, E., Montes, C., Waite, A.J., 2014. Consequences of shoaling of the Central American Seaway determined from modeling Nd isotopes. 29, 176-189.

Sherwood, S.C., Webb, M.J., Annan, J.D., Armour, K.C., Forster, P.M., Hargreaves, J.C., Hegerl, G., Klein, S.A., Marvel, K.D., Rohling, E.J.J.R.o.G., 2020. An assessment of Earth's climate sensitivity using multiple lines of evidence. 58, e2019RG000678.

Shevenell, A.E., Ingalls, A.E., Domack, E.W., Kelly, C., 2011. Holocene Southern Ocean surface temperature variability west of the Antarctic Peninsula. Nature 470, 250-254.

Sievers, H., Nowlin Jr, W., 1988. Upper ocean characteristics in Drake Passage and adjoining areas of the Southern Ocean, 39 W-95 W, Antarctic Ocean and resources variability. Springer, pp. 57-80.

Sievers, H.A., Nowlin Jr, W.D.J.J.o.G.R.O., 1984. The stratification and water masses at Drake Passage. 89, 10489-10514.

Sijp, W.P., England, M.H., Huber, M.J.P., 2011. Effect of the deepening of the Tasman Gateway on the global ocean. 26.

Sikes, E.L., Umling, N.E., Allen, K.A., Ninnemann, U.S., Robinson, R.S., Russell, J.L., Williams, T.J., 2023. Southern Ocean glacial conditions and their influence on deglacial events. Nature Reviews Earth & Environment 4, 454-470.

Simões Pereira, P., van de Flierdt, T., Hemming, S.R., Frederichs, T., Hammond, S.J., Brachfeld, S., Doherty, C., Kuhn, G., Smith, J.A., Klages, J.P., Hillenbrand, C.-D., 2020. The geochemical and mineralogical fingerprint of West Antarctica's weak underbelly: Pine Island and Thwaites glaciers. Chemical Geology 550, 119649.

Singh, S.P., Singh, S.K., Goswami, V., Bhushan, R., Rai, V.K., 2012. Spatial distribution of dissolved neodymium and εNd in the Bay of Bengal: Role of particulate matter and mixing of water masses. Geochimica et Cosmochimica Acta 94, 38-56.

Skinner, L., Sadekov, A., Brandon, M., Greaves, M., Plancherel, Y., de La Fuente, M., Gottschalk, J., Souanef-Ureta, S., Sevilgen, D., Scrivner, A.J.G.e.C.A., 2019. Rare Earth Elements in early-diagenetic foraminifer 'coatings': Pore-water controls and potential palaeoceanographic applications. 245, 118-132.

Smith, D.A., Hofmann, E.E., Klinck, J.M., Lascara, C.M.J.D.S.R.P.I.O.R.P., 1999. Hydrography and circulation of the west Antarctic Peninsula continental shelf. 46, 925-949.

Solodoch, A., Stewart, A., Hogg, A.M., Morrison, A., Kiss, A., Thompson, A., Purkey, S., Cimoli, L.J.G.R.L., 2022. How does antarctic bottom water cross the southern ocean? 49, e2021GL097211.

Solomon, S., Qin, D., Manning, M., Chen, Z., Marquis, M., Averyt, K., Tignor, M., Miller, H.J.C.c., 2007. IPCC fourth assessment report (AR4). 374.

Spence, P., Griffies, S.M., England, M.H., Hogg, A.M., Saenko, O.A., Jourdain, N.C.J.G.R.L., 2014. Rapid subsurface warming and circulation changes of Antarctic coastal waters by poleward shifting winds. 41, 4601-4610.

Stärz, M., Jokat, W., Knorr, G., Lohmann, G.J.N.c., 2017. Threshold in North Atlantic-Arctic Ocean circulation controlled by the subsidence of the Greenland-Scotland Ridge. 8, 15681.

Steinthorsdottir, M., Coxall, H., De Boer, A., Huber, M., Barbolini, N., Bradshaw, C., Burls, N., Feakins, S., Gasson, E., Henderiks, J.J.P., Paleoclimatology, 2021. The Miocene: the future of the past. 36, e2020PA004037.

Stichel, T., Frank, M., Rickli, J., Hathorne, E.C., Haley, B.A., Jeandel, C., Pradoux, C.J.G.e.C.A., 2012. Sources and input mechanisms of hafnium and neodymium in surface waters of the Atlantic sector of the Southern Ocean. 94, 22-37.

Subha Anand, S., Rahaman, W., Lathika, N., Thamban, M., Patil, S., Mohan, R.J.G., Geophysics, Geosystems, 2019. Trace elements and Sr, Nd isotope compositions of surface sediments in the Indian Ocean: An evaluation of sources and processes for sediment transport and dispersal. 20, 3090-3112.

Suresh, K., Kumar, A., Ramaswamy, V., Prakash Babu, C., 2021. Seasonal variability in aeolian dust deposition fluxes and their mineralogical composition over the Northeastern Arabian Sea. International Journal of Environmental Science and Technology.

Tachikawa, K., Arsouze, T., Bayon, G., Bory, A., Colin, C., Dutay, J.-C., Frank, N., Giraud, X., Gourlan, A.T., Jeandel, C.J.C.G., 2017. The large-scale evolution of neodymium isotopic composition in the global modern and Holocene ocean revealed from seawater and archive data. 457, 131-148.

Tachikawa, K., Athias, V., Jeandel, C.J.J.o.G.R.O., 2003. Neodymium budget in the modern ocean and paleo-oceanographic implications. 108.

Tachikawa, K., Piotrowski, A.M., Bayon, G.J.Q.S.R., 2014. Neodymium associated with foraminiferal carbonate as a recorder of seawater isotopic signatures. 88, 1-13.

Talarico, F.M., Sandroni, S.J.G., Change, P., 2011. Early Miocene basement clasts in ANDRILL AND-2A core and their implications for paleoenvironmental changes in the McMurdo Sound region (western Ross Sea, Antarctica). 78, 23-35.

Talley, L., Feely, R., Sloyan, B., Wanninkhof, R., Baringer, M., Bullister, J., Carlson, C., Doney, S., Fine, R., Firing, E.J.A.r.o.m.s., 2016. Changes in ocean heat, carbon

content, and ventilation: a review of the first decade of GO-SHIP global repeat hydrography. 8, 185-215.

Talley, L.D.J.E.o.G.E.C., 2002. Ocean circulation. 1, 557-579.

Tanaka, T., Togashi, S., Kamioka, H., Amakawa, H., Kagami, H., Hamamoto, T., Yuhara, M., Orihashi, Y., Yoneda, S., Shimizu, H., Kunimaru, T., Takahashi, K., Yanagi, T., Nakano, T., Fujimaki, H., Shinjo, R., Asahara, Y., Tanimizu, M., Dragusanu, C., 2000. JNdi-1: a neodymium isotopic reference in consistency with LaJolla neodymium. Chemical Geology 168, 279-281.

Thoma, M., Jenkins, A., Holland, D., Jacobs, S.J.G.R.L., 2008. Modelling circumpolar deep water intrusions on the Amundsen Sea continental shelf, Antarctica. 35.

Thomas, D.J., Via, R.K., 2007. Neogene evolution of Atlantic thermohaline circulation: Perspective from Walvis Ridge, southeastern Atlantic Ocean. Paleoceanography 22.

Thompson, A.F., Stewart, A.L., Spence, P., Heywood, K.J., 2018. The Antarctic Slope Current in a Changing Climate. Reviews of Geophysics 56, 741-770.

Tierney, J.E., Tingley, M.P., 2014. A Bayesian, spatially-varying calibration model for the TEX86 proxy. Geochimica et Cosmochimica Acta 127, 83-106.

Tierney, J.E., Tingley, M.P., 2015. A TEX86 surface sediment database and extended Bayesian calibration. Scientific Data 2, 150029.

Tigchelaar, M., Timmermann, A., Pollard, D., Friedrich, T., Heinemann, M.J.E., Letters, P.S., 2018. Local insolation changes enhance Antarctic interglacials: Insights from an 800,000-year ice sheet simulation with transient climate forcing. 495, 69-78.

Tiwari, M., Singh, A.K., Sinha, D.K., 2015. Stable isotopes: Tools for understanding past climatic conditions and their applications in chemostratigraphy, Chemostratigraphy. Elsevier, pp. 65-92.

Tomczak, M., Godfrey, J.S., 2003. Regional oceanography: an introduction. Daya books.

Tripathi, S., Tiwari, M., Lee, J., Khim, B.K., Scientists, I.E., 2017. First evidence of denitrification vis-a-vis monsoon in the Arabian Sea since Late Miocene. Scientific reports 7, 43056.

Tripathy, G.R., Singh, S.K., Bhushan, R., Ramaswamy, V., 2011. Sr–Nd isotope composition of the Bay of Bengal sediments: Impact of climate on erosion in the Himalaya. GEOCHEMICAL JOURNAL 45, 175-186.

Turner, J., Orr, A., Gudmundsson, G.H., Jenkins, A., Bingham, R.G., Hillenbrand, C.-D., Bracegirdle, T.J., 2017. Atmosphere-ocean-ice interactions in the Amundsen Sea Embayment, West Antarctica. Reviews of Geophysics 55, 235-276.

Uenzelmann-Neben, G., Gohl, K.J.G., Change, P., 2014. Early glaciation already during the Early Miocene in the Amundsen Sea, Southern Pacific: Indications from the distribution of sedimentary sequences. 120, 92-104.

Uenzelmann-Neben, G., Gohl, K.J.M.G., 2012. Amundsen Sea sediment drifts: archives of modifications in oceanographic and climatic conditions. 299, 51-62.

Uenzelmann-Neben, G., Gruetzner, J.J.M.G., 2018. Chronology of Greenland Scotland Ridge overflow: What do we really know? 406, 109-118.

Van Andel, T.H., 1975. Mesozoic/cenozoic calcite compensation depth and the global distribution of calcareous sediments. Earth and Planetary Science Letters 26, 187-194.

Van de Flierdt, T., Goldstein, S.L., Hemming, S.R., Roy, M., Frank, M., Halliday, A.N.J.E., Letters, P.S., 2007. Global neodymium–hafnium isotope systematics—revisited. 259, 432-441.

van de Flierdt, T., Griffiths, A.M., Lambelet, M., Little, S.H., Stichel, T., Wilson, D.J.J.P.T.o.t.R.S.A.M., Physical, Sciences, E., 2016. Neodymium in the oceans: a global database, a regional comparison and implications for palaeoceanographic research. 374, 20150293.

Van de Flierdt, T., Robinson, L.F., Adkins, J.F.J.G.e.C.A., 2010. Deep-sea coral aragonite as a recorder for the neodymium isotopic composition of seawater. 74, 6014-6032.

Vance, D., Thirlwall, M.J.C.G., 2002. An assessment of mass discrimination in MC-ICPMS using Nd isotopes. 185, 227-240.

von Blanckenburg, F., Nägler, T.F.J.P., 2001. Weathering versus circulation-controlled changes in radiogenic isotope tracer composition of the Labrador Sea and North Atlantic Deep Water. 16, 424-434.

von Blanckenburg, F.J.S., 1999. Tracing past ocean circulation? 286, 1862-1863.

von der Heydt, A., Dijkstra, H.A.J.P., 2006. Effect of ocean gateways on the global ocean circulation in the late Oligocene and early Miocene. 21.

Walker, D.P., Brandon, M.A., Jenkins, A., Allen, J.T., Dowdeswell, J.A., Evans, J.J.G.R.L., 2007. Oceanic heat transport onto the Amundsen Sea shelf through a submarine glacial trough. 34.

Walker, D.P., Jenkins, A., Assmann, K.M., Shoosmith, D.R., Brandon, M.A.J.J.o.G.R.O., 2013. Oceanographic observations at the shelf break of the Amundsen Sea, Antarctica. 118, 2906-2918.

Walter, H., Hegner, E., Diekmann, B., Kuhn, G.J.G.e.C.A., 2000. Provenance and transport of terrigenous sediment in the South Atlantic Ocean and their relations to glacial and interglacial cycles: Nd and Sr isotopic evidence. 64, 3813-3827.

Wang, R., Williams, T.J., Hillenbrand, C.-D., Ehrmann, W., Larkin, C.S., Hutchings, A.M., Piotrowski, A.M., 2022. Boundary processes and neodymium cycling along the Pacific margin of West Antarctica. Geochimica et Cosmochimica Acta 327, 1-20.

Weaver, A.J., Bitz, C.M., Fanning, A.F., Holland, M.J.A.R.o.E., Sciences, P., 1999. Thermohaline circulation: High-latitude phenomena and the difference between the Pacific and Atlantic. 27, 231-285.

Wei, W., Peleo-Alampay, A., 2020. Onset of North Atlantic Deep Water 11.5 million years ago triggered by climate cooling, 30th International Geological Congress, p. 57.64.

Weis, D., Kieffer, B., Maerschalk, C., Barling, J., De Jong, J., Williams, G.A., Hanano, D., Pretorius, W., Mattielli, N., Scoates, J.S.J.G., Geophysics, Geosystems, 2006. High-precision isotopic characterization of USGS reference materials by TIMS and MC-ICP-MS. 7.

Welke, B., Licht, K., Hennessy, A., Hemming, S., Pierce Davis, E., Kassab, C.J.G., Geophysics, Geosystems, 2016. Applications of detrital geochronology and thermochronology from glacial deposits to the Paleozoic and Mesozoic thermal history of the Ross Embayment, Antarctica. 17, 2762-2780.

Westerhold, T., Marwan, N., Drury, A.J., Liebrand, D., Agnini, C., Anagnostou, E., Barnet, J.S., Bohaty, S.M., De Vleeschouwer, D., Florindo, F.J.S., 2020a. An astronomically dated record of Earth's climate and its predictability over the last 66 million years. 369, 1383-1387.

Westerhold, T., Marwan, N., Drury, A.J., Liebrand, D., Agnini, C., Anagnostou, E., Barnet, J.S.K., Bohaty, S.M., De Vleeschouwer, D., Florindo, F., Frederichs, T., Hodell, D.A., Holbourn, A.E., Kroon, D., Lauretano, V., Littler, K., Lourens, L.J., Lyle, M., Pälike, H., Röhl, U., Tian, J., Wilkens, R.H., Wilson, P.A., Zachos, J.C., 2020b. An astronomically dated record of Earth's climate and its predictability over the last 66 million years. Science 369, 1383.

Westerhold, T., Marwan, N., Drury, A.J., Liebrand, D., Agnini, C., Anagnostou, E., Barnet, J.S.K., Bohaty, S.M., De Vleeschouwer, D., Florindo, F., Frederichs, T., Hodell, D.A., Holbourn, A.E., Kroon, D., Lauretano, V., Littler, K., Lourens, L.J., Lyle, M., Pälike, H., Röhl, U., Tian, J., Wilkens, R.H., Wilson, P.A., Zachos, J.C., 2020c. An astronomically dated record of Earth's climate and its predictability over the last 66 million years. 369, 1383-1387.

Whitworth III, T., Nowlin Jr, W.D.J.J.o.G.R.O., 1987. Water masses and currents of the Southern Ocean at the Greenwich Meridian. 92, 6462-6476.

Williams, G., Herraiz-Borreguero, L., Roquet, F., Tamura, T., Ohshima, K., Fukamachi, Y., Fraser, A., Gao, L., Chen, H., McMahon, C.J.N.c., 2016. The suppression of Antarctic bottom water formation by melting ice shelves in Prydz Bay. 7, 12577.

Williams, T., van de Flierdt, T., Hemming, S.R., Chung, E., Roy, M., Goldstein, S.L.J.E., Letters, P.S., 2010. Evidence for iceberg armadas from East Antarctica in the Southern Ocean during the late Miocene and early Pliocene. 290, 351-361.

Wilson, D.J., Bertram, R.A., Needham, E.F., van de Flierdt, T., Welsh, K.J., McKay, R.M., Mazumder, A., Riesselman, C.R., Jimenez-Espejo, F.J., Escutia, C., 2018. Ice loss from the East Antarctic Ice Sheet during late Pleistocene interglacials. Nature 561, 383-386.

Wilson, D.J., Piotrowski, A.M., Galy, A., Clegg, J.A., 2013. Reactivity of neodymium carriers in deep sea sediments: Implications for boundary exchange and paleoceanography. Geochimica Et Cosmochimica Acta 109, 197-221.

Wu, Y., Pena, L.D., Anderson, R.F., Hartman, A.E., Bolge, L.L., Basak, C., Kim, J., Rijkenberg, M.J., De Baar, H.J., Goldstein, S.L.J.E., Letters, P.S., 2022. Assessing neodymium isotopes as an ocean circulation tracer in the Southwest Atlantic. 599, 117846.

Yehudai, M., Tweed, L.E., Ridge, S., Wu, Y., Goldstein, S.L.J.G.R.L., 2023. Effects of Past Nd Seawater Concentrations on Nd-Isotope Paleocirculation Reconstructions: A Bayesian Approach. 50, e2023GL104489.

You, Y.J.J.o.G.R.O., 2000. Implications of the deep circulation and ventilation of the Indian Ocean on the renewal mechanism of North Atlantic Deep Water. 105, 23895-23926.

Yu, J., Menviel, L., Jin, Z.D., Anderson, R.F., Jian, Z., Piotrowski, A.M., Ma, X., Rohling, E.J., Zhang, F., Marino, G., McManus, J.F., 2020. Last glacial atmospheric CO2 decline due to widespread Pacific deep-water expansion. Nature Geoscience 13, 628-633.

Zachos, J., Pagani, M., Sloan, L., Thomas, E., Billups, K., 2001. Trends, Rhythms, and Aberrations in Global Climate 65 Ma to Present. 292, 686-693.

Zachos, J.C., Dickens, G.R., Zeebe, R.E.J.n., 2008. An early Cenozoic perspective on greenhouse warming and carbon-cycle dynamics. 451, 279-283.

Zachos, J.C., Kroon, D., Blum, P., 2004. Leg 208 Summary, Proceedings of the Ocean Drilling Program Initial Reports. Ocean Drilling Program, College Station, TX, pp.

112.

Zalasiewicz, J., Williams, M., 2021. Climate change through Earth history, Climate change. Elsevier, pp. 49-65.

Zhao, K., Wulder, M.A., Hu, T., Bright, R., Wu, Q., Qin, H., Li, Y., Toman, E., Mallick, B., Zhang, X., Brown, M., 2019. Detecting change-point, trend, and seasonality in satellite time series data to track abrupt changes and nonlinear dynamics: A Bayesian ensemble algorithm. Remote Sensing of Environment 232, 111181.

List of Publications

Publications from the thesis:

- **Prabhat, P.**, Rahaman, W., Lathika, N. *et al.* Modern-like deep water circulation in Indian Ocean caused by Central American Seaway closure. ***Nature communications*** 13, 7561 **(2022)**. https://doi.org/10.1038/s41467-022-35145-0.

Other Publications:

- Deepak Kumar, N.V. Chalapathi Rao, Aparajita Tripathi, B. Belyatsky, **Priyesh Prabhat**, Waliur Rahaman, M. Satyanarayanan, U-Pb Neoproterozoic age and petrogenesis of a calc-alkaline shoshonitic lamprophyre from Simdega area, Chhotanagpur Gneissic Complex (Eastern India): Implication for the evolution of the Central Indian Tectonic Zone and Rodinia tectonics, **Chemical Geology**, Volume 631, **2023**, 121512, ISSN 0009-2541. https://doi.org/10.1016/j.chemgeo.2023.121512.

- Waliur Rahaman, N. Lathika, **Priyesh Prabhat**, Mohd. Tarique, K.S. Arya, Ravi Mishra, Meloth Thamban, Eolian versus fluvial supply to the northern Arabian Sea during the Holocene based on Nd isotope and geochemical records, **Geoscience Frontiers**, Volume 14, Issue 5, **2023**, 101618, ISSN 1674-9871, https://doi.org/10.1016/j.gsf.2023.101618.

- Deepak Kumar, N.V. Chalapathi Rao, **Priyesh Prabhat**, Amitava Chatterjee, Waliur Rahaman, Petrochemistry and Sr-Nd isotopes of post-collisional Neoproterozoic (ca. 950 Ma) amphibolite dykes of continental flood basalt affinity from the Simdega area: Implications for the geodynamic evolution of the Chhotanagpur Gneissic Complex, Eastern India, **Lithos**, Volumes 428–429, **2022**, 106810, ISSN 0024-4937, https://doi.org/10.1016/j.lithos.2022.106810.

- Waliur Rahaman, Mohd Tarique, A.A. Fousiya, **Priyesh Prabhat**, Hema Achyuthan, Tracing impact of El Niño Southern Oscillation on coastal hydrology using coral $^{87}Sr/^{86}Sr$ record from Lakshadweep, South-Eastern Arabian Sea, **Science of The Total Environment**, Volume 843, **2022**, 157035, ISSN 0048-9697, https://doi.org/10.1016/j.scitotenv.2022.157035.

List of Conferences

- **Prabhat, P.**, Rahaman, W., Lathika, N., Tarique, M., & Mishra, R., Timing and mechanism for the onset of modern like deep water circulation in the Indian Ocean. In **Frontiers in Geosciences Research Conference (FGRC-2021)** online by Physical Ocean Research Laboratory, Ahmedabad, India (**2021, 27–28 September**).

- **Prabhat, P.**, Rahaman, W., Lathika, N., Tarique, M., & Mishra, R., Late Miocene to Early Pleistocene Deep Water Circulation in the Arabian Sea. In **American Geophysical Union (AGU-2020)** Fall Meeting Abstracts (Vol. 2020, pp. PP001-0004) held online by American Geophysical Union (**2020, 1–17 December**).

- **Prabhat, P.**, Rahaman, W., Lathika, N., & Mishra, R., Reconstruction of late Miocene deep-watermass circulation in the Arabian Sea using authigenic Neodymium isotope record. In **National Conference on Polar Sciences (NCPS-2019)** at National Centre For Polar And Ocean Research, Goa, India (**2019, 19–22 August**).